Fast and accurate hot-spot estimation in electrical machines

Pietro Romanazzi
St Hilda's College
University of Oxford

A thesis submitted for the degree of
Doctor of Philosophy

Trinity 2017

Declaration

I, Pietro Romanazzi, hereby declare that except where specific reference is made to the work of others, the contents of this dissertation are original and have not been submitted in whole or in part for consideration for any other degree or qualification in this, or any other university. This dissertation is my own work and contains nothing which is the outcome of work done in collaboration with others, except as specified in the text and Acknowledgements. Parts of the work have been presented at conferences and published in journal papers; these are specified in the text and referenced accordingly.

Pietro Romanazzi
June 2017

Acknowledgements

To begin I'd like to thank my supervisors Dr David Howey and Dr Maria Bruna for their guidance, patience and invaluable support in the last three years. Thanks to their advice I managed to get the most out of this experience. I express my gratitude to the European Union that founded this research through the Marie Curie ITN ADEPT project. I would also like to thank all the partners and researchers from the ADEPT project; in particular, due to valuable assistance and countless discussions, I would like to mention (not in order of importance) Sabrina Ayat and Dr Rafal Wrobel (Bristol University), Kesavan Ramakrishnan and Prof Gianpiero Mastinu (Politecnico di Milano), Dr Valerio Galizzi, Alessio Miotto and Fabio Carbone (Brempo Spa), Fabien Chauvicourt (Siemens Industry Software NV), Dr Nuwantha Fernando (Royal Melbourne Institute of Technology), Dr Stjepan Stipetic (University of Zagreb), Prof Johan Gyselinck (Université libre de Bruxelles), Mitrofan Curti (Eindhoven University of Technology) and Korawich Niyomsatian (Triphase NV). I would like to thank all the friends from Oxford, in particular the Holder group and the rest of the Energy and Power Group, the OU volleyball team and everyone who has participated to this memorable adventure. Finally, my greatest gratitude goes to all the friends and family that came to visit me and stayed at the "Italian embassy" in Oxford or supported me from home. And to my wife, Arianna, because without her I would not have started this challenge and, more importantly, I would not have finished this work.

Abstract

Temperature is one of the parameters that limits the output torque and reduces the lifespan of electrical machines. Models that can provide accurate estimation of the temperature field in the most critical components (e.g. windings) at lower computational effort can be useful to improve the design process and reduce the time to market. Depending on the application, engineers usually rely on hi-fidelity models, e.g. based on the finite elements method (FEM), or lower order models, e.g. thermal equivalent circuits (TECs). The aim of the present work is to provide new tools and methodologies to obtain the temperature distribution within the windings using reduced order hi-fidelity models or improved TEC that could account for any working condition, including AC effects.

A new methodology, based on the multiple scales method (MSM), is introduced which homogenises the complex windings domain and allows for the estimation of its effective thermal properties. The homogenisation through the MSM is performed solving a single elementary cell. The MSM also allows for the reconstruction of the actual thermal field. Extensive numerical and experimental validation is provided, in particular for the case of electrical windings encapsulated with epoxy.

The thermal homogenisation is then combined with an electromagnetic homogenisation technique to estimate winding losses including AC effects, such as proximity and skin effects. The coupled analysis is validated numerically on reference test problems, and experimentally, on a suitably built "motorette". The method is proven to correctly predict losses including thermal effects and to estimate magnitude and location of the temperature hotspot within the winding domain.

This work also introduces a new approach for building thermal equivalent circuits that represents the most commonly employed modelling technique for electrical machine thermal analysis. Here the TEC approaches are thoroughly analysed, highlighting limitations. The proposed new technique extends the range of numerical accuracy, accounting for high Biot numbers (up to Bi = 2) and internal heat generation. The result of this approach is higher spatial resolution about the temperature field within the winding domain and thus enables improved information on hotspot location and magnitude. The method is experimentally validated and also applied to model an electrical machine for full-electric in-wheel vehicle propulsion.

Contents

List of Figures

List of Tables

Nomenclature

Abbreviations

AC	alternating current
ATF	automatic transmission fluid
CFD	computational fluid dynamics
DC	direct current
DLC	distributed loss and capacitance
EM	electromagnetic
FE	finite element
FEM	finite element method
IPM	internal permanent magnet
MOT	maximum operating temperatures
MSM	multiple scale method
SPM	surface mounted permanent magnet
SyRM	synchronous reluctance machine
SRM	switched reluctance machine
rms	root mean square
TEAM	thermal, electrical, ambient (environmental) and mechanical
TEC	thermal equivalent circuit

Roman symbols

$\boldsymbol{A}$	Magnetic vector potential [Vs/m]
$\boldsymbol{B}$	Magnetic flux density [T]
Bi	Biot number
c	constant
c_p	specific heat capacity [J/ kg K]
$\boldsymbol{E}$	electric field
f	frequency [Hz]
f_δ	reduced frequency

g	airgap thickness [m]
h	convection heat transfer coefficient [W/m^{2}K]
$\boldsymbol{H}$	magnetic field [A/m]
$\boldsymbol{I}$	current [A]
$\boldsymbol{J}$	current density [A/m^3]
k	thermal conductivity [W/mK]
l	periodicity distance [m]
L	distance [m]
$\dot{m}$	mass flow [kg/s]
Nu	Nusselt number
n_w	number of wires per slot
$\mathbf{n}$	unit surface normal vector
$\boldsymbol{S}$	Poynting vector [W/m^2]
Pr	Prandtl number
$\dot{q}$	specific heat transfer rate [W/m^3]
P	power [W]
r	radius [m]
R	resistance
Re	Reynolds number
T	temperature [°C]
$\bar{T}$	average temperature [°C]
t	time [s]
Ta	Taylor number
u	fluid speed magnitude [m/s]
V	voltage [V]
x, y, z	Cartesian coordinates [m]
$\mathbf{X}$	macroscopic coordinate system [m]
$\mathbf{Y}$	microscopic coordinate system [m]
Z	impedance [Ω]

Greek symbols

α	temperature coefficient [1/°C]
α_p	dimensionless thermal capacity

β	dimensionless thermal conductivity
$\mathbf{\Gamma}$	vector function in the micro domain
ϵ_S	emissivity
ε	conductor radius [m]
δ	ratio l/L
δ_{skin}	skin depth [m]
δ_T	temperature boundary layer [m]
δ_u	velocity boundary layer [m]
Θ	dimensionless temperature
λ	filling ratio - volume fraction
$\hat{\mu}$	dynamic viscosity [kg/sm]
μ	permeability [H/m]
$\hat{\nu}$	kinematic viscosity [m^2/s]
ν	reluctivity [m/H]
ρ	density [kg/m^3]
ρ_J	electrical resistivity [Ω m]
σ	electrical conductivity [S/m]
σ_{SB}	Stefan-Boltzmann constant $5.67 \times 10^{-8}\,\mathrm{W/m^2K^4}$
τ	dimensionless time
$\Delta\Phi$	insulation endurance [h]
Ψ	dimensionless heat generation
ω	angular velocity [rad/s]
Ω	cell domain

Subscripts

c	conductor material
cond	conduction
cont	contact
conv	convection
core	laminated core
cu	copper
eq	effective property
ew	end winding domain

f	filling material
full, fine	brute force solution
i	insulation material
MS	multiple scales
rad	radiation
ref	reference value
S	surface
wj	water jacket
∞	ambient condition
’	real part
”	imaginary part

Chapter 1

Introduction

This research is part of the ADvanced Electric Powertrain Technology (ADEPT) project, an EU funded Marie Curie ITN project. The main goal of the ADEPT project is to create a virtual library to assist the design and analysis of novel electric propulsion systems. The ADEPT program combines an international research community from a number of European universities and industries. Within this framework, the objective of this work is to create and improve methodologies to estimate and monitor the temperatures in electrical machines, in particular the hot-spot, validated with suitable experimental tests.

Due to the significant level of greenhouse gas (GHG) emissions from vehicles and other means of transport (13% of the overall GHG emissions according to [5]), there is increasing interest to move towards hybridization or electrification of powertrains. This tread has already started, as evidenced by the number of hybrid or full electric cars available on the market. Much work must be done to improve the fundamental components of these novel powertrains, such as the electric motor, the power electronics and the batteries, to optimise the driving range. To enable industry to design more efficient components and fine-tune the behaviour of the whole powertrain, "fast" and "accurate" tools that can predict and monitor the temperatures in the electric ma-

chine are needed, that can speed up the time to market and, thus, reduce production costs.

In this chapter we introduce the thermal issues to be considered for a correct design of an electrical machine, describe the common and novel cooling approaches, highlight the importance of thermal modelling and give the objectives of the present work. A detailed literature is given within each subsequent chapter in order to properly introduce the discussed methodologies and topics.

1.1 Thermal analysis of electrical machines

As far as the design of electrical machines is concerned, the heat transfer problem is of equal importance to the electromagnetic one, because the hot-spot temperature is one of the parameters that mostly affects the maximum output torque of the machine. Regardless of the machine topology and operating principles, there are thermal limitations to bear in mind. During operation, e.g. constant load or a driving cycle, the energy conversion in an electrical machine generates losses that result in temperature rise of the various components. Each element cannot tolerate long exposure to temperatures higher than specific thresholds. This is particularly important for windings and magnets, which are the most sensitive to thermal stresses.

1.1.1 Critical components and their thermal limits

Reference machine sections are presented in Fig. 1.1. Fig. 1.1(a) presents a fan-cooled induction machine. Fig. 1.1(b) shows a diagram of a liquid-cooled radial-flux internal-permanent-magnet (IPM) machine, a common machine topology for car propulsion [6]. Several other topologies have been developed and described in the literature. These topologies differ in the working mechanisms, e.g. flux (radial or axial), permanent magnets (no, surface, internal), windings (concentrated or distrib-

(a)

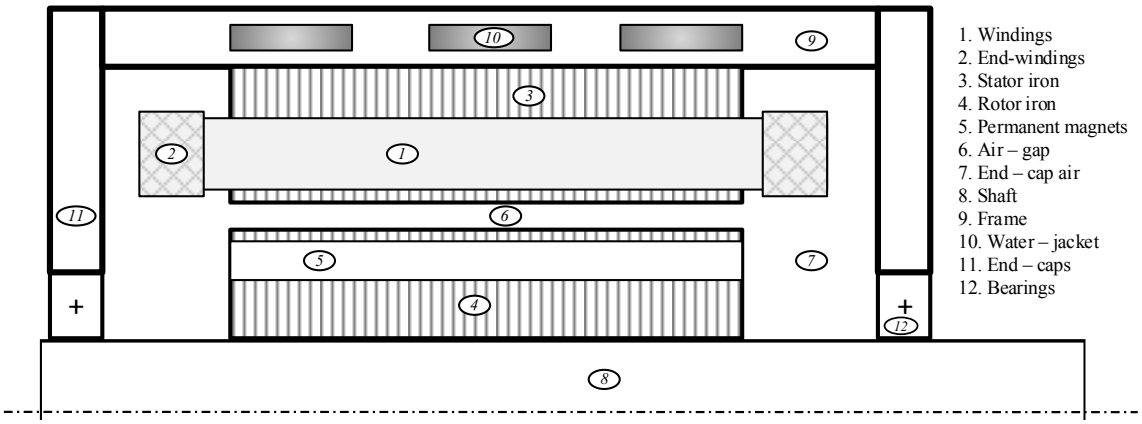

(b)

Figure 1.1: (a) Cross-section view of a fan-cooled induction machine (Courtesy of TU/Eindhoven, EPE group). (b) Sketch of the cross-section of a liquid-cooled radial-flux internal-permanent-magnet (IPM) machine

uted) and others, resulting in different performances and limitations. Fig 1.1(b) helps to visualise the elements that usually compose an electrical machine. Among these, the windings (elements 1 and 2) and the magnets (element 5) are the most critical components due to their relatively low threshold temperature and their conversion losses. In fact, problems in windings are responsible for 25% of low voltage ($< 4\,\mathrm{kV}$) machine failures [7].

Permanent magnets

Permanent magnets allow an electrical machine to achieve higher torque densities compared to other electrical machines. This is due to the remenance (residual magnetism) left in the magnet that increases the magnetic flux density in the airgap without requiring brushes and conducting rings to supply the rotor current and create the rotor magnetic field components that need to be serviced periodically. This justifies the application of permanent-magnet-assisted machines in the automotive industry [8,9]. The most common types of permanent magnets for electrical machines are rare-earth materials, such as Samarium-Cobalt (SmCo) and Neodymium-IronBoron (NdFeB), and ferrites, such as Barium ferrite (BaO·6Fe2O3) and Strontium ferrite (SrO·6Fe2O3) [10]. All these materials have high coercivity [9], that is, the property of withstanding an external magnetic field without demagnetising. However, irreversible demagnetisation can be triggered also if the so-called "Curie temperature" is reached. For ferrites the Curie temperature is $\approx 450\,^{\circ}\mathrm{C}$, while for SmCo and NdFeB is $\approx 825\,^{\circ}\mathrm{C}$ and $\approx 310\,^{\circ}\mathrm{C}$, respectively. For each permanent magnet a maximum operating temperatures (MOT) is also defined by manufactures; MOT represents to the temperature at which the magnet flux loss is equal to a certain level (often 5% loss) [10]. MOTs reference values are $\approx 250\,^{\circ}\mathrm{C}$ for ferrites, $\approx 350\,^{\circ}\mathrm{C}$ for SmCo, and $\approx 110\,^{\circ}\mathrm{C}$ for NdFeB [11]. The use of SmCo is less attractivedue due to its cost, which is highly dependent on the variable market price of Sm and Co [12]. Another factor

is the remenance, with ferrites having lower remenance ($\approx 0.3\,\mathrm{T}$) compared to SmCo ($\approx 0.9\,\mathrm{T}$) [13]. Moreover, for each magnet the remenance is not constant, but it usually reduces with increased temperature, accordingly affecting the performance of the machine [12]. Brittleness is another property of ferrites, which makes them more difficult to machine [11].

For these reasons alternative topologies to permanent magnet (PM) machines have been sought (in academia and industry) in the recent years. Machines that do not employ magnets, such as synchronous reluctance machines (SyRM) or switched reluctance machine (SRM), seem the most suitable for this purpose as they allow cost reduction and increased reliability [14].

Windings

An electrical machine winding is a coil of insulated conductors (see Fig. 1.2(a)). The conductors are usually kept together by a filling (varnish or epoxy as shown in Fig. 1.2(b)), which allows the winding to keep its shape and optimise the amount of conductors inside a slot. Moreover, an additional electrical insulation is added between the winding compound and the stator core, usually referred to as slot liner [15]. The function of the conductor insulation is to prevent turn-to-turn short circuits while the slot liner main task is to prevent turn-to-ground failures; while the former can still allow operations, turn-to-ground stops the machine functioning [16]. During operation, the insulation strength is subjected to a number of stresses, which are usually summarised under the acronym "TEAM": thermal, electrical, ambient (environmental), and mechanical [17]. The exposure to such stresses leads to ageing of the insulation material, which may result in the insulation failure. Interturn faults can be difficult to detect until the machine stops working [18]. Accordingly methodologies have been studied to detect and diagnose incipient insulation faults. These are based on the analysis of the signals that are affected by the fault induced imbalances,

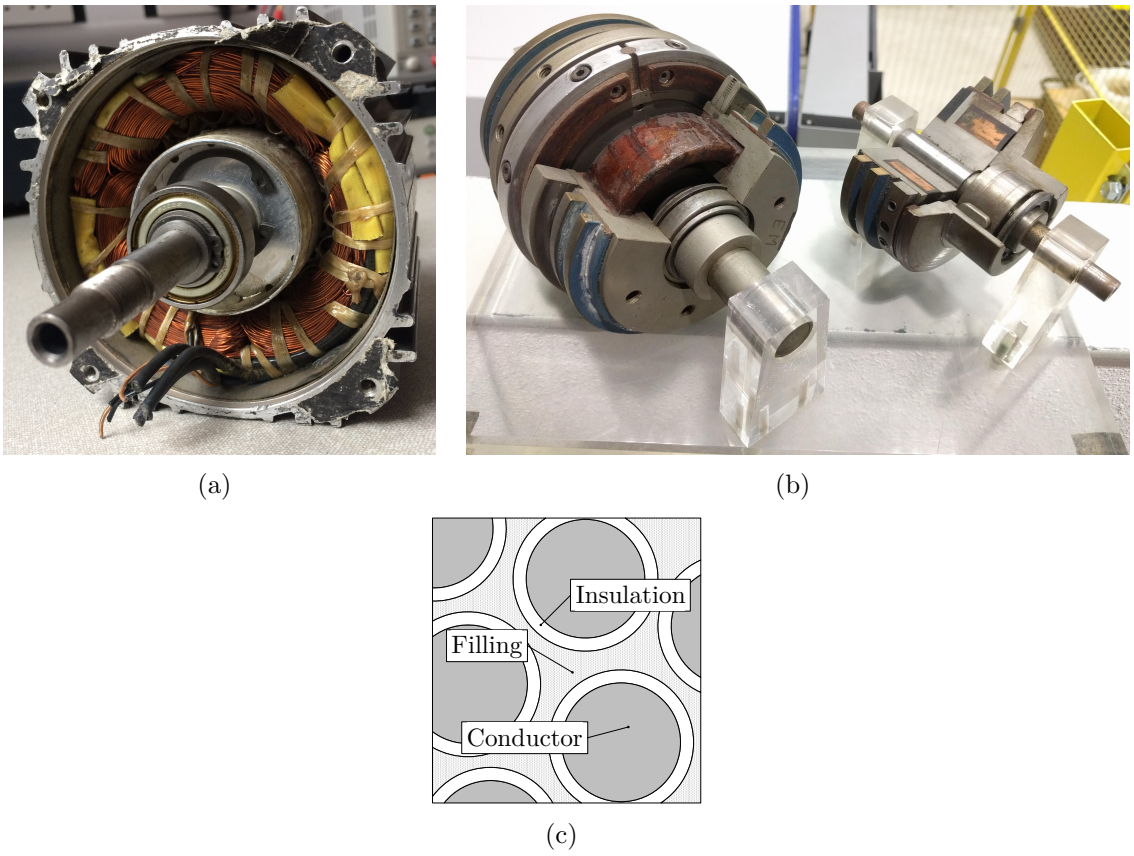

Figure 1.2: View of electrical machine stator windings (a) without encapsulation (Courtesy of Bristol University) and (b) after varnish and epoxy encapsulation (Courtesy of TU/Eindhoven, EPE group). (c) Cross-section of a reference winding

such as torque, air-gap flux, stator currents, and others [19].

Although insulation degradation depends on a combination of all the TEAM factors [20], temperature plays a particularly important role. High temperature exposure can modify the material structure, varying the electrical [21], mechanical [22], and thermal [20] properties, or induce mechanical stresses due to thermal expansion and shear between neighbouring conductors [23].

According to Underwriters Laboratories standardisation [2], the insulation material characteristics are divided into classes, as listed in Table 1.1. Each class ensures continuous operations for at least 20 000 hours (2.5 years) if the winding hot-spot temperature is lower than the prescribed thermal threshold. As suggested in the pioneering work of Montsinger [24], the insulation lifespan should be halved for each

Table 1.1: Insulation classes according to Underwriters Laboratories [2]

Insulation class	Thermal rating [°C]
A	105
B	130
F	155
H	180
N	200
R	220

10 °C increase above the threshold. This means that a slight increase of the working temperature above limits leads to an exponential growth of failure probability [25]. In [26] the use of an Arrhenius law for the modelling of the insulation thermal degradation is proposed:

$$\Delta\Phi = c_1 \, e^{\frac{c_2}{T}}, \tag{1.1}$$

where $\Delta\Phi$ is the insulation endurance [h], c_1 and c_2 are constants, and T is the absolute temperature. This formula combined with a machine thermal model ideally enables the prediction of when the machine should fail, depending on the particular driving cycle [27].

The field of prognostics for electrical machines is relatively new, and thus far no model has been able to provide accurate estimations of the machine expected lifespan, something extremely beneficial for the automotive industry. In order to develop a reliable thermal degradation model, one has to know the temperature distribution within the winding and, in particular, the hot-spot. Currently, it is difficult to obtain embedded winding temperatures [28] due to the large number of sensors required and the complexity of placing them during the manufacturing process. As such, one has to rely on estimations using models that describe the thermal behaviour of an electrical machine, considering the specific geometry, material properties, boundary conditions, and losses. Before introducing electrical machine thermal models, it is useful to take a

more in-depth look at a reference electrical machine topology and describe the various heat paths that need to be considered to estimate the temperatures of the various components.

1.1.2 Heat paths in an electrical machine

To avoid overheating of an electrical machine or any other electromagnetic equipment, the heat generated during operation has to be removed by means of a coolant. As described in later sections, the components that generate heating losses are the windings, the stator iron, the magnets, the rotor iron, and the bearings. In addition, the air enclosed in the machine produces "windage losses", due to friction. Fig. 1.3 describes a common cooling arrangement and helps discussing the possible heat paths. Indeed, the generated heat has to flow through various mediums before reaching the coolant, i.e. the water flowing in the water jacket or the surrounding ambient air.

Let us consider, as an example, the paths that the heat can take from the windings to the coolant. As shown in Fig. 1.3(a), one option is for the heat to flow though the teeth and yoke to the housing. Here, the driving heat transfer phenomenon is conduction. Conduction refers to energy transport in a medium driven by a thermal gradient [3] and is governed by Fourier's law

$$\dot{q}_{\text{cond}} = -k\frac{\partial T}{\partial x} \tag{1.2}$$

where $\dot{q}_{\text{cond}}$ is the specific heat flowing along the reference direction x, T is the temperature, and k [W/mK] is the thermal conductivity, the ability of a material to transport heat for a given temperature difference. The heat is then transferred, in this example, to the liquid coolant via convection. Convection is an energy transport mechanism that takes place in fluids, since it consists of the combination of diffusion and the macroscopic motion of the fluid [3]. In this case the specific heat $\dot{q}_{\text{conv}}$ ex-

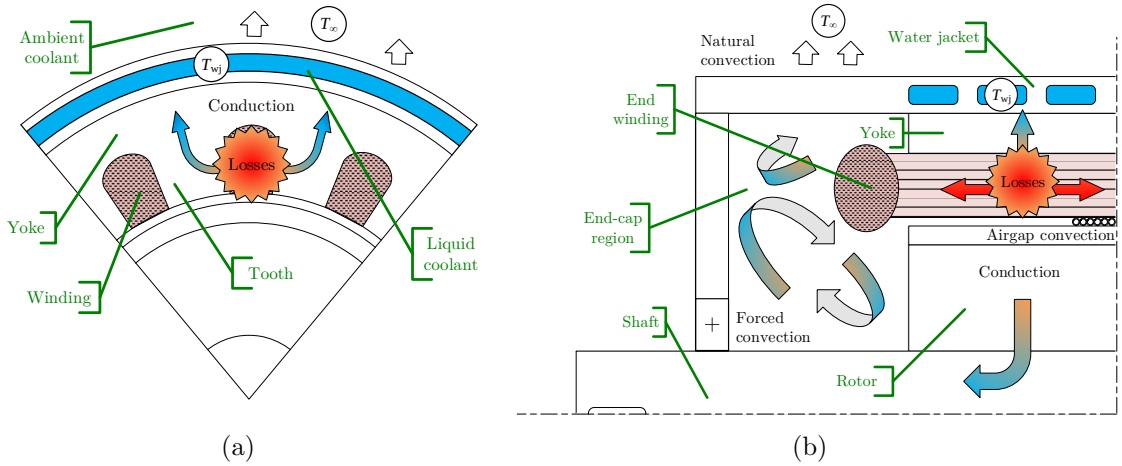

Figure 1.3: Visualisation of the heat paths from the windings to the coolant from a (a) front and (b) lateral view of a liquid cooled surface-mounted permanent-magnet machine (SPM)

changed at the boundary between the solid and the fluid can be described with the Newton's law of cooling

$$\dot{q}_{\text{conv}} = h\,(T_S - T_\infty) \tag{1.3}$$

where T_S is the surface temperature, T_∞ is the temperature of the ambient air (outside the thermal boundary layer), and h [W/m^{2}K] is the convection heat transfer coefficient. To understand better the meaning of this coefficient we need to introduce the concept of boundary layer, which can be defined as a function of the developing temperature and velocity fields in a fluid when it flows along a solid surface. For instance, let us consider the flow over a flat plate, as depicted in Fig. 1.4. It is assumed that the flow speed in contact with the plate is equal to $u(0) = 0$, and that the velocity amplitude increases until reaching the free stream velocity, u_∞. We can now introduce the velocity boundary layer, δ_u, as the distance from the plate surface at which $u(\delta_u) = 0.99\,u_\infty$ [3]. Similarly, we can define as well a thermal boundary layer. Assuming that the plate surface is heated at a uniform $T(0) = T_S$, the thermal boundary layer, δ_T, is the distance from the plate surface at which $T_S - T(\delta_T) = 0.99\,(T_S - T_\infty)$ [3], where T_∞ is the surrounding ambient temperat-

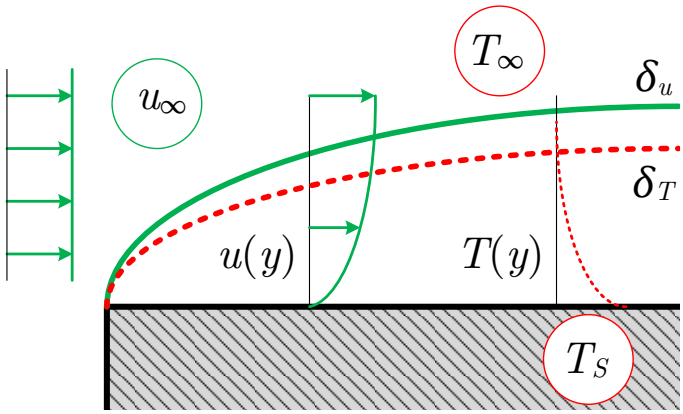

Figure 1.4: Development of the velocity and temperature boundary layers on a flat surface

ure. One can now understand how the temperature and velocity profiles within the related boundary layers are affected by the fluid flow conditions (e.g. turbulent or laminar) and by the geometry of the surface to be cooled. As a consequence, these parameters strongly affect the heat transfer coefficient h, since the heat flux at the surface is transferred by convection is equal to [3]

$$\dot{q}_{conv} = -k_{fluid} \frac{\partial T}{\partial y}\Big|_{y=0}, \tag{1.4}$$

which combined to (1.3) gives

$$\dot{q}_{conv} = \frac{-k_{fluid} \partial T/\partial y|_{y=0}}{(T_S - T_\infty)}. \tag{1.5}$$

In Table 1.2 typical values of the convection heat transfer coefficient are given as a function of the cooling media and mechanism. These values highlight the difference between natural convection, where the fluid motion is driven by buoyancy forces due to density gradients, and forced convection, where the fluid movement is promoted by imposed pressure gradients due to the work performed by a fan or a pump. Moreover, Table 1.2 shows that a liquid coolant can be more effective compared to a gas due to the higher thermal conductivity ($k_{\text{water}} \approx 0.58\,\text{W/mK}$ Vs. $k_{\text{air}} \approx 0.024\,\text{W/mK}$), as

Table 1.2: Reference values for the convection heat transfer coefficient [3]

Coolant	Cooling condition	h [W/m^{2}K]
Gas	Natural convection	2 - 25
	Forced convection	25 - 250
Liquid	Natural convection	50 - 1000
	Forced convection	100 – 20 000

confirmed by (1.5). It must be noted that these values are approximations, computed as the surface average value of the convection heat transfer coefficient. The precise magnitude of h and its surface distribution can be only measured with bespoke experimental tests or estimated with computationally demanding CFD (computational fluid dynamics) simulations.

The second heat path is through the air in the end-cap region, as depicted in Fig. 1.3(b). Here, convection is the main mechanism to transfer heat to the coolant and the ambient environment. In the presence of a water-jacket, a very limited percentage of heat generated by the windings flows along this path. This is due to the low heat transfer coefficient between the end-windings and the end-cap air (maximum 250 W/m^{2}K according to Table 1.2), and the low heat capacity of air that leads its temperature to increase quickly.

Radiation consists of energy emissions from the external surface of a body that is at nonzero temperature [3]. The specific emitted energy rate is a function of the surface temperature according to the Stefan-Boltzmann law

$$\dot{q}_{\text{rad}} = -\epsilon_S \sigma_{SB} T_S^4 \tag{1.6}$$

where σ_{SB} is the Stefan-Boltzmann constant ($\sigma_{SB} = 5.67 \times 10^{-8}\,\text{W/m}^2\text{K}^4$) and ϵ_S is emissivity, which represents the efficiency of the surface in radiating compared to a blackbody ($0 \leq \epsilon_S \leq 1$) [3]. According to [29], however, the amount of heat

transferred via radiation is significant only when a machine is cooled via natural convection. In [29] a totally enclosed fan cooled induction machine of 150 W rated power was tested with the rotor spinning a 2800 rpm; in this specific working condition the heat generation was about 7 W. It was measured that around the 40% of this loss was removed via natural convection and the remaining 60% via radiation.

If a more "power dense" cooling approach is employed, i.e. forced convection, this contribution becomes negligible. In this thesis we are only dealing with forced convection cooled machines (via liquid cooling) or electromagnetic equipments. Thus, the effect of radiation is neglected.

From Fig. 1.3 it is also apparent that the elements that are most difficult to cool are the windings, because the heat has to travel the longest distance to reach the coolant. The magnets can also be complicated to cool. However, we must bear in mind that the permanent magnets' heat generation rate is significantly lower than the windings for most working conditions [30] and sometimes they can also be neglected [27,31,32]. Indeed, magnet losses are generated by induced eddy currents, which magnitude is a function of the rotational speed, which again is a function of current frequency f [33–35]. In general, the amount of losses in the magnets depends on a number of factors further to f, as for instance the magnet material properties, especially electrical conductivity [33], magnet location with respect to the rotor geometry (interior or surface-mounted) [33,36], number of slots per pole pair [34,37] and current waveform due to PWM [34,35,37,38]. Accordingly, it is difficult to generalise the magnet loss contribution, however, they seldom count for more then 10% of the total loss [32,33, 38]. Moreover, since the rotor is connected through the shaft to a bigger domain, e.g. the vehicle chassis, the magnets can exploit a much larger exchanging surface and heat capacity. Accordingly, the main focus is to reduce the thermal resistance from the windings to the coolant, in order to increase the machine torque density.

1.1.3 Convection heat transfer in electrical machines

As mentioned in Section 1.1.2, the accurate evaluation of the convection heat transfer coefficient requires particular care due to its dependence on the physical properties of the fluid as well as the characteristics of the flow and boundary layer. In the field of electrical machines thermal analysis, much attention has been devoted to the heat transfer coefficient related to the end windings [1,39–43]. Due to the geometrical differences of the end-cap region, linked to the machine topology and optimised design, it is not yet possible to define a general correlation that could express h as a function of ω and the air flow velocity.

In [1] it is shown that the experimental measurements of the end-cap heat transfer coefficient h_S obtained by various authors can be expressed in the form

$$h_S = k_1(1 + k_2\ u^{k_3}), \tag{1.7}$$

where k_1, k_2, and k_3 are curve fitting coefficients and u is the local fluid velocity (m/s), which is a function of the rotational speed. This means that once a prototype is available, a reduced number of tests are required to obtain the parameters and have a good approximation of the convection heat transfer coefficient for a large range of rotational speeds.

It is also important to accurately estimate the convection heat transfer between the external surface of the machine and the ambient environment, or inside the water-jacket ducts with the coolant, as it ultimately defines the amount of heat removed from the machine. In [44] a collection of the most relevant correlations from the literature is provided. For generality, these correlations are expressed in terms of dimensionless groups

$$\mathrm{Nu} = c_1\ \mathrm{Re}^{c_2}\ \mathrm{Pr}^{c_3}, \tag{1.8}$$

where $\mathrm{Nu} = h_S L_{\mathrm{ref}}/k_{\mathrm{fluid}}$ is the Nusselt number comparing convection and conductive

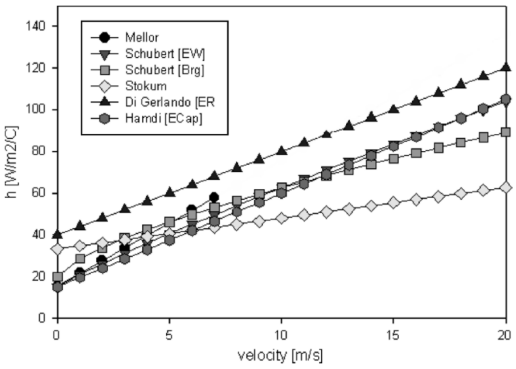

Figure 1.5: End-space convection correlations from the literature [1]

heat transfer in the fluid flow; Re is the Reynolds number that represents the ratio of inertial forces to viscous forces within a fluid, $\mathrm{Re} = \rho u L_{\mathrm{ref}}/\hat{\mu}_{\mathrm{fluid}}$, with $\hat{\mu}_{\mathrm{fluid}}$ the fluid dynamic viscosity; Pr is the Prandtl number that helps to assess the momentum diffusivity compared to the thermal diffusion rate, $\mathrm{Pr} = c_p \hat{\mu}_{\mathrm{fluid}}/k_{\mathrm{fluid}}$. In the literature, a large number of correlations are provided that should cover all the various geometrical and fluid flow conditions for the particular machine design. These, however, must be handed with extreme care, making sure to respect all the conditions related to the experiment from which the correlation was obtained, in particular the choice of the reference length L_{ref}, or the locations of the temperature measurements used to evaluate h.

It is important now to mention a particular convection heat path that connects the stator to the rotor: the airgap (element 6 in Fig. 1.1). Ideally, the width of airgap layer g would be null in order to reduce the reluctance of the magnetic circuit. In reality, due to obvious mechanical limitations, usually this layer thickness is larger then 0.5 mm. This thermal connection is quite important as it is the main path the heat can travel from the windings to the rotor, and accordingly affect the magnet temperature.

At low rotational speed ω the thin layer of air in the airgap acts as a thermal insulator, due to the low thermal conductivity of air ($k_{\mathrm{air}} = 0.0257\,\mathrm{W/mK}$, $k_{\mathrm{cast\ iron}} = 58\,\mathrm{W/mK}$, $k_{\mathrm{copper}} = 400\,\mathrm{W/mK}$). With increasing rotational speed, this heat transfer

path is governed by convection and usually the theory developed by Taylor [45] is applied. Taylor studied the instability that develops in an annulus between two smooth cylinders where the inner one is rotating. He found that pairs of counter-rotating vortices appear in the along the axial direction (Fig. 1.6(a)) above a specific rotational speed ω. Assuming the case of adiabatic flow between infinitely long smooth cylinders and very narrow gaps, i.e. $g/R_i \approx 0$ where R_i is the inner radius of the annulus, Taylor found that the onset of the instability occurs at $\mathrm{Ta}_c = 1697$, where Ta is a dimensionless group called the Taylor number, defined as [46]

$$\mathrm{Ta} = \frac{\omega^2 r_m g^3}{\hat{\nu}_{\mathrm{air}}^2}, \tag{1.9}$$

where r_m is the mean radius defined as $r_m = b/\ln((R_i + b)/r_i)$ with $b = A/2\pi r_i$ and A the airgap cross-section surface, and $\hat{\nu}_{\mathrm{air}}$ is the kinematic viscosity of air. This nondimensional group expresses the ratio of the centrifugal to the viscous forces; the critical value represents the condition when centrifugal forces become predominant and the instability starts to grow.

In the case of non-adiabatic flow, with heat transfer between the fluid flow and the boundary walls, Becker and Kaye [47] derived and proved that the Taylor vortices should appear at $\mathrm{Ta}_c = 1740$. Analysing the results of their experiments, Becker and Kaye [47] obtained the following correlation to describe the convection heat transfer as a function of the rotational speed, which is plotted in Fig. 1.6(b):

$$\mathrm{Nu} = 1 \qquad \text{for} \qquad \mathrm{Ta} < \mathrm{Ta}_c \tag{1.10a}$$

$$\mathrm{Nu} = 0.064\ \mathrm{Ta}^{0.367} \qquad \text{for} \qquad \mathrm{Ta}_c < \mathrm{Ta} < 10^4 \tag{1.10b}$$

$$\mathrm{Nu} = 0.205\ \mathrm{Ta}^{0.241} \qquad \text{for} \qquad 10^4 < \mathrm{Ta} < 10^6 \tag{1.10c}$$

This particular correlation refers to smooth cylinders, but correlations to account for the presence of grooves or slots have also been derived from experimental or simulated

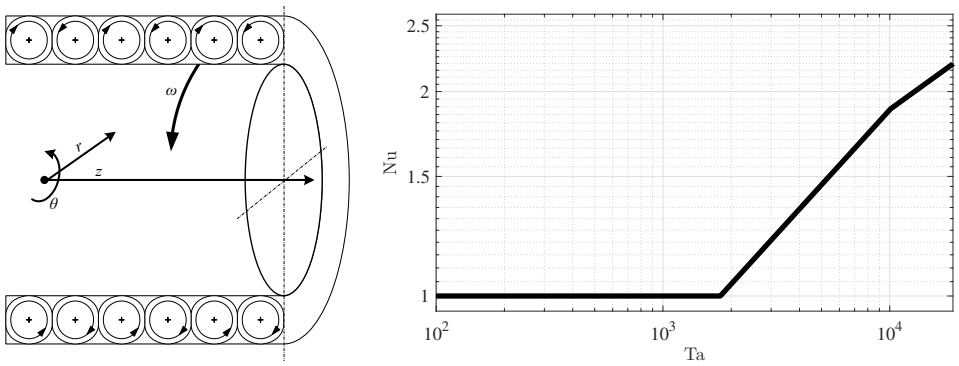

(a) (b)

Figure 1.6: (a) Taylor instability visualisation and (b) Becker and Kaye correlation [47]

data [46,48,49]. The comparison of the results available from the literature showed that it is difficult to define a unique correlation between the slot shape and the magnitude of the convective heat transfer [48]. However, the presence of slots in the annulus' boundaries affects the fluid flow pattern and accordingly influences the local and surface averaged heat transfer coefficient [46,50]. The recirculation developing within the slots also affects the onset of the instability [46,48,49].

1.1.4 Electrical machine cooling approaches

For each machine design one should ideally develop a tailored cooling system, depending on the particular application of the machine. Due to the complexity of a machine's internal arrangement and the costs involved, it is common practice to simply cool machines through their external housing. Cooling via natural convection is limited to very small machines, which can be slightly oversized to increase the exchanging surfaces and avoid reaching the thermal limits. This is not an ideal approach to achieve an optimised design with reduced dimensions. More effective cooling methods employ fans forcing air to circulate across suitably designed surface fins, or water-jackets where a coolant fluid (usually a water-glycol mixture) flows thanks to the pressure gradient imposed by a pump. The choice between these two approaches depends on

the machine application and design constraints.

Fan cooling is mostly employed for simple industrial applications, where machines are required to deal with constant loads or high torques for a very limited amount of time and the geometrical constraints are not very restrictive. The downside of fan cooling is that the fin slots can accumulate dirt, especially in an industrial environment, and require constant maintenance to avoid reducing the fan cooling effectiveness. Also, since the fan is usually placed at one of the machine ends (e.g. in the right end in Fig. 1.1(a)), the cooling performance can be imbalanced along the machine axis [51]. Since the fan is usually mounted on the machine shaft, the cooling stops only when the machine fails.

The torque demand in a vehicle-propelling machine changes at every instant. Also, the available space and machine weight are usually heavily restricted. Accordingly, to obtain high torque densities, fluid cooling via water-jacket is the preferred choice, as seen in the powertrain arrangements available on the electric vehicles market [52]. The design of the path that the water-jacket ducts follow within the housing is quite challenging, since the objective is to maximise the heat removal and obtain balanced cooling around the whole machine circumference [53]. Furthermore, including a pump in our system necessarily reduces the system reliability (the pump could fail) and system efficiency (pump requires energy to create the pressure gradient).

Recently, the tendency has been to reduce the thermal resistance between the windings and the coolant. A simple but very effective technique is to encapsulate the windings with highly thermally conductive resins ($k_{\text{resin}} = 0.7 - 3.2\,\text{W/mK}$), such as epoxies or silicone-based materials [32,54–58]. The advantage is twofold: not only is the thermal performance improved, but also the windings can be kept firmly in place. Of course these epoxies are selected to have a low electrical conductivity and accordingly they add another level of electrical insulation between neighbouring conductors. The only challenge is related to the manufacturing process, since some

epoxies require injection at high pressures to fill all the gaps, due to the fluid's high viscosity. To eliminate air bubbles that may be trapped within the compound, usually the windings are put in vacuum chambers [58].

The heat extraction effectiveness can also be enhanced with "direct winding cooling". This is achieved either by filling the end-cap region with coolant fluid [59,60] or by circulating the coolant in ducts within the stator slot [61,62]. The downside of the first technique is that the higher viscosity of the coolant, compared to air, increases the resistance to the rotation and accordingly reduces the machine efficiency. To avoid these issue, a carbon fibre stator sleeve can be introduced to limit the cooling oil to the stator area, although requiring an increased airgap width [60]. In contrast, the second option leads to a reduction of the slot filling ratio, that is the amount copper compared to available slot surface area, accordingly lowering the magnetic performance [61]. Also, the manufacturing of such windings with embedded or surrounding ducts can be extremely challenging and, due to the high cost, can be only applicable to high performance machines [62].

Direct winding cooling can be also achieved via jet impingement. For instance, this method was introduced in the Toyota Prius machine [63], where the automatic transmission fluid (ATF) is sprayed at the end windings from nozzles located around the housing circumference. This promotes the heat transfer from the conductors to the machine casing, where the coolant flows. Using ATF as a cooling medium is quite convenient due to its dielectric properties [64]. The analysis of [64] showed that jet impingement can provide surface averaged h as high as $10\,000\,\mathrm{W/m^2K}$. In particular, the combination of epoxy encapsulation and jet impingement cooling significantly enhances the thermal performance of electromagnetic equipment [65]. The issue with this approach is that the surface heat transfer coefficient varies significantly moving from the centre of jet, up to $\Delta h = 2000\,\mathrm{W/m^2K}$ per cm as measured in [65]. Accordingly, a large number of spraying nozzles may be required to avoid undesired local

hotspots, increasing design complexity and cost.

1.2 Thermal modelling of electrical machines and related challenges

From the analysis given in the previous section, one can understand how cooling an electrical machine is challenging, as it is not possible to create a general cooling solution that fits the requirements of any design.

The first works related to thermal analysis of electrical machines date back to the 1920s when Luke [66,67] performed experiments to estimate convection heat transfer coefficients over typical surfaces. Hoseason [68] gives a good overview of thermal analysis in those early days, exploring the effectiveness of the various cooling options. However, for a long time in industry, design was carried out using simple rules of thumb [69], sizing the machine using scaling rules based on the dimensions and performances of reference machines. Only recently, more attention has been paid to creating accurate tools for the estimation of the temperature distribution within a machine, due to the need for increasing the torque density and efficiency whilst reducing costs, even in small and medium size machines [1].

To model the heat transfer taking place within the machine and estimate temperatures T of each component one has to solve the heat equation

$$\rho \, c_p \frac{\partial T}{\partial t} = \frac{\partial}{\partial x}\left(k_x \frac{\partial T}{\partial x}\right) + \frac{\partial}{\partial y}\left(k_y \frac{\partial T}{\partial y}\right) + \frac{\partial}{\partial z}\left(k_z \frac{\partial T}{\partial z}\right) + \dot{q} \tag{1.11}$$

where $\dot{q}$ is the specific heat source, after considering suitable conditions at the boundaries.

The accuracy of the model (1.11) to estimate the machine temperatures compared to actual measured data, is a function of a number of factors

- model solution approach,
- parameter estimation and empirical build factors, and
- loss distribution evaluation.

We are now discussing each of these in detail, highlighting the major research challenges.

1.2.1 Model solution approach

Model (1.11) can be solved with various approaches. The common practice is to rely either on numerical methods, such as the finite element method, or reduced order methods, with the most common being "thermal equivalent circuits" (TECs). The first approach is able to provide highly spatially accurate solutions, but at a high computational cost due to the large mesh used to discretise (1.11). TECs discretise a machine system with a very limited number of nodes (a few per component), whose temperatures are assumed to be the average temperatures of each element. A thorough description of TECs is given in Chapter 5. Although this approach has reduced accuracy, due to the contained computational burden these models are suitable for real-time temperature monitoring applications [70–72], duty cycle evaluations [27], and of early stage design and structure selection. Methods that could improve the numerical and spatial accuracy of TECs could be extremely useful for all these applications.

1.2.2 Parameter estimation and empirical build factors

A number of parameters have to be chosen for the solution (1.11) using the boundary condition (1.3) which are a function of the geometry and the material properties. In previous sections we presented the various approaches to estimate the convection heat transfer coefficient h. Density ρ, heat capacity c_p and thermal conductivity k

depend only on the material. It is also useful to reduce the complexity of composite elements, e.g. laminated structures, treating them as homogenised materials with effective material properties. In particular, the homogenisation of the winding domain significantly reduces the model complexity due to the large number of conductors that are usually placed in the slot. This simplification can be inaccurate since it is complicated to correctly estimate the effective material properties due to the large number of variables they depend on.

Empirical factors refer to thermal parameters that are strictly related to the manufacturing procedure. In an electrical machine thermal model these consist of thermal contact resistances, which account for discontinuities between two solid materials. A contact resistance takes into account the temperature drop on each contact interface [73], which is due to the surface finish and contact pressure. On a microscopic level the heat transfer between contact surfaces actually takes place through direct contacts and micro air pockets, while radiation can be ignored [74,75]. Although a number of methods are available to estimate these resistances [75], the parameters required in the formulas are difficult to evaluate or practically impossible to assess before manufacturing a prototype. The main thermal contact resistances to be considered are those from the windings to the iron tooth and yoke, and from the stator yoke to the frame. Moreover, since the winding and shrink fit coupling procedures are often manual, another level of complexity is added in the estimation and standardisation of the contact resistance values.

1.2.3 Loss distribution evaluation

The source term $\dot{q}$ in (1.11) is composed of the heating losses generated within the machine components due to machine operation. These losses need to be estimated in each working condition. For simplicity, electrical machine heating losses are usually grouped into three categories:

- conduction losses,
- core losses, and
- mechanical or friction losses.

Conduction losses can be further divided into two components: DC and AC losses. The former are due to ohmic effects and can be determined with $P_{cu} = I^2R$ where I is the direct current (DC) flowing through the conductor and R is the phase electrical resistance. With an alternating current (AC), magnetic interactions result in an unbalanced current distribution across the conductor cross-section. This is due to circulating eddy currents and these effects are usually referred to as the skin and/or proximity effects. A detailed description of these phenomena is provided in Chapter 3.

The correct assessment of conduction losses including AC effects is more complicated and computationally expensive. In fact, one should consider the contribution of each individual wire in the electrical machine slot, to be able to simulate the induced eddy currents. AC effects can significantly reduce the machine efficiency and cannot be neglected when doing a proper temperature assessment in the winding. Moreover, both DC and AC components are temperature dependent according to the thermal characteristics of the electrical resistance. Reduced order models are needed to accurately assess AC loss distribution at a cheaper computational cost, and that can also include temperature effects.

The fluctuations of magnetic flux within the iron core, which is usually composed of a set of electrical steel laminations, generates hysteresis, eddy currents and excess losses [76]. The iron loss heat generation P_{iron} can be approximated using the modified Steinmetz equation [77]:

$$P_{iron} = \ af B_{\text{peak}}^{d} \ + bf^2 B_{\text{peak}}^{2} \ + \ ef^{1.5} B_{\text{peak}}^{1.5} \tag{1.12}$$

where f is the frequency of the oscillating magnetic field, B_{peak} is the magnetic flux

density peak value, d is the Steinmetz coefficient (which depends on the core hysteresis behaviour), and a, b and e are empirical constants (which depend on the geometry and material properties) [78]. Usually these constants are provided by the core manufacturer or measured through specific tests. To calculate P_{iron} using (1.12) the distribution of the magnetic flux density has to be obtained. This can be achieved only through simulations, applying either numerical or analytical methods. We note that the modified Steinmetz equation (1.12) only works for sinusoidal flux density variations, whereas for more noisy or non-sinusoidal magnetic flux density time functions the core loss assessment is more complicated.

Ideally, the magnets should not generate losses as the magnetic field in the airgap rotates synchronous to the stator field. However, there are some components of the magnetic field that do not rotate in synchronism with the rotor. These induce eddy currents in the rotor magnets, which in some cases can generate significant losses [32]. Similarly to the core losses, this effect becomes significant only at very high speed because the magnitude of the induced eddy currents is a function of the variation rate of the magnetic field experienced by the magnets.

The mechanical losses are usually overlooked at the start of the design process and only considered at later stages [15]. They come mostly from friction in the bearings and the fluid flow. An analytical approximation to describe bearing losses is available, as described in [79]. This however is not easily applicable due to complexity of assessing the rolling and sliding friction contributions and the high number of parameters related to the bearing geometry and lubricant properties. As measured by Goss [80], friction losses increase linearly with the rotational speed and become comparable to conduction losses only at very high speeds and low torques. Empirical correlations to account for the air friction losses, usually referred to as windage losses, are given in [81,82] for typical motor geometries. As windage losses can vary noticeably for different machine types, rotor shapes and sizes, rotational speeds, air-gap sizes, and

rotor surface finishes, CFD may be used for precise estimations [83]. If estimated after the machine is built, these losses are measured in no-load tests with the rotor driven at different rotational speeds, using a non-magnetic dummy motor.

Each of these loss components has to be thoroughly evaluated to consider the actual machine efficiency, as performed in [80]. In general, the core and mechanical loss contributions are lower compared to conduction losses and they become comparable only when the switching frequency is high and the rotational speed increases. It is important to mention that the rotational speed is proportional to the switching frequency and the number of poles.

1.3 Research focus and contributions

The objective of this thesis is to provide tools that can assist the design of novel electrical machines or estimate the temperatures during operation. The specific purpose is the accurate estimation of the temperature field and the thermal hotspot location and magnitude with a reduced computational burden.

The most employed methods to estimate the machine temperatures rely on hi-fidelity models, e.g. based on the finite elements method (FEM), or lower order models, e.g. thermal equivalent circuits (TECs). In this work we aim at creating "middle ground" models between these two approaches. The goal is to obtain a model that can preserve the high accuracy of FEM based models, but with a reduced model complexity.

More specifically, the research focus is on the winding region. On the one hand the windings are one of the machine components that generate the highest amount of losses. On the other hand, the hot-spot temperature is expected to be located within the winding domain; this is because, as discussed in Section 1.1.2, it is challenging to remove the the heat generated within the winding domain.

The techniques proposed in this work are based on homogenisation methods. This approach entails the substitution of the complicated winding domain with and homogenised material with effective material properties. Also, we introduce a new approach to improve TECs. The main contributions of this work can be summarised as follows:

1. estimation of electrical windings effective material properties,
2. estimation of winding losses including DC and AC components and thermal effects at a reduced computational burden,
3. evaluation of thermal contact resistances magnitude using experimental data,
4. hot-spot temperature location and magnitude assessment due to either a DC or AC load, with experimental validation,
5. improvement of the numerical and spatial accuracy of TEC for electrical machines thermal modelling to overcome limitations due to non linear thermal gradients, and to assess the expected winding temperature field.

1.4 Thesis outline

Chapter 2 (Thermal homogenisation of electrical machine windings) introduces the multiple scale method and presents its application to the electrical winding domain for the homogenisation of the thermal problem with temperature field reconstruction. Numerical and experimental validation is provided (based on my publication [84]).

Chapter 3 (Coupled electromagnetic and thermal homogenisation of electrical machine windings) introduces the loss contribution due to AC effects, discusses the homogenisation of a 2D electromagnetic problem, and describes the coupling with the thermal homogenisation. Numerical validation of the method is provided

by way of example, modelling a reference electrical machine slot (based on my publication [85]).

Chapter 4 (Experimental validation of the coupled electromagnetic and thermal homogenisation) extends the coupled electromagnetic and thermal homogenisation to 3D problems. Experimental validation of the approach is provided, describing manufacturing of the specimen designed to exaggerate AC losses, and showing the model accuracy in assessing the winding temperature field and hot-spot magnitude and location (based on my publication [86]).

Chapter 5 (Improved thermal equivalent circuit element for electrical machines thermal modelling) discusses numerical accuracy issues encountered by TEC thermal models and proposes a novel approach to overcome them. Experimental validation is presented based on the specimen described in the Chapter 4. The method is also applied to model a novel in-wheel machine design for vehicle propulsion (based on my publication [87]).

Chapter 6 (Conclusions) summarises the work undertaken in this thesis and makes suggestions for future work.

Chapter 2

Thermal homogenisation of electrical machine windings

This chapter is based on publication [84].

2.1 Introduction to homogenisation

As discussed in Chapter 1, accurate assessment of temperature distribution within electrical windings is fundamental for a better evaluation of machine performance and lifespan. However, it is not practical to measure hot-spot temperature experimentally in most commercial machines, since a large number of temperature sensors would be required. For this reason, mathematical models that can predict the entire thermal field can be very useful. This is not a trivial task since the windings are a complex composite domain, consisting of insulated conductors usually bonded together with varnish or epoxy, see Fig. 2.1(a).

A common approach to finding the hot-spot temperature is to solve the thermal problem in the full domain where every single wire is modelled individually, using for example the finite element method (FEM). One must solve for the temperature

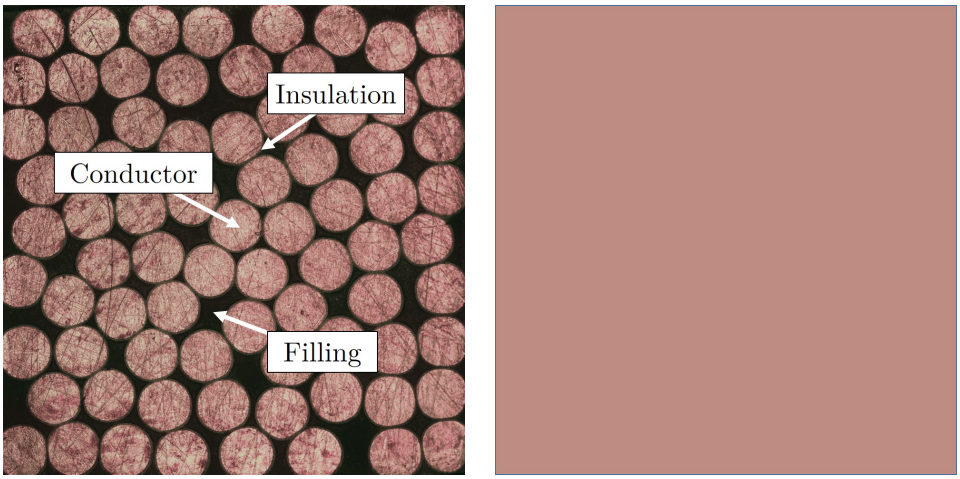

(a) (b)

Figure 2.1: (a) Cross section of an electrical winding compound composed of insulated wires, $\varnothing = 1\,\text{mm}$, and epoxy filling. (b) Visualisation of the homogenised winding domain

$T(\mathbf{X}, t)$ satisfying the heat equation in each of the phases

$$\rho_p c_p \frac{\partial T}{\partial t} = k_p \nabla^2_{\mathbf{X}} T + \dot{q}, \tag{2.1}$$

where k_p, c_p and ρ_p are the thermal conductivity, heat capacity and density of the pth phase respectively, $\dot{q}$ is the source term and $\nabla^2_{\mathbf{X}}$ stands for the Laplacian operator. However, the mesh sizes required to capture the thermal gradients between each wire are unsuitable for fast simulations. The standard approach to overcome this is to "homogenise" the compound and treat the mixture of conductors, insulation and bonding material as a continuum (see Fig. 2.1(b)) with equivalent thermal parameters that do not depend on the coordinate $\mathbf{X}$ [88–91], satisfying the following "homogenised heat equation"

$$\rho_{eq} c_{eq} \frac{\partial T}{\partial t} = k_{eq} \nabla^2_{\mathbf{X}} T + \dot{q}_{eq}, \tag{2.2}$$

where ρ_{eq}, c_{eq} and k_{eq} are the effective thermal parameters of the homogenised domain and $\dot{q}_{eq}$ is the effective heat source. The advantage of (2.2) over (2.1) is that, with the correctly homogenised parameters, it can be solved quickly with a low order approach

across the entire domain of a slot while still predicting the hot-spot temperature accurately.

The downside of homogenisation, as shown in Fig. 2.2, is that we lose information about the original domain and in particular the temperature gradients across each wire, as they are smoothed by the effective material properties. However, the smaller the ratio l/L is, where l is the inter-wire distance and L represents the characteristic dimension of the total winding compound or slot size, the more accurate is the matching between the solution of the "Full model" (2.1) and "Homogenised model" (2.2).

The complexity of the homogenisation procedure lies in correctly calculating the equivalent thermal parameters in (2.2) based on the geometry of the domain, the material properties, and filling ratio. In particular, the biggest challenge is to obtain the anisotropic equivalent thermal conductivity k_{eq} as a function of such parameters, meaning that the thermal conductivity along each direction has different values. In the literature various techniques have been used to evaluate k_{eq} of this compound [54,88,92–96], each with strengths and weaknesses. Experimentally, it is possible to directly measure the k_{eq} [88,92–94]; however, this requires appropriate bespoke test equipment and suitably manufactured winding specimens, making the approach expensive and time-consuming. Alternatively, many authors have relied on numerical methods or analytical formulae to estimate k_{eq} (which must, of course, be validated using the kinds of experimental methods just described) [54,95,96]. The simplest and oldest formula, proposed by Wiener [97], gives upper and lower bounds for the effective thermal conductivity. However, this formula do not account for the shape of the conductors, as we discuss in section 2.1.1. These bounds can be improved, accounting for the particular case of circular conductors, using the Hashin and Shtrikman (HS) formula [98].

Both these approaches neglect the thin layer of insulation around the copper,

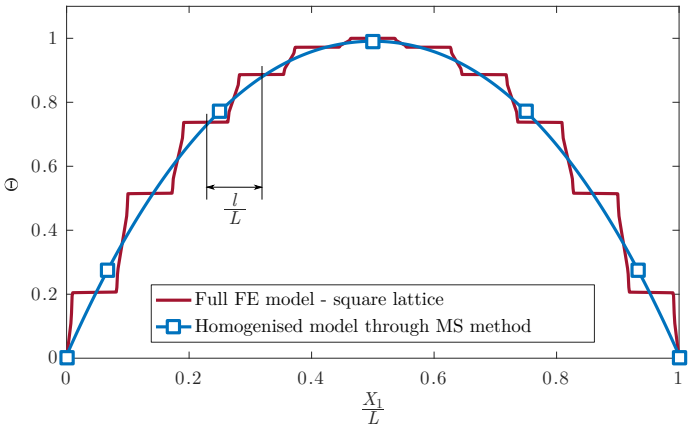

Figure 2.2: Normalised steady-state temperature $\Theta = T/T_{max}$ in a simulation of the mid-cross-section of a winding with internal heat generation and fixed temperature at the boundaries, obtained from the full model (2.1) and the homogenised model (2.2). $l/L = 1/11$ indicates the relative distance between adjoining wires

which results in a more complex thermal problem. This electrical insulation, due its very low thermal conductivity compared to the conductor (usually copper), acts as a good thermal insulator. This impacts the domain's temperature field and, accordingly, influences the estimation of the homogenised conductivity k_{eq}. Attempts by Kanzaki [99], Simpson [54] and the "multi layer" method by Nategh [89] to include a third phase for the insulation only slightly improved the accuracy. The key limitation of these analytical formulae is their strong dependence on a specific wire geometry, wire distribution, and the set of material properties. From this analysis it results that the only accurate and reliable way to obtain the effective parameters in (2.2) is to solve the full model (2.1) and this view is supported by others [54,99].

In this chapter therefore we propose a completely different technique, based on the multiple scales method (MSM) [91,100] to systematically derive the homogenised thermal problem (2.2) in a principled way. This, in turn, enables us to define a general, accurate and efficient method to estimate the equivalent thermal features of composite electrical windings, regardless of the conductors' cross-section geometry and distribution inside the slot. Additionally, the technique can reconstruct the original thermal field, allowing for a more precise evaluation of the thermal hot-spot

magnitude and location.

2.1.1 Wiener bounds

Before starting the discussion on the MSM, we present the Wiener bounds for effective material properties, also known as the "rule of mixtures" due to their simplicity and widespread application in many engineering fields [90].

The Wiener bounds are defined as such because they bound the equivalent conductivity of any two-phase composite

$$k_{eq}^{-} \; < \; k_{eq} \; < \; k_{eq}^{+}. \tag{2.3}$$

This property can be observed analysing a simple example. Let us consider a two-phase laminate composite (see Fig. 2.3(a)), where each phase p ($p = 1, 2$) is characterised by volume fraction λ_p and isotropic thermal conductivity k_p. We assume the problem to be 2D, with the laminates having infinite depth in the direction perpendicular to the page. Also, the laminates have periodicity l. In such domain the upper k_{eq}^{+} and lower k_{eq}^{-} Wiener bounds describe the effective conductivity along the direction X_1 and X_2, respectively

$$k_{eq}^{+} = k_{eq,X_1} = \lambda_1 k_1 + \lambda_2 k_2, \tag{2.4a}$$

$$k_{eq}^{-} = k_{eq,X_2} = \left(\frac{\lambda_1}{k_1} + \frac{\lambda_2}{k_2} \right)^{-1}. \tag{2.4b}$$

These formulae represent respectively the series and parallel combination of the phases thermal resistances, as depicted in Fig. 2.3(b).

The accuracy of Wiener's approach is, however, restricted to the case of laminated structures, such as the one in Fig. 2.3. It is easy to understand why the bounds (2.4) are too loose when the composite material is more complex, e.g. made of a matrix

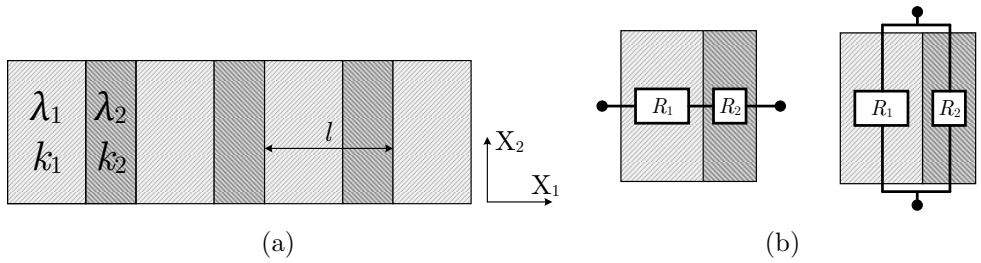

Figure 2.3: (a) Two-phase laminated composite material and (b) equivalent circuit representation of the upper and lower Wiener bounds

with circular or rectangular shaped inclusions. In these cases other methods can be employed, such as the MSM. Indeed, the same outcome (2.4) can be achieved with the MSM for the case of laminated structures [101].

2.1.2 Introducing the multiple scales method

The method of multiple scales method (MSM) relies on the separation of length scales between the microscopic and the macroscopic domains, and typically assumes periodicity in the microstructure. The microscopic length scale measures variations within a periodic cell (i.e. from copper to insulation to local impregnation in the case of an electrical machine winding) and the macroscopic length scale measures variations within the macroscopic region of interest (i.e. across the whole slot where a winding is located). Starting from a full model such as (2.1), the MSM yields a homogenised equation of the type (2.2) with the effective coefficients containing the microscopic information such as filling volume and wire arrangement. The method has been widely applied in various engineering branches for the study of equivalent properties (thermal, structural, etc.) of periodic structures [102–108].

2.2 Problem set-up and governing equations

We model the windings in the first instance as insulated circular conductors distributed within a periodic square lattice, Fig. 2.4(a). For simplicity, we assume that

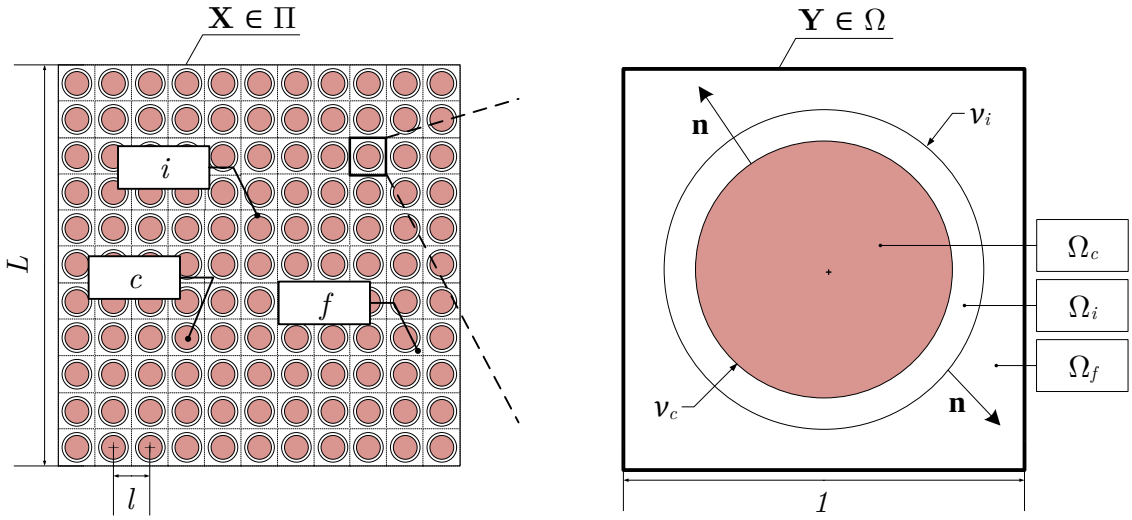

Figure 2.4: (a) Macroscopic domain Π, with insulated conductors in a square periodic lattice separated by a distance $l \ll L$. (b) Microscopic domain or unit cell Ω with one conductor at its centre of radius $\nu_c = \varepsilon_c/l$ surrounded by insulation to radius $\nu_i = \varepsilon_i/l$

all the conductors are equally spaced with inter-wire distance l. Each wire has the same external radii, ε_c and ε_i for the conductor and the insulation, respectively. This means that the microstructure is perfectly periodic, in line with the standard assumption of the MSM as discussed above. We note that this assumption can be relaxed as discussed in [109] if one wanted to account for gradual variations in the material distribution. We use the subscripts c, i and f to refer to the conductor, insulation and filling phases, respectively, according to Fig. 2.4. Finally, we assume that there is perfect contact between the materials. In general, to achieve an accurate homogenisation we require a good separation of lengthscales, i.e. $L \gg l$. The quality of the homogenisation is then a function of the ratio $\delta = l/L$ and the matching improves asymptotically with $\delta \to 0$ [110].

The starting point is the heat equation (2.1) defined in the original windings domain. The heat source term $\dot{q}$ in (2.1) is assumed to be from ohmic heating i.e. $\dot{q} = J^2/\sigma$ where J is the current density magnitude in the conductors (which we take

to be constant) and σ is electrical conductivity. Therefore, the source term appears in the conductor phase only, $\dot{q} = 0$ if $\|\mathbf{X} - \mathbf{c}_j\| > \varepsilon_c$ for all j, where $\mathbf{c}_j$ represents the coordinates of the centre of the jth conductor.

On the boundaries between the phases we assume continuity of temperature and heat flux, namely

$$k_c \nabla_{\mathbf{X}} T \cdot \mathbf{n} = k_i \nabla_{\mathbf{X}} T \cdot \mathbf{n} \quad \text{on } \|\mathbf{X} - \mathbf{c}_j\| = \varepsilon_c, \tag{2.5a}$$

$$k_i \nabla_{\mathbf{X}} T \cdot \mathbf{n} = k_f \nabla_{\mathbf{X}} T \cdot \mathbf{n} \quad \text{on } \|\mathbf{X} - \mathbf{c}_j\| = \varepsilon_i, \tag{2.5b}$$

where $\mathbf{n}$ stands for the outward unit normal (outward of Ω_c in (2.5a) and outward of Ω_i in (2.5b)). We scale the variables via $T = \tilde{T}\,\hat{T}$, $\mathbf{X} = L\hat{\mathbf{X}}$, $t = \tilde{t}\,\hat{t}$, where $\tilde{T}$ is the characteristic temperature and $\tilde{t}$ is the characteristic time. Using these scaling factors in (2.1) and (2.5), we obtain the dimensionless equations

$$\alpha_p \frac{\partial \hat{T}}{\partial \hat{t}} = \beta_p \nabla^2_{\hat{\mathbf{X}}} \hat{T} + \Psi_p, \tag{2.6a}$$

$$\beta_c \nabla_{\hat{\mathbf{X}}} \hat{T} \cdot \mathbf{n} = \beta_i \nabla_{\hat{\mathbf{X}}} \hat{T} \cdot \mathbf{n} \qquad \text{on} \quad \|\mathbf{X} - \mathbf{c}_j\| = \varepsilon_c, \tag{2.6b}$$

$$\beta_i \nabla_{\hat{\mathbf{X}}} \hat{T} \cdot \mathbf{n} = \beta_f \nabla_{\hat{\mathbf{X}}} \hat{T} \cdot \mathbf{n} \qquad \text{on} \quad \|\mathbf{X} - \mathbf{c}_j\| = \varepsilon_i, \tag{2.6c}$$

where we introduce the dimensionless groups

$$\alpha_p = \frac{L^2}{\tilde{t}} \frac{c_p \rho_p}{k_f}, \qquad \beta_p = \frac{k_p}{k_f}, \qquad \Psi_p = \frac{L^2}{\tilde{T}} \frac{J^2}{\sigma k_f} \delta_{pc},$$

for $p = c, i, f$, and δ_{pc} stands for the Kronecker delta (so that $\Psi_c = 1$ and $\Psi_i = \Psi_f = 0$). The values of the dimensional parameters are given in Table 2.1. From now on we refer to dimensionless quantities, dropping hats for ease of notation.

Table 2.1: Reference values and material properties from [4]

Variable	Value
L	$2.2 \times 10^{-2}\,\mathrm{m}$
l	$2 \times 10^{-3}\,\mathrm{m}$
ε_c	$0.8 \times 10^{-3}\,\mathrm{m}$
ε_i	$0.835 \times 10^{-3}\,\mathrm{m}$
σ	$5.96 \times 10^{7}\,\Omega\mathrm{m}$
k_c	$385\,\mathrm{W/mK}$
c_c	$386\,\mathrm{J/kgK}$
ρ_c	$8890\,\mathrm{kg/m^3}$
k_i	$0.26\,\mathrm{W/mK}$
c_i	$1000\,\mathrm{J/kgK}$
ρ_i	$1440\,\mathrm{kg/m^3}$
k_f	$0.85\,\mathrm{W/mK}$
c_f	$1700\,\mathrm{J/kgK}$
ρ_f	$1766\,\mathrm{kg/m^3}$

2.3 The multiple scales method

We now use the MSM to derive an averaged model for the temperature T, valid over many wires in the limit $\delta \ll 1$. We retain $\mathbf{X}$ as the macroscale variable, spanning the entire compound, and introduce $\mathbf{Y} = \mathbf{X}/\delta$ as the microscale variable, measuring distance over the scale of the wire separation. As usual in the MSM, we treat these two variables as independent and impose that the solution is exactly periodic in $\mathbf{Y}$; small variations from one wire to the next are thereby captured through the macroscale variable $\mathbf{X}$. We define $\nu_c = \varepsilon_c/l$ and $\nu_i = \varepsilon_i/l$ as the conductor and insulator external radii relative to the unit cell $\mathbf{Y} \in \Omega = [-1/2, 1/2]^2$ (see Fig. 2.4(b)).

We look for a solution of the form $T = T(\mathbf{X}, \mathbf{Y}, t)$. Accordingly, using the chain rule, the derivation of any function now should be performed with

$$\nabla_{\mathbf{X}} T(\mathbf{X}, \mathbf{Y}) \to \nabla_{\mathbf{X}} T(\mathbf{X}, \mathbf{Y}) + \frac{\partial \mathbf{Y}}{\partial \mathbf{X}} \nabla_{\mathbf{Y}} T(\mathbf{X}, \mathbf{Y}) \tag{2.7}$$

and recalling that by definition $\mathbf{Y} = \mathbf{X}/\delta$, we can generalise spatial derivatives trans-

forms as

$$\nabla_{\mathbf{X}} \to \nabla_{\mathbf{X}} + \frac{1}{\delta}\nabla_{\mathbf{Y}}, \tag{2.8a}$$

$$\nabla^2_{\mathbf{X}} \to \nabla^2_{\mathbf{X}} + 2\frac{1}{\delta}\nabla_{\mathbf{X}} \cdot \nabla_{\mathbf{Y}} + \frac{1}{\delta^2}\nabla^2_{\mathbf{Y}}. \tag{2.8b}$$

Under the transformation (2.8), equations (2.6) become

$$\delta^2 \alpha_p \frac{\partial T}{\partial t} = \beta_p \left(\delta^2 \nabla^2_{\mathbf{X}} T + 2\delta \nabla_{\mathbf{X}} \cdot \nabla_{\mathbf{Y}} T + \nabla^2_{\mathbf{Y}} T\right) + \delta^2 \Psi_p, \tag{2.9a}$$

$$\beta_c \left(\delta \nabla_{\mathbf{X}} T + \nabla_{\mathbf{Y}} T\right) \cdot \mathbf{n} = \beta_i \left(\delta \nabla_{\mathbf{X}} T + \nabla_{\mathbf{Y}} T\right) \cdot \mathbf{n} \quad \text{on} \quad \|\mathbf{Y}\| = \nu_c, \tag{2.9b}$$

$$\beta_i \left(\delta \nabla_{\mathbf{X}} T + \nabla_{\mathbf{Y}} T\right) \cdot \mathbf{n} = \beta_f \left(\delta \nabla_{\mathbf{X}} T + \nabla_{\mathbf{Y}} T\right) \cdot \mathbf{n} \quad \text{on} \quad \|\mathbf{Y}\| = \nu_i. \tag{2.9c}$$

Following the standard MSM, we now seek an asymptotic solution to (2.9) in the limit of small δ of the form

$$T(\mathbf{X}, \mathbf{Y}, t) = T^{(0)}(\mathbf{X}, \mathbf{Y}, t) + \delta T^{(1)}(\mathbf{X}, \mathbf{Y}, t) + \delta^2 T^{(2)}(\mathbf{X}, \mathbf{Y}, t) + \cdots, \tag{2.10}$$

that is periodic in $\mathbf{Y}$, while treating $\mathbf{X}$ and $\mathbf{Y}$ as independent. The governing equations must be satisfied for each order of δ. Accordingly, we evaluate (2.9) at increasing powers of δ.

Leading order, $\delta^{(0)}$

Considering only the terms in $\delta^{(0)}$ allows us to rewrite (2.9) in the following form:

$$\beta_p \left(\nabla^2_{\mathbf{Y}} T^{(0)}\right) = 0, \tag{2.11a}$$

$$\left(\beta_c \nabla_{\mathbf{Y}} T^{(0)} - \beta_i \nabla_{\mathbf{Y}} T^{(0)}\right) \cdot \mathbf{n} = 0 \quad \text{on} \quad \|\mathbf{Y}\| = \nu_c, \tag{2.11b}$$

$$\left(\beta_i \nabla_{\mathbf{Y}} T^{(0)} - \beta_f \nabla_{\mathbf{Y}} T^{(0)}\right) \cdot \mathbf{n} = 0 \quad \text{on} \quad \|\mathbf{Y}\| = \nu_i. \tag{2.11c}$$

with $T^{(0)}$ periodic on the external boundary. The solution of this problem is simply

$$T^{(0)} = c, \tag{2.12}$$

where c is a constant. As a consequence, we conclude that $T^{(0)} = T(\mathbf{X}, t)$ and does not vary with $\mathbf{Y}$. This is an important outcome, as it means that $T^{(0)}$ should be sufficient to describe the macroscopic thermal behaviour of our domain. In other words, this result means that $T^{(0)}$ does not include information about the microscopic variations of temperature between wires because the solution of the problem (2.11) calculated for the microscopic domain Ω is equal to a constant. This is the characteristic of a macroscopic filed distribution.

First order, $\delta^{(1)}$

The order δ of (2.9) is

$$\beta_p \left(\nabla^2_{\mathbf{Y}} T^{(1)} + 2\nabla_{\mathbf{X}}\nabla_{\mathbf{Y}} T^{(0)}\right) = 0, \tag{2.13a}$$

$$\beta_c \left(\nabla_{\mathbf{X}} T^{(0)} + \nabla_{\mathbf{Y}} T^{(1)}\right) \cdot \mathbf{n} = \beta_i \left(\nabla_{\mathbf{X}} T^{(0)} + \nabla_{\mathbf{Y}} T^{(1)}\right) \cdot \mathbf{n} \quad \text{on} \quad \|Y\| = \nu_c, \tag{2.13b}$$

$$\beta_i \left(\nabla_{\mathbf{X}} T^{(0)} + \nabla_{\mathbf{Y}} T^{(1)}\right) \cdot \mathbf{n} = \beta_f \left(\nabla_{\mathbf{X}} T^{(0)} + \nabla_{\mathbf{Y}} T^{(1)}\right) \cdot \mathbf{n} \quad \text{on} \quad \|Y\| = \nu_i, \tag{2.13c}$$

which, thanks to the outcome from the leading order (2.12), can be simplified to

$$\beta_p \left(\nabla^2_{\mathbf{Y}} T^{(1)}\right) = 0, \tag{2.14a}$$

$$\beta_c \left(\nabla_{\mathbf{X}} T^{(0)} + \nabla_{\mathbf{Y}} T^{(1)}\right) \cdot \mathbf{n} = \beta_i \left(\nabla_{\mathbf{X}} T^{(0)} + \nabla_{\mathbf{Y}} T^{(1)}\right) \cdot \mathbf{n} \quad \text{on} \quad \|Y\| = \nu_c, \tag{2.14b}$$

$$\beta_i \left(\nabla_{\mathbf{X}} T^{(0)} + \nabla_{\mathbf{Y}} T^{(1)}\right) \cdot \mathbf{n} = \beta_f \left(\nabla_{\mathbf{X}} T^{(0)} + \nabla_{\mathbf{Y}} T^{(1)}\right) \cdot \mathbf{n} \quad \text{on} \quad \|Y\| = \nu_i. \tag{2.14c}$$

Since $T^{(0)}$ is independent of $\mathbf{Y}$ and (2.14) is linear, we can write the solution $T^{(1)}$ as a linear combination of a vector function $\mathbf{\Gamma}(\mathbf{Y})$ and $T^{(0)}(\mathbf{X})$

$$T^{(1)} = -\mathbf{\Gamma}(\mathbf{Y}) \cdot \nabla_{\mathbf{X}} T^{(0)}. \tag{2.15}$$

The components of the vector function $\Gamma_i(\mathbf{Y})$ are the solutions of the so-called "cell problem", which will be discussed in detail in section 2.3.2.

Order 2, $\delta^{(2)}$

The time derivative and the source terms in (2.9) appear at order δ^2

$$\alpha_p \frac{\partial T^{(0)}}{\partial t} = \beta_p \left(\nabla^2_{\mathbf{Y}} T^{(2)} + 2\nabla_{\mathbf{X}} \cdot \nabla_{\mathbf{Y}} T^{(1)} + \nabla^2_{\mathbf{X}} T^{(0)} \right) + \Psi_p, \tag{2.16a}$$

$$\beta_c \left(\nabla_{\mathbf{X}} T^{(1)} + \nabla_{\mathbf{Y}} T^{(2)} \right) \cdot \mathbf{n} = \beta_i \left(\nabla_{\mathbf{X}} T^{(1)} + \nabla_{\mathbf{Y}} T^{(2)} \right) \cdot \mathbf{n} \quad \text{on} \quad \|Y\| = \nu_c, \tag{2.16b}$$

$$\beta_i \left(\nabla_{\mathbf{X}} T^{(1)} + \nabla_{\mathbf{Y}} T^{(2)} \right) \cdot \mathbf{n} = \beta_f \left(\nabla_{\mathbf{X}} T^{(1)} + \nabla_{\mathbf{Y}} T^{(2)} \right) \cdot \mathbf{n} \quad \text{on} \quad \|Y\| = \nu_i, \tag{2.16c}$$

and $T^{(2)}$ periodic on the external boundary.

We now introduce the average operator $\langle \cdot \rangle$, defined on any cell-periodic function $T(\mathbf{Y})$ by [91]

$$\langle T \rangle = \frac{1}{\|\Omega\|} \int_{\Omega} T(\mathbf{Y}) dY, \tag{2.17}$$

which allows us to smooth the local oscillating terms; $\|\Omega\|$ is the measure of the surface Ω.

Accordingly, the next step is to apply $\langle \cdot \rangle$ to (2.16a) over each sub-domain of Ω,

i.e. Ω_c, Ω_i, and Ω_f, as follows

$$\frac{1}{\|\Omega_c\|}\int_{\Omega_c}\alpha_c\frac{\partial T^{(0)}}{\partial t}d\Omega_c = \frac{1}{\|\Omega_c\|}\int_{\Omega_c}\big[\beta_c\big(\nabla_{\mathbf{Y}}\left(\nabla_{\mathbf{Y}}T^{(2)}+\nabla_{\mathbf{X}}T^{(1)}\right) + \nabla_{\mathbf{X}}\left(\nabla_{\mathbf{Y}}T^{(1)}+\nabla_{\mathbf{X}}T^{(0)}\right)\big)+\Psi_c\big]dY, \quad (2.18a)$$

$$\frac{1}{\|\Omega_i\|}\int_{\Omega_i}\alpha_i\frac{\partial T^{(0)}}{\partial t}d\Omega_i = \frac{1}{\|\Omega_i\|}\int_{\Omega_i}\beta_i\big(\nabla_{\mathbf{Y}}\left(\nabla_{\mathbf{Y}}T^{(2)}+\nabla_{\mathbf{X}}T^{(1)}\right) + \nabla_{\mathbf{X}}\left(\nabla_{\mathbf{Y}}T^{(1)}+\nabla_{\mathbf{X}}T^{(0)}\right)\big)dY, \quad (2.18b)$$

$$\frac{1}{\|\Omega_f\|}\int_{\Omega_f}\alpha_f\frac{\partial T^{(0)}}{\partial t}d\Omega_f = \frac{1}{\|\Omega_f\|}\int_{\Omega_f}\beta_f\big(\nabla_{\mathbf{Y}}\left(\nabla_{\mathbf{Y}}T^{(2)}+\nabla_{\mathbf{X}}T^{(1)}\right) + \nabla_{\mathbf{X}}\left(\nabla_{\mathbf{Y}}T^{(1)}+\nabla_{\mathbf{X}}T^{(0)}\right)\big)dY. \quad (2.18c)$$

Now the divergence theorem can be applied, leading to

$$\frac{1}{\|\Omega_c\|}\int_{\Omega_c}\alpha_c\frac{\partial T^{(0)}}{\partial t}d\Omega_c = \frac{1}{\|\Omega_c\|}\int_{\Omega_c}\left[\beta_c\left(\nabla_{\mathbf{X}}\left(\nabla_{\mathbf{Y}}T^{(1)}+\nabla_{\mathbf{X}}T^{(0)}\right)\right)+\Psi_c\right]dY + \frac{1}{\|\Omega_c\|}\int_{\partial\Omega_c^+}\beta_c\nabla_{\mathbf{Y}}\left(\nabla_{\mathbf{Y}}T^{(2)}+\nabla_{\mathbf{X}}T^{(1)}\right)\cdot\mathbf{n}\,dS, \quad (2.19a)$$

$$\frac{1}{\|\Omega_i\|}\int_{\Omega_i}\alpha_i\frac{\partial T^{(0)}}{\partial t}dY = \frac{1}{\|\Omega_i\|}\int_{\Omega_i}\beta_i\left(\nabla_{\mathbf{X}}\left(\nabla_{\mathbf{Y}}T^{(1)}+\nabla_{\mathbf{X}}T^{(0)}\right)\right)d\Omega_i + \frac{1}{\|\Omega_i\|}\int_{\partial\Omega_i^-}\beta_i\left(\nabla_{\mathbf{Y}}\left(\nabla_{\mathbf{Y}}T^{(2)}+\nabla_{\mathbf{X}}T^{(1)}\right)\right)\cdot\mathbf{n}\,dS + \frac{1}{\|\Omega_i\|}\int_{\partial\Omega_i^+}\beta_i\left(\nabla_{\mathbf{Y}}\left(\nabla_{\mathbf{Y}}T^{(2)}+\nabla_{\mathbf{X}}T^{(1)}\right)\right)\cdot\mathbf{n}\,dS, \quad (2.19b)$$

$$\frac{1}{\|\Omega_f\|}\int_{\Omega_f}\alpha_f\frac{\partial T^{(0)}}{\partial t}dY = \frac{1}{\|\Omega_f\|}\int_{\Omega_f}\beta_f\left(\nabla_{\mathbf{X}}\left(\nabla_{\mathbf{Y}}T^{(1)}+\nabla_{\mathbf{X}}T^{(0)}\right)\right)d\Omega_f + \frac{1}{\|\Omega_f\|}\int_{\partial\Omega_f^-}\beta_f\left(\nabla_{\mathbf{Y}}\left(\nabla_{\mathbf{Y}}T^{(2)}+\nabla_{\mathbf{X}}T^{(1)}\right)\right)\cdot\mathbf{n}\,dS + \frac{1}{\|\Omega_f\|}\int_{\partial\Omega_f^+}\beta_f\left(\nabla_{\mathbf{Y}}\left(\nabla_{\mathbf{Y}}T^{(2)}+\nabla_{\mathbf{X}}T^{(1)}\right)\right)\cdot\mathbf{n}\,dS, \quad (2.19c)$$

where $\partial\Omega_p$ indicates the boundaries limiting Ω_p, and the subscripts $+$ and $-$ refer to the direction of unit normal $\mathbf{n}$ to $\partial\Omega_p$ (towards the outside or inside, respectively). Recalling the periodicity of $T^{(1)}$ and $T^{(2)}$ over the cell domain, and using the boundary

conditions (2.16b) and (2.16c), all the surface integrals vanish. Moreover, using (2.15) in (2.19a) yields, for $p = c$, i and f,

$$\frac{1}{\|\Omega_p\|}\int_{\Omega_p}\alpha_p\frac{\partial T^{(0)}}{\partial t}d\Omega_p = \frac{1}{\|\Omega_p\|}\int_{\Omega_p}\left[\beta_p\nabla_{\mathbf{X}}\left(\nabla_{\mathbf{X}}T^{(0)} - \nabla_{\mathbf{X}}T^{(0)}\mathbf{\Gamma}(\mathbf{Y})\right) + \Psi\right]d\Omega_p, \tag{2.20}$$

which can be rearranged in a more convenient manner

$$\frac{1}{\|\Omega_p\|}\int_{\Omega_p}\alpha_p\frac{\partial T^{(0)}}{\partial t}d\mathbf{Y} = \frac{1}{\|\Omega_p\|}\int_{\Omega_p}\left[\beta_p\nabla_{\mathbf{X}}\left([\mathrm{I}] - [\mathrm{Q}](\mathbf{Y})\right)\nabla_{\mathbf{X}}T^{(0)} + \Psi\right]dY, \tag{2.21}$$

where [I] is the identity matrix and

$$([\mathrm{Q}])_{ij} = \frac{\partial \Gamma_i}{\partial Y_j} \tag{2.22}$$

where $\mathbf{\Gamma}$ is yet to be defined (see section 2.3.2).

2.3.1 Homogenised heat equation

We now add up the three integrated equations (2.21), noting again that the time derivative and the source terms are independent of the microscopic variable, to obtain a homogenised equation of the form (2.2) over the whole domain

$$\mathrm{A}\frac{\partial T^{(0)}}{\partial t} = \nabla_{\mathbf{X}}\cdot\left([\mathrm{B}]\nabla_{\mathbf{X}}T^{(0)}\right) + \Psi_c\frac{\|\Omega_c\|}{\|\Omega\|}, \tag{2.23}$$

where A is the equivalent heat capacity and $\bar{\mathrm{B}}$ is the thermal conductivity matrix, given by

$$\mathrm{A} = \frac{1}{\|\Omega\|}\sum_p \alpha_p\|\Omega_p\|, \tag{2.24}$$

$$[\mathrm{B}] = \frac{1}{\|\Omega\|}\sum_p\left[\beta_p\int_{\Omega_p}[\mathrm{I}] - [\mathrm{Q}](\mathbf{Y})dY\right], \tag{2.25}$$

where the sum is over $p = c, i, f$. We find that the equivalent thermal capacity A can be calculated by area weighting the contributions of the three materials; in this case the disposition of the wires has no effect. On the other hand, the equivalent thermal conductivity matrix [B] is a function of $\mathbf{\Gamma}(\mathbf{Y})$, obtained from the solution of the cell problem, which we discuss next.

2.3.2 The cell problem

In the previous section we assumed the solution of problem (2.14) is of the form (2.15). Our goal is now to determine the boundary value problem that allows us to obtain the vector-valued function $\mathbf{\Gamma}(\mathbf{Y})$. This can be done by inserting (2.15) into (2.14)

$$-\beta_p \nabla^2_{\mathbf{Y}} \left(\mathbf{\Gamma}(\mathbf{Y}) \nabla_{\mathbf{X}} T^{(0)} \right) = 0, \tag{2.26}$$

which reduces to

$$\nabla^2_{\mathbf{Y}} \mathbf{\Gamma}(\mathbf{Y}) = 0, \tag{2.27}$$

due to (2.12). Similarly, the flux boundary conditions (2.13b) and (2.13c) between each phase become

$$\beta_c \left(\nabla_{\mathbf{Y}} \mathbf{\Gamma}(\mathbf{Y}) \nabla_{\mathbf{X}} T^{(0)} - \nabla_{\mathbf{X}} T^{(0)} \right) \cdot \mathbf{n} = \beta_i \left(\nabla_{\mathbf{Y}} \mathbf{\Gamma}(\mathbf{Y}) \nabla_{\mathbf{X}} T^{(0)} - \nabla_{\mathbf{X}} T^{(0)} \right) \cdot \mathbf{n} \quad \text{on} \quad \|Y\| = \nu_c, \tag{2.28a}$$

$$\beta_i \left(\nabla_{\mathbf{Y}} \mathbf{\Gamma}(\mathbf{Y}) \nabla_{\mathbf{X}} T^{(0)} - \nabla_{\mathbf{X}} T^{(0)} \right) \cdot \mathbf{n} = \beta_f \left(\nabla_{\mathbf{Y}} \mathbf{\Gamma}(\mathbf{Y}) \nabla_{\mathbf{X}} T^{(0)} - \nabla_{\mathbf{X}} T^{(0)} \right) \cdot \mathbf{n} \quad \text{on} \quad \|Y\| = \nu_i. \tag{2.28b}$$

Using $T^{(0)} = T^{(0)}(\mathbf{X}, t)$, we can group and rearrange as

$$\beta_c \nabla_{\mathbf{X}} T^{(0)} \left(\nabla_{\mathbf{Y}} \mathbf{\Gamma}(\mathbf{Y}) - [\mathrm{I}]\right) \cdot \mathbf{n} = \beta_i \nabla_{\mathbf{X}} T^{(0)} \left(\nabla_{\mathbf{Y}} \mathbf{\Gamma}(\mathbf{Y}) - [\mathrm{I}]\right) \cdot \mathbf{n}$$
$$\text{on} \quad \|Y\| = \nu_c, \quad (2.29a)$$

$$\beta_i \nabla_{\mathbf{X}} T^{(0)} \left(\nabla_{\mathbf{Y}} \mathbf{\Gamma}(\mathbf{Y}) - [\mathrm{I}]\right) \cdot \mathbf{n} = \beta_f \nabla_{\mathbf{X}} T^{(0)} \left(\nabla_{\mathbf{Y}} \mathbf{\Gamma}(\mathbf{Y}) - [\mathrm{I}]\right) \cdot \mathbf{n}$$
$$\text{on} \quad \|Y\| = \nu_i. \quad (2.29b)$$

Finally, we can cancel out the terms $\nabla_{\mathbf{X}} T^{(0)}$ on each side, leading to the "cell problem"

$$\nabla^2_{\mathbf{Y}} \mathbf{\Gamma}(\mathbf{Y}) = 0, \quad (2.30a)$$

$$\beta_c \left(\nabla_{\mathbf{Y}} \mathbf{\Gamma}(\mathbf{Y}) - [\mathrm{I}]\right) \cdot \mathbf{n} = \beta_i \left(\nabla_{\mathbf{Y}} \mathbf{\Gamma}(\mathbf{Y}) - [\mathrm{I}]\right) \cdot \mathbf{n} \quad \text{on} \quad \|Y\| = \nu_c, \quad (2.30b)$$

$$\beta_i \left(\nabla_{\mathbf{Y}} \mathbf{\Gamma}(\mathbf{Y}) - [\mathrm{I}]\right) \cdot \mathbf{n} = \beta_f \left(\nabla_{\mathbf{Y}} \mathbf{\Gamma}(\mathbf{Y}) - [\mathrm{I}]\right) \cdot \mathbf{n} \quad \text{on} \quad \|Y\| = \nu_i, \quad (2.30c)$$

and $\mathbf{\Gamma}$ periodic on the external boundary. We note that (2.30) is defined up to a constant. To ensure the uniqueness of the solution we impose the following condition

$$\frac{1}{\|\Omega\|} \int_{\Omega} \mathbf{\Gamma}(\mathbf{Y}) dY = 0. \quad (2.31)$$

2.3.3 Solution of the cell problem

For simple geometries (like the one depicted in Fig. 2.4(b)) the cell problem can be solved analytically and the thermal conductivity matrix [B] can be computed exactly [111]. However, the method is general and the resulting homogenised model (2.23) is valid for any unit cell geometry. Therefore in most cases [B] will be computed numerically by solving (2.30) using FEM software.

In order to show how the solution of the cell problem can be achieved, we focus for simplicity on the first component of $\mathbf{\Gamma}$, that is Γ_1. The other components are

obtained similarly.

$$\nabla^2_{\mathbf{Y}}\Gamma_1 = 0, \tag{2.32a}$$

$$\beta_c\left(\nabla_{\mathbf{Y}}\Gamma_1 - e_1\right)\cdot\mathbf{n} = \beta_i\left(\nabla_{\mathbf{Y}}\Gamma_1 - e_1\right)\cdot\mathbf{n} \quad \text{on} \quad \|Y\| = \nu_c, \tag{2.32b}$$

$$\beta_i\left(\nabla_{\mathbf{Y}}\Gamma_1 - e_1\right)\cdot\mathbf{n} = \beta_f\left(\nabla_{\mathbf{Y}}\Gamma_1 - e_1\right)\cdot\mathbf{n} \quad \text{on} \quad \|Y\| = \nu_i, \tag{2.32c}$$

with Γ_1 periodic in Y and where e_1 is the unit vector along the first direction, e.g. $(1, 0)$ in two dimensions.

Using the material properties listed in Table 2.1 and the cell domain depicted in Fig. 2.4(b) we can obtain the cell problem solution Γ_1 to (2.32), as shown in Fig. 2.5, where we also plot Γ_2.

In the software employed for this work, the uniqueness of the cell-problem solutions is ensured by imposing a Dirichlet condition on one of the domain corners, $\Gamma_1 = 0$ in, e.g., $(0.5, 0.5)$, instead of the condition (2.31). This allows increased stability of the solver and reduced the computational time.

It is also important to notice that to obtain the effective thermal conductivity only the gradient of $\mathbf{\Gamma}$ appears in (2.25). Therefore the uniqueness condition could also be $\Gamma_1 = c$, with c a constant. The choice of the particular constant, however, has some impacts on the reconstruction procedure, as described in section 2.5.

Once the solution is obtained, the effective thermal conductivity of our initial composite should be evaluated filling the matrix (2.25) and restoring dimensions.

2.4 Numerical Validation

To validate the homogenised model (2.23), in this section results are compared against a full FEM model including each individual insulated wire and the epoxy filling.

We first consider the matrix of 11×11 wires arranged in a regular square lattice

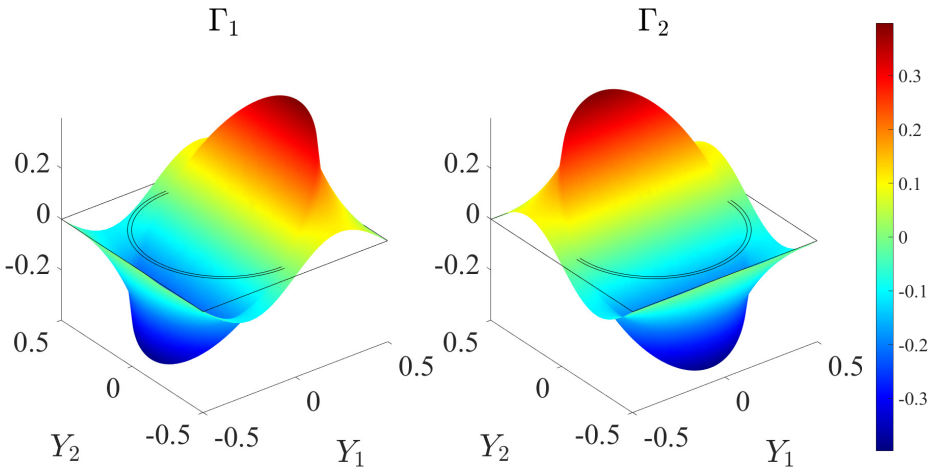

Figure 2.5: Solution of the two components of the cell problem (2.30) Γ_1 and Γ_2 according to the properties in Table 2.1

as depicted in Fig. 2.4(a) with the properties and dimensions listed in Table 2.1; the reference material properties are taken from [54]. This configuration leads to a filling ratio of $\lambda = 0.5$, defined as the ratio of the conductor total area to the whole available area

$$\lambda = \frac{n_w \pi \varepsilon_c^2}{L^2} \equiv \|\Omega_c\|, \tag{2.33}$$

with n_w denoting the total number of wires.

As anticipated before, to obtain the dimensional equivalent thermal conductivity we need to restore the dimensions with $k_{eq} = k_f[\mathrm{B}]_{11}$, leading for this particular case to

$$k_{eq,\mathrm{S}} = 2.05\,\mathrm{W/mK},$$

where we use the subscript S to denote the square lattice configuration. It should be noted that, in the particular case of symmetric geometries (e.g. circular conductors) the solution of the cell problem is symmetric (see Fig. 2.5) and solving for Γ_1 allows to obtain both $k_{eq,1}$ and $k_{eq,2}$.

The full (2.1) and homogenised (2.23) temperature fields are presented in Fig. 2.6, where $\delta = 1/11$, with internal heat generation ($\dot{q} = 1 \times 10^7\,\mathrm{W/m^3}$) and fixed temperature ($T = 0\,^\circ\mathrm{C}$) at the boundaries. To better evaluate the accuracy of the solution of

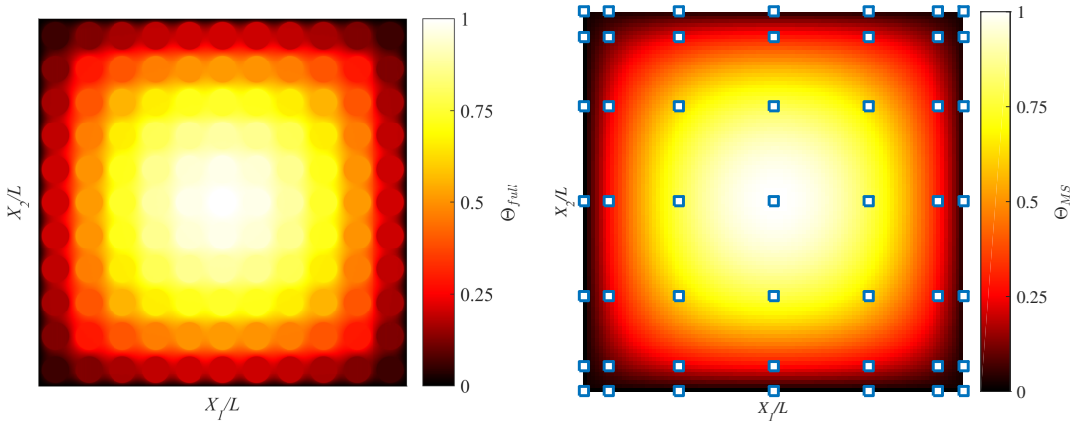

(a) (b)

Figure 2.6: (a) 2D Temperature distribution obtained from the full model Θ_{full} and (b) the homogenised model Θ_{MS} with wires distributed in a square lattice with $\delta = 1/11$, with internal heat generation and Dirichlet boundary conditions

the homogenised model, the two distributions are compared on the mid-cross-section of the domain in Fig. 2.2.

The full model (2.1) is solved with with FEM ($\approx 140\,000$ elements). The homogenised model is solved with a Chebyshev spectral collocation method [112] using 25 grid points. The solution on the Chebyshev points (shown by squares in Fig. 2.6 and the following figures) is then interpolated with the Matlab embedded `interp2` function. We plot the normalised temperature $\Theta = \frac{T}{T_{max}}$ versus the normalised coordinate $\frac{X_1}{L}$, where the reference maximum temperature T_{max} is taken from the solution of the full model. We observe a very good agreement between the two solutions, in particular in the central area of the domain in correspondence with the hot spot. As expected, the limitation of the homogenised solution is that is unable to capture the localised temperature plateaus due to each individual wire. The homogenised model (2.23) is asymptotic in the limit of small δ and, as such, the solution improves as $\delta \to 0$ as shown in Fig. 2.7(a), where we take $\delta = 1/31$. In Fig. 2.7(b) we compare the absolute error $\Theta_{full} - \Theta_{MS}$ in the hot-spot temperature estimation between the full and homogenised model. As expected, the error decreases asymptotically as δ decreases.

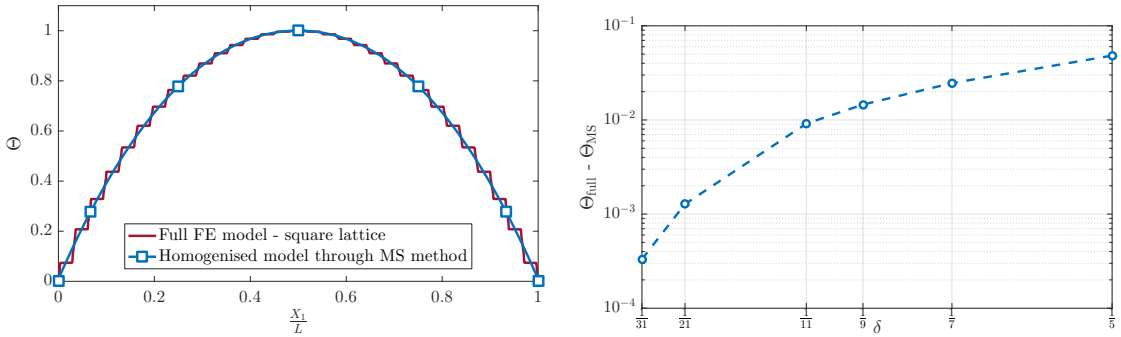

(a) (b)

Figure 2.7: (a) Temperature distribution obtained from the full model Θ_{full} and the homogenised model Θ_{MS} in the mid-cross-section of wires distributed in a square lattice with $\delta = 1/31$, with internal heat generation and Dirichlet boundary conditions. (b) Relative error $\Theta_{full} - \Theta_{MS}$ over a range of δ

2.4.1 Effects of wire distribution in the macro scale domain

We now examine the effects that the microscopic wire configuration has on the effective windings properties. First the MSM model is applied with a different periodic configuration - hexagonal lattice whose unit cell is depicted in Fig. 2.8(a). This configuration achieves the highest filling ratio λ with circular wires, and as a result it is likely to be found in a real winding environment (Fig. 2.1(a)). The first component Γ_1 of the cell problem (2.30) in an hexagonal lattice is presented in Fig. 2.8(b) for the case of $\lambda = 0.5$. This leads to an equivalent thermal conductivity of

$$k_{eq,\mathrm{H}} = 2.03\,\mathrm{W/mK},$$

where the subscript H refers to the hexagonal lattice configuration.

In Fig. 2.9 we compare the equivalent thermal conductivities for a square and a hexagonal lattice over a range of filling ratios using the MS method. We see that the difference between the effective coefficients $k_{eq,\mathrm{S}}$ and $k_{eq,\mathrm{H}}$ only becomes evident for filling ratios $\lambda > 0.5$. This is consistent with the results in the context of an effective diffusion coefficient in porous media [109].

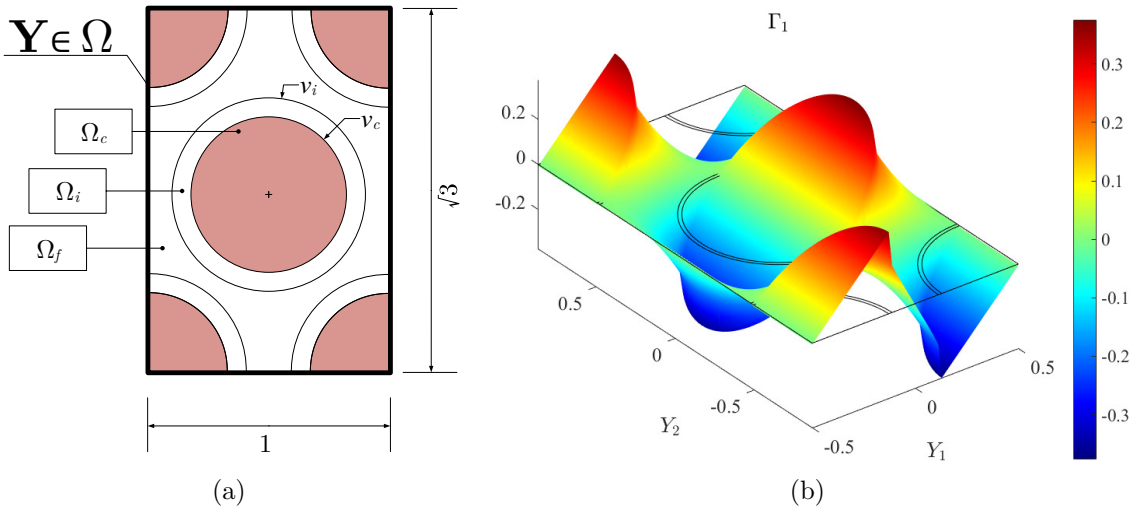

Figure 2.8: (a) Microscopic domain $Y \in \Omega$ related to the hexagonal lattice wires and (b) Γ_1 distribution for the case hexagonal lattice with $\lambda = 0.5$

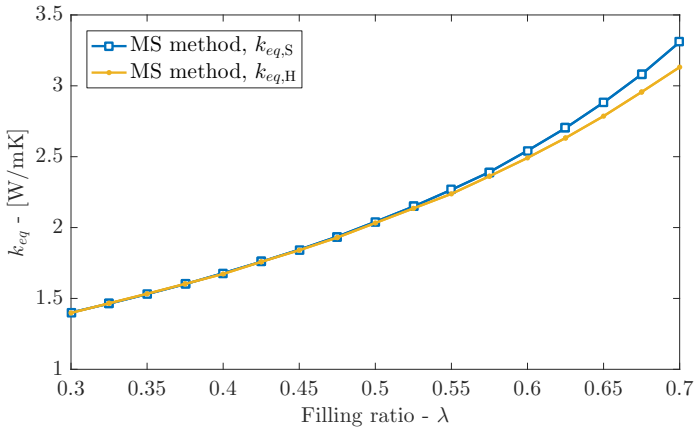

Figure 2.9: Effective thermal conductivity k_{eq} over a range of λ using the MSM and different regular lattices

One could argue that the assumption of perfectly periodic wire distributions (arranged on a square or hexagonal lattice) may not hold in practice. To assess the discrepancy that may rise due to a random distributions of wires, we solved the full FE model with uniformly distributed and non-overlapping wires and we evaluated 100 randomised configurations for each filling ratio λ. To generate the random uniform distributions, we initialised the system at a given λ with a periodic square lattice, as per Fig. 2.10(a). A wire is then randomly selected and allowed to move to a new random location within the domain. The new position is accepted if the wire does not overlap any other conductor and it does not fall out of the domain boundaries. This procedure, known as the Metropolis-Hastings algorithm [113], is repeated $300n_w$ times. Fig. 2.10(b) shows one of the random configurations, enabling the tracking of the movement of each insulated wire. Repeating the process starting from a hexagonal rather than square lattice gives the same results, indicating that enough steps have been taken to lose any initial configurations.

For each configuration we computed the equivalent thermal conductivity $k_{eq,\mathrm{R}}$, where the subscript R stands for random distribution. In the FE simulations a thermal gradient is applied to the domain, setting fixed temperature conditions on two opposite boundaries and no-flux condition on the remaining two boundaries. The equivalent thermal conductivity is then calculated with

$$k_{eq,\mathrm{R}} = \frac{\dot{Q}}{\Delta T}\frac{L}{A_w}, \tag{2.34}$$

where $\dot{Q}$ is the total heat flux evaluated on a cross section of area A_w perpendicular to the domain and ΔT is the imposed thermal gradient. We plot the average together with the 95% error bars in Fig. 2.11. As we can see, the differences between the effective conductivity from the random distribution, $k_{eq,\mathrm{R}}$, and the periodic ones are barely noticeable. Interestingly, the set of data follows the behaviour of the periodic square

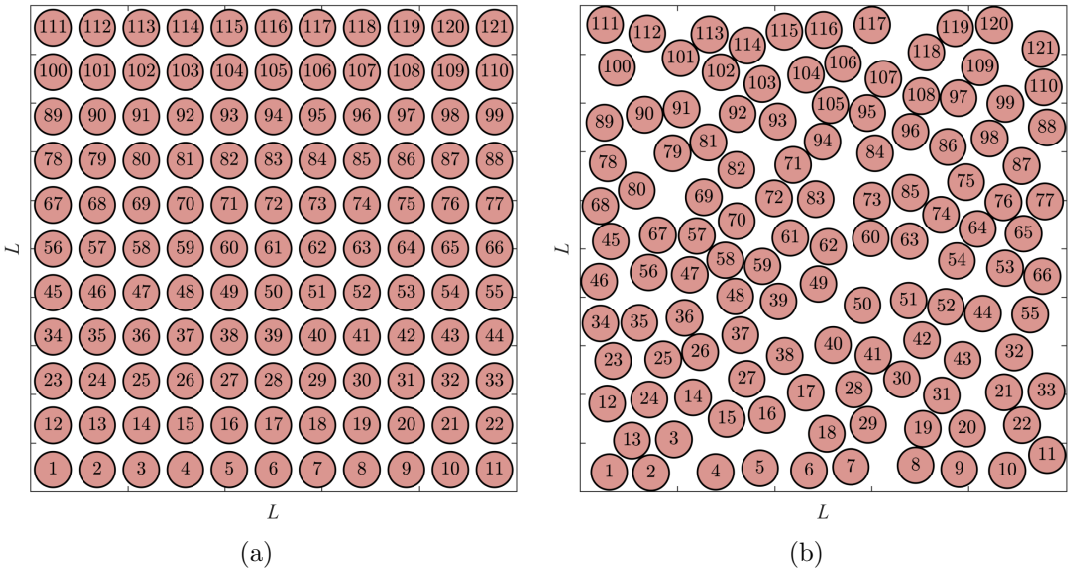

Figure 2.10: Process of creating a random distribution of wires with $\lambda = 0.5$, (a) starting from a square lattice, to (b) a randomised configuration

lattice distribution quite closely. Therefore, this suggests that the MSM approach to estimate k_{eq} may be a suitable method to obtain accurate estimates for real windings, not just theoretical periodically arranged windings.

For comparison purposes, in Fig. 2.11 we also include two commonly used analytical formulae, namely the lower HS bound [54]

$$k^{-}_{eq,\mathrm{HS}} = k_f \frac{(1+\lambda)k_c + (1-\lambda)k_f}{(1-\lambda)k_c + (1+\lambda)k_f}, \tag{2.35}$$

$$\tag{2.36}$$

and the lower Wiener bound (2.4b).

The 2-phase HS formula always outputs a higher k_{eq} than the correct estimation, which leads to an unacceptable underestimation of the hot-spot temperature. This is clearly shown in Fig. 2.12, where we compare the homogenised solutions using $k^{-}_{eq,\mathrm{HS}}$ and $k_{eq,\mathrm{S}}$ with the full solutions using random wire configurations at $\lambda = 0.5$. This is due to the fact that the insulation domain is neglected in (2.35), leading to an overestimation of the effective thermal conductivity. Fig. 2.12 also shows the average

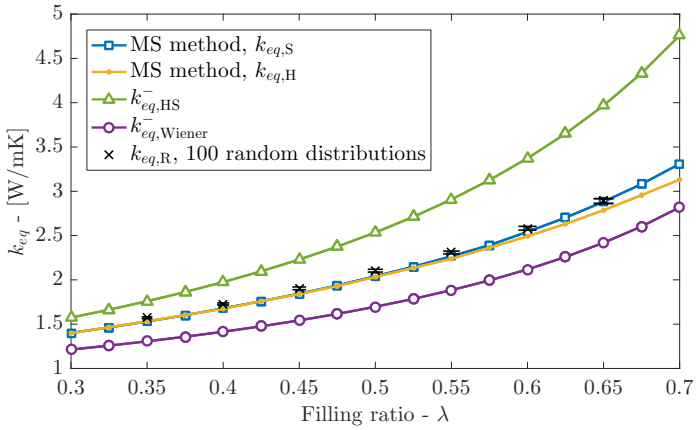

Figure 2.11: Effective thermal conductivity k_{eq} over a range of λ using Wiener's lower bound (2.4b), HS formula (2.35), the MS method for a square and hexagonal lattice and obtain with 100 random configurations (mean value with 95% error bars)

distribution obtained averaging over the 100 configurations, as well as the distributions of the two configurations that gave the highest and lowest hot-spot temperatures. The MSM estimation follows the average random solution very well. This result indicates that the MSM can provide an accurate estimation of the macroscopic thermal behaviour of the electrical windings, therefore leading to a reliable approximation of the hot-spot temperature.

2.4.2 Transient results

After proving the reliability of the MSM for steady state problems, we now investigate its performance over transients. We refer to the case of $\lambda = 0.5$ with wires distributed on a square lattice as in Fig. 2.4(a) where $\delta = 1/11$. The equivalent heat capacity can be estimated restoring the dimensions of A, given by (2.24), with:

$$C_{eq} = \mathrm{A}\frac{k_f \tilde{t}}{L^2} = 3.12 \times 10^6 \,\mathrm{J/m^3K}.$$

As mentioned before, this quantity is independent of the wire distribution and only depends on the relative filling of each phase.

To solve the homogenised model (2.23), we used an explicit forward Euler method

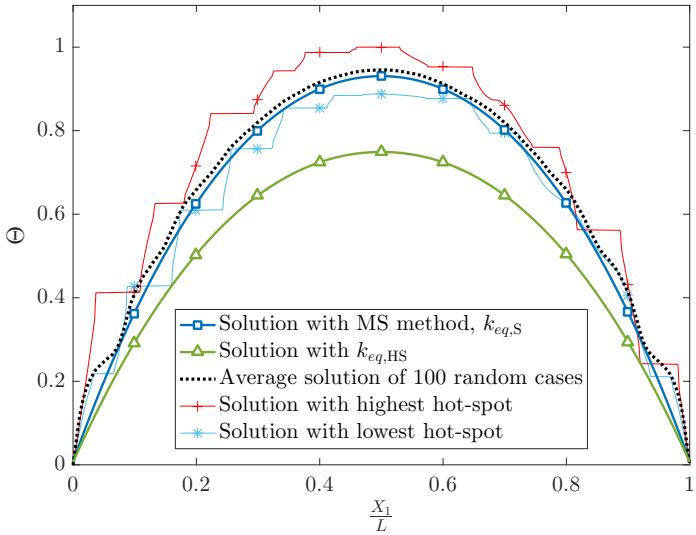

Figure 2.12: Steady-state temperature distribution for random distributions at $\lambda = 0.5$ compared with the macroscopic solution, homogenising the problem using the MS method or HS formula (2.35)

in time and the same spectral method in space as before. Accordingly, for a fixed time step t_{step}, at each instant we solve the following linear system

$$[\Theta]^{\tau} = \frac{t_{step}}{C_{eq}}[\dot{q}_{eq}] + \frac{t_{step}}{C_{eq}} k_{eq,\mathrm{S}}[\mathrm{D}][\Theta]^{\tau-1} + [\Theta]^{\tau-1}, \tag{2.37}$$

where $[\Theta]^{\tau}$ is the vector of the dimensionless temperatures at the τth instant and the nodal points, [D] the discretisation matrix and $[\dot{q}_{eq}]$ the equivalent heat generation vector at the nodal points.

In Fig. 2.13 we compare the thermal hot-spot $\Theta_{\mathrm{hot-spot}}$ obtained from the homogenised and full models as a function of the Fourier number $\tau = t\frac{k_{eq,\mathrm{S}}}{C_{eq}L^2}$ and Θ is again nondimensionalised using the steady-state maximum temperature of the full model. We set the initial condition to 0 °C and let the domain heat up applying a uniformly distributed internal heat generation. Dirichlet boundary conditions ($T = 0\,°\mathrm{C}$) are imposed on the four lateral edges as in the previous tests.

The root mean square relative error between the two estimations evaluated for m

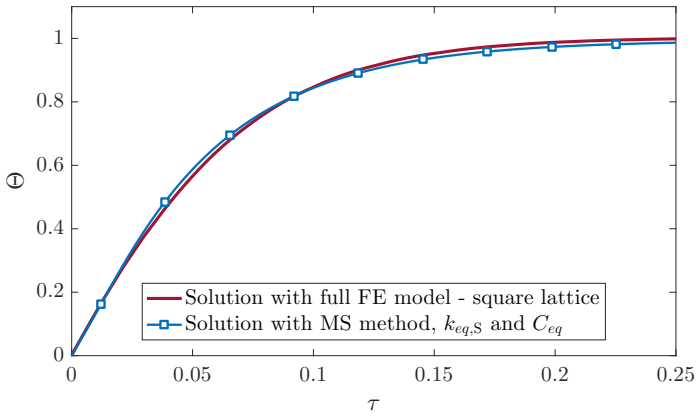

Figure 2.13: Transient temperature $\Theta = T/T_{max}$ as a function of the Fourier number $\tau = t\frac{k_{eq}}{C_{eq}L^2}$ in centre of the domain obtained with the MSM homogenised model the full model using a square lattice wire distribution with $\delta = 1/11$

points is

$$\sqrt{\frac{\sum_{\tau=1}^{m}\left(\Theta^{\tau}_{\text{full,hot-spot}} - \Theta^{\tau}_{\text{MS,hot-spot}}\right)^2}{m}} = 1.3\%, \tag{2.38}$$

which once more confirms the high accuracy of the MSM.

2.5 Temperature field reconstruction

We now come back to the discussion of the MSM before providing the experimental validation. Making reference to the model derivation of Section 2.3, we recall that the ansatz for the temperature field is expressed by an asymptotic expansion in powers of δ, (2.10). We found that the equation for $T^{(0)}$ describes macroscopic thermal behaviour, and that microscopic effects only appear at $o(\delta)$ in $T^{(1)}$. We used an averaged function of $T^{(1)}$ to close the equation for $T^{(0)}$. It is interesting to examine if we can use the non-averaged $T^{(1)}$ to reconstruct a solution displaying the microscopic variations from wire to wire observed in the full FEM solution. In other words, we try to apply an inverse process, rebuilding the actual temperature field using the macroscopic and cell solutions as depicted in Fig. 2.14.

In (2.15) we defined $T^{(1)}$ as a linear combination of the cell problem solution $\mathbf{\Gamma}$

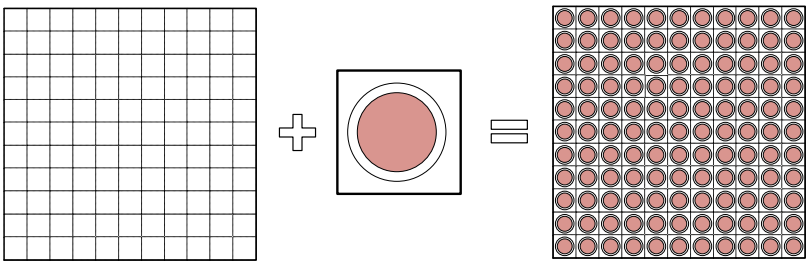

Figure 2.14: Process of temperature field reconstruction

and the gradient of the macroscopic temperature distribution $T^{(0)}$. These terms have already been obtained before, thus making the calculation of $T^{(1)}$ a fairly easy task. Indeed we shall evaluate

$$T^{(1)} = -\left(\frac{\partial T^{(0)}}{\partial X_1}\Gamma_1 + \frac{\partial T^{(0)}}{\partial X_2}\Gamma_2\right). \tag{2.39}$$

In Fig. 2.15(a) the steady state distribution of $T^{(1)}$ in the domain middle cell, i.e. wire n° 61 in Fig. 2.10(a), is presented in terms of dimensionless temperature Θ and normalised coordinates.

The temperature field can now be reconstructed using (2.10) truncated at the first order

$$T = T^{(0)} + \delta T^{(1)}. \tag{2.40}$$

The result is shown in Fig. 2.15(b), where we can already see an excellent matching with the solution of Fig. 2.6(a). To allow for a better (quantitative) comparison, we plot the solution along $X_2/L = 0.5$ obtained with the full model and with the reconstructed solution (2.40) in Fig. 2.16. Introducing a second term in the expansion allows to almost perfectly include the microscopic effects due to insulated wires. With reference to the solutions in Fig. 2.16, the RMS relative error is

$$\sqrt{\frac{\sum_{\text{pos}=1}^{m}\left(\Theta_{\text{full,pos}} - \Theta_{\text{MS}^{(1)},\text{pos}}\right)^2}{m}} = 0.87\%. \tag{2.41}$$

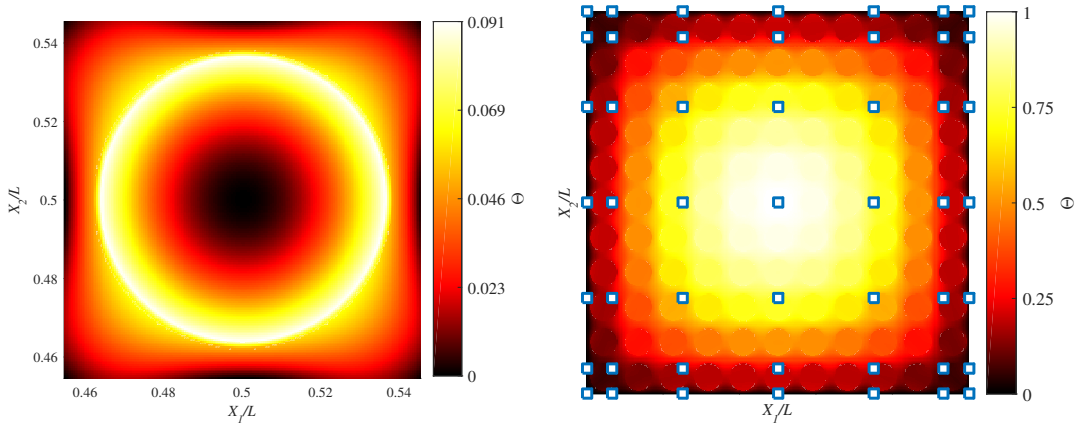

(a) (b)

Figure 2.15: (a) Steady-state $\Theta^{(1)}$ distribution in the central cell of the winding domain, Fig. 2.4(a) and (b) reconstructed temperature field using expressed in terms of dimensionless temperature

A big advantage is that, using an Intel i7 (3.2 GHz and 32 Gb RAM) to solve the full model with the commercial software takes 9.4 s while the homogenised model only takes 0.22 s, of which 5×10^{-4} s is spent for solving the macroscopic temperature distribution with the collocation method. It has to be said that we did not include the time to solve the cell problem, which takes 3 s, since it has to be solved only once per each filling ratio λ.

Fig. 2.16 confirms that the improvement obtained adding $T^{(1)}$ to the macroscopic solution justifies the added computational effort and that we can stop the truncation of the expansion at this term.

2.6 Experimental validation

In this section we validate the approach with measured data available on the literature, [54]. Estimations are compared to experimental measurements on encapsulated thin conductors ($\emptyset 1$ mm $\rightarrow$ 0.05 mm).

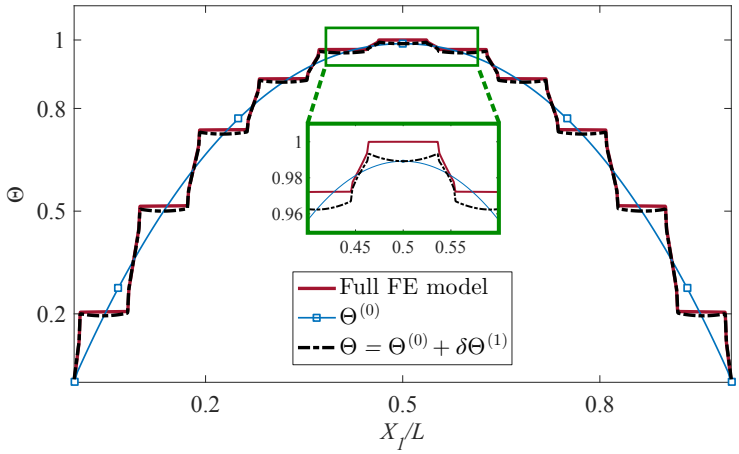

Figure 2.16: Steady-state temperature distribution obtained from the full model Θ_{full} and the homogenised model truncated at the leading $\Theta^{(0)}$ and first $\Theta^{(1)}$ order in the mid-cross-section of wires distributed in a square lattice with $\delta = 1/11$, with internal heat generation and Dirichlet boundary conditions

2.6.1 Experimental data from the literature

Simpson et al. [54] presents the measured equivalent thermal conductivity of electrical windings for both copper and aluminium conductors, arranged in cubes impregnated with epoxy. The thermal conductivity of aluminium is assumed to be $k_{Al} = 234\ \mathrm{W/m^2}$ and all the remaining relevant properties are as presented in Table 2.1.

As simulated in the previous section, the equivalent conductivity is measured by injecting a known heat flux into a cube boundary, with the opposite boundary in contact with a cooling plate. In this manner the heat flows in a single direction, assuming all the remaining boundaries are well insulated. The equivalent conductivity is then evaluated with (2.34), knowing the temperature gradient between the hot and cold boundaries.

For the MSM, the square lattice cell was used, in accordance with Fig. 2.11. Fig. 2.17 shows that the mismatch between measurements and estimations is less than 4%.

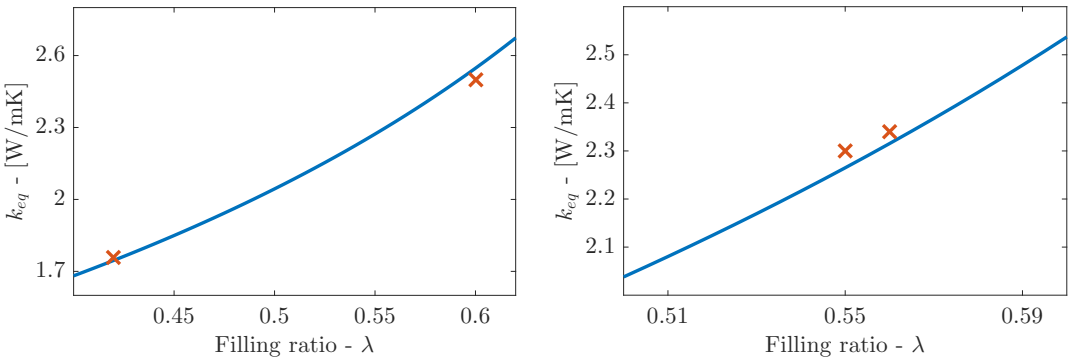

Figure 2.17: Comparison of k_{eq} estimated via the MS method, using the square lattice cell, with experimental measurements from [54] with (a) copper and (b) aluminium conductors at various filling ratios

2.6.2 Equivalent thermal conductivity of Litz wire windings

We are now validating the model against a set of experimental data we collected. Similarly to the analysis performed in [54], the specimens consisted of cubes of wires encapsulated with epoxy compound, i.e. 832TC from MG Chemicals with $k_f = 0.7\,\mathrm{W/mK}$ after curing. The gauge of the wires under test is very small, ranging from $\emptyset 1\,\mathrm{mm}$ to $0.05\,\mathrm{mm}$, and thus the cube size was approximately $1\,\mathrm{cm}^3$, as shown in Fig. 2.18. In particular, four cubes for each wire size were manufactured, i.e. $\emptyset$ 1, 0.2, 0.1, and $0.05\,\mathrm{mm}$. These very thin conductors, put in parallel and twisted with particular patterns, are usually called "Litz wires" and employed in application where the current is driven at high frequency (the reason for this will be extensively discussed in the following chapters). The cubes were built and analysed as part of a project involving the development of a high-torque-density prototype machine to be employed in a "supercar" powertrain.

2.6.3 Test arrangements

In Fig. 2.19(a) we show the schematics of the tests we performed. The cube was housed between an heating cartridge and a fan cooled plate. To ensure a one di-

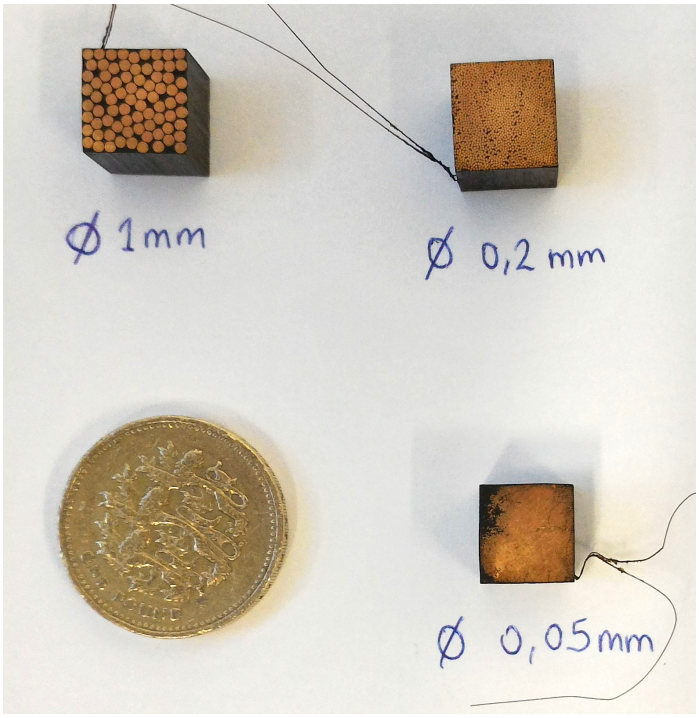

Figure 2.18: Some exemplars analysed during the tests

mensional heat flow, the specimen and the cartridge were surrounded by thermal insulation resistant to high temperatures. To improve thermal contact and allow uniform heat transfer between and cartridge and the cube and between the cube and cold plate, thermally conductive thermal paste was applied.

The equivalent thermal conductivity was evaluated using (2.34). In particular, ΔT was measured using three thermal sensors (type K thermocouples) on each of the top and bottom sides of the cube. Dimensions of the cubes were accurately measured with a Mitutoyo Digital Caliper. As shown in Fig. 2.19(b), the injected power was measured with a Yokogawa PX8000 power analyser. Per each test, the "hot" and "cold" side temperatures were recorded using a NI data acquisition compactRIO.

Test were performed injecting three ranges of power, i.e. 0.6, 1.68 and 2.61 W. Fig. 2.20 shows and example of test measurement for the case of 2.61 W injected power. The condition for each test convergence was set to $\Delta T_{hot-cold} < 0.5\,°\text{C}$ in the last 3 minutes. As highlighted in the figure, the thermal conductivity was evaluated

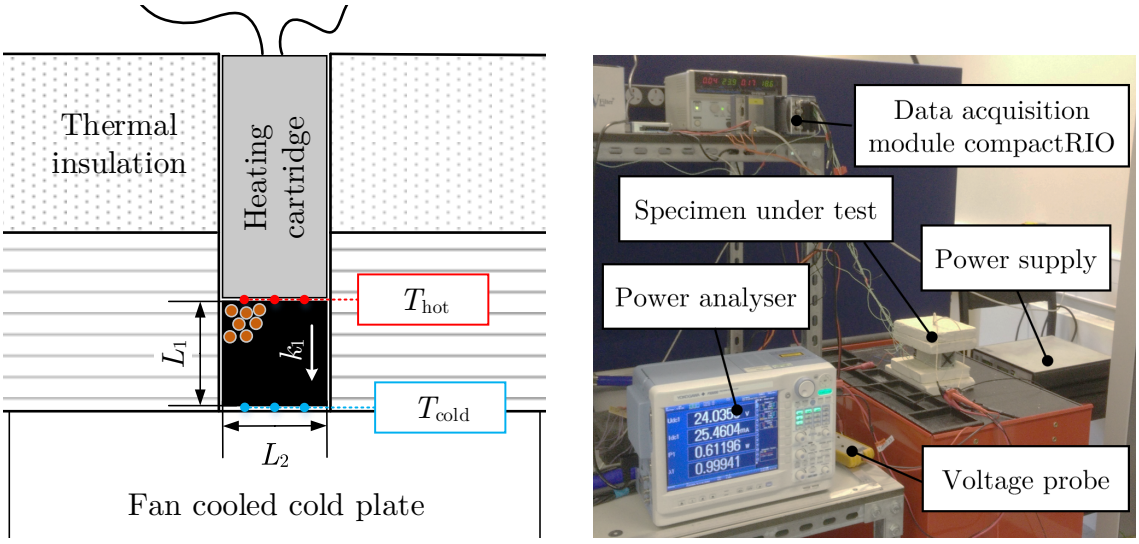

Figure 2.19: (a) 2D schematics of the performed tests and (b) arrangement created to perform the tests

at steady state, averaging the results from the last 100 s.

Before showing the outcome of the measurement, it is important to discuss the approach applied to evaluate the cube filling ratio. This is no easy task since, as shown in Fig. 2.18, the very small gauge of the wires makes it impossible to distinguish them with the naked eye. Accordingly, each of the cubes was analysed with an optic microscope (Alicona Infinite Focus 3D Profilometer). The high definition pictures taken, e.g. Fig. 2.21, allowed us to measure the size of the insulation coating and evaluate the filling ratio. To do so, the pictures were post-processed with Matlab, and by comparing the emissions of each material we were able to measure the ratio $\lambda = \frac{\Pi_c}{\Pi}$, where Π_c is the copper surface and Π is the complete compound surface. The results are listed in Table 2.2; due to a surface imperfection we were not able to evaluate the filling ration of cube 5D, which accordingly will not be taken into consideration in the following analysis.

Individual test results are also presented in Fig. 2.22, where the plots are divided depending on the wire size and power injected. The error bars related to each

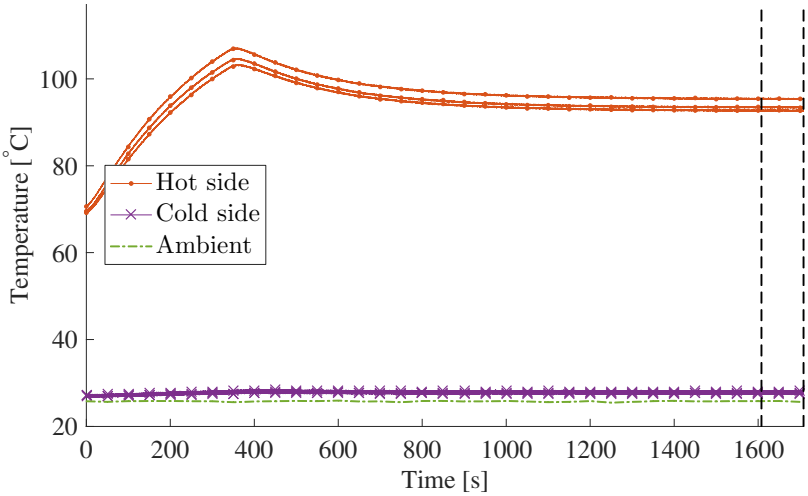

Figure 2.20: Temperature measurements for the cube #20C, with 2.61 W injected power

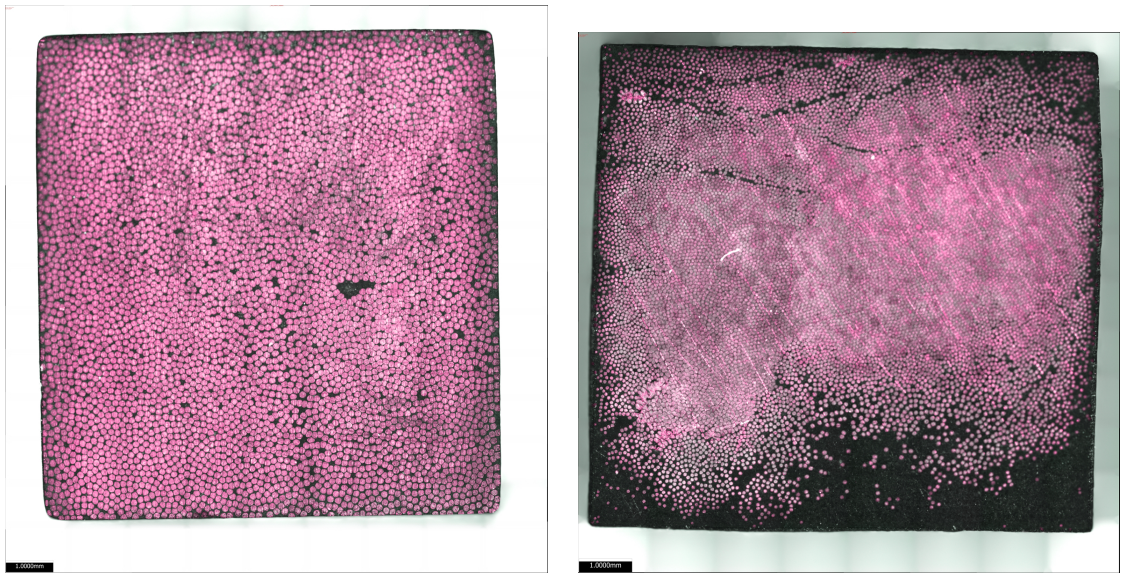

(a) (b)

Figure 2.21: High quality pictures of the cube (a) #10B and (b) #5C taken with the Alicona Infinite Focus 3D Profilometer

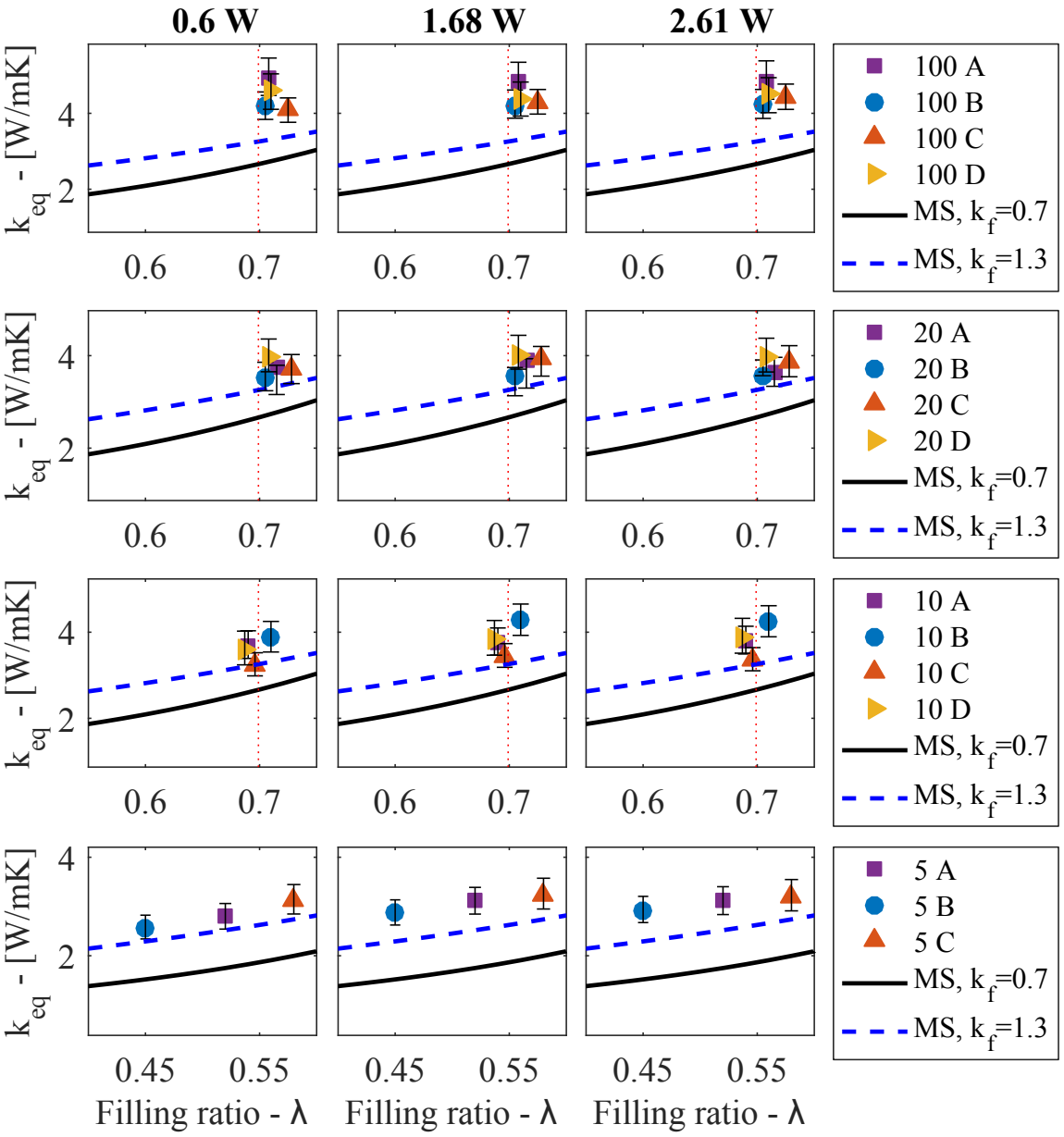

Figure 2.22: Experimental results from test on sample of various size and as a function of power injected

Table 2.2: Measured dimensions and filling ratios λ of the cubes under test

Variable	Cube 100	Cube 20	Cube 10	Cube 5
r_c [mm]	0.5	0.1	0.05	0.025
r_i [mm]	0.53	0.106	0.053	0.0265
$L_{1,\mathrm{A}}$ [mm]	10.3	9.97	10.11	9.64
$A_{w,\mathrm{A}}$ [mm^2]	9.75	10	9.49	9.37
λ_{A}	0.708	0.715	0.69	0.52
$L_{1,\mathrm{B}}$ [mm]	10.4	9.71	10.32	9.17
$A_{w,\mathrm{B}}$ [mm^2]	9.9	9.97	9.58	9.53
λ_{B}	0.705	0.705	0.71	0.45
$L_{1,\mathrm{C}}$ [mm]	9.8	9.93	9.6	9.57
$A_{w,\mathrm{C}}$ [mm^2]	9.87	10	9.94	9.11
λ_{C}	0.725	0.728	0.696	0.58
$L_{1,\mathrm{D}}$ [mm]	9.98	9.76	10.03	-
$A_{w,\mathrm{D}}$ [mm^2]	9.88	9.93	9.71	-
λ_{D}	0.71	0.708	0.687	-

measurement account for random measurement uncertainties, namely:

- as shown in Fig. 2.20, a small spread in the measurements was recorded, which may be due to slight movements of the sensors. Accordingly, in (2.34) the temperature gradient can be defined as $\Delta\bar{T}$, $\Delta T_{\max}$ or $\Delta T_{\min}$, representing the different between the average of the measurements on the hot and cold side, the maximum and the minimum temperaeture difference, respectively;

- although a number of insulation layers were used, some of the heat generated by the cartridge could escape from the top of the experimental rig (see Fig. 2.19). We can estimate this power loss with

$$\dot{Q}_{top} = A_{top} h_\infty \left(T_{top} - T_\infty\right) \tag{2.42}$$

where A_{top} is the top surface of the hole ($r = 0.945 \times 10^{-3}$ m), h_∞ the convection coefficient with ambient ($h_\infty = 10\,\mathrm{W/m^2K}$ [3]), T_{top} the mean of the hot side temperature measurements, and T_∞ is the measured ambient temperature. For

all the tests $\dot{Q}_{top}$ accounted for $\approx 8\%$ of the total injected power.

- the movement of the sensors implied that L_1 in (2.34) could increase compared to the measured distance. We accounted for this error with $\Delta L_1 = 0.5 \times 10^{-3}\,\mathrm{m}$.

Systematic errors, such as the type K thermocouples 1 °C accuracy, were neglected. In conclusion, in Fig. 2.22 the marker corresponds to $k_{eq} = \frac{\dot{Q}-0.5\dot{Q}_{top}}{\Delta\bar{T}} \frac{L_1+0.5\Delta L_1}{A_w}$ and the top and bottom error bars relate to $k_{eq}^{+} = \frac{\dot{Q}}{\Delta T_{min}} \frac{L_1+\Delta L_1}{A_w}$ and $k_{eq}^{-} = \frac{\dot{Q}-\dot{Q}_{top}}{\Delta T_{max}} \frac{L_1}{A_w}$, respectively.

2.6.4 Analysis of measurements

The first outcome of the tests is that the equivalent thermal conductivity (within the analysed range) is independent of temperature, as the measured k_{eq} do not vary significantly with the level of power injected $\dot{Q}$.

The vertical dotted lines in Fig. 2.22 represent the maximum filling ratio that can be ideally achieved with a coated circle in a square lattice, which is the upper limit for the MSM estimation. Accordingly, to obtain estimates at higher filling ratios, we interpolate the trend obtained from the range of available λ with a third grade polynomial. As mentioned earlier, the solutions from the MSM are obtained using the square lattice configuration, and thermal conductivities of $k_c = 401\,\mathrm{W/mK}$, $k_i = 0.26\,\mathrm{W/mK}$ and, $k_f = 0.7\,\mathrm{W/mK}$.

Generally speaking, the estimations provided by the MSM underestimate the equivalent thermal conductivity on average by 32%. One of the reasons for this discrepancy may be due to a wrong assessment of the epoxy thermal conductivity. The epoxy compound is composed of a mixture of two parts, the resin and the hardener, which should be mixed with prescribed ratios. Accordingly, the conductivity of the cured material can vary significantly if the ratio is not respected. If, for instance, we set $k_f = 1.3\,\mathrm{W/mK}$ (see the dashed line in Fig.2.22), the discrepancy decreases,

reducing the mean error to 16%.

It is important to notice that the improvement is more significant for the cubes with $r_c = 0.025\,\text{mm}$, characterised by lower λ. To achieve higher λ, the shape of the conductors is modified by the external pressure applied. Accordingly, the MSM based on the cell Fig. 2.4(b) cannot properly describe the thermal properties of the cube, highlighting the limits of the polynomial interpolation. Indeed, the measurements related to the cubes with $r_c = 0.025\,\text{mm}$ follow closely the trend given by the MSM.

Chapter 3

Coupled electromagnetic and thermal homogenisation of electrical machine windings

This chapter is based on publication [85].

In this chapter we present a multiphysics analysis of electrical windings, showing how to couple the homogenisation technique presented in Chapter 2 with another method, suitable for homogenising the electromagnetic problem. The objective is to provide a model able to accurately assess the loss and temperature distribution within the winding domain as a function of the current frequency and other important parameters, such as temperature itself.

3.1 Introduction

In Chapter 2 we introduced (2.1) and (2.2) to describe the heat transfer phenomena in electrical windings. These were modelled according to two physical representations, either considering every single wire or the winding as an homogeneous material, re-

spectively. In both cases, a specific source term appears, which in electrical windings is a function of the square of the current density $\boldsymbol{J}$ and the material conductivity σ. In the previous chapter we assumed the current density distribution to be uniform within each conductor and constant in time. Although this is a good approximation when a direct current (DC) is injected in the conductors, this may not always be the case when alternating currents (AC) are involved. The use of AC may induce eddy currents that circulate within the conductor, leading to a non-uniform distribution of $\boldsymbol{J}$ that in turn could mean significantly higher specific losses. In the literature the "AC effects" are usually divided into two major contributions, the "skin" and the "proximity" effect [114–119]. These effects are both a function of the angular frequency ω, where $\omega = 2\pi f$ and f frequency, conductor shape and dimension, filling ratio λ, and temperature T [85]. To accurately assess these effects, computationally expensive simulations are usually completed, with models describing the behaviour of every single conductor [115,120]. If some assumptions hold, however, the computational effort can be dramatically reduced when the governing equations are suitably homogenised, employing effective material properties, similarly to (2.2).

3.1.1 Governing equations

Before looking at the homogenisation technique and the particular AC effects, let us introduce the governing equations of the electromagnetic problem, i.e. Maxwell's equations:

$$\nabla \times \boldsymbol{H} = \boldsymbol{J}_0 + \boldsymbol{J}_\epsilon, \tag{3.1a}$$

$$\nabla \times \boldsymbol{E} = -\frac{\partial \boldsymbol{B}}{\partial t}, \tag{3.1b}$$

$$\nabla \cdot \boldsymbol{B} = 0, \tag{3.1c}$$

where we neglected the contribution of displacement currents as in this thesis we are dealing with low frequencies (or with good conductors) with $\boldsymbol{H}$, $\boldsymbol{B}$, and $\boldsymbol{E}$ the magnetic field, magnetic flux density and electric field, respectively; $\boldsymbol{J}_0$ and $\boldsymbol{J}_\epsilon$ are source, and induced current densities, respectively. The following constitutive laws hold:

$$\boldsymbol{B} = \mu \boldsymbol{H}, \qquad \boldsymbol{H} = \nu \boldsymbol{B}, \tag{3.2}$$

$$\boldsymbol{J} = \sigma \boldsymbol{E}, \qquad \boldsymbol{E} = \rho_J \boldsymbol{J}, \tag{3.3}$$

with μ permittivity ($\nu = \mu^{-1}$ reluctivity) and ρ_J electrical resistivity. In the winding domain all the constitutive laws are assumed to be linear, with constant material properties.

The objective of homogenisation is to transform the constitutive laws

$$[\boldsymbol{H}; \boldsymbol{E}] = [\mathrm{M}][\boldsymbol{B}; \boldsymbol{J}], \tag{3.4}$$

into effective constitutive laws [121,122]

$$[\boldsymbol{H}_M; \boldsymbol{E}_M] = [\mathrm{M}_{eq}][\boldsymbol{B}_M; \boldsymbol{J}_M], \tag{3.5}$$

where $[\mathrm{M}_{eq}]$ is block diagonal when $\boldsymbol{H}_M$ and $\boldsymbol{E}_M$ are independent from $\boldsymbol{J}_M$ and $\boldsymbol{B}_M$, respectively, and the subscript M refers to macroscopic quantities. In the more general case, where there are non-zero elements in the non-diagonal blocks, the material is defined as "chiral" [123].

3.1.2 The magnetic vector potential formulation

It is sometimes useful to describe (3.1) using the magnetic vector potential $\boldsymbol{A}$ [124]

$$\boldsymbol{B} = \nabla \times \boldsymbol{A}. \tag{3.6}$$

Accordingly, we can rewrite Maxwell's equations as

$$\nabla \times \nu \left(\nabla \times \boldsymbol{A} \right) = \boldsymbol{J}_0 + \boldsymbol{J}_\epsilon, \tag{3.7a}$$

$$\nabla \times \boldsymbol{J}_\epsilon = -\sigma \frac{\partial}{\partial t} \left(\nabla \times \boldsymbol{A} \right), \tag{3.7b}$$

$$\nabla \cdot \left(\nabla \times \boldsymbol{A} \right) = 0. \tag{3.7c}$$

We highlight the fact that the last equation is meaningless as this property applies to any vector field. Exchanging the derivatives, from (3.7b) we find that $\boldsymbol{J} = \sigma \partial \boldsymbol{A} / \partial t$. Moreover, recalling that

$$\nabla \times \nabla \times \boldsymbol{A} = -\nabla^2 \boldsymbol{A} + \nabla \left(\nabla \cdot \boldsymbol{A} \right), \tag{3.8}$$

(3.7a) becomes

$$\nabla^2 \boldsymbol{A} + \sigma \mu \frac{\partial \boldsymbol{A}}{\partial t} = \mu \boldsymbol{J}_0, \tag{3.9}$$

where we choose $\nabla \cdot \boldsymbol{A} = 0$, known as the "Coulomb gauge", an auxiliary condition needed to solve Maxwell equations expressed in terms of $\boldsymbol{A}$. It is important to notice that (3.1) and (3.9) can be simplified in the frequency domain. If $\boldsymbol{A}(t) = \boldsymbol{A} e^{i\omega t}$ is an harmonic function in time, with i the imaginary unit, time derivatives become $\partial \boldsymbol{A}(t) / \partial t = i\omega \boldsymbol{A}(t)$ treating the vector fields as complex values. Accordingly, we have

$$\nabla^2 \boldsymbol{A} + i\omega\sigma\mu \boldsymbol{A} = \mu \boldsymbol{J}_0, \tag{3.10}$$

where $\boldsymbol{A}$ now is a complex number. This formulation of Maxwell's equations will be used in Section 3.3.

3.1.3 Poynting's theorem

As mentioned earlier, in this chapter we want to analyse the thermal behaviour of the winding domain as a function of losses. Thus, it is fundamental to introduce the law for the conservation of energy applied to electromagnetic fields in the winding domain, which is expressed by a simplified form of the Poynting's theorem (here we follow the description given in [125])

$$\underbrace{\frac{1}{\sigma}\int_{\Sigma}|\boldsymbol{J}|^2\,d\Sigma}_{\substack{\text{total dissipated power}\\ \text{within the volume } \Sigma}} + \underbrace{\int_{\Sigma}\boldsymbol{H}\cdot\frac{\partial\boldsymbol{B}}{\partial t}\,d\Sigma}_{\substack{\text{variation rate of the}\\ \text{stored magnetic energy}\\ \text{within the volume } \Sigma}} = -\underbrace{\int_{\partial\Sigma}(\boldsymbol{E}\times\boldsymbol{H})\cdot\boldsymbol{n}\,ds}_{\substack{\text{flux of the Poynting vector}\\ \text{across the surface } \partial\Sigma}}, \tag{3.11}$$

where Σ is a representative volume, enclosed by the surface $\partial\Sigma$. This theorem is graphically sketched in Fig. 3.1.

Physically speaking, (3.11) means that the sum of the ohmic losses and the power absorbed by the magnetic field is equal to the inwards flux of the vector $\boldsymbol{S} = \boldsymbol{E} \times \boldsymbol{H}$, called the Poynting vector. For sinusoidally changing vectors, we introduce the complex Poynting vector $\boldsymbol{S} = \frac{1}{2}(\boldsymbol{E} \times \boldsymbol{H}^*)$, which represents a time averaged density of power flow. Accordingly, this yields

$$\underbrace{\frac{1}{2\sigma}\int_{\Sigma}|\boldsymbol{J}|^2\,d\Sigma}_{\substack{\text{total dissipated power}\\ \text{within the volume } \Sigma}} + \int_{\Sigma}+i2\omega\,\underbrace{\left[\frac{\mu}{4}\int_{\Sigma}|\boldsymbol{H}|^2\,d\Omega\right]}_{\text{stored magnetic energy}} = -\underbrace{\int_{\partial\Sigma}\frac{1}{2}(\boldsymbol{E}\times\boldsymbol{H}^*)\cdot\boldsymbol{n}\,ds}_{\substack{\text{flux of the}\\ \text{complex Poynting vector}\\ \text{across the surface } \partial\Sigma}}, \tag{3.12}$$

where, e.g., $|\boldsymbol{J}|^2 = \boldsymbol{J}\boldsymbol{J}^*$ and J the peak value of the signal; also, $\boldsymbol{J}^*$ represents the complex conjugate of $\boldsymbol{J}$. Similarly, here we see that the real part of $\boldsymbol{S}$ is the ohmic (Joule) loss, while the imaginary part is 2ω times the time averaged magnetic

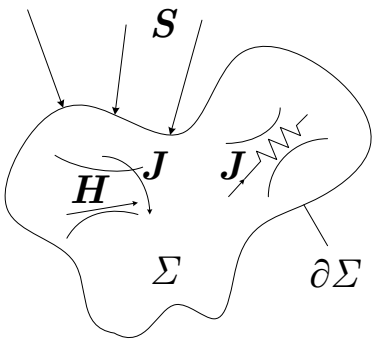

Figure 3.1: Visual representation of the Poynting's theorem

energy. We will refer to this formulation in Section 3.3 to obtain the effective material properties.

3.2 AC effects

3.2.1 The skin effect

When an alternating source current I_0, with $I_0 = \int_{\Omega_c} \boldsymbol{J}_0 d\Omega_c$ and Ω_c the cross-sectional surface of the conductor, is injected in a conductor located in the free space, it generates a time varying magnetic field, that, according to Faraday's law (3.1b), self-induces eddy currents in the conductor. The result is an uneven current density distribution that tends to concentrate near the surface (skin) of the conductor. This is known as the "skin" effect. The particular current distribution causes higher ohmic losses, which can be evaluated with

$$P_{skin} = \int_{\Omega_c} \frac{\boldsymbol{J}_{rms}\boldsymbol{J}^*_{rms}}{\sigma} d\Omega_c, \tag{3.13}$$

with the subscript rms representing the root mean square value of $\boldsymbol{J} = \boldsymbol{J}_0 + \boldsymbol{J}_\epsilon$, in accordance with (3.12). In general the losses P_{skin} are higher compared to the DC case, where the same net current I_0 would uniformly distribute over the conductor's

cross-section, i.e.

$$P_{skin} > P_{\mathrm{DC}} = \frac{I_0^2}{\sigma \Omega_c}. \tag{3.14}$$

This effect can be described analytically if we look at a simpler problem of a conductive slab (homogeneous and isotropic) surrounded by a non-conductive material, e.g. air, as in Fig. 3.2(a). Let us consider a sinusoidal current flowing through the slab along the vertical direction y, referring to Fig. 3.2(a). Since the slab width L_1 is smaller than all the other dimensions, we can reduce the analysis to 1D (x), assuming all the fields to be invariant with y and z. Accordingly, in the time domain (3.1) can be reduced to [125]

$$\frac{\partial^2 H_z}{\partial x^2} = \mu\sigma \frac{\partial H_z}{\partial t}, \tag{3.15}$$

better known as the wave equation, which in the frequency domain becomes

$$\frac{d^2 H_z}{dx^2} = i\omega\mu\sigma H_z. \tag{3.16}$$

The general solution of the Helmholtz equation (3.16) is

$$H_z = C_1 e^{\frac{(1+i)}{\delta_{\mathrm{skin}}}x} + C_2 e^{-\frac{(1+i)}{\delta_{\mathrm{skin}}}x}, \tag{3.17}$$

where we introduced the "skin depth"

$$\delta_{\mathrm{skin}} = \sqrt{\frac{2}{\omega\mu\sigma}}. \tag{3.18}$$

The imposed current I_0 can be modelled applying the following boundary conditions on both lateral edges of the conductor

$$H\left(\frac{L_1}{2}\right) = -H\left(-\frac{L_1}{2}\right) = H_m. \tag{3.19}$$

If we assume the length of the slab in the z direction to be L_3, with $L_3 \gg L_1$, H_m is

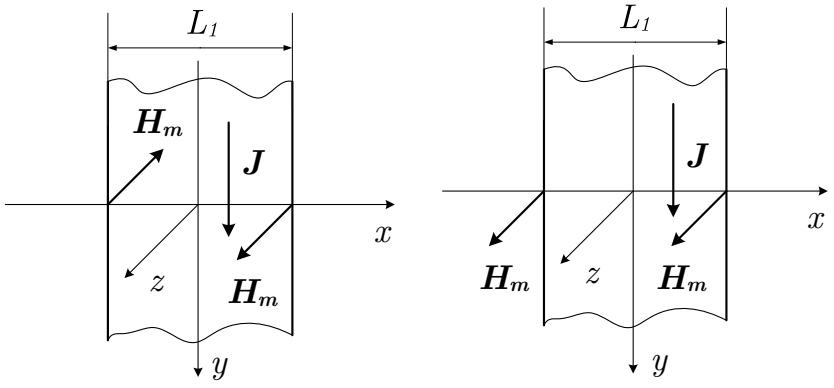

Figure 3.2: Cross section of a semi-infinite conductive slab, representative of the (a) skin and (b) proximity effects

evaluated using the integral form of (3.1a) [126],

$$H_m 2L_3 = \oint \boldsymbol{H} dl = \int \boldsymbol{J} \cdot \boldsymbol{n} ds = I_0, \tag{3.20}$$

with dl is part of the closed line circumscribing the conductor cross-section; this yields to $H_m = \frac{I_0}{2L_3}$. Exploiting (3.19), we obtain the following particular solutions

$$H_z = H_m \frac{\sinh\left((1+i)(\frac{x}{\delta_{\text{skin}}})\right)}{\sinh\left(\frac{(1+i)}{2}(\frac{L_1}{\delta_{\text{skin}}})\right)}, \tag{3.21a}$$

$$J_z = -H_m \frac{(1+i)}{\delta_{\text{skin}}} \frac{\cosh\left((1+i)(\frac{x}{\delta_{\text{skin}}})\right)}{\sinh\left(\frac{(1+i)}{2}(\frac{L_1}{\delta_{\text{skin}}})\right)}, \tag{3.21b}$$

whose moduli are plotted in Fig 3.3 in dimensionless units, where J_{DC} is the uniform DC current density.

The nondimensional parameter $f_\delta = \frac{L_1}{\delta_{\text{skin}}}$, known as the reduced frequency, helps to generalise the skin effect; the larger f_δ is, the more significant the skin effect is. As shown in Fig. 3.3, with $f_\delta = 10$ almost no current flows in the middle of the conductor, since the current density is concentrated next to the skin. As highlighted with a vertical dashed line in Fig. 3.3(b), δ_{skin} represents the distance from the conductor

skin where the current density decreases by $1/e$ (this is why δ_{skin} is called "skin depth"). From (3.18) we can notice that δ_{skin} depends on the injected current, f, and the conductor material, σ, whereas f_δ depends also on the conductor size. This means that if we want to limit the skin effect at a certain frequency, the solution is to reduce the size of the conductor. For instance, in many high frequency applications, the so-called "Litz" wires are usually employed. These wires consist of strands connected in parallel to form bundles of very thin wires that replace one wire of thicker cross-section that may face unacceptable AC losses. It must be said that reducing the cross section of the conductor implies increasing the DC resistance per unit length

$$R_{DC} = \left(\int_{\Omega_c} \sigma d\Omega. \right)^{-1}. \tag{3.22}$$

Therefore, one must find a trade-off between reducing AC effects and increasing R_{DC} when selecting the strand size [127]. To simplify the evaluation of the skin effect contribution, in particular when $\delta_{\text{skin}} \ll L_1$, one could assume that all the current flows within the area delimited by the skin-depth. On the other hand, as shown in Fig. 3.3(b), with $L_1 < \delta_{\text{skin}}$ AC effects can be neglected.

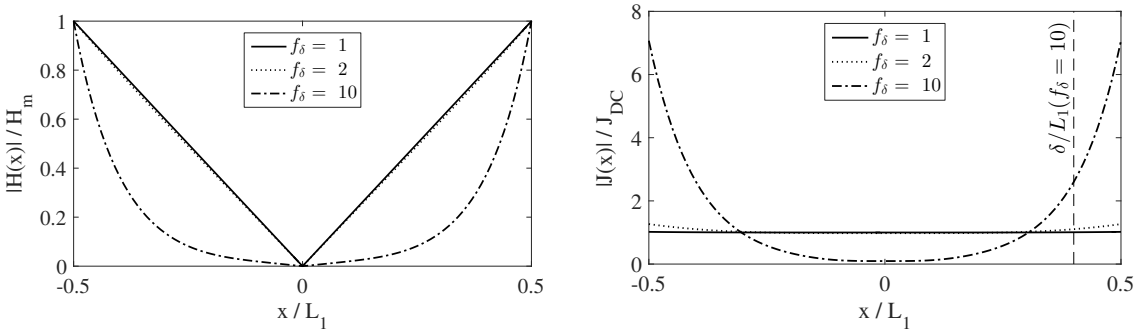

(a) (b)

Figure 3.3: Solution of the 1D skin effect problem (imposed current I_0) for the dimensionless (a) magnetic field norm $|H(x)|/H_m$ and (b) current density norm $|J(x)|/J_{DC}$ as a function of the reduced frequency f_δ

3.2.2 The proximity effect

The proximity effect owes its name to the eddy currents induced from the magnetic field produced by neighbouring current carrying conductors. This effect is independent from the net current carried by the conductor and for simplicity we can assume that the net current injected in the conductor is null ($I_0 = 0$). In electrical windings, which usually consist of a large number of turns, the resulting current density distribution accounting for the proximity effect can be considerably complex. However, it can be useful to show the effect of a representative uniform magnetic field that crosses a conductor, as sketched in Fig 3.2(b). Similar to the skin effect case, this is a 1D problem described by Helmholtz equation (3.16). Applying the boundary conditions, $H(L_1/2) = H(-L_1/2) = H_m$, the following distributions for the magnetic field and current density result

$$H_z = H_m \frac{\cosh\left((1+i)(\frac{x}{\delta_{\text{skin}}})\right)}{\cosh\left(\frac{(1+i)}{2}(\frac{L_1}{\delta_{\text{skin}}})\right)}, \tag{3.23a}$$

$$J_z = H_m \frac{(1+i)}{\delta_{\text{skin}}} \frac{\sinh\left((1+i)(\frac{x}{\delta_{\text{skin}}})\right)}{\cosh\left(\frac{(1+i)}{2}(\frac{L_1}{\delta_{\text{skin}}})\right)}. \tag{3.23b}$$

These distributions are plotted in dimensionless terms in Fig 3.4 as a function of f_δ, where we used [125]

$$\left|J\left(\frac{L_1}{2}\right)\right| = \frac{\sqrt{2}H_m}{\delta_{\text{skin}}} \left(\frac{\cosh(\frac{L_1}{\delta_{\text{skin}}}) - \cos(\frac{L_1}{\delta_{\text{skin}}})}{\cosh(\frac{L_1}{\delta_{\text{skin}}}) + \cos(\frac{L_1}{\delta_{\text{skin}}})}\right). \tag{3.24}$$

This tells us that the surface value of the current density at the conductor border depends on the field intensity and δ_{skin}. It is worth noting that in this case the current density exhibits an uneven symmetry. As for the skin effect, f_δ is the parameter that enables the assessment of the severity of the effect. However, as can be seen from (3.24), the proximity effect can still produce a significant increase in conductive loss

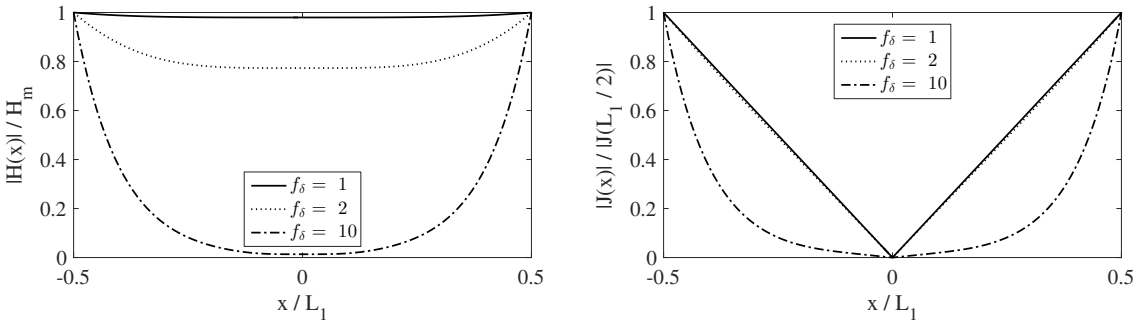

(a) (b)

Figure 3.4: Solution of the 1D proximity effect problem (imposed magnetic field $|H_m|$) for the dimensionless (a) magnetic field norm $|H(x)|/H_m$ and (b) current density norm $|J(x)|/|J(L_1/2)|$ as a function of the reduced frequency f_δ

at low values of f_δ if the magnitude of the external magnetic field is high. This makes the proximity effect responsible for the greatest increase in power loss in an electrical winding, compared to the skin effect.

3.3 Electromagnetic homogenisation of electrical windings

As anticipated in section 3.1.1, the goal of electromagnetic homogenisation is to enable a correct description of the macroscopic behaviour of the analysed domain. This is achieved by employing effective material properties, as in (3.5), that can capture local effects, i.e. eddy currents at cell level, that in turn affect the macroscopic fields. As discussed in [122], the fields in Maxwell's equations can be represented as the sum of a macroscopic component, e.g. $\boldsymbol{J}_M$, and a periodic microscopic effect, e.g. $\boldsymbol{j}$

$$\boldsymbol{J} = \boldsymbol{J}_M + \boldsymbol{j}, \qquad \boldsymbol{E} = \boldsymbol{E}_M + \boldsymbol{e},$$
$$\boldsymbol{B} = \boldsymbol{B}_M + \boldsymbol{b}, \qquad \boldsymbol{H} = \boldsymbol{H}_M + \boldsymbol{h}.$$

While $\boldsymbol{B}_M$ and $\boldsymbol{J}_M$ are equal to the average over the analysed domain of $\boldsymbol{B}$ and $\boldsymbol{J}$, respectively, the same is not true for $\boldsymbol{E}_M$ and $\boldsymbol{H}_M$ (see Fig. 3.5). For instance, looking at Fig. 3.5(a), the imposed macroscopic current $\boldsymbol{J}_M$ coming out of the sheet generates a local magnetic field $\boldsymbol{h}$ that in turn induces local curls of current $\boldsymbol{j}$. This means that at the cell level we have electric dipoles that affect the electric macroscopic behaviour. In a similar manner, a uniform macroscopic flux density $\boldsymbol{B}_M$ is affected by the induced curls that generate magnetic dipoles, that changes the macroscopic magnetic behaviour [122]. The goal now is to include these effects in the constitutive laws.

According to [128], Dowell [129] and Ferreira [130] first provided some analytical formulae to compute the effective material properties of the electrical windings. These analytical approximations, however, resulted in low accuracy (error $> 50\%$) compared to 2D FE simulations [128]. This error is mainly due to the fact that analytical methods cannot account for any conductor geometry or any periodic configuration. Thus, in general, they are limited to 1D problems, that can only satisfy very particular applications.

There is, however, a solution to significantly reduce this error for 2D problems. This is to evaluate the equivalent material properties from the study of cell problems using FEM. A number of publications cover this topic, in particular [116,131,132]. Among these, in our work we decided to follow the methodology presented in [131], because it enables the evaluation of both square and hexagonal lattices. A thorough discussion of this method is presented in the following sections. The methodologies proposed allow to homogenise the electromagnetic problem in the frequency domain. In [133], a technique to homogenise this problem in the time domain is introduced, allowing noisy signals to be accounted for.

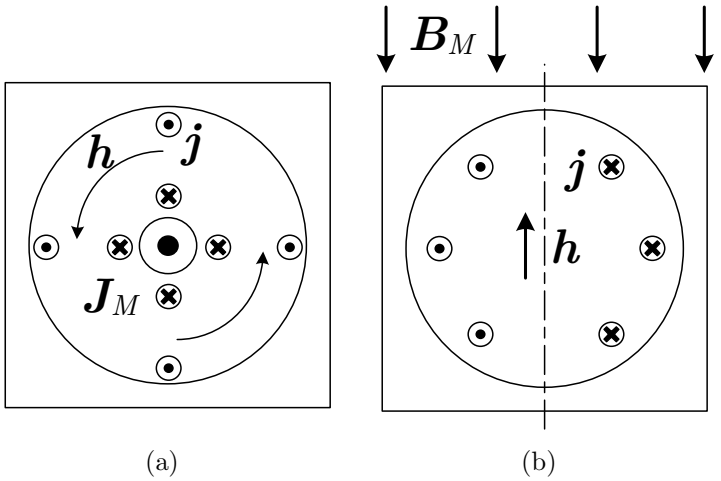

Figure 3.5: 2D Representation of the (a) skin and (b) proximity effect in a circular wire

3.3.1 Orthogonality between skin and proximity effect in conductors

The first condition to simplify the evaluation of the effective electromagnetic properties is orthogonality between the skin and proximity effects. This allows consideration of the two effects separately. This condition is respected if the conductor has an axis of symmetry [130]. For instance, we can refer to the skin effect as depicted in Fig. 3.5(a), where a uniform macroscopic current density $\boldsymbol{J}_M$ is injected, and $\boldsymbol{B}_M = 0$. Thanks to the symmetry of the conductor, the cell mean $\langle \boldsymbol{h} \rangle$ is null, which ensures that $\langle \boldsymbol{B}_M \rangle = \mu_0 \langle \boldsymbol{H}_M \rangle$. Accordingly, if $\boldsymbol{B}_M = 0$ then $\boldsymbol{H}_M = 0$ confirming the independence of the electrical from the magnetic problem [122].

The same can be proven following the demonstration presented in [130] where we define separately the current densities resulting from the skin $\boldsymbol{J}_s$ and proximity $\boldsymbol{J}_p$ effects. In general, according to (3.12) the power loss is

$$P = \frac{1}{2\sigma} \int_{\Sigma} (\boldsymbol{J}_s + \boldsymbol{J}_p)(\boldsymbol{J}_s^* + \boldsymbol{J}_p^*) d\Sigma. \tag{3.25}$$

However, if the conductor has an axis of symmetry, then $\boldsymbol{J}_s$ and $\boldsymbol{J}_p$ have an even and

odd symmetry, respectively. This yields to

$$P = \frac{1}{2\sigma} \int_{\Sigma} (\boldsymbol{J}_s \boldsymbol{J}_s^* + \boldsymbol{J}_p \boldsymbol{J}_p^*) d\Sigma. \tag{3.26}$$

This is the reason why in this work we consider only symmetric conductors, i.e. with circular or rectangular cross sections.

3.3.2 Skin effect

The objective now is to isolate the skin effect using symmetric conductors, e.g. circular. In practice, we need to reproduce the problem sketched in Fig. 3.5(a), where a sinusoidally time-varying current at various frequencies is injected in the conductor (net current $I_0 = \int_{\Omega_c} \boldsymbol{J}_M d\Omega$, with $\Omega_c = \pi r^2$ and r the conductor radius) which is surrounded by a non conductive material, e.g. air. The insulation domain does not need to be included as, electromagnetically, in this case it behaves as air. On average the magnetic flux density is null, $\langle \boldsymbol{B} \rangle = \boldsymbol{B}_M = 0$.

The problem is solved using the magnetic vector potential (MVP) formulation (3.10), where the source current can be easily imposed. Since the problem is 2D, the MVP has a single component in the plane normal to the conductor cross section: $\boldsymbol{A} = A_z \boldsymbol{z}$. To ensure $\langle \boldsymbol{B} \rangle = 0$, since $\nabla \cdot \boldsymbol{B} = 0$, we need to impose $\boldsymbol{B} \cdot \boldsymbol{n} = 0$ on the cell external boundary $\partial\Omega$, where $\boldsymbol{n}$ is the unit vector normal to $\partial\Omega$. This boundary condition is applied imposing $A_z = 0$ on $\partial\Omega$ [131].

To obtain the effective material properties we evaluate the complex power (3.12) absorbed by the cell comparing macroscopic and local quantities [122]

$$S = \frac{1}{2} \int_{\Omega} \rho_J \boldsymbol{J} \boldsymbol{J}^* d\Omega + i \frac{\omega}{2} \int_{\Omega} \nu \boldsymbol{B} \boldsymbol{B}^*, \tag{3.27a}$$

$$S_M = \frac{1}{2} \int_{\Omega} \rho_{J,eq} \boldsymbol{J}_M \boldsymbol{J}_M^* d\Omega + i \frac{\omega}{2} \int_{\Omega} \nu_{eq} \boldsymbol{B}_M \boldsymbol{B}_M^*, \tag{3.27b}$$

where in this case the second term on the right hand side of (3.27b) is null, since $\boldsymbol{B}_M = 0$. Thus, the effective conductivity $\rho_{J,eq} = \rho'_{eq} + i\rho''_{eq}$ of the wire in the z direction is given by

$$\rho'_{eq} = \frac{1}{\|\Omega\|} \frac{\int_{\Omega_c} \rho_J \boldsymbol{J}\boldsymbol{J}^* d\Omega}{\boldsymbol{J}_M \boldsymbol{J}_M^*} d\Omega, \tag{3.28a}$$

$$\rho''_{eq} = \frac{\omega}{\|\Omega\|} \frac{\int_{\Omega} \nu \boldsymbol{B}\boldsymbol{B}^* d\Omega}{\boldsymbol{J}_M \boldsymbol{J}_M^*} d\Omega, \tag{3.28b}$$

where $\|\Omega\|$ is the area of the cell and $\nu = \nu_0$, the permeability of free space. From a physical point of view, this means that with rising frequency the conductor exhibits an increasing inductive behaviour. Accordingly, in the electric circuit equations an impedance should be used $Z_{eq} = \frac{1}{\sigma_{eq}} n_w^2 \|\Omega_c\|$, with Ω_c the conductor domain and $\sigma_{eq} = \rho_{J,eq}^{-1}$ [122].

The real and imaginary components of a copper conductor of radius $r = 0.008\,\mathrm{m}$ and $\rho_J = 1.76 \times 10^{-8}\,\Omega\mathrm{m}$ are plotted in Fig. 3.6(a). We must add that, according to [131], the FE cell model should consist of a unitary cell surrounded by a layer of cells. This allows the error to be reduced at high f_δ [131]. A representative solution of the cell problem that reproduces the skin effect at various current frequencies is presented in Fig. 3.7, where the current density distribution $\boldsymbol{J}$ is shown along with the flux lines.

In compliance with [131], the effective conductivity can be expressed in terms of non dimensional parameters p_I and q_I in the equation of the equivalent impedance

$$Z_{eq} = p_I R_{DC} + i\ q_I \omega \frac{\mu_0 L}{8\pi\lambda}, \tag{3.29}$$

where L is the length of the conductor and λ is the filling ratio. The imaginary part comes from the inductance of a round conductor, considering the internal field only [131].

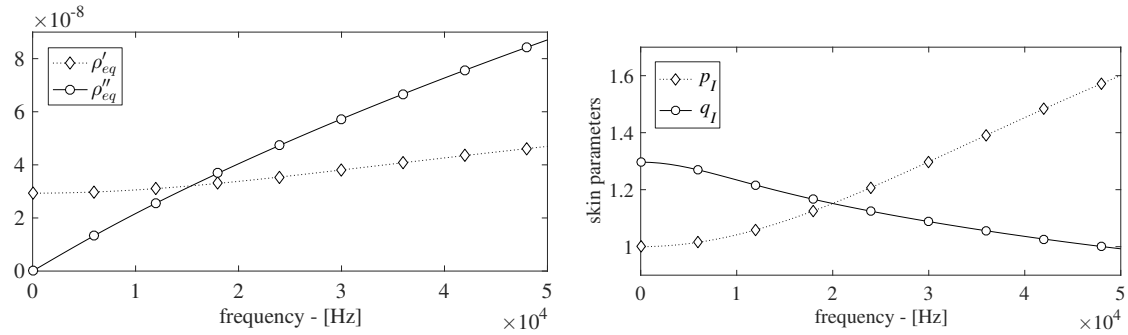

Figure 3.6: (a) Real and imaginary components of the effective electrical conductivity $\rho_{J,eq}$ and (b) skin effect parameters p_I and q_I over a range of f for a circular conductor on a square lattice with $\lambda = 0.6$

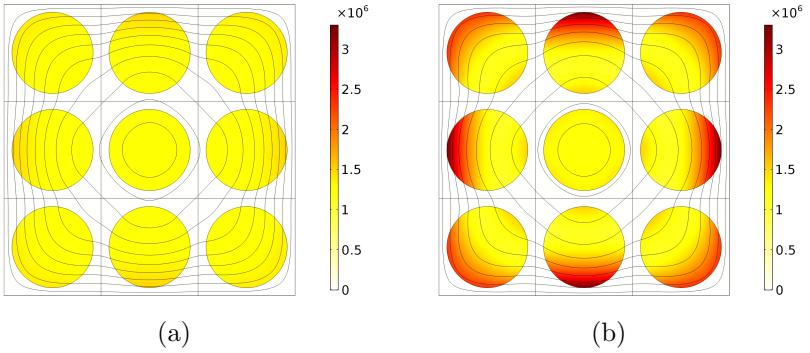

Figure 3.7: Solution of the skin effect cell problem for f (a) 5 kHz and (b) 20 kHz in terms of current density distribution $\boldsymbol{J}$ and flux lines for a square lattice distribution and $\lambda = 0.6$

3.3.3 Proximity effect

To consider the contribution of the proximity effect we should model the frequency dependent problem of Fig. 3.5(b), where a uniform magnetic flux density is imposed on a direction, $\langle \boldsymbol{B} \rangle = \boldsymbol{B}_M$, and the net current flowing in the conductor is null, $\langle \boldsymbol{J}_M \rangle = I_0 = 0$. The zero current condition is easily enforced, whereas the uniform magnetic flux density is achieved imposing on $\partial\Omega$ the following condition for the MVP component along z

$$A_z = B_x y + B_y x, \tag{3.30}$$

where, e.g., $B_x = B_M$ and $B_y = 0$ for a uniform magnetic flux density along x. The process to obtain the effective reluctivity, $\nu_{eq} = \nu'_{eq} + i\ \nu''_{eq}$, is similar to the one presented for the skin effect, the difference being that the non zero term in (3.27b) is now the second on the right hand side. Thus, the real and imaginary parts are calculated with the following ratios related to the central unitary cell

$$\nu'_{eq} = \frac{1}{|\Omega|} \frac{\int_\Omega \nu \boldsymbol{B}\boldsymbol{B}^* d\Omega}{\boldsymbol{B}_M \boldsymbol{B}_M^*}, \tag{3.31a}$$

$$\nu''_{eq} = \frac{1}{|\Omega|} \frac{\int_{\Omega_c} \rho_J \boldsymbol{J}\boldsymbol{J}^* d\Omega}{\omega \boldsymbol{B}_M \boldsymbol{B}_M^*}, \tag{3.31b}$$

which are plotted in Fig. 3.8(a). It is worth noting that for circular conductors, the effective permeability in x and y has identical values. The same cannot be said for rectangular conductors, as we are going to show later in this work. The meaning of complex permeability can be explained looking at Fig. 3.5(b). The imaginary part allows the opposing magnetic field generated by the curls of current circulating in the conductor to be accounted for. A representative solution of the cell problem reproducing the proximity effect at various inductance frequencies is presented in Fig. 3.9, where the current density distribution $\boldsymbol{J}$ is shown along with the flux lines. It is possible to appreciate how, by adjusting the boundary conditions, we can impose

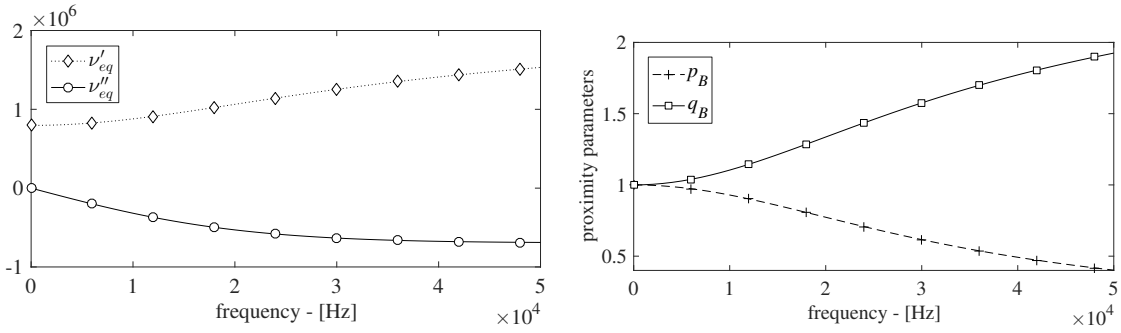

(a) (b)

Figure 3.8: (a) Real and imaginary components of the effective permeability ν_{eq} and (b) proximity effect parameters p_B and q_B over a range of f for a circular conductor on a square lattice with $\lambda = 0.6$

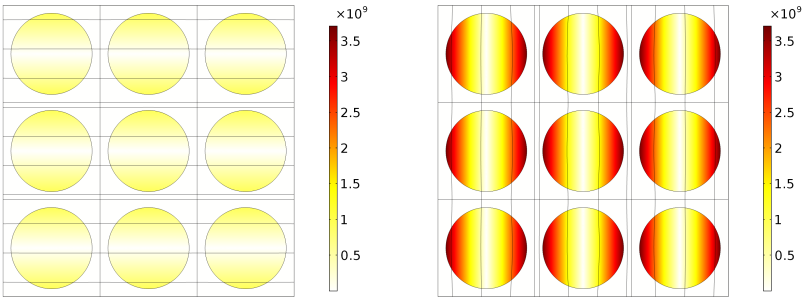

(a) (b)

Figure 3.9: Solution of the proximity effect cell problem for (a) $f = 5\,\text{kHz}$ with $B_x = 1$ and $B_y = 0$ and (b) $f = 20\,\text{kHz}$ with $B_x = 0$ and $B_y = 1$ in terms of current density distribution $\boldsymbol{J}$ and flux lines for a square lattice distribution and $\lambda = 0.6$

a uniform flux inductance along x or y.

As for the skin effect impedance, the effective reluctivity can be expressed in terms of dimensionless parameters p_B and q_B [133]

$$\nu_{eq} = q_B \nu_0 + i\, p_B \frac{\lambda r^2 \omega}{4\rho_J}, \tag{3.32}$$

where the imaginary part follows from the analytical expression for low-frequency proximity losses in a round conductor [133].

3.3.4 Effect of wire distribution

It is now interesting to look at the response of the effective parameters to a varying filling ratio or employing different wire distributions, namely on a hexagonal lattice or with a random configuration.

In Fig. 3.10 the effect of different filling ratios λ on the dimensionless parameters for the skin and proximity effect is shown. The parameter p_I is clearly not affected by λ and, thus, in this section we can neglect to present further results with respect to p_I and q_I, whose impact on the winding behaviour we can expect to be limited [131]. On the other hand, both p_B and q_B increase with λ.

When the wires are arranged on an hexagonal lattice, the cell problem is set up as shown in Fig. 3.11, where the proximity effect is excited at 50 kHz. The dimensionless parameters for the proximity effect, however, are not affected by the different distribution of the conductors, as plotted in Fig. 3.12(a).

It is important to highlight that a similar result can be achieved for any distribution. Similarly to the analysis carried out in Section 2.4.1, 100 random distributions are considered, each with $\lambda = 0.4$ or $\lambda = 0.6$. In Fig. 3.12(b) we plot the average of the proximity effect parameters together with the 95% error bars against the values obtained with a square lattice; the difference is very limited, confirming that the magnetic homogenisation is applicable to any wire distribution.

3.3.5 Temperature coupling

In this section temperature effects are investigated. It is well known that the temperature dependence of the electrical resistivity of a conductor can be approximated with

$$\rho_J(T) = \rho_{J,0}\left(1 + \alpha(T - T_0)\right), \tag{3.33}$$

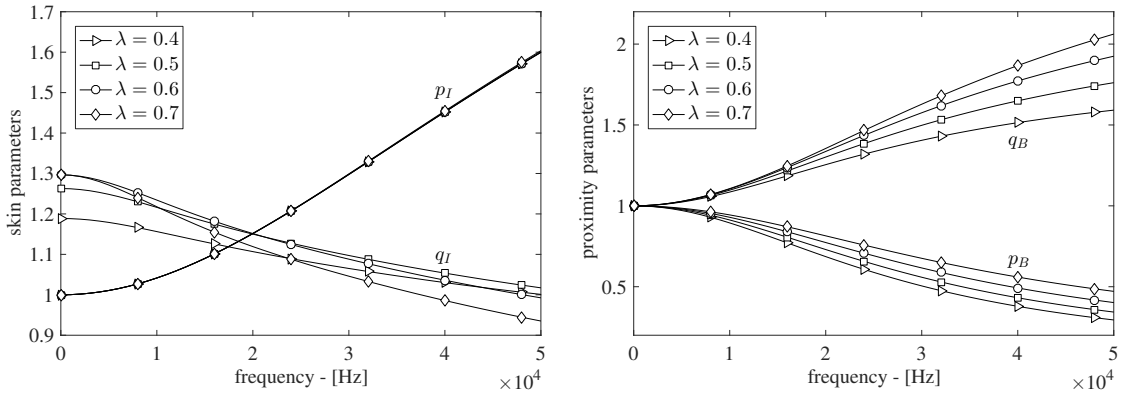

(a) (b)

Figure 3.10: Dimensionless parameters for the (a) skin and (b) proximity effect as a function of a f and λ for a circular conductor on a square lattice

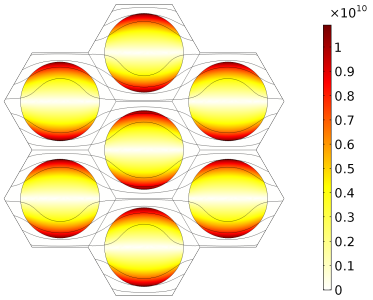

Figure 3.11: Solution of the skin effect cell problem for f at 50kHz in terms of current density distribution $\boldsymbol{J}$ and flux lines for an hexagonal lattice distribution and $\lambda = 0.6$

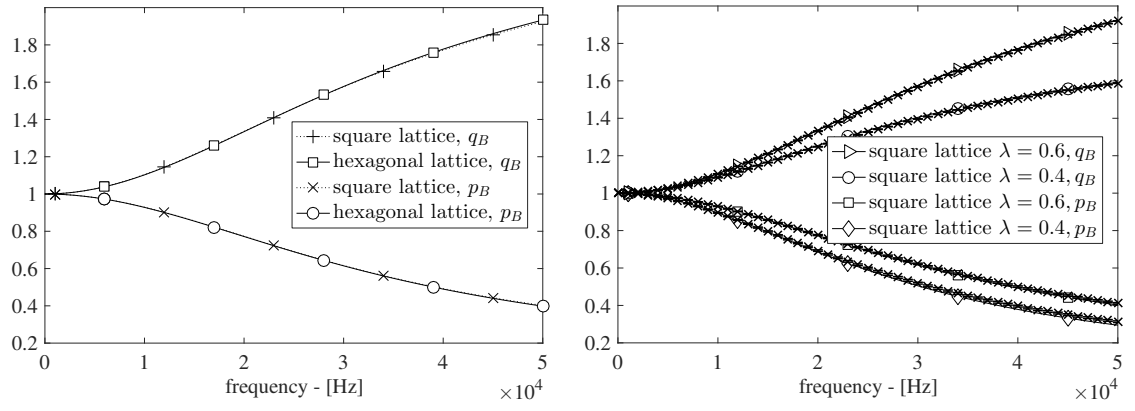

(a) (b)

Figure 3.12: Comparison between the dimensionless proximity effect parameters obtained (a) with a square lattice and hexagonal lattice with $\lambda = 0.6$ and (b) with random distribution with $\lambda = 0.4$ and $\lambda = 0.6$

where T is temperature, $\rho_{J,0}$ is the resistivity at the reference temperature T_0, and α is the temperature coefficient; e.g. for copper $\rho_J = 1.76 \times 10^{-8}\,\Omega\text{m}$ at $T_0 = 20\,^\circ\text{C}$ and $\alpha = 0.003\,75\,^\circ\text{C}^{-1}$. As discussed in the previous chapter (see Table 2.1), the thermal conductivity of copper is very high compared to the thermal conductivity of the insulation and epoxy, thus we can assume that the temperature distribution within a conductor is always uniform. To analyse the parameters, at, e.g. $T = 150\,^\circ\text{C}$, in the cell problem we adjust the conductor's resistivity to $rho_J = rho_J(150\,^\circ\text{C})$ using (3.33). In Fig. 3.13(a) and 3.13(b), p_I, q_I, p_B, and q_B are plotted as a function of f, for the case of $\lambda = 0.6$, distribution on a square lattice, and temperatures ranging from 20 °C to 150 °C. It is important to highlight that, with increasing T the parameters describing the real components of the effective properties decrease. In fact, an increased electrical resistivity allows the effect of eddy currents to be contained. For the same reason the imaginary part of the parameters increases with T.

The fact that the temperature dependence of the electrical resistivity is linear simplifies the analysis. We know that the reduced frequency f_δ is a function of the resistivity and, accordingly, it can include the temperature effect

$$f_\delta(T) = r\sqrt{\frac{2\ \rho(T)}{\omega\mu}}. \tag{3.34}$$

Thanks to linearity, the reduced frequency can be used to collapse the curves at different temperatures into a single line, as shown in Fig. 3.14. The multiphysics homogenisation is thus simplified, since we only need to estimate a single set of four parameters, which include the temperature effects.

We are now able to formalise the formula for coupling the electromagnetic with the thermal problem, i.e. the source term in the heat equation resulting from the flowing currents. In a fine model, where every wire is included and, thus, the actual

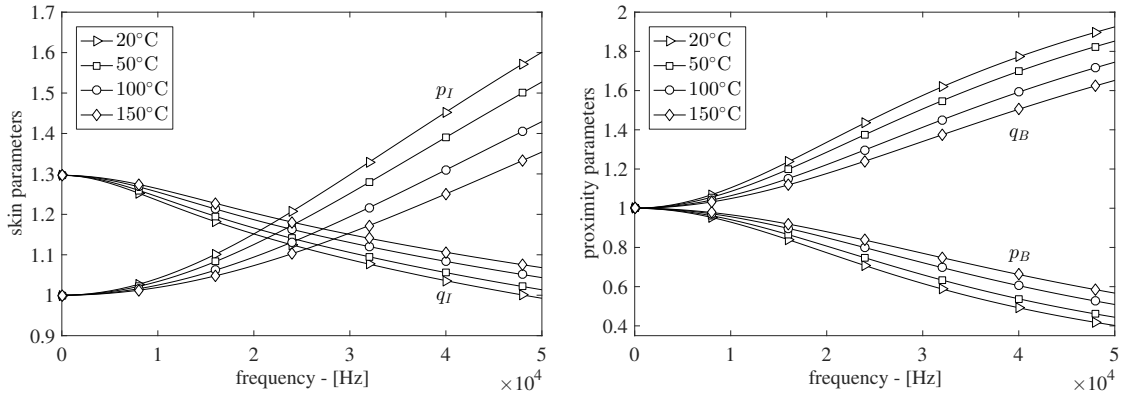

(a) (b)

Figure 3.13: Eddy-current parameters for wires on a square lattice with $\lambda = 0.6$; (a) skin effect parameters p_I and q_I and (b) proximity effects p_B and q_B at various temperatures against frequency

current density distribution is known, the heating loss is calculated with the real component of (3.27a). On the other hand, for the homogenised model one should refer to (3.27b), including both the contribution of the skin and proximity effects

$$\begin{aligned} P_h &= \int_{\Pi_w} \left(\rho'_{eq} \boldsymbol{J}_M \boldsymbol{J}_M^* + \nu''_{eq} \omega \boldsymbol{B}_M \boldsymbol{B}_M^*\right) d\Omega \\ &= \int_{\Pi_w} \left(p_I R_{DC} \boldsymbol{J}_M \boldsymbol{J}_M^* + p_B \frac{\lambda r^2 \omega^2}{4\rho} \boldsymbol{B}_M \boldsymbol{B}_M^*\right) d\Omega, \end{aligned} \tag{3.35}$$

where Π_w represents the whole winding domain. For the correct coupling, in (3.35) the values of p_I and p_B should be taken as a function of $f_\delta(T)$, i.e. $p_I(f_\delta(T))$ and $q_I(f_\delta(T))$. Moreover, the amplitude of the macroscopic current density shall be defined as $J_M = \frac{\lambda |I|}{\pi r^2}$, which is applied uniformly on the winding domain; on the other hand, $\boldsymbol{B}_M$ results from the solution of the electromagnetic problem, e.g. with FE. Solving a fully coupled electromagnetic and thermal problem, the loss profile accounts for the temperature field within the winding domain that results from the solution of the heat equation with the prescribed thermal boundary conditions.

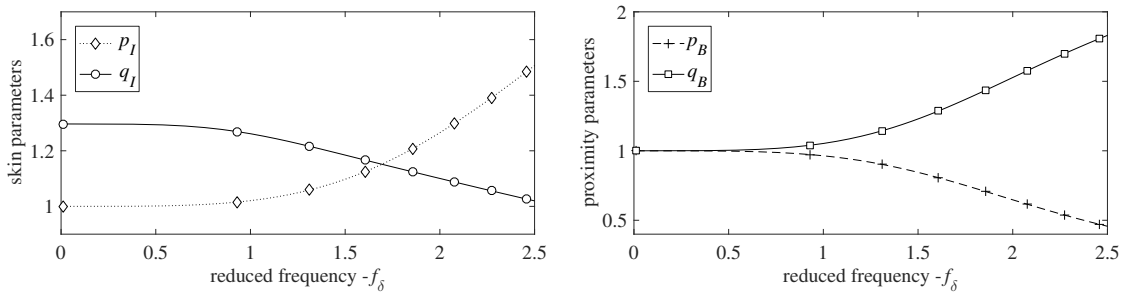

(a) (b)

Figure 3.14: Dimensionless parameters for the (a) skin and (b) proximity effect as a function of the temperature dependent reduced frequency $f_\delta(\rho_J(T))$

3.4 Numerical validation

By way of example, we compare the fine and homogenised models in estimating the winding electromagnetic (EM) behaviour and resulting losses and temperatures, by applying the approaches to the reference electrical machine open slot shown in Fig. 3.15. The geometry and dimensions are given in Fig. 3.15 with the material properties of Table 3.1. For this case study we assume the core (M270-35A) to be linear and lossless (constant real-valued permeability). This simplification does not reduce the generality of the numerical results presented in this analysis as the focus is on the winding domain. The effective material properties for the homogenised winding domain for the electromagnetic problem can be obtained from the parameters given in Fig. 3.14. For instance, for a given current frequency f and temperature T we first calculate the reduced frequency f_δ using (3.34). Then, from the graph of Fig. 3.14 we get the set of dimensionless parameters: p_I and q_I can be plugged in (3.29) to obtain the equivalent impedance; similarly, the effective reluctivity is evaluated with (3.32) using p_B and q_B.

We now feed the winding with a sinusoidal current with $|I_0| = 5\,\mathrm{A}$ rms value at various frequencies; this means applying to the homogenised winding domain a uniform macroscopic current distribution of $\boldsymbol{J}_M = |I_0|\lambda/(\pi r_c^2)$, with r_c the conductor radius. As an initial step, we assume the EM and thermal problems to be decoupled,

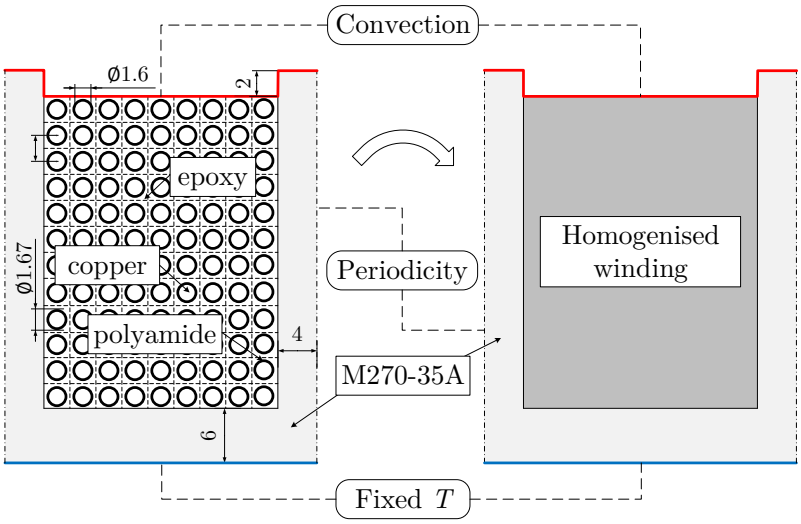

Figure 3.15: Homogenisation of an open slot with 108 conductors arranged on a square lattice (12 layers of 9 wires), $\lambda = 0.6$; dimensions are in [mm] and material properties are given in Table 3.1

Table 3.1: Reference material properties for the electromagnetic and thermal problems

	Copper	Polyamide	Epoxy	M270-35A
k [W/mK]	400	0.26	0.7	22
c_p [J/kgK]	386	1000	1700	-
ρ [kg/m^3]	8890	1440	1766	-
$\rho(20\,°\text{C})$ [Ωm]	1.76	0	0	0
α [°C^{-1}]	3.75×10^{-3}	-	-	-
μ [Hm]	μ_0	μ_0	μ_0	$1200\mu_0$

using a fixed electrical conductivity, $\rho_J = \rho_J(20\,°\text{C})$. This is done to evaluate the effectiveness of the EM homogenisation first. In Fig. 3.16 we compare the solution of the fine and homogenised models in estimating the magnetic field $\boldsymbol{H}$ and $\boldsymbol{H}_M$ and flux lines for $f = 5\,\text{kHz}$. In particular, in Fig. 3.16(c) we show the magnetic field norm along a line in the middle of the first and the central wire columns. From the fine model solution we can appreciate the effect of each wire. The macroscopic solution of the homogenised model cannot account for the local effects, but provides the correct cell-averaged solution.

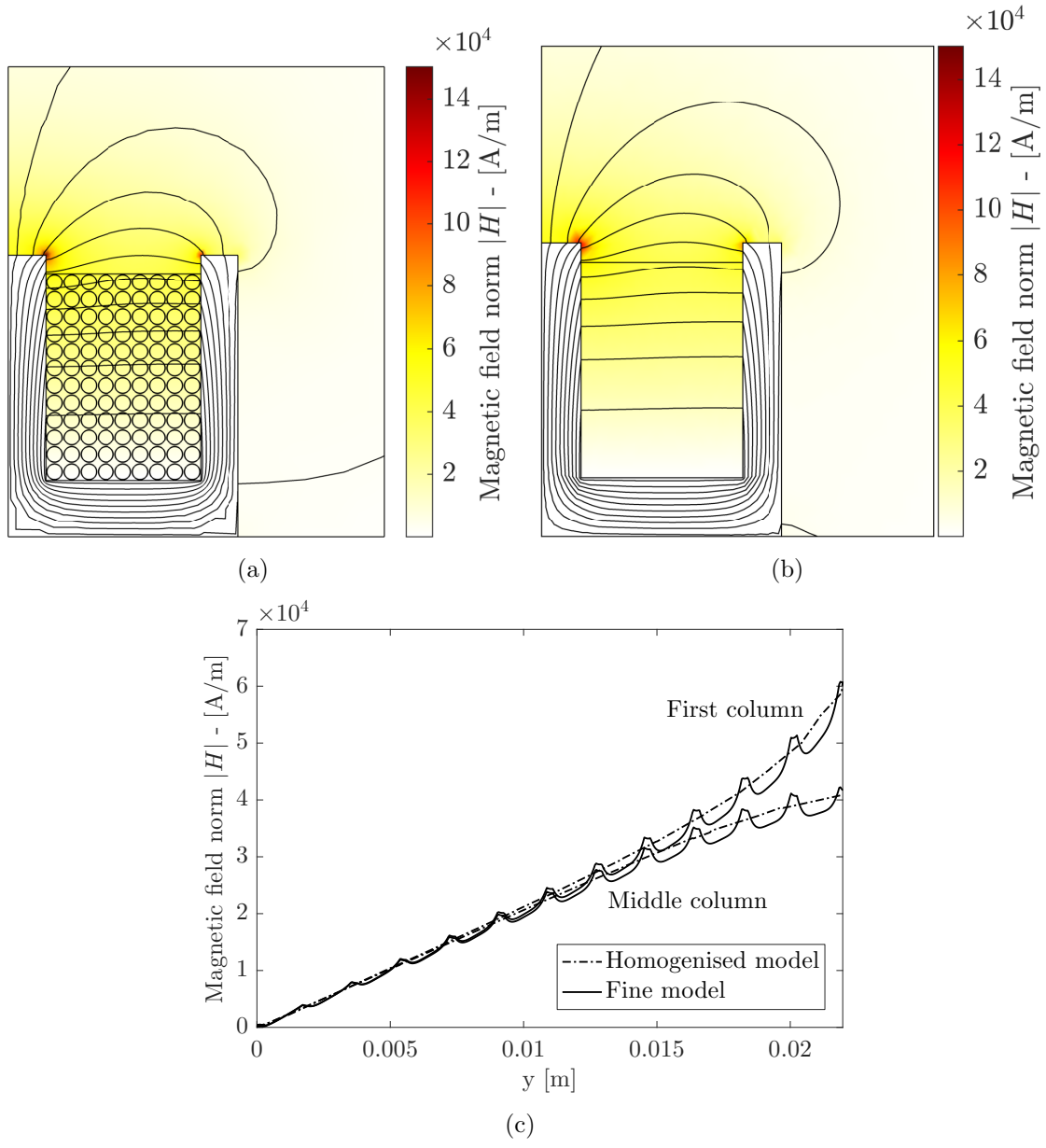

Figure 3.16: Magnetic field norm distribution $|\boldsymbol{H}|$ and flux lines obtained with (a) the fine and (b) homogenised models for the case of $|I_0| = 5\,\text{Arms}$ and $f = 5\,\text{kHz}$. (c) comparison between the two solutions along a line in the middle of the first and the central wire columns

We can now focus on the estimation of the loss distribution within the winding domain. At low frequencies the AC effects are negligible and the losses are almost uniformly distributed between the wires. Increasing the frequency, the leakage flux due to the slot opening produces high proximity losses in the wires at the top of the winding domain. This was expected based on the analysis of Fig. 3.16. In Fig. 3.17 we compare the estimation of the loss distribution in the fine and homogenised winding domains at $f = 5\,\text{kHz}$ and $|I_0| = 5\,\text{Arms}$. The fine model, Fig. 3.17(a), provides a very accurate distribution of the losses within each wire, with the highest peaks in the wires sitting in the top corners. The homogenised model gives the macroscopic loss distribution shown in Fig. 3.17(b). The peaks in the homogenised model are still located in the top corners, however the maximum values are significantly lower since we lose information about the wire geometry (although in a cell-average sense the losses are equivalent).

In Fig. 3.18 the two models are compared in the loss estimation as a function of f, expressed as usual in terms of the ratio R_{AC}/R_{DC}, where $R_{AC} = P/|I_0|^2$ is the equivalent winding resistance including AC effects. The agreement between the two models is very good, with a relative error lower than 0.5% up to $f = 20\,\text{kHz}$.

The formula (3.35) employed for the evaluation of the winding loss in the homogenised model P_h allows to separate the contributions of the various effects affecting the winding, namely the DC, the skin effect and the proximity effect contribution, as a function of f. In Fig. 3.19 we show these contributions normalised with respect to the total measured winding loss for each frequency. Already for $f = 1\,\text{kHz}$ the DC component is responsible only for the 40% of the total loss and the remaining 60% is mostly due to the proximity effect. It also appears that the skin effect contribution is negligible ($< 0.1\%$) for the whole range of analysed frequencies. The proximity effect is responsible for the increase in heating loss in the winding as a function of f, due to the leakage flux.

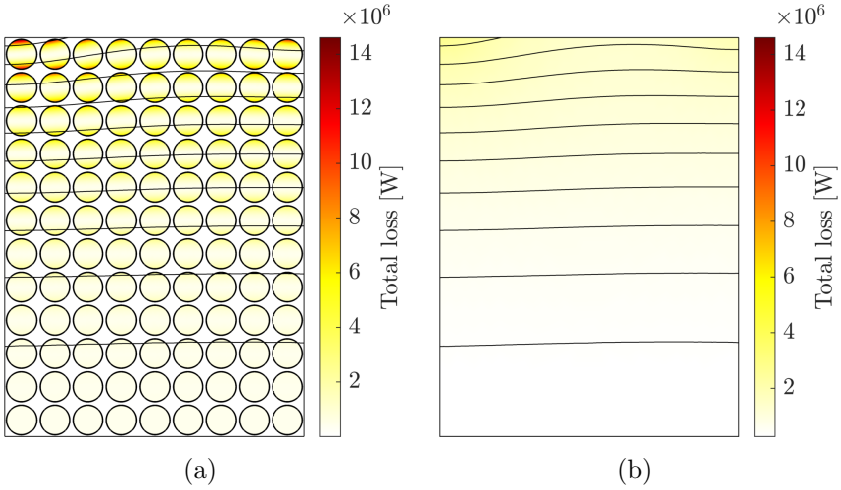

Figure 3.17: Estimation of the total winding loss and magnetic flux lines in the winding domain at $f = 1\,\text{kHz}$ and $|I_0| = 10\,\text{Arms}$ with (a) the fine model and (b) the homogenised model. Wires distributed on a square lattice with $\lambda = 0.6$ and constant electrical resistivity $\rho = \rho(20\,°\text{C})$

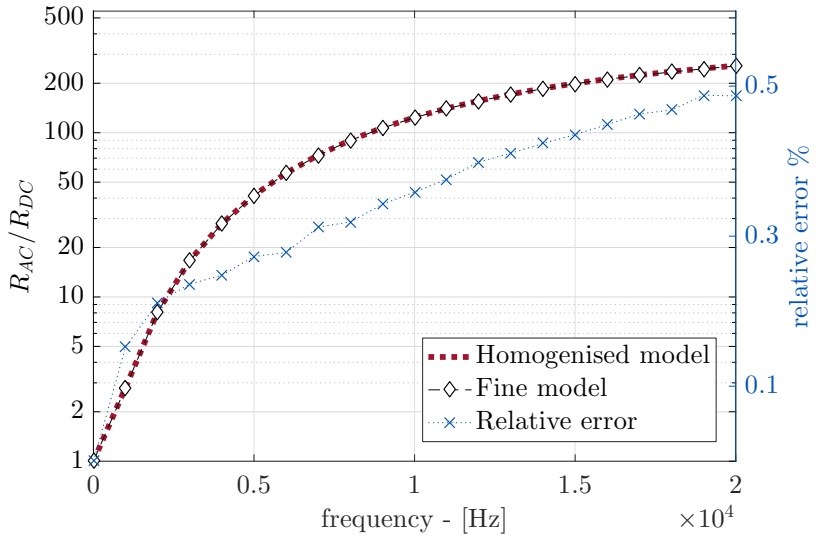

Figure 3.18: Evaluation of AC losses in the slot of Fig. 3.15 in terms of the ratio R_{AC}/R_{DC} at various frequencies with the fine and homogeneous models, with relative error

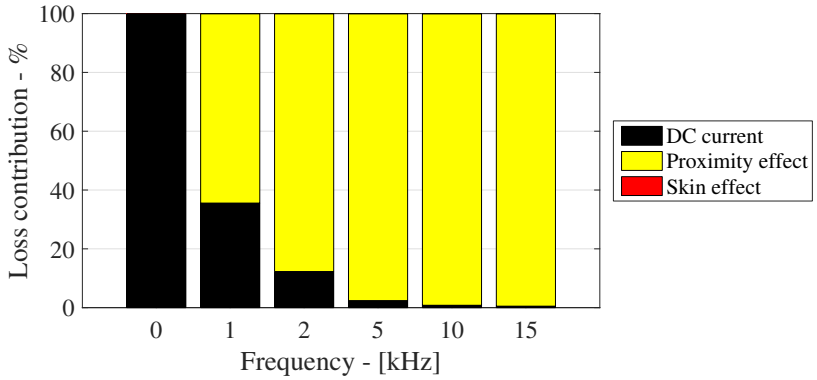

Figure 3.19: Evaluation of normalised loss partition among DC, skin and proximity components as a function of f

3.4.1 Coupled model

Having proved the quality of the EM homogenisation, we can now show the results obtained with a coupled homogenised model, where the EM and thermal problems are solved iteratively, updating the electrical conductivity as a function of temperature. As discussed in the previous chapter, to correctly account for the winding thermal behaviour in the fine model, the conductor insulation domain shall be included, significantly increasing the size of the discretising mesh. Employing the MSM for the thermal problem allows for a dramatic reduction of the numerical effort. For the winding described in Fig. 3.15 and the material properties of Table 3.1 we obtain $k_{eq} = 2.27\,\mathrm{W/mK}$. For the thermal problem we look at the steady state temperature distribution imposing the boundary conditions shown in Fig. 3.15, where $T_{fixed} = 20\,^{\circ}\mathrm{C}$ and the convection is modelled with the law $\dot{q}_{conv} = h(T - T_{\infty})$, where $h = 20\,\mathrm{W\,m^{-2}K^{-1}}$ and $T_{\infty} = 20\,^{\circ}\mathrm{C}$; thermal periodicity is imposed on the lateral edges. These boundary conditions can be representative of a machine stator, cooled with a water jacket.

The results are presented in Fig. 3.20. In the fine model the temperature within each conductor is uniform, Fig. 3.20(a), confirming the assumption made in Section 3.3.5 . The macroscopic temperature $T^{(0)}$ distribution is presented in Fig. 3.20(b),

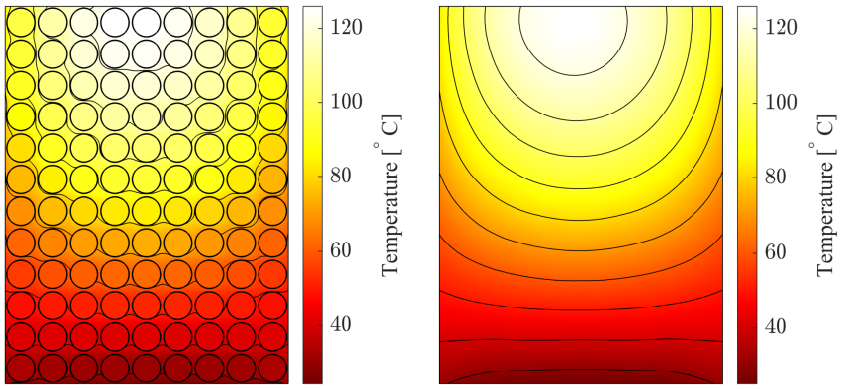

(a) (b)

Figure 3.20: Estimation of the temperature distribution in the winding domain at $f = 5\,\text{kHz}$ and $|I_0| = 5\,\text{Arms}$ with (a) the fine model and (b) the homogenised model

showing a good agreement with the "fine" solution. As discussed in Section 2.5, the macroscopic solution can be improved by adding the first order of the asymptotic expansion $T^{(1)}$. This is shown in Fig. 3.21 where we can see an almost perfect matching with the solution in Fig. 3.20(a). In particular, this can be better appreciated in Fig. 3.21(b) where we plot the T profile along the vertical mid-cross section (central wire column) within the winding domain. The difference between the fine and reconstructed solutions is barely noticeable, with the difference between the hot-spot temperature using the presented model being lower than 0.1 °C.

As mentioned in the previous sections, temperature affects the electrical resistivity of the conductors according to (3.33). The temperature dependence of the resistivity ρ_J cannot be neglected in order to obtain a proper assessment of the losses and the hot-spot temperature [134]. To capture this in the homogenised model, we should account for the variation of the effective parameters as a function of f and $T(\boldsymbol{x})$. In Fig. 3.22 we present the loss estimation with the coupled EM and thermal model in terms of R_{AC}/R_{DC}, referring to the same case study of Fig. 3.15.

At low frequencies the solution of the coupled EM-thermal problem leads to a higher hot-spot temperature. This is because the AC effects are smaller and the temperature dependence of ρ_J implies higher R_{DC}. This is shown in Fig. 3.23(b)

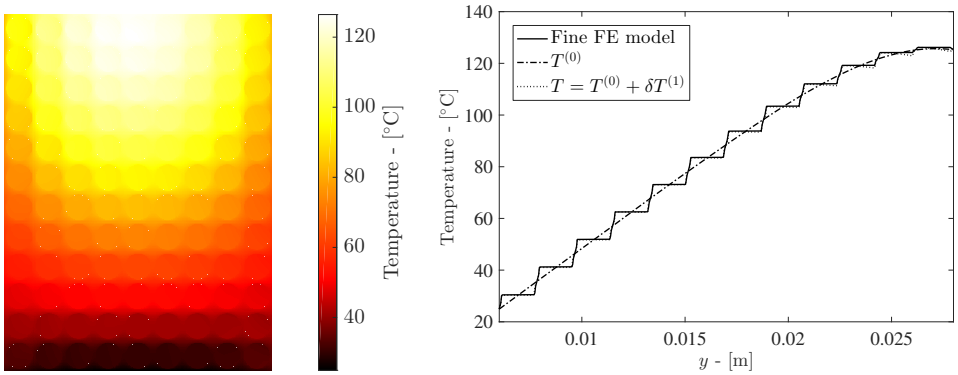

(a) (b)

Figure 3.21: (a) Reconstruction of the temperature distribution in the winding domain at $f = 5\,\text{kHz}$ and $|I_0| = 5\,\text{Arms}$ with MS method; 3.21(b) comparison between the presented solutions along the mid-domain vertical line

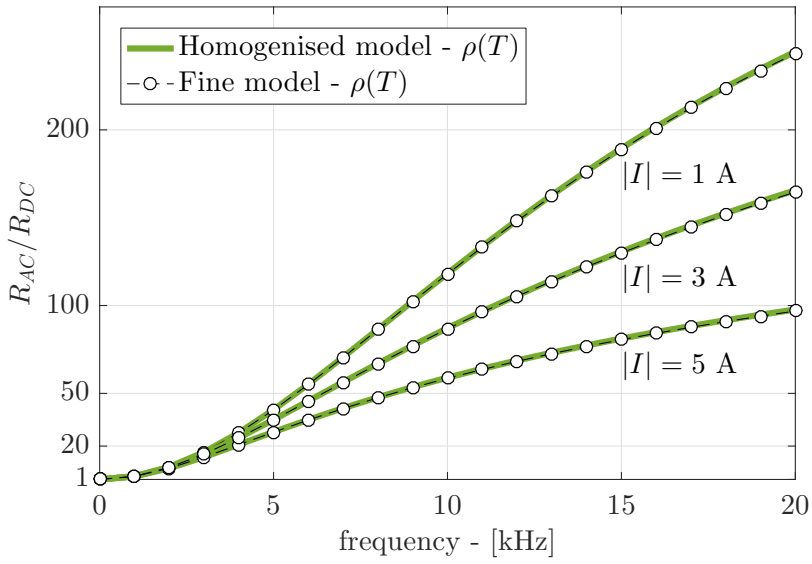

Figure 3.22: Evaluation of AC losses in the slot of Fig. 3.15 in terms of the ratio R_{AC}/R_{DC} at various frequencies and loading current amplitude with the fine and homogeneous models

where we compare the temperature estimation with $\rho_J(20\,°\mathrm{C})$ or $\rho_J(T)$ with a feeding current $|I_0| = 35\,\mathrm{Arms}$ at $f = 100\,\mathrm{Hz}$. In all the temperature profiles of Fig. 3.23 the difference in the estimation of the hot-spot is within $0.1\,°\mathrm{C}$ between the homogenised and fine model.

Fig. 3.23 helps to highlight how different loss profiles influence the temperature field. The results of Fig. 3.23(b) refer to the case of uniformly distributed losses. Here, the solution given by the homogenised model can be approximated with a quadratic function. At high frequencies the losses are concentrated in the neighbourhood of the slot opening, due to the proximity effect. Accordingly, the thermal gradient is linear far from the loss concentration. Therefore, assuming uniformly distributed losses $P_h = R_{AC}|I|^2$ in a thermal model under these conditions would lead to an incorrect temperature distribution, as discussed in section 5.3.3.

3.5 Model limitations

We want here to highlight the limitations related to the EM homogenisation.

Since we said that $\boldsymbol{J}_M$ should be uniform within the winding domain, this means that we cannot homogenise windings that are divided into parallel paths with the method presented in this chapter. In fact, in this case f affects the amount of net current flowing in each conductor of the same bundle due to the effect known as "circulating currents" [135–139]. The resulting current distribution (among the conductors of the same bundle and within each conductor) depends on a number of parameters, including self and mutual inductance between each strand, electrical resistance, and possible flux linkages [135]. Due to this complexity demanding 3D analyses must be performed in order to obtain the correct net current flowing in each strand. In some cases, however, the disequilibrium can be fixed using transpositions [137], making the homogenisation still applicable [140].

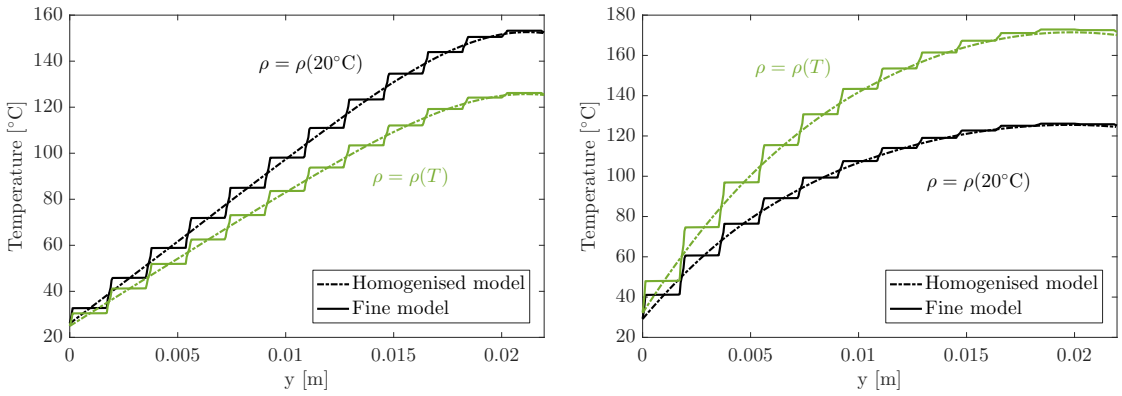

Figure 3.23: Comparison of the temperature distribution along the vertical mid-cross section within the winding domain for the fine and homogenised models with $\rho(20\,^{\circ}\mathrm{C})$ and $\rho(T)$ for the case (a) $|I_0| = 5\,\mathrm{A}rms$ at $f = 5\,\mathrm{kHz}$ and (b) $|I_0| = 35\,\mathrm{A}rms$ at $f = 100\,\mathrm{Hz}$

Another issue is related to local steep variations of the magnetic field that introduce local effects that cannot be perfectly captured by the homogenised model. This is the case, for instance, if we try to close the slot opening as shown in Fig. 3.24(a). This modification in the magnetic circuit changes the pattern of the magnetic field, which, accordingly, affects the winding loss distribution and magnitude. Reducing the slot opening, the loss density becomes more uneven and almost all concentrated in the central top wire. If we look at the error in the estimation of the ratio R_{AC}/R_{DC} using the fine and homogenised models (Fig. 3.18), we notice how the error increases if we reduce the slot opening, see Fig. 3.24(b).

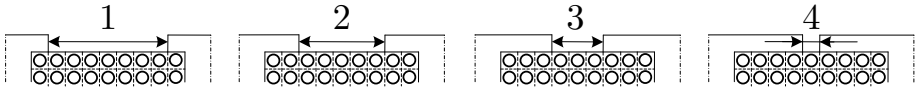

(a)

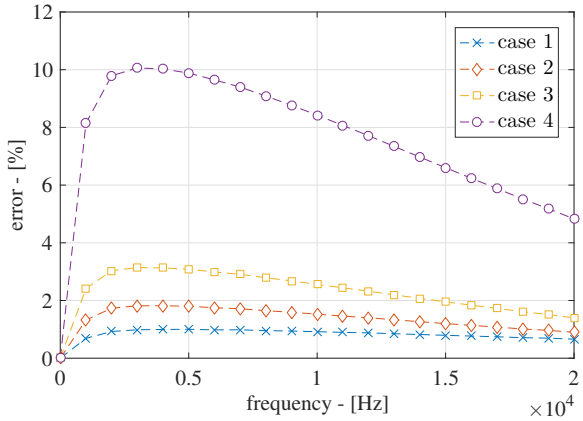

(b)

Figure 3.24: (a) Representation of the four test cases. (b) Evaluation of error in the estimation of the ratio R_{AC}/R_{DC} a function of f using the fine and homogenised model for the four cases presented in (a).

Chapter 4

Experimental validation of the coupled electromagnetic and thermal homogenisation

This chapter is based on publication [86].

In Chapter 3 a technique is proposed to couple the thermal and electromagnetic homogenisation of electrical windings in 2D to accurately calculate the loss and temperature fields as a function of f and T. An extensive numerical validation is provided. It is now useful to prove the effectiveness of the method experimentally, to confirm the outcomes of the numerical analysis.

In general, 2D models are not accurate enough when trying to represent the behaviour of electromagnetic components as a function of frequency, such as inductors or electrical machines, since we need to include the effect of the end windings. The amount of losses generated in the end region is lower compared to the active region [134]. However, results from the literature [93,141] showed that the estimation of the loss contribution of the end region cannot be simplified assuming that this

region is not affected by the skin or proximity effects. The end windings experience reduced AC effects, being located far from the core, but that can be captured only with fine 3D simulations [93,141]. Due to the large discretising mesh size, these simulations can become computationally prohibitive, in particular if we want to couple the electromangetic and thermal problems. Accordingly, in this chapter we extend the methodology presented in Chapter 3 applying the coupled homogenisation to any 3D geometry. The 3D analysis presented in [142] is limited to purely axi-symmetric windings, without including the thermal effects and the experimental validation. The objective is to evaluate the effectiveness of the model in predicting the loss distribution within the winding domain, accounting for the loss temperature dependence, and the resulting thermal field. From a computational point of view, this technique enables a factor 30 reduction in simulation time with the same level of accuracy.

In practice, we are analysing the hardware arrangement sketched in Fig. 4.1 representative of an open-slot modular stator-winding assembly with profiled conductors. For simplicity, from now on we refer to this specimen as a "motorette". The winding domain consists of $n_w = 64$ rectangular conductors connected in series and excited with sinusoidal current at various frequencies in turn. This hardware demonstrator has been designed to purposely exaggerate the AC effects and prove the performance of the proposed model.

4.1 3D Homogenisation of electrical windings

We start this analysis looking at the active region (see Fig. 4.1). In this area all the conductors are laid parallel to each other, with the current flowing along the z axis. This means that the generated magnetic field here should not have z components, $H_z = 0$. Accordingly, we can apply the same 2D homogenisation methodology presented in the previous chapter, since the reluctivity along z can be kept $\nu_z = \nu_0$ as

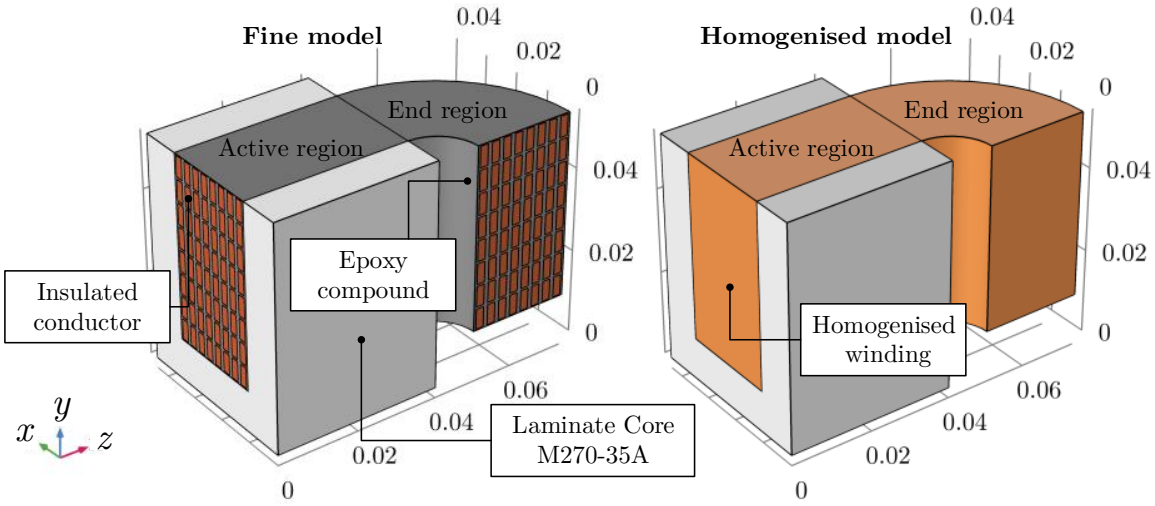

Figure 4.1: 3D Model of the analysed specimen – one quarter of the whole motorette. Active winding total length 80 mm, teeth height 44 mm and slot opening 24 mm. Fine model (left) with 64 turns of insulated copper conductor 2×5mm with epoxy potting, and homogenised model (right)

it should not capture any magnetic field generated by the eddy currents. The main difference with the previous chapter is that now we deal with rectangular conductors, which exhibit different effective permeability values along x and y. This can be appreciated in Fig. 4.2(a) and Fig. 4.2(b), where the proximity effect is excited with a uniform magnetic flux density along x and y, respectively. We can then write the effective reluctivity for the constitutive relation

$$[\nu_{eq}] = \begin{bmatrix} \nu_{eq,x} & 0 & 0 \\ 0 & \nu_{eq,y} & 0 \\ 0 & 0 & \nu_0 \end{bmatrix}, \tag{4.1}$$

where $\nu_{eq,x}$ and $\nu_{eq,y}$ can be obtained substituting the nondimensional parameters in Fig. 4.2(c) into (3.32), where now $r = \sqrt{|\Omega_c|/\pi}$ is an equivalent conductor radius. The skin effect changes conductivity in the axial direction, however, as discussed before, it has a very limited impact in this problem. For the thermal problem we should obtain an effective thermal conductivity in each direction. For $k_{eq,x}$ and $k_{eq,y}$

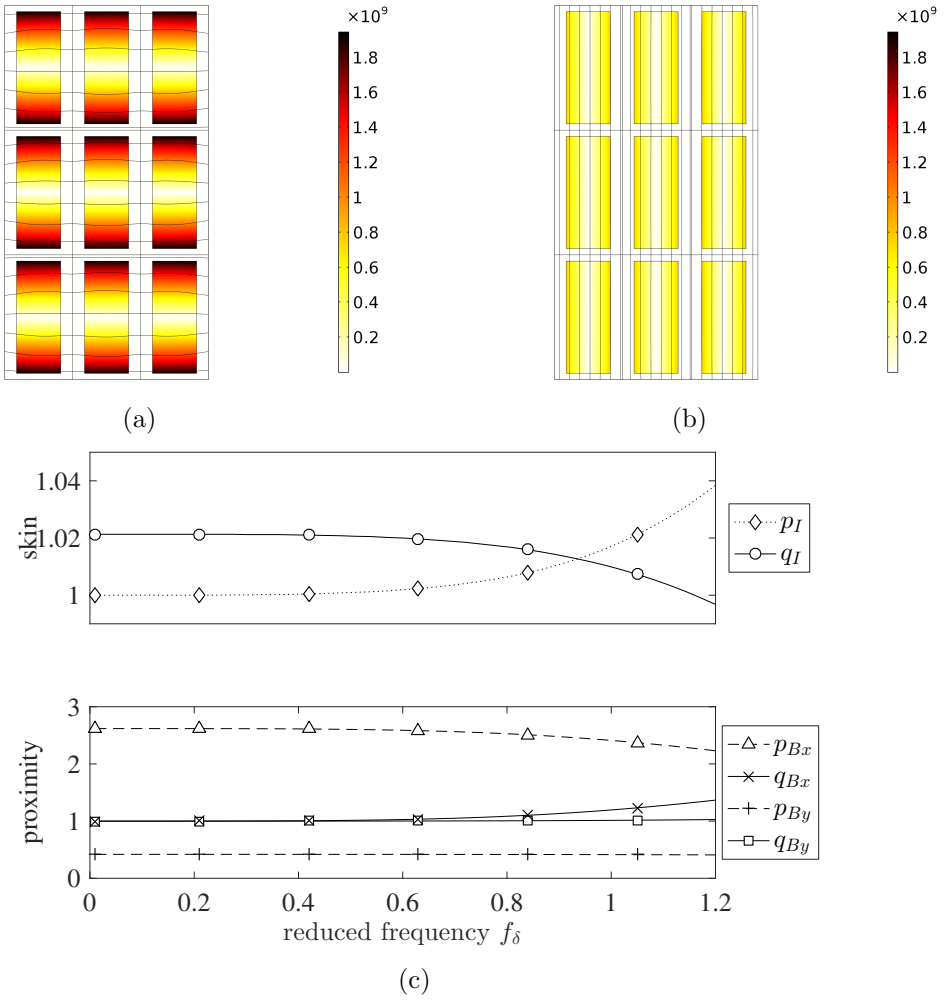

Figure 4.2: Solution of the proximity effect cell problem due to a unit average magnetic flux density along (a) x and (b) y axis, showing the resulting magnitude of the current density and flux lines. (c) Dimensionless parameters for (top) skin and (bottom) proximity effect for 2×5mm conductor with $\lambda = 0.606$ (slot dimensions 24×22mm) against reduced frequency

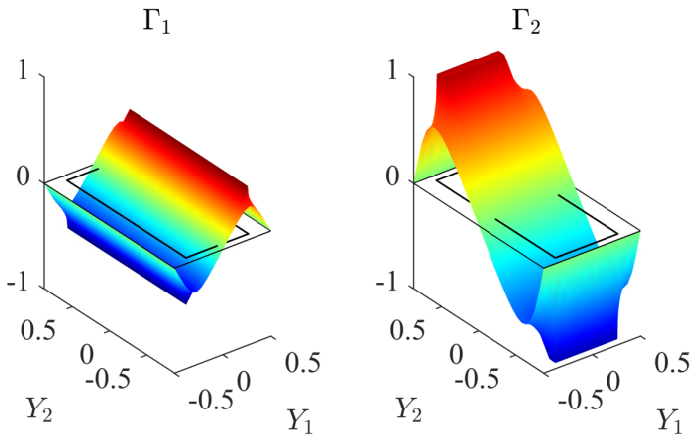

Figure 4.3: Solution of the two components of the cell problem Γ_1 and Γ_2 for rectangular conductors and material properties in Table 3.1

we can refer to the MSM as discussed in Chapter 2. In Fig. 4.3 we show the solutions of the cell problem Γ_1 and Γ_2 that enables us to obtain the two parameters. It is easier to deal with the z direction. Since all the wires lay parallel to the z axis, as discussed in Sxxection 2.1.1 we can simply apply the higher bound of the Wiener formula, $k_{eq\ z} = \lambda_c k_c + \lambda_i k_i + \lambda_e k_e$, with λ_c, λ_i and λ_e being the conductor, insulation and epoxy filling ratio, respectively ($\lambda_c + \lambda_i + \lambda_e = 1$).

4.1.1 End-winding homogenisation

The complexity of applying the method to the end winding region is due to the material being anisotropic, and the curved geometry. Accordingly, the anisotropic equivalent properties in the end-winding region should be evaluated at each angle using the elemental rotation matrix about the y axis $[R_y]$, e.g. $[\nu_{eq}]_{ew} = [R_y][\nu_{eq}]$, where the subscript ew stands for end-winding region. For more complex winding arrangements, suitable transformation matrices should be employed. This can be understood more easily looking at Fig. 4.4 where we plot the variation of $k_{eq,x}$ and $k_{eq,z}$ within the winding domain. In particular, these two parameters exchange their values in the active and end winding regions. The same applies for the reluctivity. We must add that also the laminated core (M270-35A) domain can be modelled as

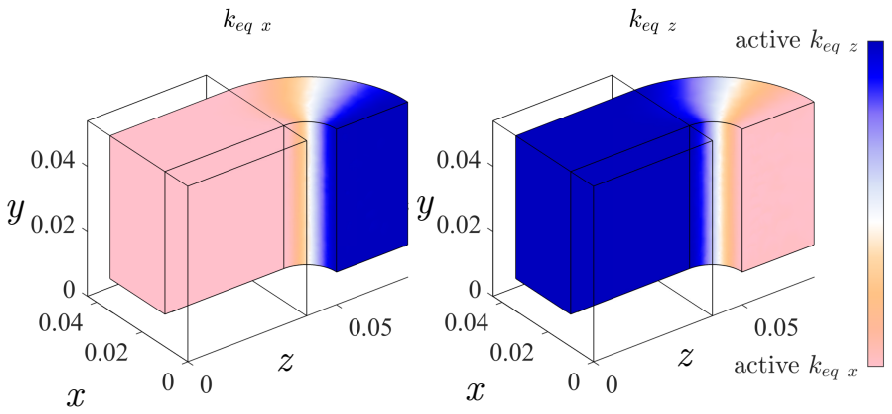

Figure 4.4: Variation of $k_{eq,x}$ and $k_{eq,z}$ within the 3D homogenised winding domain

an homogeneous anisotropic material. However, as discussed in Section 2.1.1, the upper and lower bounds of Wiener formula can help to homogenise this domain for the thermal and electromagnetic problems. This may not always be true for the electromagnetic problem if eddy currents circulate in the lamination, but this condition falls out of the range of frequencies analysed in this chapter (lamination thickness 0.35 mm) [143].

4.1.2 Numerical validation

The coupled 3D homogenisation technique presented here is now applied to the reference motorette described in Fig. 4.1. To reduce the mesh size of the full 3D problem in this numerical validation the conductor insulation domain is neglected for both the electromagnetic and thermal problems. This does not reduce the generality of this numerical validation since in this section we want to prove the effectiveness of the homogenisation technique compared to a fine model. Also, for the same reason, at this initial stage the build factors (i.e. thermal contact resistances) will not be included in the model. These parameters will be introduced when comparing the model estimations with the experimental measurements in the next section. Regarding the thermal boundary conditions, a fixed temperature of 40 °C is applied to the base, as if

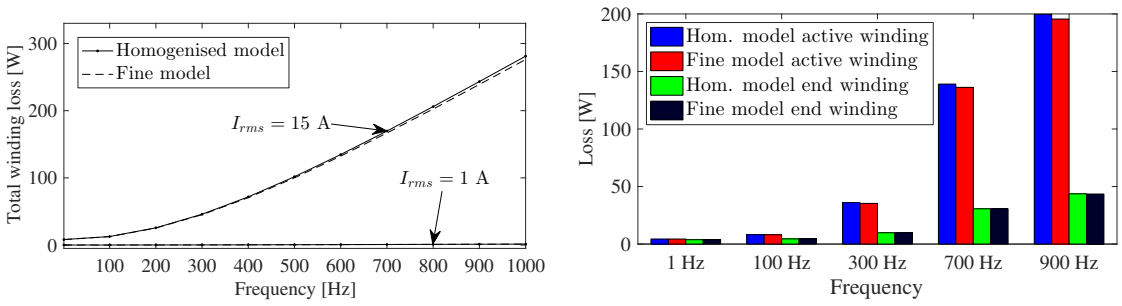

(a) (b)

Figure 4.5: Comparison between the fine and homogenised models in the estimation of (a) total loss for different frequencies and current amplitude (I_0 is current rms value) and (b) loss split between active and end winding for the case of $I_0 = 15\,\text{Arms}$

the specimen was placed on a cold plate, whereas convection with ambient is assumed to all the remaining free surfaces ($h_\infty = 15\,\text{W/(m}^2\text{K)}$ and $T_\infty = 40\,^\circ\text{C}$). The model considers the non-linear behaviour of the laminated core and the losses are estimated using the modified Steinmetz equation with the parameters given in [93].

The results from the coupled electromagnetic and thermal homogenisation in the reference motorette in terms of steady-state winding loss estimation are presented in Fig. 4.5. Fig. 4.5(a) presents the total loss estimation obtained with the fine and homogenised model for different current amplitude and at growing frequency. The match between the models is very close, with a maximum relative error of around 2%. If we split the loss contribution from the active and the end winding, as shown in Fig. 4.5(b) for the case of $I_0 = 15\,\text{Arms}$, we can see that the bigger discrepancy is concentrated in the active region. In the end of the active length the current, in correspondence of the change of direction of the eddy current curls, exhibits components along directions other than z [93], see Fig. 4.6, reducing the validity of the 2D approximation.

In general the solution time for the coupled electromagnetic-thermal steady-state analysis on an Intel i7 (3.2 GHz and 32 Gb RAM) is on average around 2700 s and 96 s with the fine and homogenised models, respectively.

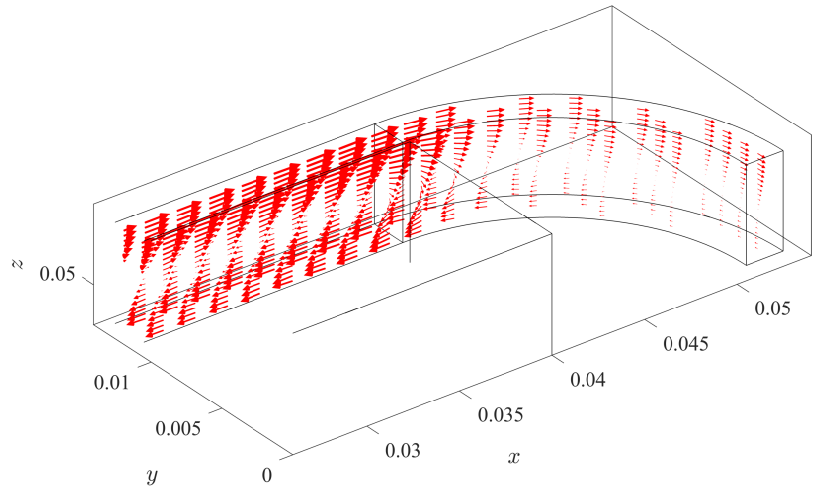

Figure 4.6: Current density vector $\boldsymbol{J}$ in the top right conductor in slot at $f = 1\,\text{kHz}$

The coupled electromagnetic-thermal analysis enables the evaluation of the temperature distribution within the domains, obtained, as mentioned in the previous chapter, by iteratively updating the thermal model with the loss distribution from the electromagnetic model as a function of $\rho_J = \rho_J(T)$. As an example for the 3D domain, in Fig. 4.7 we present the loss and temperature distribution obtained with the fine and homogenised models, respectively, for the case of $I_0 = 15\,\text{Arms}$ and $f = 500\,\text{Hz}$. It is important to note that in Fig. 3.17, where the losses are plotted using a logarithmic scale, the homogenised model provides only the cell averaged loss. This prevents the ability to show the precise loss distribution resulting from the circulating eddy currents in each conductor. However, since the copper has a high thermal conductivity compared to the rest of the materials (see Table 3.1), this does not affect the homogenised thermal model, which is able to estimate the temperature field with high accuracy, Fig. 4.7(b).

In Fig. 4.8(a) the hot-spot and mean temperature calculated with the fine and homogenised models are compared. The maximum temperature difference between the models is within $1\,^{\circ}\text{C}$, which is mainly due to the error in the loss estimation. It is interesting to notice how the mean temperature, shown only for the case of $I_0 = 15\,\text{Arms}$, is about 25% lower than the hotspot at high frequencies.

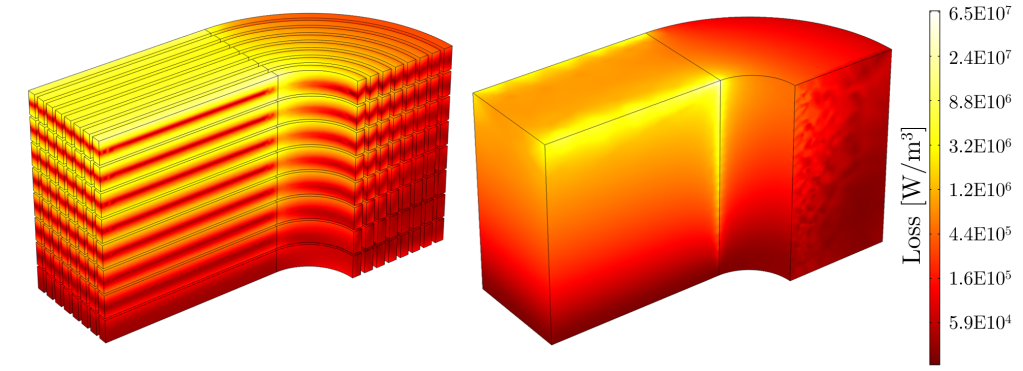

(a)

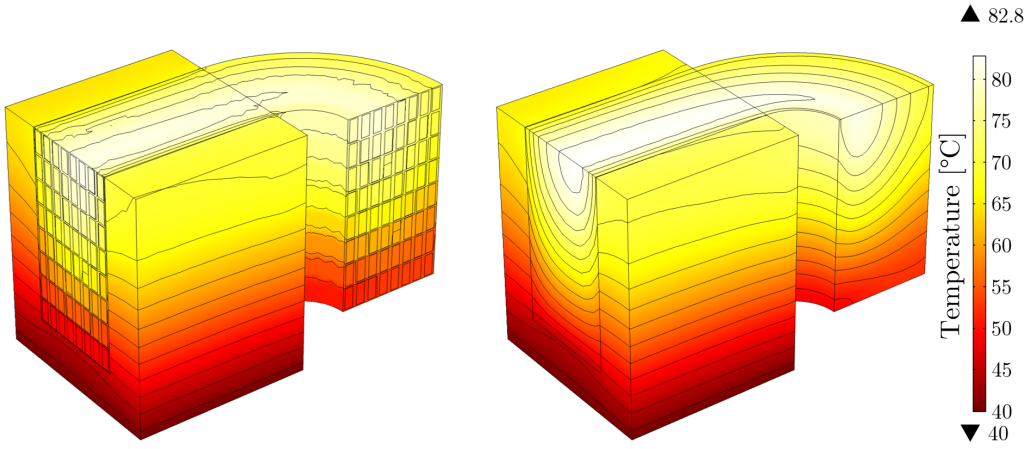

(b)

Figure 4.7: Comparison between the fine and homogenised model in the estimation of the (a) loss and (b) temperature distribution within the motorette with $I_0 = 15\,\text{Arms}$ and $f = 500\,\text{Hz}$

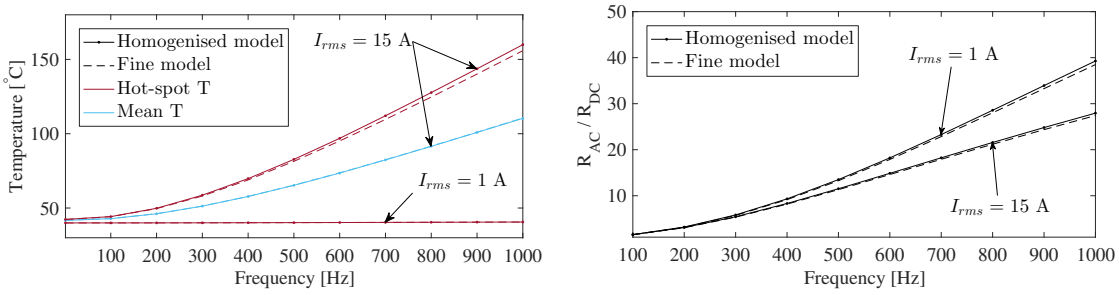

Figure 4.8: (a) Winding hot-spot (dark line) and mean (light line) temperature obtained with the fine (dashed line) and homogenised (dot marker) model. (b) Resistance ratio $R_{\mathrm{AC}}/R_{\mathrm{DC}}$ obtained with the fine (dashed line) and homogenised (dot marker) model at different working conditions

The advantage of the coupled electromagnetic and thermal analysis is that it enables the accurate evaluation of the ratio $R_{\mathrm{AC}}/R_{\mathrm{DC}}$ usually employed to describe AC loss contribution. In fact, Fig. 4.8(b) clearly shows how the AC contribution is strictly dependent on the load: higher current leads to higher temperatures, and accordingly increased electrical resistance which reduces the AC effects.

We conclude this section by presenting Fig 4.9, where the temperature distribution due to a DC load is depicted. In this case the hotspot is located in the end winding region. This is in conflict with the results of the analysis with AC current. One may argue that this is due to the fact that with AC the contribution of the core losses leads the hotspot to move towards the active region. However, our simulation showed that loss contribution of the core is limited (a few percentage points of the total loss) and that the same outcome is observable when the core loss contribution is removed. Indeed, the large AC losses concentrated close to the slot opening lead the hot spot to move to the middle of the active region, notwithstanding the worse cooling conditions of the end winding.

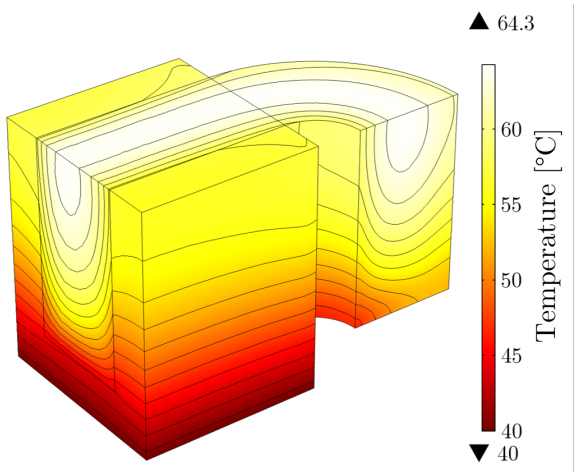

Figure 4.9: Steady-state temperature distribution resulting from a DC load of $I = 50\,\mathrm{A}$

4.2 Experimental validation

The remaining part of this chapter is devoted to the experimental validation of the proposed coupled electromagnetic-thermal homogenisation. As mentioned earlier, the experimental hardware was designed and built in accordance with the sketch in Fig. 4.1 to exaggerate the AC effects. We start by describing the components and the assembly procedure followed to obtain accurate results. Then, the measurements on the motorette are presented and compared with the model predictions.

4.2.1 The laminated core

The motorette analysed here is composed of two main elements, namely the winding and the laminated core. We start describing the latter, moving afterwards to the description of the conductor assembly. As can be guessed from the description, the core is made out of a set of thin insulated electrical steel laminations, which are glued together. The particular shape of the core, a so-called "E-core", is usually employed for inductors or transformers. However, since we could not find an off-the-shelf E-core that could match our geometrical requirements and that could be assembled in small quantities, we opted for a custom design (see Appendix B), manufactured by a

local supplier. The designed shape of each lamination was obtained via wire erosion, and not through laser cutting which may change the characteristics of the electrical steel. To limit the amount of losses induced in the core by the alternating current, M270-35A steel was selected, with a lamination thickness of 0.35 mm.

Measuring the loss on the motorette means evaluating the real power at the terminals of the winding; this means that the measurement includes the contribution of the core. Accordingly, to be able to isolate the winding loss we need to first evaluate the core loss as a function of frequency and temperature.

4.2.2 Core loss measurement procedure

To evaluate the core loss, we wound the core with a coil that is not affected by AC effects. Keeping in mind that our analysis is covering a frequency range up to 1 kHz, the wire size is chosen by looking at the skin depth δ_{skin} at the maximum frequency:

$$\delta_{\text{skin}} = \sqrt{\frac{2\rho}{\omega\mu_0}} = 2.1 \times 10^{-3}\,\text{m}. \tag{4.2}$$

Accordingly, a conductor diameter at least lower than δ_{skin} should be selected. The thin size of the wire means having a high conductor DC resistance that leads to high loss density and, in turn, fast temperature rise. An automated procedure needed to be developed to limit the winding exposure to the load as much as possible and, thus, avoid reaching critical temperatures. For this purpose, initially a coil without magnetic core was employed with a conductor of size 1 mm.

The test arrangement is presented in Fig. 4.10. The coil was excited with a Kikusui PBZ60-6.7 that can generate current with a wide range of waveforms with peaks voltage and current up to 60 V and 6.7 A, respectively. The voltage and current measurents were read by an oscilloscope (Agilent InfiniiVision 4000 X-series). In addition, the specimen was equipped with three thermocouples, embedded within the

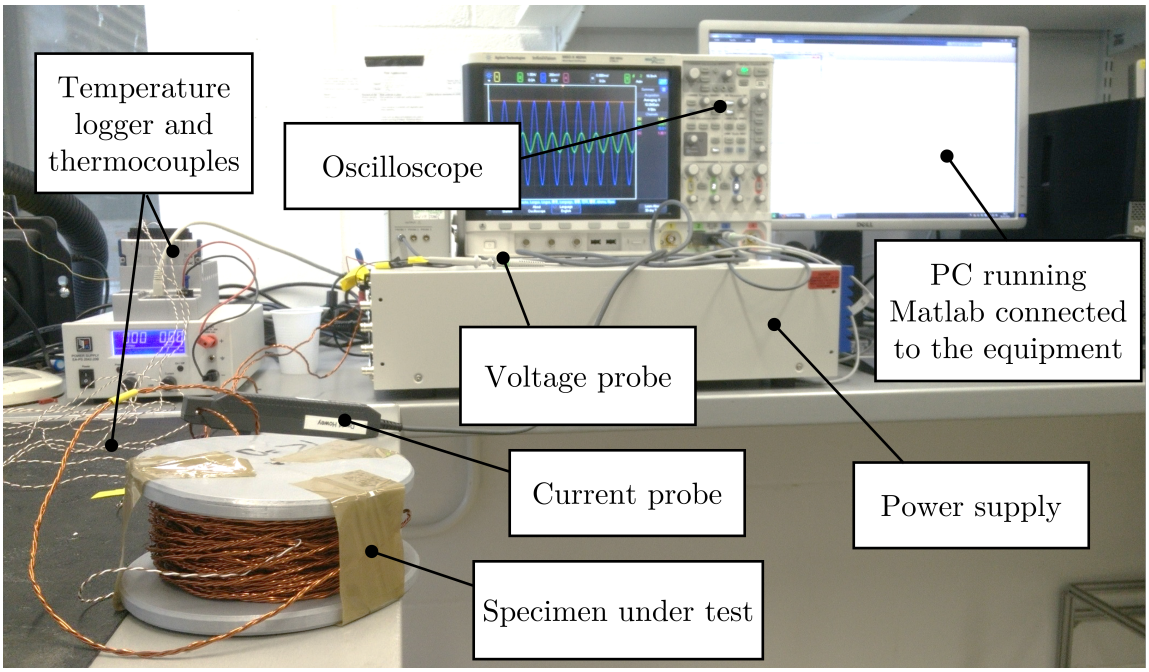

Figure 4.10: Test arrangement for the development of the automated procedure for the core loss evaluation

turns, to monitor the wire temperature. Temperature readings were performed using type K (for ambient) and type T (for the coil) connected to a data acquisition module that translated the voltage measurement.

All the pieces of equipment were controlled by a PC from Matlab. This ensured measurements as short as possible, to prevent overheating. The test procedure is detailed in Fig. 4.11. Each test consisted of two steps. First the coil was excited with DC current and the DC resistance R_{DC} was measured. Then, the DC component was removed and a sinusoidal AC current at the frequency f was injected. By reading the voltage V and current I, the real power was obtained by averaging the instantaneous power $P(t) = I(t)V(t)$ over a number of cycles. The equivalent AC resistance was then calculated with $R_{AC} = \frac{P}{I_{rms}^2}$ and compared with R_{DC}. Performing a DC test followed by an AC test ensured that the temperature variation of R_{DC} was included and, accordingly, the ratio R_{AC}/R_{DC} could be evaluated more accurately. Temperature measurements were taken before and after every single set of electrical measurements,

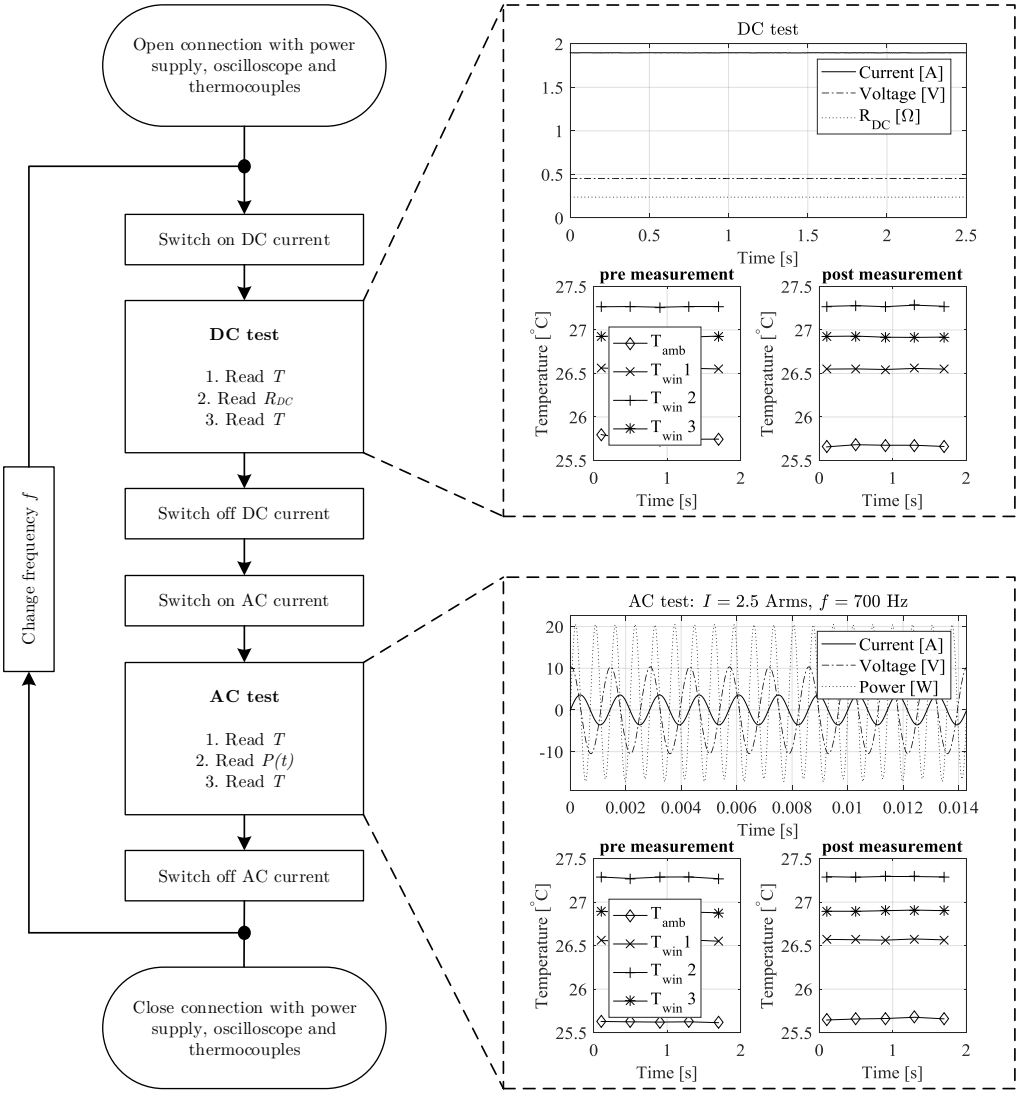

Figure 4.11: Testing procedure

first, to note at which temperature the resistance was measured and, second, to make sure the specimen did not overheat.

In Fig. 4.12 a reference set of measurements for $I_0 = 3\,\text{Arms}$ and varying f is presented. In the plot we can notice the increase in the ratio R_{AC}/R_{DC} with f and also appreciate the rise of DC resistance with T. This data also informs us that the selected wire is not suitable for measurements of the core losses and that a conductor with smaller gauge should be employed.

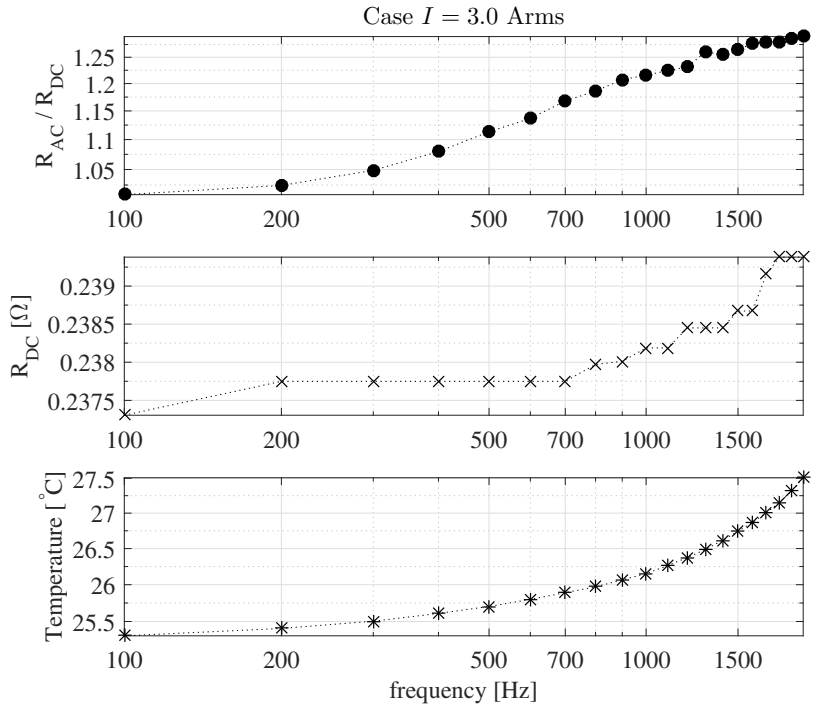

Figure 4.12: R_{AC}/R_{DC} measurements on the 1 mm wire coil at a number of frequencies along with measurements of R_{DC} and T at which these were taken

4.2.3 Core loss measurement results

In accordance with the outcome of the previous section a conductor of diameter 0.2 mm was subsequently selected (Fig. 4.13(a)). Due to the reduced cross-section, 20 conductors were put in parallel and twisted to reduce circulating currents. The procedure presented in the previous section was repeated for a number of current amplitudes. To account for the temperature dependence of the core losses, the wound core was placed in a thermal chamber, as depicted in Fig. 4.13(b). The core temperature was monitored with a thermocouple placed in a hole drilled in the top of the middle tooth. In this case, to obtain the core loss magnitude, the winding loss must be removed from the real power measured at the winding terminals. The winding loss is assumed to be composed of the DC component only and, therefore, easily handled. The results in terms of core loss and AC over DC resistance for the core at 21 °C, 30 °C, and 40 °C are presented in Fig. 4.14. We can notice how, similarly for the

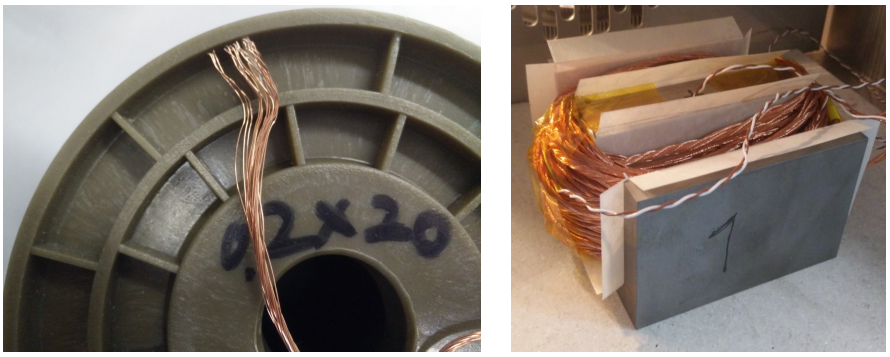

(a) (b)

Figure 4.13: (a) The conductor chosen for the measurement of the core loss magnitude and (b) the core under test

windings, the ratio R_{AC}/R_{DC} drops with temperature for the thermal dependence of the laminated steel with T.

As the range of current amplitudes and frequencies were limited by the power supply specifications, for each f and T we evaluated an equivalent core resistance $R_{core}(f,T)$ by interpolating the data as shown in Fig. 4.15. Assuming a linear behaviour of the core (no saturation), this allows us to widen the range of the available data to cover all the testing conditions of the motorette.

To better record the thermal behaviour of the core during the tests, a number of thermocouples were placed in holes drilled in the core. In particular four sensors per each tooth were used, with the purpose of having more information to calculate the thermal contact resistances.

4.2.4 Motorette assembly

Once the characterisation of the core was completed, the winding could be prepared and the motorette assembled, as described in Fig. 4.16. To simplify the winding procedure a former was designed and manufactured. While winding the conductor (64 turns in total), thermocouples were placed in particular locations in order to properly monitor the thermal behaviour of the winding during the tests. The size of

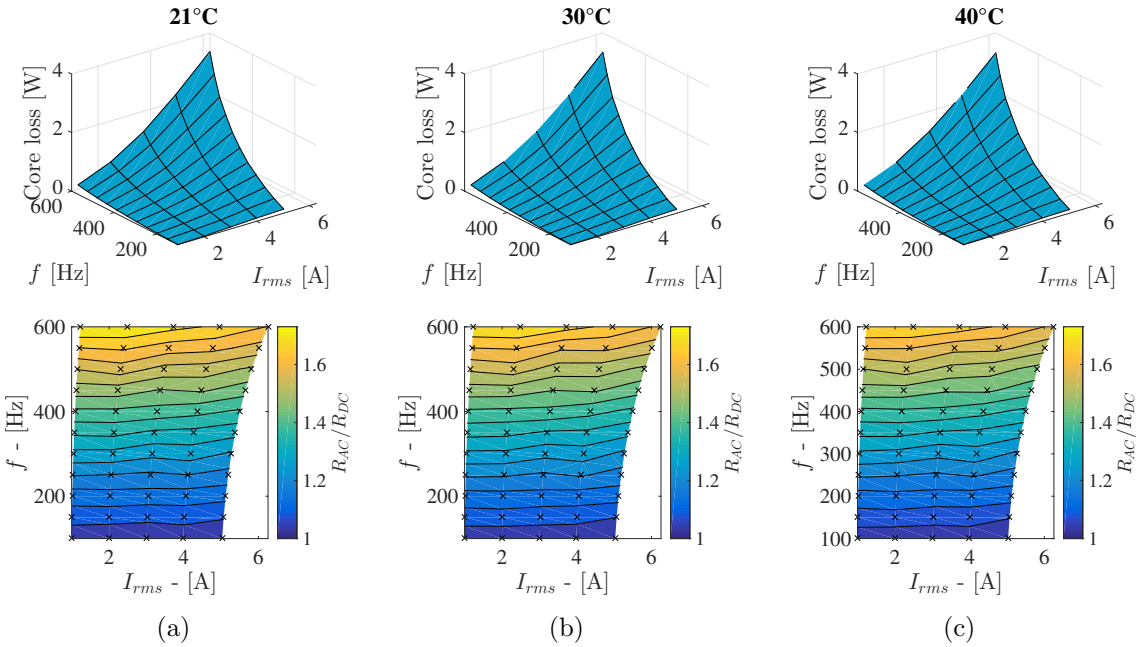

Figure 4.14: Core losses and R_{AC}/R_{DC} for a number of frequencies and loading current with the core at (a) 21 °C, (b) 30 °C, and (c) 40 °C

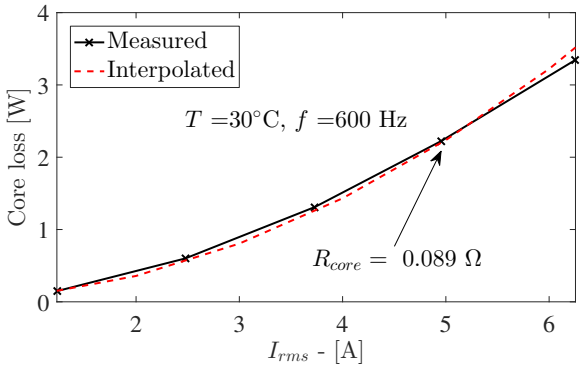

Figure 4.15: Evaluation of the equivalent core resistance via interpolation of the measured data

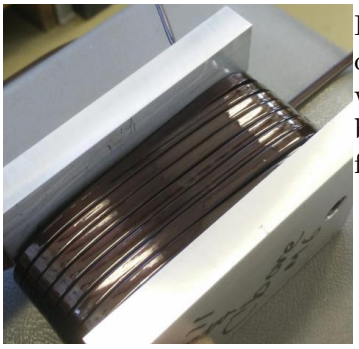

Rectangular conductor manual winding using a bespoke winding former

Placing a thermocouple during the winding process

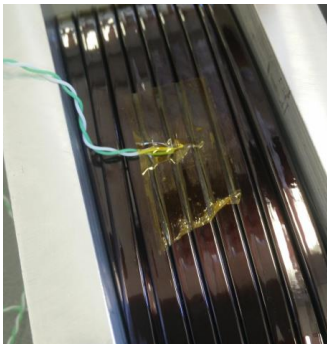

Moving the winding from the former to the laminated core

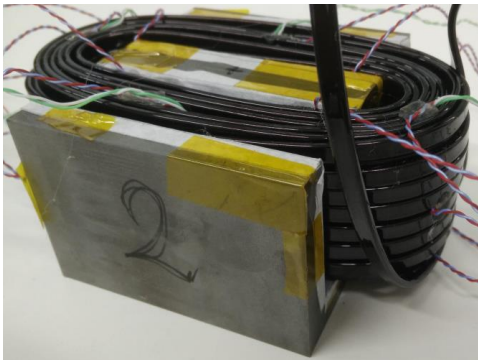

Preparing the mould with the inhadesive material

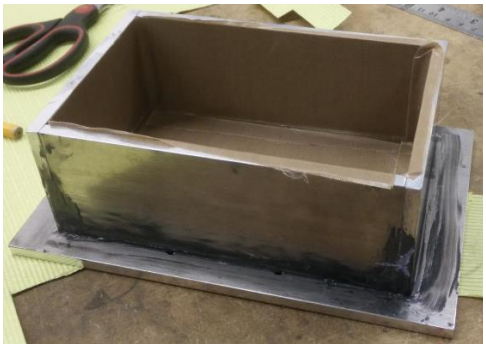

Pre encapsulation

Degassification

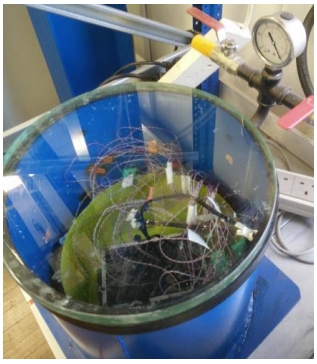

End product

Figure 4.16: Motorette assembly process

the conductor ($2 \times 5\,\text{mm}$) allowed the winding to maintain its shape while fitting it into the E-core slots.

For the encapsulation, a suitable mould was designed and manufactured. To facilitate the process of removing the motorette after the epoxy had solidified, the mould was covered with inadhesive material. The epoxy compound (Epoxylite EIP 4260) is a 1:10 mixture of hardener to resin. To avoid trapping air bubbles in the epoxy compound, the mould was placed in a container where a vacuum was created by means of a pump. The degassing process was completed when bubbles did not appear on the motorette upper surface. Removing the air allows the thermal performance of the epoxy to be maximised. After this last activity, the motorette was left to cure at room temperature.

4.3 Measurements and results

The built motorette was used to validate the coupled homogenisation technique, see Fig. 4.17(a) where the motorette is shown before encapsulating the windings with epoxy. The material properties are listed in Table 3.1. In particular, the insulation coating thickness was taken as 0.25 mm and the thermal conductivity of the epoxy compound was given by the manufacturer. The anisotropic thermal conductivity of the core was assumed based on the experimental work provided by [144], i.e. $k_x = k_y = 22\,\text{W/mK}$ and $k_z = 2\,\text{W/mK}$. On the other hand, the BH curve was provided by the manufacturer. Between the winding and the core, a thin layer of liner ($k_{\text{liner}} = 0.195\,\text{W/m K}$ and thickness 0.025 mm) was added.

As shown in Fig. 4.17(a), the winding was equipped with a large number of thermocouples (type K and type T) to accurately monitor the thermal behaviour during the tests. As described in Fig. 4.17(b), the thermocouples were placed in specific locations in the middle of the active and end winding regions: i.e. the top, bottom, centre,

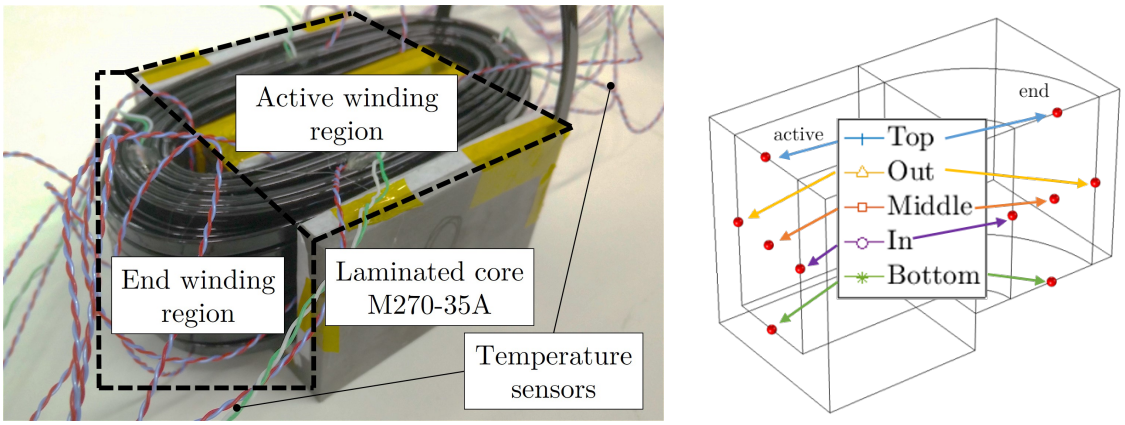

(a) (b)

Figure 4.17: (a) Motorette assembly before adding the thermocouples on the core and encapsulating the winding with epoxy and (b) sketch showing the locations where the sensors were placed in the winding.

inner, and outer sides of the windings domain. The position of the sensors not only facilitates the calibration procedure, but also enables the collection of temperature distribution data within the slot.

4.3.1 DC Tests for thermal model calibration

To finalise the thermal model calibration, DC tests were performed. As depicted in Fig. 4.18, the motorette was placed in a insulating chamber, suitably mounted on a liquid-cooled temperature-controlled plate. The winding and core temperatures were recorded while the motorette was loaded with a DC power supply. The test enabled the identification of the build factors, including the thermal contact resistance between both the winding and the core and between the motorette and the cooling plate.

In Fig. 4.19 a graphical description of the physical meaning of the thermal contact resistance R_{cont} is given. As anticipated in Section 1.2.2, this resistance captures the temperature discontinuity between the winding and core domains, which is due to the imperfect surface contact. Moreover, the contact is also affected by the presence of the slot liner, the layer of insulating paper depicted in Fig. 4.19 that electrically

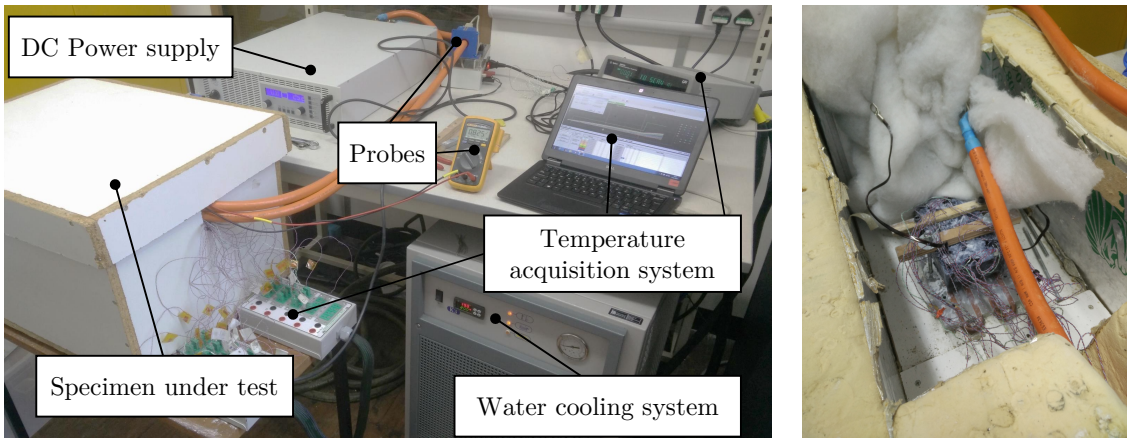

(a) (b)

Figure 4.18: (a) Experimental setup while performing DC tests and (b) view inside the thermal chamber

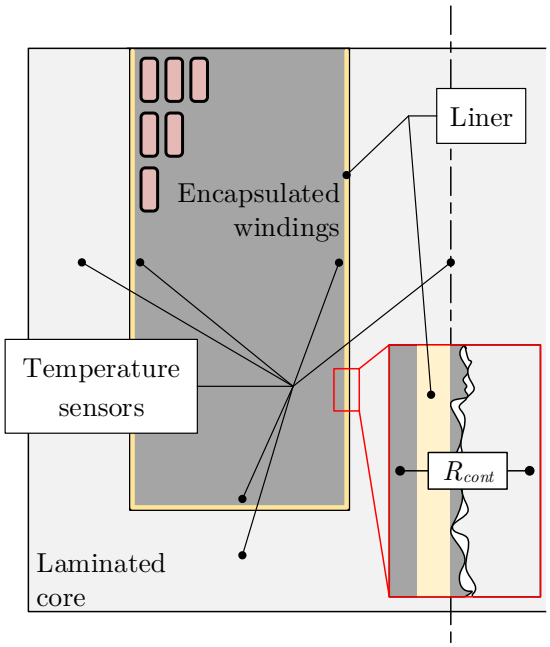

Figure 4.19: Physical representation of the thermal contact resistance

isolates the conductors from the core. Accordingly, the resistance R_{cont} includes the thermal effects of the liner and the limited contact area.

The magnitude of the contact resistances was obtained by minimising the error between simulated and measured temperatures in the specific locations where the thermocouples were placed in the core and in the winding, as highlighted in Fig. 4.19. In particular, a single value of contact resistance was defined for the three surfaces connecting the winding to the core. In the commercial software we employed for this work (COMSOL Multiphysics v 5.2), this can be achieved adding a "thin layer" between the domains, similarly to [145], defined as

$$R_{cont} = \frac{L_{eq}}{k_{\text{liner}} A} \tag{4.3}$$

where A is the area of contact between the winding and core and L_{eq} is the equivalent length of the resistor. The same approach was followed to model the contact resistance between the motorette and the cold plate; in this case, a thermal paste ($k_{\text{paste}} = 2.9\,\text{W/mK}$) was spread on the plate before placing the motorette with the purpose of filling the gaps and improving the heat transfer. The specific values of the two resistances were found to be $R'_{cont,\text{w-c}} = 3.59 \times 10^{-2}\,\text{K/m}^2\text{W}$ and $R'_{cont,\text{c-p}} = 6.89 \times 10^{-4}\,\text{K/m}^2\text{W}$ for the winding-core and core-place contacts, respectively. The value of the resistor between winding and core is 2 orders of magnitude larger compared the other contact resistance.

In the model, a fixed temperature is imposed at the motorette base (20 °C), while on the remaining external boundaries a no-flux condition is applied. Indeed, the chamber was insulated with glass and rock wool placed on the walls and the empty chamber spaces allowing the heat to flow only towards the cold plate, see Fig. 4.18(b). Also, as shown in Fig. 4.18(b), the motorette was secured to the cold plate using some wood bars with the aim of reducing the contact resistance.

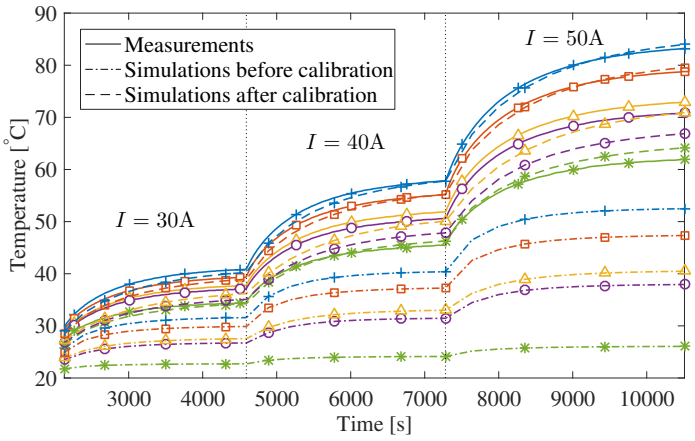

Figure 4.20: Comparison between measured and estimated winding transient temperatures before and after calibration with the motorette loaded with 30, 40, and 50 ADC until a thermal steady state is reached for each condition. Temperatures refer to the mid-cross section of the active windings

The results of the DC tests are plotted in Fig. 4.20. In particular, the figure shows the temperatures measured in the active-region mid-cross section compared to the model estimations, before and after the calibration. During the transient the load was increased when thermal steady state was reached. After the calibration, a good match is achieved in all five locations, showing also the good quality of the applied thermal homogenisation. It is important to note that without calibration, which is almost impossible to address analytically, we would have significantly underestimated the top temperatures.

To confirm the accuracy of the calibration, the model is compared to another set of DC tests, with the load at 25 and 35 ADC, in Fig. 4.21. In this case, the model estimations are compared also to the temperatures in the end region (see Fig. 4.21(b)), always referring to the locations highlighted in Fig. 4.17(b). From Fig. 4.21(b) a large disagreement can be noticed in the measurements in the end-winding bottom sensor; this is due to the fact that the sensor detached from the winding during the encapsulation process, which makes this data not credible.

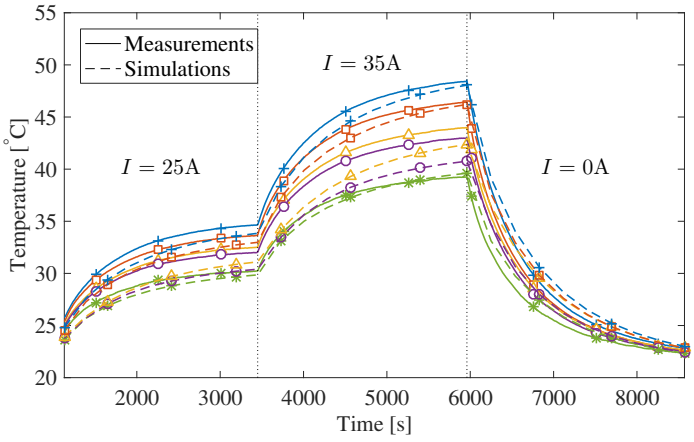

(a)

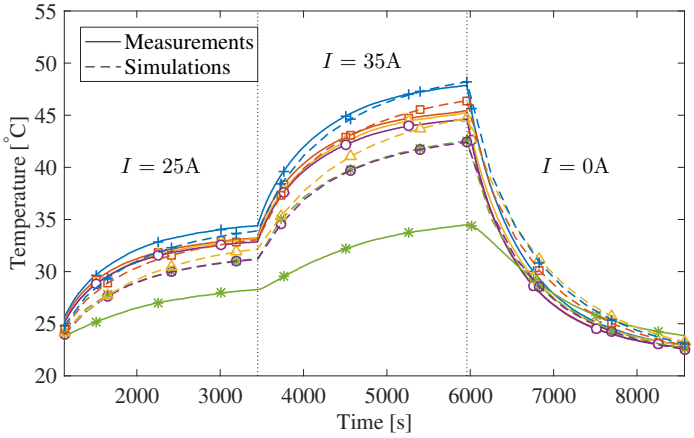

(b)

Figure 4.21: Comparison between measured and estimated winding transient temperatures after calibration with motorette loaded with 25 and 35 ADC, and without load until thermal steady state is reached for each condition. Temperatures refer to (a) the mid-cross section of the active winding and (a) the mid-cross section of the end region

4.3.2 AC Tests

DC tests are used to calibrate various heat transfer effects, whereas the AC tests are usually performed to identify potential issues associated with "additional loss" due to manufacture, e.g. higher than expected core loss.

To perform the AC tests, the arrangement shown in Fig. 4.18(a) was kept, only changing the power supply. Each test consisted of injecting an AC sinusoidal load in the motorette until thermal steady state was reached (a convergence strategy of $\Delta T < 1\,°\mathrm{C}$ over the last 10 min was applied) and then the real power was measured with the help of a power analyser. The losses were then compared to the case without temperature effects, that is injecting the AC load for few seconds avoiding the windings temperature changing significantly.

The total motorette loss due to a load of $I_0 = 5\,\mathrm{Arms}$ with the frequency varying from 600 Hz to 1100 Hz and $I_0 = 10\,\mathrm{Arms}$ with $f = 100\,\mathrm{Hz}$ to 600 Hz are compared in Fig. 4.22(a) and Fig. 4.23(a), respectively, where the dashed line highlights the total loss at ambient temperature (22 °C) and the solid line shows the measurements and simulations at thermal steady state. Separately, in Fig. 4.22(b) and Fig. 4.23(b), we compares the winding loss, which is obtained removing the core contribution from the total loss. The coupled electromagnetic-thermal model slightly overestimates the winding loss, with a maximum error of $\approx 20\%$ compared to the measured values. The core losses are underestimated by the model, balancing the winding loss discrepancy. Accordingly, the simulated total loss follow closely to the measurements. In general, predictions follow the same loss trend as in the measurements and, more importantly, the winding loss reduction due to thermal effects is captured with good accuracy.

Part of the discrepancy with the loss measurements is systematic and due to homogenisation; indeed, as shown in Section 4.1.2, the model order reduction through homogenisation introduces an error of about 2%. Another part of the error could be due to the modelling of the laminated core. Indeed, the results showed a discrepancy

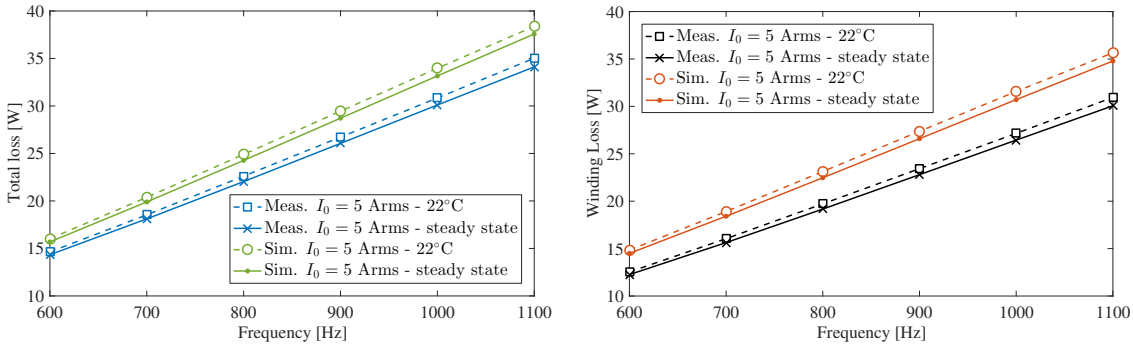

(a) (b)

Figure 4.22: Predicted and measured (a) total (including core) and (b) winding loss with the motorette loaded with $I_0 = 5\,\text{Arms}$ and $f = 600 \rightarrow 1100\,\text{Hz}$ at 22 °C (dashed line) and at thermal steady state (solid line)

between the measured and simulated core loss. This error could be associated with the selection of the parameters for the Steinmetz equation. As discussed, we employed parameters taken from the literature, from a work where a core with the same lamination thickness and similar geometry. Indeed, a different manufacturing process might have affected the core behaviour modifying such parameters. Moreover, the manufacturing process that involved gluing and cutting through wire erosion could have affected the accuracy of the B-H curves provided by the manufacturer of the electrical steel lamination. The manufacturing process could have affected the resulting magnetic field density distribution, leading to a wrong evaluation of the fringing flux. Additionally, in the model we assumed that the wires were periodically distributed and all laid in parallel. In Chapter 2 we showed that this simplification has a reduced effect of the macroscopic temperature field. However, this simplification might affect the loss distribution since the contribution of the induced eddy current is a function of the magnitude of the magnetic field, which varies significantly depending on the location within the slot, in particular in the neighbourhood of the slot opening. Other reason for the discrepancy in the values shown in Fig. 4.22 and 4.23 could be due to measurements intrinsic errors.

Comparing the AC resistance of the motorette for the two loads, as depicted in

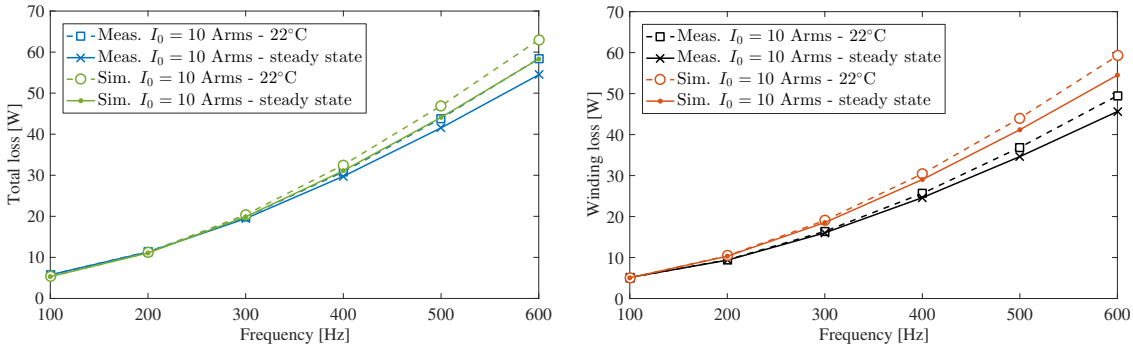

Figure 4.23: Predicted and measured (a) total (including core) and (b) winding loss with the motorette loaded with $I_0 = 10\,\text{Arms}$ and $f = 100 \rightarrow 600\,\text{Hz}$ at 22 °C (dashed line) and at thermal steady state (solid line)

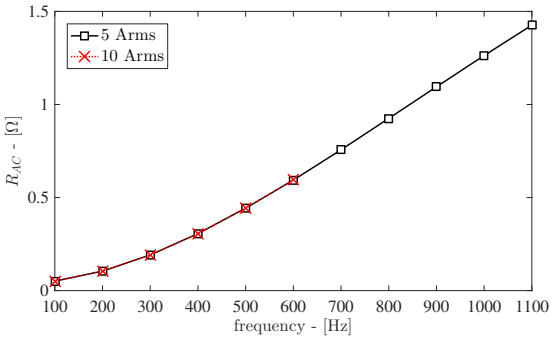

Figure 4.24: Comparison of measured AC resistance R_AC with the current at $I_0 = 5\,\text{Arms}$ and $I_0 = 10\,\text{Arms}$ at various frequencies

Fig. 4.24, we can obtain a perfect data overlap, confirming that the analysed load did not lead to saturation of the laminated core.

It is now interesting to check the accuracy of the proposed model in the prediction of the temperature distribution within the slot. Similarly to Fig. 4.21, in Fig. 4.25 and Fig. 4.26 we compare temperatures in the same five locations within the mid-cross section of the active and end-winding regions, referring to Fig. 4.17(b). The model is able to accurately predict the large thermal gradient developing in the slot not only at steady state, but also during the whole transient. Compared to the DC test, we can clearly notice how the particular loss distribution, concentrated in the neighbourhood of the slot opening, leads to a significantly steeper temperature

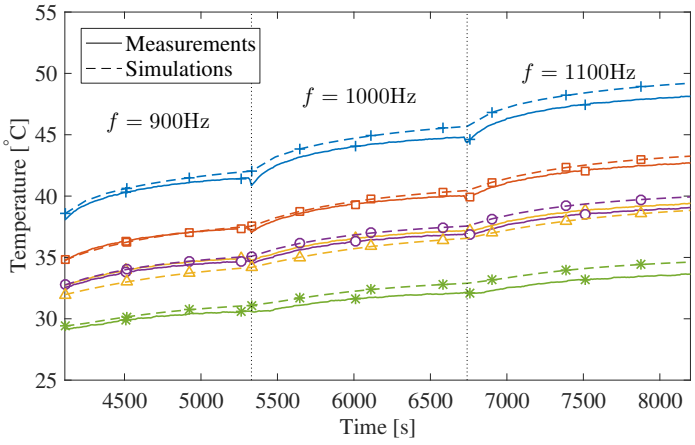

(a)

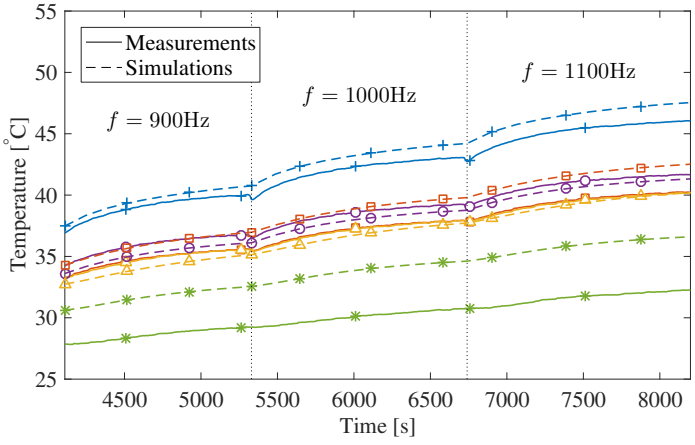

(b)

Figure 4.25: Comparison between measured and estimated winding transient temperatures after calibration with motorette loaded with $I_0 = 5$ Arms at 900, 1000, and 1100 Hz until thermal steady state is reached for each condition. Temperatures refer to (a) the mid-cross section of the active winding and (b) the mid-cross section of the end region

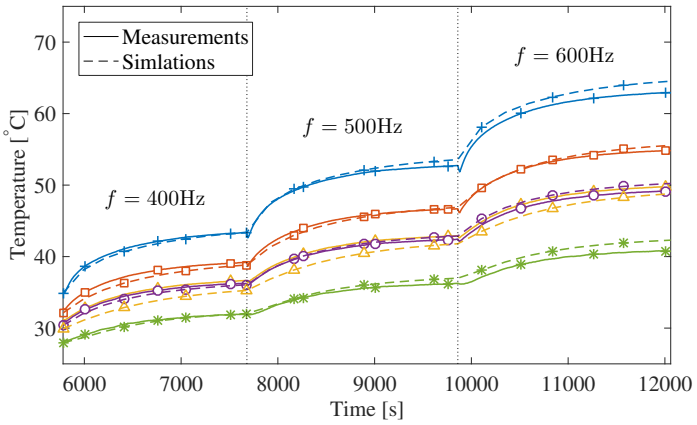

(a)

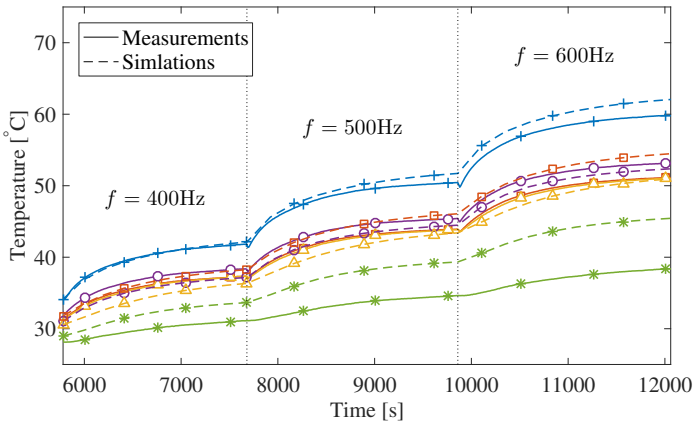

(b)

Figure 4.26: Comparison between measured and estimated winding transient temperatures after calibration with motorette loaded with $I_0 = 10\,\text{Arms}$ at 400, 500 and 600 Hz until thermal steady state is reached for each condition. Temperatures refer to (a) the mid-cross section of the active winding and (b) the mid-cross section of the end region

gradient. As an example we can consider the temperature distributions due to a similar amount of power loss in DC or AC. In the first case ($P = 58\,\mathrm{W}$ with $I = 40\,\mathrm{A\,DC}$) the temperature difference measured between the top and bottom of slot is $\Delta T_{\mathrm{DC}} = 12\,^{\circ}\mathrm{C}$ as shown in Fig. 4.20. On the other hand, the gradient when a current of amplitude $I_0 = 10\,\mathrm{Arms}$ at $600\,\mathrm{Hz}$ is injected ($P = 50\,\mathrm{W}$) was $\Delta T_{\mathrm{AC}} = 22\,^{\circ}\mathrm{C}$ (see Fig. 4.26(a)).

In Table 4.1 we compare the steady-state "top" temperatures in the active and end regions obtained either through measurements or estimated by the model. The agreement between experimental and simulated data is very good, with the maximum error falling below $3\,^{\circ}\mathrm{C}$. In Section 4.1.2 we showed how, according to the numerical results, the hot-spot temperature for the DC load should be located in the end-winding region. This outcome does not seems to be respected by the measurements, since we always recorded the highest temperature in the active region, for both AC and DC tests (see Table 4.1). However, the ΔT between end and active "top" temperatures for DC tests was very narrow ($< 1.5\,^{\circ}\mathrm{C}$); this small difference does not allow us to discriminate the actual hot-spot location. On the contrary, with AC loads this difference is significantly larger, with $\Delta T > 1.5\,^{\circ}\mathrm{C}$ and highest value of $\Delta T = 3.1\,^{\circ}\mathrm{C}$ for $I_{rms} = 10\,\mathrm{A}$ and $f = 600\,\mathrm{Hz}$.

Table 4.1: Top temperatures in active and end winding regions with DC and AC

Current	Active winding "top" temperature			End winding "top" temperature		
	Meas. [°C]	Sim. [°C]	$\Delta T_{\text{S-M}}$ [°C]	Meas. [°C]	Sim. [°C]	$\Delta T_{\text{S-M}}$ [°C]
$I = 30\,\text{A}$ DC	40.7	40.3	-0.4	40.4	40.4	0
$I = 40\,\text{A}$ DC	57.6	57.8	0.2	56.8	58	2.2
$I = 50\,\text{A}$ DC	83.2	84	0.8	81.7	84.4	2.7
$I_0 = 5\,\text{Arms at } 900\,\text{Hz}$	41.4	41.9	0.5	39.9	40.6	0.7
$I_0 = 5\,\text{Arms at } 1000\,\text{Hz}$	44.7	45.5	0.8	43	44	1
$I_0 = 5\,\text{Arms at } 1100\,\text{Hz}$	48.7	48.9	1.2	45.9	47.3	1.4
$I_0 = 10\,\text{Arms at } 400\,\text{Hz}$	43.2	43.4	0.2	41.6	42.1	0.5
$I_0 = 10\,\text{Arms at } 500\,\text{Hz}$	52.6	53.6	1	50.3	51.7	1.4
$I_0 = 10\,\text{Arms at } 600\,\text{Hz}$	62.9	64.5	1.6	59.8	62.1	2.3

Chapter 5

Improved thermal equivalent circuit element for electrical machine thermal modelling

This chapter is based on publication [87].

In the previous chapters we provided solutions to improve some of the common issues related to electrical machine thermal modelling, i.e. thermal model parameter estimation, loss assessment and separation as a function of frequency, and build factors such as contact resistance. The final problem, which we are going to cover in this chapter, is accuracy in relation to the model formulation. So far we have mostly employed finite element (FE) based models to estimate the temperatures in the analysed winding or entire motorette domains to obtain accurate results. However, in the literature most electrical machine thermal models are developed based on reduced order approaches, more precisely thermal equivalent circuits (TECs). One reason for this is the fact that TEC based models are mathematically simpler, allowing engineers to easily write in-house codes to simulate the thermal behaviour of the designed electro-

magnetic equipment, avoiding the use of commercial software. Moreover, the reduced computational cost makes the simulation of long transients significantly faster. Indeed, to complete the design of a new electrical machine, in particular when employed for propulsion, one has to assess the thermal behaviour as a function of time for a succession of loads, i.e. a driving cycle. As we are going to show, the major limitations of TECs are accuracy and resolution. The first problem comes from the fact that a TEC is not always able to provide correct results for any working condition (various current or rotational speeds) [87]. Instead, TECs usually provide only the average element temperature, which lacks information about temperature distribution within the components [92,146,147]. To overcome the TEC accuracy limitations Qi [148,149] and Simpson [150] proposed to highly refine the nodal discretisation in critical areas. The main advantage of this is that accounts for non-uniformly distributed losses. It can also assess the temperature in a particular position, for instance where thermal sensors are located. However, some of the beauty of using a TEC is lost, namely the simplicity of building a network with a very limited number of connections. Accordingly, in this chapter a new network element is proposed to overcome the mentioned limitations and improve the thermal information obtained with a TEC whilst keeping a minimal nodal discretisation.

5.1 Introduction to thermal equivalent circuits

The discretisation of a domain using a TEC is performed assigning to each element (e.g. winding, rotor, etc.) a node. The nodes are then connected together with thermal resistances, which model the main thermal phenomena, i.e. conduction and convection. Let us refer to the simple 2D problem described in Fig. 5.1(a), an isotropic rectangle with adiabatic lower and upper surfaces. The thermal resistance for

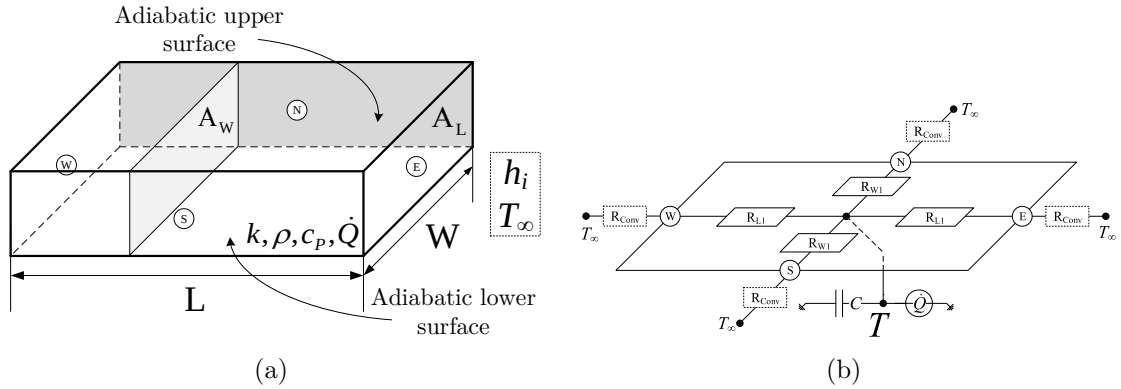

Figure 5.1: (a) Reference 2D thermal problem solved with TEC using the (b) Classic element

conduction is defined from Fourier's law as

$$R_{cond} = \frac{L}{kA}, \tag{5.1}$$

where A is the cross sectional area normal to L; for instance, $R_{\mathrm{L1}} = (\mathrm{L}/2)/kA_{\mathrm{W}}$. The thermal resistance modelling convection at ith external surface is defined as

$$R_{conv} = \frac{1}{A_i h_i}. \tag{5.2}$$

The heat equation (2.1) is then simplified as

$$C\frac{\partial T}{\partial t} = \frac{\Delta T}{R_{cond}} + \dot{Q}, \tag{5.3}$$

where ΔT represents the thermal gradient between two neighbouring nodes and we define $C = \rho V c_p$ as the element thermal capacitance, with $V = LA_{\mathrm{W}}$ the element volume.

To assess the accuracy of the Classic TEC discretisation (Fig. 5.1(b)), we analyse the simple problem depicted in in Fig. 5.1(a), where an internally heated rectangular geometry is exposed to convection on its lateral boundaries, with the upper and

lower surfaces adiabatic. The heat transfer coefficient is assumed to have a fixed value on the four boundaries. The solution of the TEC model outputs the central node temperature $\bar{T}$, which should represent the element average temperature. In the network equations, the total internal heat generation $\dot{Q}$ and thermal capacitance C are both introduced in the central node. For the steady-state temperature we solve

$$\frac{(\bar{T}-T_\infty)}{R_{conv,\mathrm{N}}+R_{\mathrm{W1}}}+\frac{(\bar{T}-T_\infty)}{R_{conv,\mathrm{S}}+R_{\mathrm{W1}}}+\frac{(\bar{T}-T_\infty)}{R_{conv,\mathrm{W}}+R_{\mathrm{L1}}}+\frac{(\bar{T}-T_\infty)}{R_{conv,\mathrm{E}}+R_{\mathrm{L1}}}=\dot{Q}. \tag{5.4}$$

The accuracy of the solution is strictly dependent on the Biot number Bi, which is a dimensionless parameter that defines how significant the temperature gradient within an element is compared to the gradient at the surface:

$$\mathrm{Bi}=\frac{L_{ref}h}{k}, \tag{5.5}$$

where L_{ref} is the problem reference length, which is commonly computed as the ratio V/A_{ext}, where A_{ext} is the total surface exposed to convection, h is the convection coefficient, and k is the thermal conductivity of the solid. For low values of Bi, generally Bi < 0.1, the temperature distribution is almost uniform and the linear approximation is reasonable. Thus, the accuracy of a TEC built using the Classic approach (Fig. 5.1(b)) is good only for low Bi.

5.1.1 The T-network

Bi is not the only parameter the affects the temperature gradient within an element. Assuming a fixed temperature applied to the element boundaries, the internal heat generation $\dot{Q}$ drives the final temperature distribution. Accordingly, the Classic discretisation should fail again to accurately estimate the element average temperature. To account for this effect, [146] introduced the so-called T-network, Fig. 5.2, where the Classic network is implemented with a third resistance in each direction. This

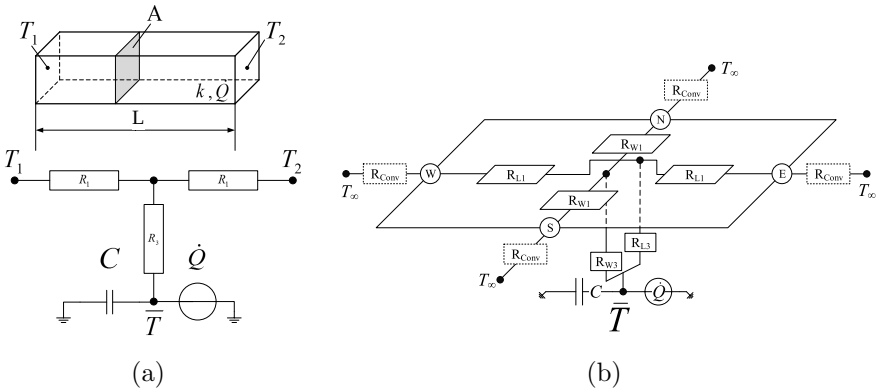

Figure 5.2: (a) 1D T-network and (b) discretisation of the 2D thermal problem of Fig.5.1(a) using the T-network

allows an improvement of the accuracy of the Classic element.

As described in [92] and referring to Fig. 5.2(a), the magnitude of the third resistance is obtained from the analytical solution of the 1D heat equation with uniform internal heat generation ($\dot{q} = \dot{Q}/(A_W L)$) and fixed temperature (e.g. $T_1 = T_2 = 0$) at the boundaries. At steady state the temperature distribution is

$$T(x) = \frac{\dot{q}L^2}{2k}\left(\frac{1}{4} - \frac{x^2}{L^2}\right), \tag{5.6}$$

which allows us to calculate the average temperature

$$\bar{T} = \frac{1}{L}\int_{-\frac{L}{2}}^{\frac{L}{2}} \frac{\dot{q}L^2}{2k}\left(\frac{1}{4} - \frac{x^2}{L^2}\right) dx = \frac{\dot{q}L^2}{12k}. \tag{5.7}$$

Recalling that $R_1 = \frac{L}{2kA}$, the magnitude of R_3 is then obtained from

$$\frac{\bar{T}}{R_3 + \frac{R_1}{2}} = \dot{q}LA, \tag{5.8}$$

which leads to

$$R_3 = -\frac{L}{6kA} = -\frac{R_1}{3}. \tag{5.9}$$

For instance, the 2D problem of Fig. 5.1(a) can be modelled with the network of

Fig. 5.2(b), which describes the following system of equations

$$\frac{(\hat{T}-T_\infty)}{R_{conv,\mathrm{N}}+R_{\mathrm{W1}}}+\frac{(\hat{T}-T_\infty)}{R_{conv,\mathrm{S}}+R_{\mathrm{W1}}}+\frac{(\tilde{T}-T_\infty)}{R_{conv,\mathrm{W}}+R_{\mathrm{L1}}}+\frac{(\tilde{T}-T_\infty)}{R_{conv,\mathrm{E}}+R_{\mathrm{L1}}}=0, \tag{5.10a}$$

$$\frac{(\bar{T}-\tilde{T})}{R_{\mathrm{W3}}}+\frac{(\bar{T}-\hat{T})}{R_{\mathrm{L3}}}=\dot{Q}, \tag{5.10b}$$

The T-network can be applied to run transient simulations for various geometries enabling the simulation of a full machine [4,92,151].

5.1.2 Numerical accuracy assessment

Example outputs of the two presented TEC models, i.e. Classic Fig. 5.1(b) and T-network Fig. 5.2(b), are given in Fig. 5.3. Here, the central node temperature of a rectangular geometry with aspect ratio $AR = L/W = 2$ is compared with the solution given by a FE based model. The TECs are integrated in time using an explicit forward Euler method as previously described in Section 2.4.2. The temperatures and time are presented in a non dimensional form according to:

$$\Theta = \frac{T-T_\infty}{T_0-T_\infty} \qquad \text{if } \dot{Q}=0, \tag{5.11a}$$

$$\Theta = \frac{T-T_\infty}{T_{ss}-T_\infty} \qquad \text{if } \dot{Q}\neq 0, \tag{5.11b}$$

$$\tau = \frac{\alpha\ t}{L_{ref}}, \tag{5.11c}$$

where $\alpha = k/\rho c_p$, T_0 is the initial condition and T_{ss} is the steady-state solution given by the FE model. In Fig. 5.3(a) we can see that for Bi = 0.1 the thermal gradient within the element is almost negligible, therefore the temperature at coordinates $(L/2;W/2)$ almost perfectly matches the average element temperature. Classic and T-network models provide very similarly accurate solutions. Keeping $\dot{Q} = 0$ and increasing the Biot number to Bi = 2.0, as in Fig. 5.3(b), leads to a less uniform temperature distribution within the element. The T-network manages to provide a

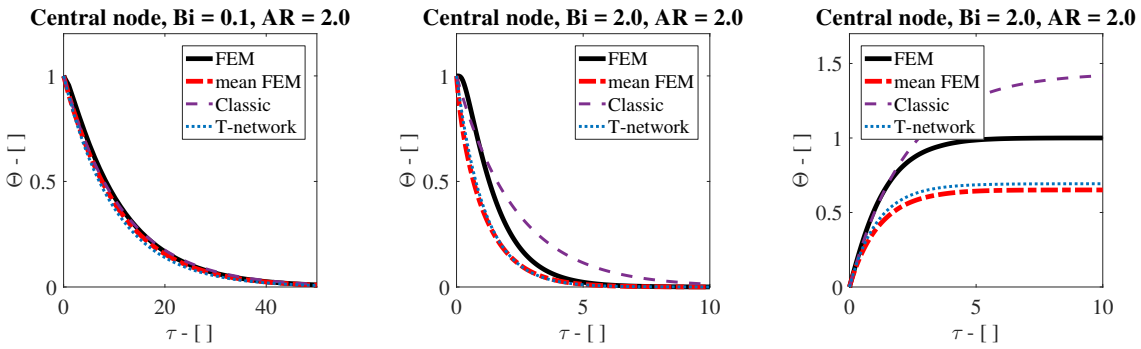

Figure 5.3: Comparing the solution of the thermal problem in Fig. 5.1(a) using the Classic TEC (Fig. 5.1(b)), T-network (Fig. 5.2) and FEM (element central and mean temperature) for the cases of (a) Bi = 0.1 no internal generation, (b) Bi = 2.0 no internal generation and (c) Bi = 2.0 with uniform internal heat generation

quite accurate solution, whereas the Classic approach is not able to follow the mean nor central temperature. Introducing $\dot{Q} \neq 0$ with Bi = 2.0, from Fig. 5.3(c) we can see that the internal gradient is increased and that the T-network again is able to give a better average temperature solution.

As far as the steady-state solutions are concerned, the problems without internal heat generation are trivial as the temperature distribution will uniformly settle at T_∞. For the case of $\dot{Q} \neq 0$, the T-network always gives a better solution compared to the Classic element in terms of disagreement with the FE solution. However, average temperatures does not provide sufficient information for a proper design and control of a machine. Therefore, in the next section we introduce a tool that can help to assess local hotspot temperatures and, accordingly, give a better insight about the temperature distribution within the elements.

5.2 The Distributed Loss and Capacitance element

In this section we introduce a new approach to inject loss and capacitance into the Classic element to improve its accuracy for Bi > 0.1 and $AR \neq 1$. Due to its

characteristics we refer to it as the Distributed Loss and Capacitance (DLC) element.

5.2.1 Steady-state solution

Let us consider a steady-state problem with uniform distributed internal heat generation $\dot{Q}^*$, see Fig. 5.4(a). Gerling and Dajaku [152–154] showed that for a 1D problem with Dirichlet boundary conditions on both sides and internal heat generation, the heat introduced in the central node should be halved in order to match exactly the local steady-state temperature in the centre of the domain. This comes by the fact that the solution of this problem is a quadratic function, according to (5.6), and the heat flux varies linearly according to Fourier's law:

$$\dot{Q}_x = -kA\frac{\partial T}{\partial x}. \tag{5.12}$$

This means that the average heat flowing through each of the two resistors is $\dot{Q}^*/4$, as depicted in Fig. 5.4(b). Since we are using linear resistors, to estimate the exact central temperature of the 1D element the heat introduced in the central node should match the average heat flux flowing along the distance represented by the thermal resistor. For the case of the 1D problem, this corresponds exactly to $\Lambda\dot{Q}$, where $\Lambda = 0.5$. However, this does not apply to 2D problems as for instance the rectangle exposed to convection of Fig. 5.1(a), since the temperature distribution at steady-state is a paraboloid.

Making reference to Fig. 5.5(a), following the approach by Gerling and Dajaku, we should estimate the correct amount of loss to be introduced in the central node of a 2D square geometry by evaluating the average heat flux normal to the dashed cross section along the A-B path. Results from FE simulations show that for this problem the heat flowing in each of the 4 directions is $|\mathbf{\Phi}_{AB}| \approx 0.1\ \dot{Q}$, meaning that the loss ratio Λ to be injected into the model should be equal to $\Lambda = 0.4$. However,

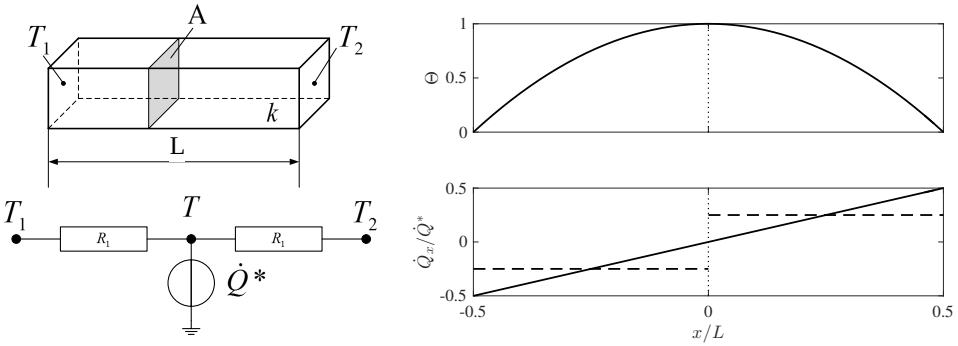

(a) (b)

Figure 5.4: (a) 1D Steady-state thermal problem with uniform internal heat generation and (b) resulting dimensonless temperature Θ and heat flux $\dot{Q}_x/\dot{Q}^*$ distributions

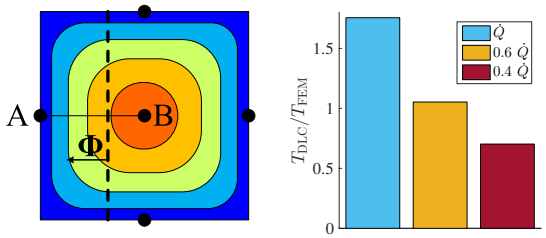

(a) (b)

Figure 5.5: (a) Evaluating the heat flux and (b) assessing the loss to be injected in the central node

this leads to an underestimation of the central temperature due to the fact that we assumed the heat fluxes in the four directions to be independent, which is not the case for a 2D geometry. Using the Matlab built-in `fmincon` function and trying to minimise the cost function $|T_{\mathrm{FEM}} - T_{\mathrm{DLC}}|$, where T_{FEM} and T_{DLC} are both element central temperatures estimated with different methods, we can find that the correct amount of loss ratio Λ to be introduced in the central node should be equal to $\Lambda \approx 0.6$. In other words, to correctly account for 2D effects we should consider that the heat flowing in each of the four directions is equal to $|\mathbf{\Phi}_{AB}| \approx 0.15\ \dot{Q}$. In Fig. 5.5(b) we compare the element central steady-state temperature obtained varying the injected loss in the middle node with the FE solution; the bars represents the ratios of the element's central temperatures $T_{\mathrm{DLC}}/T_{\mathrm{FEM}}$.

We restore the heat balance by injecting the remaining loss, i.e. $0.4\ \dot{Q}$, into the

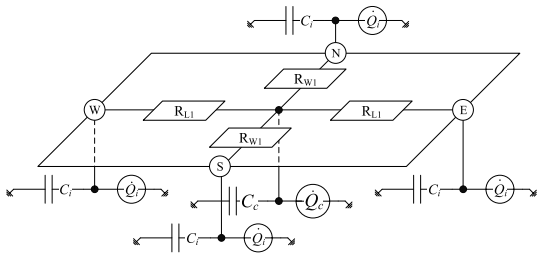

Figure 5.6: Representation of the DLC element: $C_c = 0.6\ C$, $\dot{Q}_c = 0.6\ \dot{Q}$, $C_i = 0.4\ C\frac{A_i}{A_{ext}}$ and $\dot{Q}_i = 0.4\ \dot{Q}\frac{A_i}{A_{ext}}$

boundary nodes. In particular, to account for $AR \neq 1$ the loss introduced into the lateral nodes should be proportional to the exposed surface:

$$\dot{Q}_i = 0.4\ \dot{Q}\ \frac{A_i}{A_{ext}} \tag{5.13}$$

where A_{ext} represents the total external surface.

The proposed configuration with distributed loss and capacitance is sketched in Fig. 5.6. The DLC element has been tested over a range of AR and Bi comparing central node solution with the steady-state temperature in the middle of the domain of the FE based model. We solved the reference problem with internal heat generation and fixed heat transfer coefficient on the lateral boundaries. The results, depicted in Fig. 5.7, show that the DLC element ensures high accuracy, where the accuracy is expressed as relative percentage error $\frac{|T_{\mathrm{DLC}} - T_{\mathrm{FEM}}|}{T_{\mathrm{FEM}}}$. Good accuracy is achieved even at high Bi for geometries with $AR < 2$. Similarly, the T-network has been evaluated in terms of percentage error in the estimation of element's mean temperature $\frac{|T_{\text{T-network}} - T_{\mathrm{FEM,mean}}|}{T_{\mathrm{FEM,mean}}}$.

5.2.2 Transient solution

The main problem related to transient simulations with the available TEC approaches at high Bi with internal heat generation is that they give a poor approximation of the heat transfer at the boundaries. The boundary temperatures are estimated by

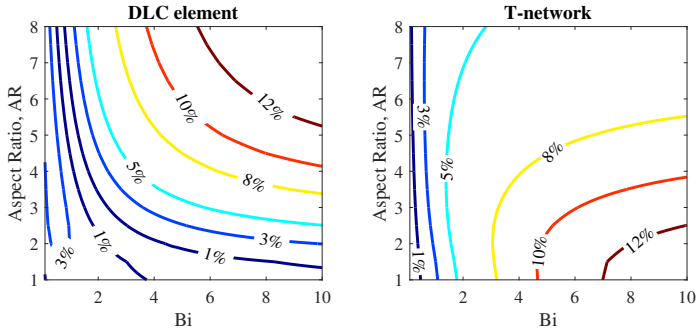

Figure 5.7: Accuracy of the DLC element and the T-network in estimating the central and average steady-state temperature for a thermal problem with internal heat generation and fixed heat transfer coefficient at the boundaries on a rectangular geometry for $AR = 1$ to 8 and $\mathrm{Bi} = 0.1$ to 10

a simple linear interpolation of the two known temperatures, i.e. central or mean and ambient temperatures. This affects the solution in particular at the beginning of a transient, as shown in Fig. 5.8(a). To address the problem we follow the same approach applied before, distributing the capacitance between the 5 available nodes following the same ratios:

$$C_c = 0.6\ C, \tag{5.14a}$$

$$C_i = 0.4\ C \frac{A_i}{A_{ext}} \tag{5.14b}$$

In Fig. 5.8(b) and 5.8(c) transient solutions of a 2D reference thermal problem are presented without and with internal heat generation respectively. The graphs show the improved accuracy of the DLC element compared to the Classic element during the transients and at steady-state for high Bi and $AR \neq 1$.

5.2.3 Axisymmetric hollow cylinder

Similarly to what was achieved for a rectangular geometry, the DLC element can be applied to an axisymmetric hollow cylinder. This is an important geometry for modelling electrical machines as it can represent many parts of components such as

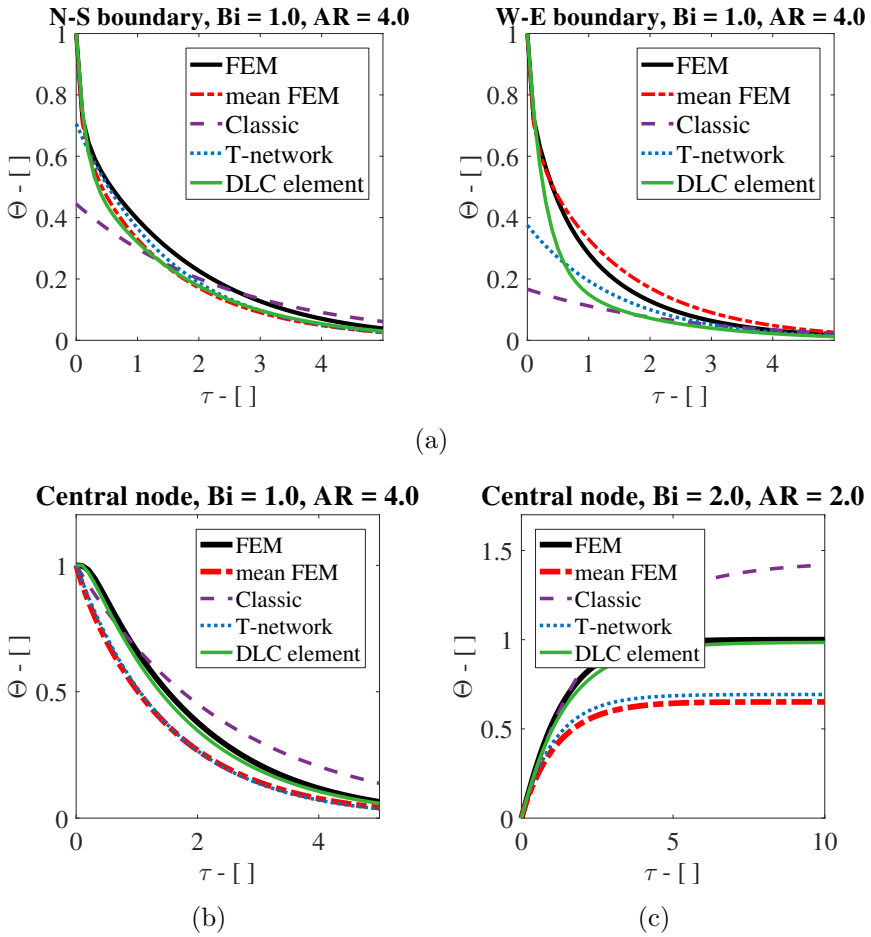

Figure 5.8: Evaluating the DLC element transient solution at (a) boundaries with $AR = 4$ and $\dot{Q} = 0$, (b) central node with $AR = 4$ and $\dot{Q} = 0$ and (c) central node with $AR = 2$ and $\dot{Q} \neq 0$

the stator or the rotor.

The definition of the radial thermal resistances of this geometry comes from the analysis of the 2D steady-state problem with no internal heat generation, as shown in Fig. 5.9. In the figure, r_i and r_o are the inner and outer radii, where we assume a fixed temperature T_i and T_o, respectively. Fourier's law in cylindrical coordinates becomes:

$$\dot{Q}_{cyl} = -kA(r)\frac{dT}{dr}\Big|_r, \tag{5.15}$$

where $\dot{Q}_{cyl}$ is the heat [W] flowing in the radial direction, and $A(r) = 2\pi r$. The thermal resistor is obtained by integrating (5.15) from r_i to r_o

$$\int_{r_i}^{r_i} \frac{\dot{Q}_{cyl}}{2\pi r} dr = -\int_{r_i}^{r_i} k dT, \tag{5.16}$$

which gives

$$\dot{Q}_{cyl} = 2\pi k \frac{T_i - T_o}{\ln(r_o/r_i)} = \frac{T_i - T_o}{R_r}, \tag{5.17}$$

where we introduced the thermal resistance in the radial direction R_r, defined as

$$R_r = \frac{\ln(r_o/r_i)}{2\pi k}. \tag{5.18}$$

Making reference to Fig. 5.10, the resistances for this geometry are defined in the case of the DLC element as:

$$R_{a1} = \frac{L}{2k\pi(r_o^2 - r_i^2)}, \tag{5.19a}$$

$$R_{r1} = \frac{\ln(\frac{r_m}{r_i})}{2k\pi L}, \tag{5.19b}$$

$$R_{r2} = \frac{\ln(\frac{r_o}{r_m})}{2k\pi L}, \tag{5.19c}$$

where $r_m = (r_o + r_i)/2$ represents mean radius, L is the hollow cylinder axial length, and R_{a1} is the thermal resistance along the axial direction. The definition of the

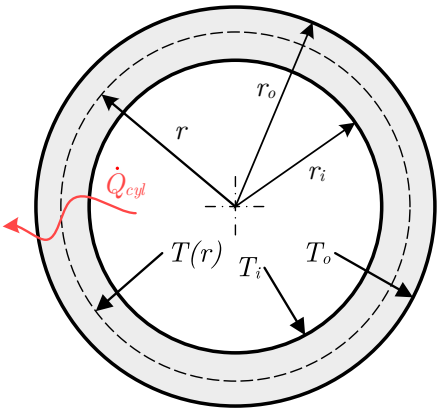

Figure 5.9: Steady-state heat conduction in a 2D hollow cylinder

resistors for the T-network are provided in [147],

$$R_{a1} = \frac{L}{2k\pi(r_o^2 - r_i^2)}, \tag{5.20a}$$

$$R_{a3} = -\frac{L}{6k\pi(r_o^2 - r_i^2)}, \tag{5.20b}$$

for the axial resistors, whereas for the radial resistors we have

$$R_{r1} = \frac{1}{4k\pi L}\left(\frac{2r_o^2 \ln(\frac{r_o}{r_i})}{(r_o^2 - r_i^2)} - 1\right), \tag{5.21a}$$

$$R_{r2} = \frac{1}{4k\pi L}\left(1 - \frac{2r_i^2 \ln(\frac{r_o}{r_i})}{(r_o^2 - r_i^2)}\right), \tag{5.21b}$$

$$R_{r3} = -\frac{1}{8k\pi(r_o^2 - r_i^2)L}\left(r_o^2 + r_i^2 - \frac{4r_o^2 r_i^2 \ln(\frac{r_o}{r_i})}{(r_o^2 - r_i^2)}\right). \tag{5.21c}$$

As for the case of the rectangular geometry, in Fig. 5.11 we compare the accuracy (in terms of percentage error) of these two models with the solution given by the FE model over a range of AR and Bi in estimating the steady-state solutions for the central and average temperatures. The plot is presented with a log scale on the y-axis to consider a complete range of interesting aspect ratios, defined as $AR = L/(r_o - r_i)$; for low AR the geometry represents a hollow disk. We also considered the effect of

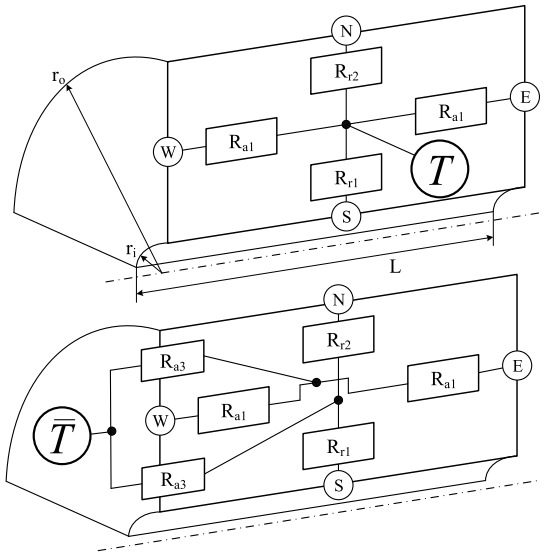

Figure 5.10: Elements for an axisymmeteric hollow cylinder, DLC element at the top and T-network at the bottom

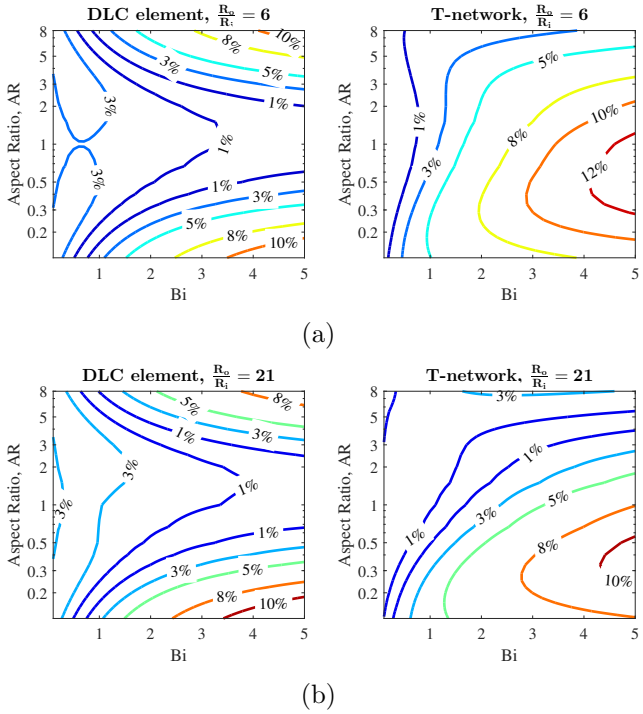

Figure 5.11: Evaluating the DLC element and T-network steady-state solutions for a hollow cylinder and $\dot{Q} \neq 0$ at different ratios $\frac{r_o}{r_i}$ and $0.125 \leq AR \leq 8$

the ratio r_o/r_i since it has a strong effect on the location of the hotspot. For low r_o/r_i the geometry is similar to the rectangular problem previously analysed and, in fact, the accuracy map matches the results shown before. At high r_o/r_i, the hotspot moves towards the symmetry axis and in general the accuracy of the DLC element is still high. It is important to point out the DLC element is again good at dealing with high Bi for geometries with $0.5 < AR < 2$, whereas the T-network seems to be more affected by the ratio r_o/r_i.

5.3 Experimental validation

For the experimental validation of the effectiveness of the DLC discretisation approach, we modelled the motorette presented in the previous chapter (Section 4.2), which we present again in Fig. 5.12(a). To compare the various TEC methods presented in this chapter, three networks are built using the Classic approach, the T-network and DLC elements, as sketched in Fig. 5.12(b), (c), and (d). In the sketches we represent the nodal discretisation of a quarter of the motorette and the connections between them with red dashed lines. Each connection represents a thermal resistor. In Fig. 5.12(c), we diversify the heat transfer along the vertical and horizontal directions with blue and red connections, respectively. It is clear that the Classic element discretisation requires the lowest number of nodes (7 nodes) as compared to the T-network and DLC, which require a higher number of nodes (21 and 26, respectively). The thermal resistances are all calculated using the geometry and the material properties given in Section 4.2. In particular, the effective thermal properties of the winding are obtained with the multiple scale method, as discussed in Chapter 2. Also, in all the three networks a resistance is included to account for the thermal contact resistance between the winding and the laminated core; the magnitude of this resistance is taken from the calibration analysis of Section 4.3.1.

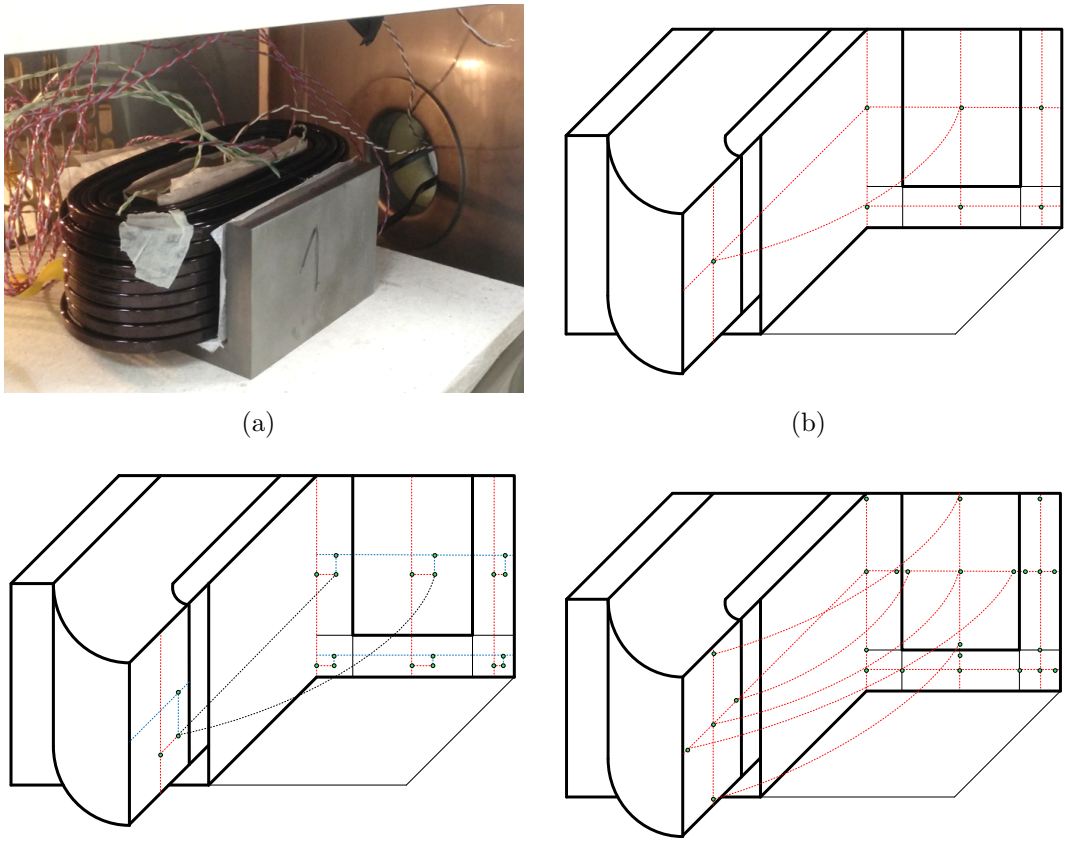

(a) (b) (c) (d)

Figure 5.12: (a) View of the motorette under test and related TECs built using the (b) Classic approach, (c) the T-network, and (d) the DLC elements

The system of m equations (5.3) solving the three TECs can be represented in matrix terms with

$$[\mathrm{C}]\frac{[T]^{\tau}-[T]^{\tau-1}}{\Delta t}=[\mathrm{G}][T]+[\dot{Q}] \tag{5.22}$$

where $[T]$ is the vector of m unknown nodel temperatures, $[\dot{Q}]$ the source vector that includes all the nodal losses and boundary conditions, Δt the fixed time step between two time instants τ, and [C] the $m \times m$ diagonal conductance matrix. [G] is the symmetric conductance matrix ($m \times m$) with $G_{i,i} = -\sum_j G_{i,j}$ and $G_{i,j} = -1/R_{i,j}$; $R_{i,j}$ is the thermal resistance between the ith and jth nodes. At each time step the vector $[\dot{Q}]$ is updated depending on the nodal temperatures, since temperature changes the conductor resistance.

5.3.1 Results with DC

The DC test is considered first, since this is the condition that ensures a uniform distribution of the losses within the winding domain.

As described earlier, for the Classic and T-network approaches the losses are all introduced in the active and end winding central nodes. Also, for the active and end winding regions only one temperature each is provided to describe the thermal behaviour. The DLC, on the other hand, allows us to spread the loss in five nodes in each of the active and end regions. With five nodes for each element (the output temperatures refer to the geometrical location of the nodes), the DLC can obtain information about the temperature distribution.

The results are presented in Fig. 5.13, where the output of the three TECs in the active and end winding are compared to the measurements over three consecutive transient DC tests, with the current at 30, 40, and 50 A. In the figure, the colours refer to the legend given in Fig. 4.17(b).

As depicted in Fig. 5.13(a) and 5.13(b), where the active and end winding tem-

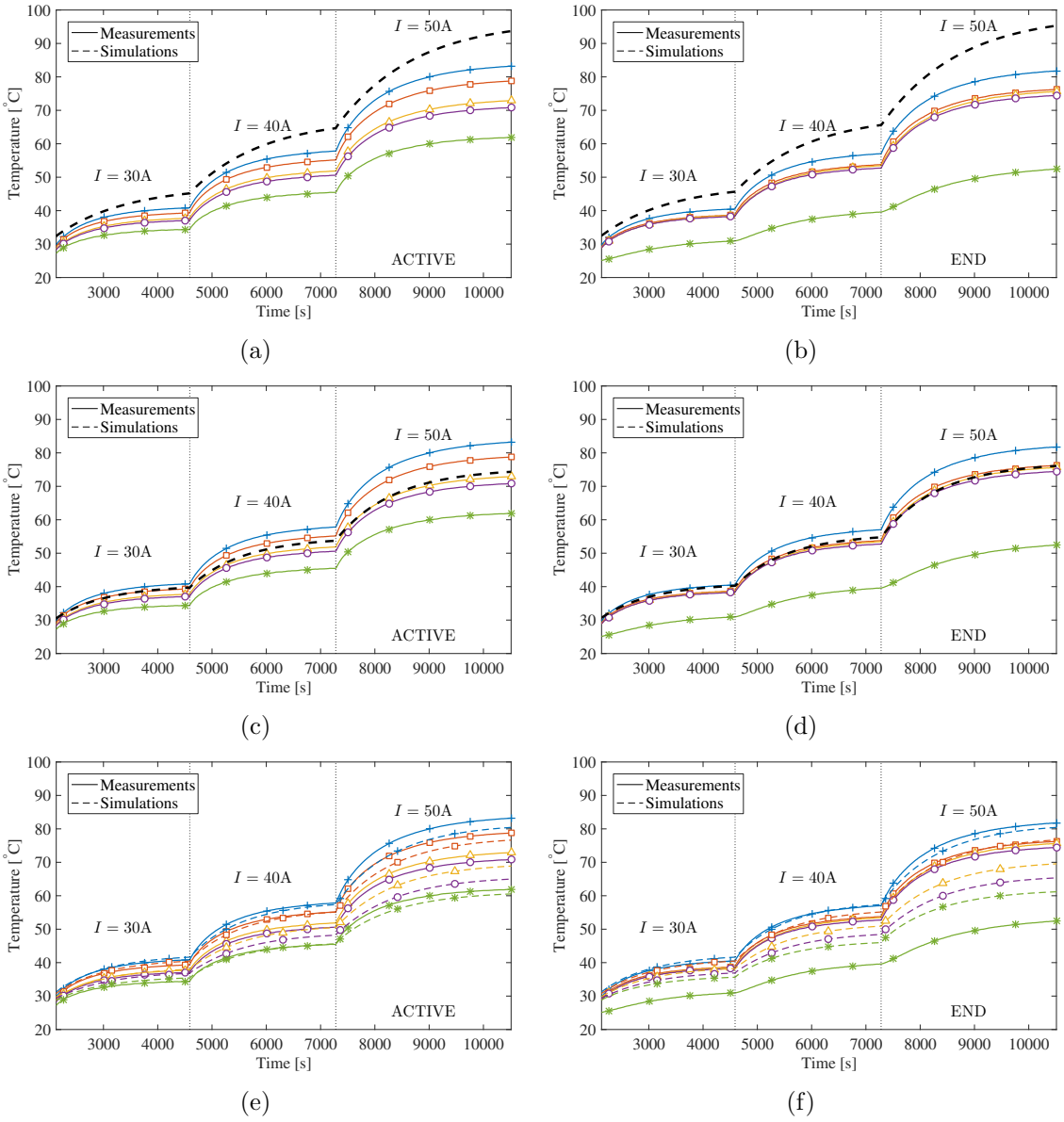

Figure 5.13: Comparison during DC tests between measurement of the motorette of Fig.5.12 and simulation using the Classic approach (a) in active and (b) end region, using the T-network (c) in active and (d) end region and the DLC elements (e) in active and (f) end region

peratures are compared, respectively, the Classic approach fails to assess accurately the local central or the average element temperature. The output winding nodal temperatures overestimate the measured hot-spot, with the error increasing with temperature. This approach is therefore not reliable.

The output of the T-network model, i.e. the mean temperature of the active and end winding, is plotted in Fig. 5.13(c) and 5.13(d), respectively. As expected, the model accurately simulates the average element temperatures over the whole transient. However, with large temperature gradients, the average temperature can be an insufficient information to asses the thermal behaviour of the winding. For example, at steady state with a 50 A DC load, the average temperature in the active winding is $\approx 15\%$ lower than the highest measured temperature.

The DLC solution is presented in Fig. 5.13(e) and 5.13(f), representing the five temperatures in each of the active and end windings. The match with the experimental measurements is good, with the model slightly underestimating the temperatures; the maximum disagreement in the peak temperatures is 5 °C. It is important to highlight that the model is able to provide accurate estimation of the temperature distribution within the elements, with the five estimated temperatures following the same trends as those measured.

5.3.2 Temperature field interpolation

Since our main goal is to locate the hot-spot temperature, we can interpolate the solutions in the five nodes of the DLC element. As an example, we consider the cross-section of the active winding region. To interpolate the five nodal temperatures, we can assume that the temperature distribution in the domain at steady state is represented by a paraboloid, which approximates the 2D heat equation solution with

internal heat generation

$$T = c_1 x^2 + c_2 y^2 + c_3 x + c_4 y + c_5 \tag{5.23}$$

where c_j for $j = 1, ..., 5$ are constants. The values of the c_j constants can be obtained using the output of the DLC element. Practically, this can be achieved by solving the following system of equations

$$[\mathrm{X_{nodes}}][c] = [T_{\mathrm{DLC}}] \tag{5.24}$$

where $[\mathrm{X_{nodes}}]$ is the matrix containing the nodal locations, whose first row related to the node 1 is $[x_1^2\ ,\ y_1^2\ ,\ x_1\ ,\ y_1\ ,\ 1]$, $[c]$ is the vector of the unknown constants, and $[T_{\mathrm{DLC}}]$ is the DLC temperatures vector. Once the system is solved, the temperature field is obtained, as depicted in Fig. 5.14(a); the five nodal temperatures are taken from the end of the transient of Fig. 5.13(e), which refers to a thermal steady-state condition of a problem with internal heat generation. Knowing the temperature distribution, the hot-spot temperature can be identified along with the domain mean. For validation purposes, we compare this solution with the output of the coupled homogenised model presented in Section 4.3.1 related to the same working condition and solved with FEM in Fig. 5.14(b). The temperature field from the two models are in good agreement with an error of about 2 °C in the estimation of the mean and maximum temperatures.

The set of constants should be evaluated for each set of nodal temperatures. However, we must bear in mind that this parabolic interpolation can be applied only if the assumptions hold, i.e. uniform internal heat generation and thermal steady-state. Accordingly, the proposed interpolation technique should provide lower accuracy when applied to transients.

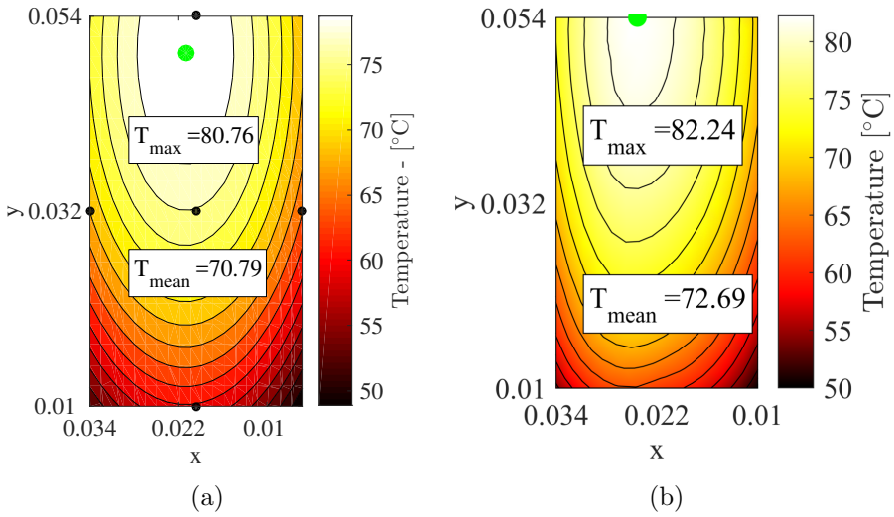

Figure 5.14: (a) Interpolated DLC solution referred to the end of the transient of the DC test and compared with (b) the solution of the homogenised model

5.3.3 Results with AC

We now test the DLC and the other TEC approaches in evaluating the thermal behaviour of the motorette when an AC load is injected at various frequencies. As we have seen in the previous chapter, the particular geometry of the specimen under test causes the losses to concentrate near the slot opening. This means that the assumption of uniformly distributed losses in the winding element no longer holds.

The losses are taken from the estimation provided by the coupled electromagnetic-thermal homogenised model presented in the previous chapter. The model can easily consider the loss contribution of the active winding, end winding, and core, separately. These losses were then injected in the network nodes as previously explained. In particular, the core losses were assumed to be evenly distributed within the E-core cross section. This simplification might not be fundamentally accurate since these are concentrated in neighbourhood of the teeth's tip. However, this should not affect the results since the magnitude of the core losses is considerably lower compared to the winding losses.

Similar to Section 5.3.1, we present the model output in Fig. 5.15, where the active

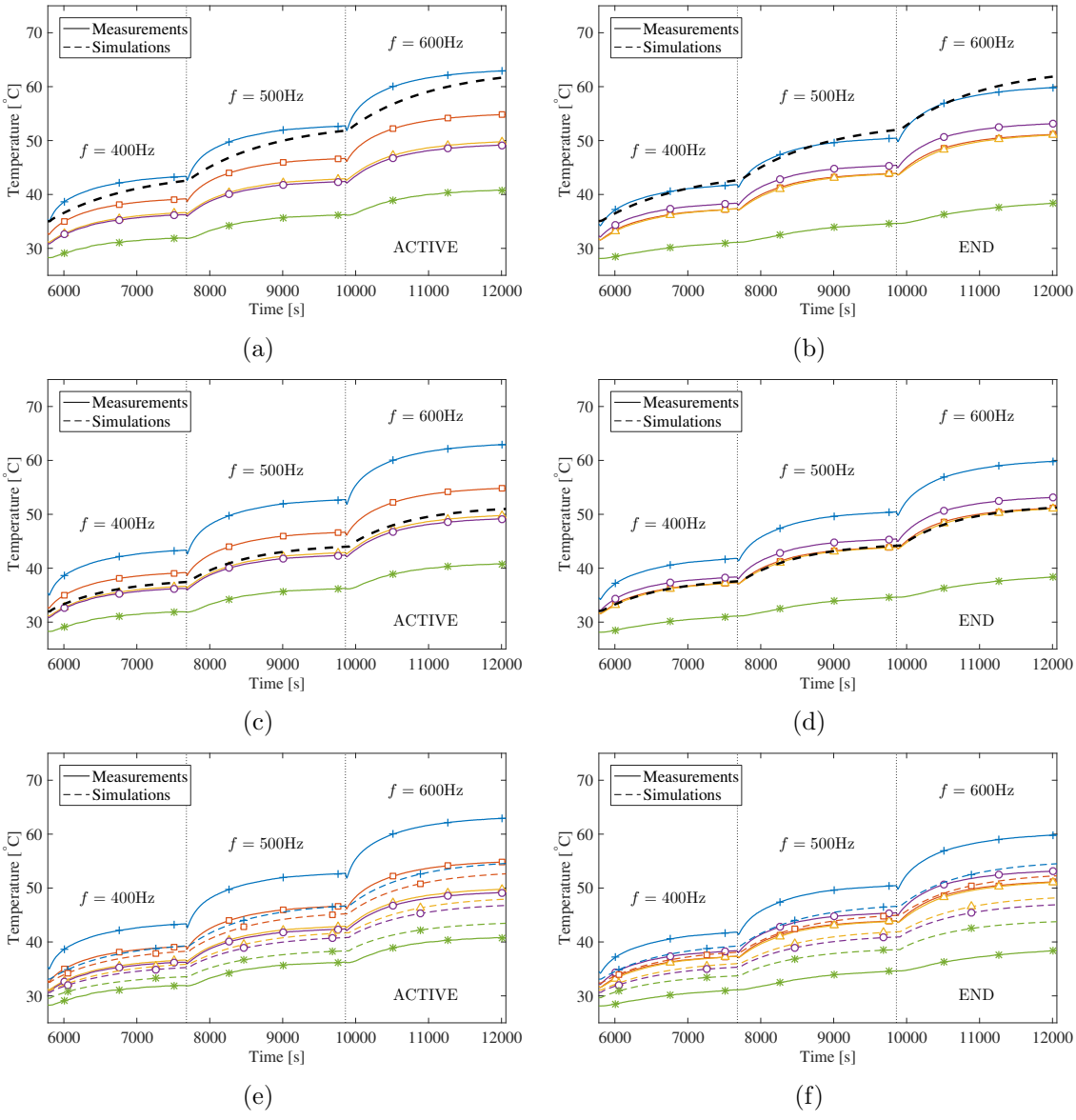

Figure 5.15: Comparison during AC tests between measurement of the motorette of Fig.5.12 and simulation using the Classic approach (a) in active and (b) end region, using the T-network (c) in active and (d) end region and the DLC elements (e) in active, and (f) end region

winding temperatures are plotted on the left, and the end region temperatures on the right. From the figure it seems that the Classic approach provides the better solution in terms of steady state highest temperature. However, this is not a general outcome, as it is related to the specific loss distribution that characterised the motorette under test. Moreover, this simpler model is not able to follow closely the transient thermal behaviour.

The uneven loss distribution inevitably reduces the accuracy of both the T-network and DLC element based models. The model estimations of temperature are below the measured data. Although reduced, the DLC provides an estimate of the large temperature gradient that winding experienced. On the other hand, the T-network averaged winding temperature output is insufficient to asses the winding thermal behaviour as the difference to the highest temperature is $> 10\,^{\circ}\mathrm{C}$.

It has to be said that a proper design of an electromagnetic device, for instance performed with the aid of the coupled model presented in the previous chapter, should limit as much as possible the AC loss contribution. Accordingly, in the final design the assumption of uniform loss distribution should hold. The DLC element based TEC is able to monitor and predict the winding hot-spot temperature with high accuracy.

5.4 Modelling an SPM machine

During this research project we collaborated with the Italian company Brembo Spa, leader in design, development, and production of braking systems. The objective of the collaboration was to model a prototype external-rotor surface-mounted permanent magnet (SPM) machine, shown in Fig. 5.16(a). The machine has been developed for in-wheel direct vehicle propulsion, as presented in Fig. 5.16(b), with the aim of creating a compact and combined electrical in-wheel propulsion-braking system. The machine's ratings are provided in Table 5.1. The application requires that the machine

(a) (b)

Figure 5.16: (a) Analysed external rotor SPM machine (b) mounted on a vehicle

Table 5.1: Nominal rating data of the external-rotor SPM machine

Efficiency	90 %
Power	60 kW
Torque	500 Nm
Speed	1200 rpm

mainly functions at high torque and relatively low speed, which represent challenging working conditions from a thermal point of view. Moreover, the machine geometrical dimensions are strongly limited by the wheel size, making the cooling fundamental to achieve the desired performance, and challenging, since a cooling loop has to reach the four wheels. Thus, the machine is cooled through a water jacket that runs tangentially in four parallel rectangular ducts on the stator side of the machine using a water - glycol 50% mixture.

5.4.1 Model discretisation

To create the thermal model of the SPM, periodicity is assumed and only one stator slot is considered. The nodal discretisation is presented in Fig. 5.17, where only a slice of the machine of half its axial length is depicted. In the figure, the DLC element is denoted by the 5-points network. For the elements with a 3-point discretisation we put half the capacitance in the central node according to [152] and the remaining part is equally split in the other two nodes. When nodes of two adjacent elements overlap, the capacitance and loss contributions are superimposed. The dashed lines

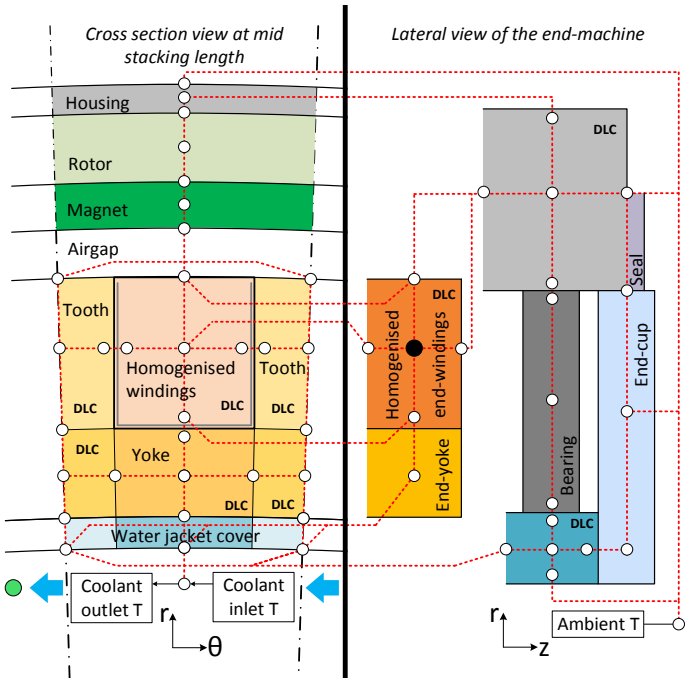

Figure 5.17: SPM nodal discretisation using the DLC element

connecting the nodes represent the allowed heat paths along which resistors are placed. The division of the "Yoke" into 2 sub-elements allows for a more accurate estimation of the heat flux flowing to the water-jacket from the windings and the teeth [148].

The conduction resistors are created based on geometry and material data, which could not be published because of a non-disclosure agreement. As in the motorette, the windings are encapsulated with highly conductive epoxy which significantly improves the thermal performance of the machine.

As discussed in Chapter 1, the airgap heat transfer is modelled according to Bouafia's correlation for slotted rotors [46] and to account for the coolant convective heat transfer the correlation given in [1] for turbulent flow was used. The inlet temperature of the water jacket and coolant flow rate were measured and used as a model input. The tangential temperature rise in the coolant could then be estimated with

$$\Delta T_{wj,s} = \frac{\dot{Q}_{wj}}{\dot{m} c_p}, \tag{5.25}$$

where $\dot{Q}_{wj}$ represents the heat flux removed by the coolant in the slice, whereas $\dot{m}$ and c_p are the coolant mass flow and heat capacity, respectively. Assuming a linear temperature rise in each slot equal to (5.25) calculated in correspondence to the water-jacket inlet section, we can estimate the temperatures of the motor at different tangential positions. In particular, the coolant temperature at the water jacket outlet side is obtained with

$$T_{wj,\text{outlet}} = s\Delta T_{wj,s} + T_{wj,\text{inlet}} \tag{5.26}$$

with s = 120, the total number of stator slots.

5.4.2 DC test results

For the validation of the external-rotor SPM machine TEC network, multiple DC tests were run at Brembo facilities. Two phases of the machine were excited with 140 A DC current, while the coolant flow rate was set to 6, 11, and 16 l/min. During the tests the external rotor was stationary. We assumed a constant heat transfer coefficient towards the ambient of $h_\infty = 25\,\text{W/m}^2\text{K}$ accounting for natural convection with 30 °C room temperature. Before starting any test, the machine was allowed to cool down to coolant temperature (between 18 and 20 °C).

The results are presented in Fig. 5.18. In particular, Fig. 5.18(a) refers to the case with 6 l/min cooling flow rate. The measured winding temperatures refer to the end-winding region at 0° and 270° mechanical degrees following the water flow; 0° corresponds to the water-jacket inlet section. The measurements were taken with NTC thermistor, which were placed in the middle of the end-windings domain and embedded in the encapsulating epoxy. Unfortunately, no other significant measurements were available, mainly because of the complexity of placing sensors inside the very limited available space within the machine. In the network, the measured temperature is related to the end-winding central node, the black filled circle in Fig. 5.17.

To evaluate the end-winding temperature at 270° mechanical degrees, the network is solved again updating the coolant temperature with (5.26), using $s = \frac{270°}{360°}180 = 135$. This initial test also allowed us to identify the thermal contact resistance, which considerably affects the resulting winding temperature, as shown in the previous chapter. The model is able to correctly follow the temperature rise in the end windings during the whole transient, and also gives an accurate understanding of the tangential thermal gradient, which is non negligible for low coolant flow rates. Fig. 5.18(a) also shows the model estimates of average temperature of the coolant at the outlet. The external heat exchanger was not modelled, but instead the measurements were used for the inlet coolant temperature. Accordingly, the transient cannot be perfectly accurate. However, the steady-state temperatures are in good agreement with the measurements, with errors $< 1\,°C$.

In Fig. 5.18(b) and 5.18(c) the results related to the test cases with 11 l/min and 16 l/min cooling flow rate are presented. The model estimations are again in good agreement with the measurements (error $< 3\,°C$). These results confirm the ability of the proposed approach to provide high accuracy independent of the thermal boundary conditions.

5.4.3 On board test results

To further validate the model, its accuracy was tested comparing the results with the machines mounted on the two front wheels of a car, similarly to Fig. 5.16(b). The car was tested on a stationary apparatus where the wheels could spin and produce torque on rollers, with the aim of pushing the machines to their limits. The test results are presented in Fig. 5.19. As depicted, the machine was quickly brought to the rated speed, producing a torque of around 800 Nm due to an injected current of 260 Arms. From the figure we can also appreciate that the machine is able to regenerate energy, as the current is non-null and negative during the braking.

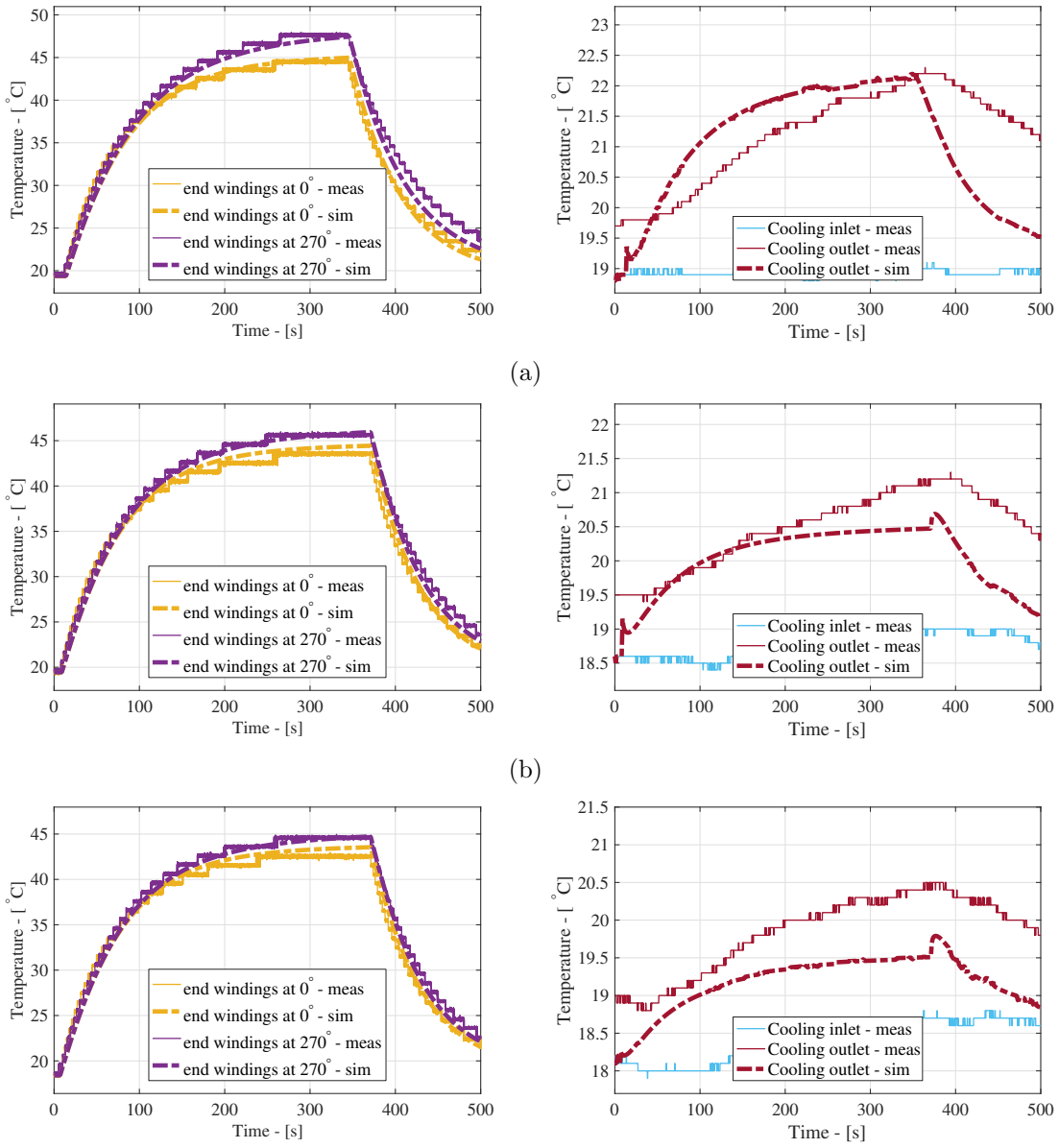

Figure 5.18: Comparison between measured and simulated temperatures of the end windings at 0° and 270° mechanical degrees (left), and coolant outlet temperature (right) for the 140 A DC test with coolant flow at (a) 6 l/min, (b) 11 l/min and (c) 16 l/min

The measured end-winding temperatures are presented in terms of an envelope because the prototype employed both PTC and NTC temperature sensors in the same location, which each gave a slightly different response. Also, in the graph the temperatures of both the right and left wheels are included. The model underestimates the measured data because the machine did not start from rest, since the temperature initial condition was not homogeneous. Accordingly, it was decided to set the initial temperature equal to the inlet coolant temperature. However, model results follow closely the warming trend and the accuracy improves during the transient. Finally, the estimated outlet coolant temperature is compared with the measured data. Here the model provides conservative estimates, but within $< 3\,^{\circ}\mathrm{C}$.

These results are promising but additional validation is required to ensure that the model correctly captures other important temperatures, such as the bearing and magnet temperatures. However, these results confirm that the model is able to track the winding and coolant thermal behaviour.

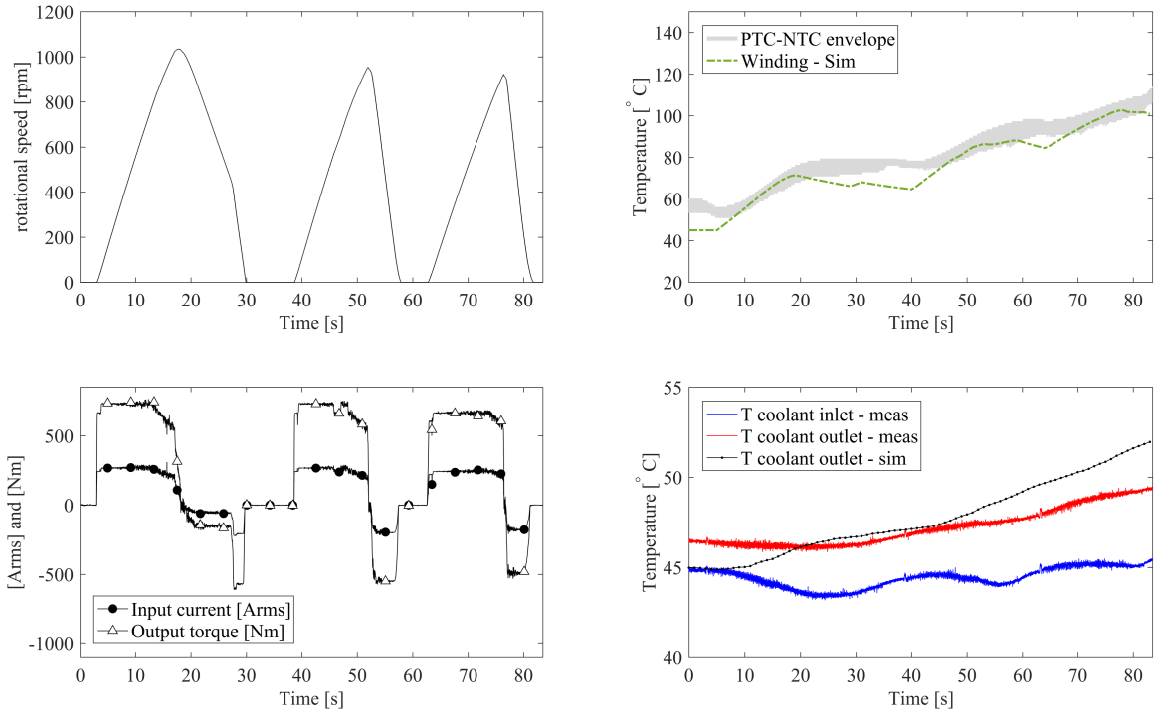

Figure 5.19: Results from the on board test: machine rotational speed (top left), injected current and produced torque (bottom left), comparison between measured and simulated end-winding temperature (top right) and comparison between measured and simulated water-jacket outlet temperature

Chapter 6

Conclusions and future work

In this thesis a number of tools are presented to reduce the order of thermal models to accurately estimate the temperature distribution in an electrical machine, particularly focusing on the winding domain, enabling assessment of the thermal hotspot. These contributions are now summarised and commented on, followed by a discussion of areas where further research is required.

6.1 Conclusions

The contributions of the thesis can be summarised into three major groups: (i) Thermal homogenisation, (ii) Coupled electromagnetic and thermal homogenisation, and (iii) Improved TEC element for thermal modelling.

6.1.1 Thermal homogenisation

In Chapter 2 we showed how to apply the MSM method to obtain the homogenised heat equation in an electrical winding compound. The MSM method provides a systematic and efficient way to estimate the equivalent thermal properties of the homogenised material. The resulting homogenised model is much less computationally

expensive than the original model incorporating the full geometry of the windings, while still capturing the essential microscopic features. The method has been shown to provide an accurate estimation of the equivalent thermal conductivities when compared with numerical values from the full model. Moreover, we proved that including the term in $T^{(1)}$ is sufficient to reconstruct the temperature field to a sufficient level of accuracy.

Although the method assumes a periodic distribution of the wires, the hot spot estimated with the model homogenised through the MSM method is still accurate when compared to random configurations of the conductors. On the other hand, the employment of analytical formulae, such as the HS (2.35) or Wiener (2.4) equations leads to a significant error in the assessment of the hot spot due to an error in the calculation of the effective thermal conductivity. This may lead to a wrong estimation of the remaining parameters related to a full machine thermal model when trying to match parameters to experimental results. This in turn will reduce the reliability of the model against varying loads and cooling conditions even after the calibration.

The experimental validation provided here once more confirms the effectiveness of the method. The only limitation of the method seems to be the modelling of non-infiltrated windings, where no epoxy or varnish are employed. With air as a filling the heat transfer process is fundamentally different and accordingly the MSM, as derived in this chapter, cannot hold. This is confirmed by other experimental measurements carried out in [56]. This allows some room for further research to be carried out.

6.1.2 Coupled electromagnetic and thermal homogenisation

In Chapters 3 and 4 a method was presented to significantly reduce the computational effort for 2D and 3D electromagnetic-thermal coupled FE analysis via homogenisation. Compared to the solution of a fine model, where every single wire is taken into account, the results presented here show that the homogenised model is able to provide

accurate estimations. In particular, the method was shown to be suitable for loss separation (active vs end winding loss contribution) thanks to the reduced model complexity. The method, here applied to a reference stator-winding assembly, can be applied to any electromagnetic device, such as transformers or electrical machines. The numerical results were confirmed by the measurements performed on a suitably built testing sample. In particular, the model was shown to predict very accurately the temperature distribution within the winding (error in the estimation of the peak temperature $< 3\,^{\circ}\mathrm{C}$), either with DC or an AC load, both at steady-state and during the whole transient.

From the results, the following conclusions can be drawn:

1. Temperature effects significantly affect the ratio $R_{\mathrm{AC}}/R_{\mathrm{DC}}$. This confirms that a coupled electromagnetic-thermal analysis, even at design stage, is needed to obtain a more accurate evaluation of the specimen performance.

2. The effect of AC losses, concentrated near the slot opening, increases the temperature gradient within the winding domain. This means that, in such conditions, the winding mean temperature can be a too reductive information to describe the winding thermal behaviour. Indeed precise estimations of the actual thermal field can help provide more reliable predictions of the conductor insulation lifespan.

3. Due to the contribution of AC effects, a significant gradient between end and active winding top temperatures is expected, with the hotspot located in the active region.

As a final remark, compared to the fine model, the homogenised model requires some pre-calculations to obtain the effective material properties. These, however, are not computationally demanding. Moreover, the homogenised model can then be straightforwardly implemented in most commercial or open source FE software

packages. Accordingly, compared to other analytical methods, this approach requires very little bespoke coding.

6.1.3 Improved TEC element for thermal modelling

In Chapter 5 an analysis of the limitations of TEC modelling approaches commonly applied for electrical machine thermal modelling is first given, comparing the Classic element with the T-network. In particular, we highlighted the impact of the Biot number, aspect ratio, and internal heat generation. Each of these factors affects the accuracy of TEC since they introduce non-linear temperature gradients within the elements. A new modelling approach is proposed, based on the Distributed Loss and Capacitance element that improves the accuracy of a TEC. The higher accuracy of the DLC based modelling is checked numerically with simple thermal problems involving a single component with constant thermal boundary conditions. The proposed technique is then tested by creating a thermal model of the specimen introduced in Chapter 4, comparing the estimation of the three main discretisation approaches with measurements. The reduced spatial accuracy of both the classic and T-network was highlighted, as their output consists of only a single temperature. Moreover the classic element provides a very conservative solution, while the T-network is able to correctly estimate the element average temperature. The DLC, on the other hand, improves the spatial accuracy, providing a good insight on the temperature distribution within elements. The inappropriateness of TECs in dealing with high levels of AC losses in the windings, due to loss uneven distribution, was also emphasised. The chapter is concluded by presenting the model of an external-rotor SPM machine for in-wheel vehicle propulsion. The nodal discretisation, based on the DLC approach, provides a good understanding of the temperature distribution in correspondence to a machine slot and at different tangential positions. The discretisation level, around 60 nodes, is reasonably contained and able to run transient simulations in very limited

computational time.

6.2 Future work

This work allowed us to outline a number of possible research paths that can extend the methods presented here to enable the definition of new models useful for machine design and other industrial applications.

6.2.1 Electromagnetic homogenisation applying the MSM

The method employed in Chapters 3 and 4 for the homogenisation of the electromagetic problem (Maxwell's equations (3.1)) is not systematic as, for instance, the multiple scales method (MSM), which was introduced in Chapter 2, since it is not based on a coherent mathematical derivation. In the literature there is no record of the application of MSM to the electrical winding domain, but only on ferromagnetic materials [155–157]. As shown in Chapter 2, the method can not only evaluate the macroscopic field distributions, but can also reconstruct the miscroscopic information. Due to the complexity of (3.1) much work is required to understand how to apply the MSM properly and obtain the expected results.

6.2.2 Coupled electromagnetic-thermal-mechanical homogenisation for winding degradation

Homogenisation techniques applied to electrical machines showed great potential and so far they have not been employed in any commercial software for simulation. Thanks to the reduced computational effort, we believe that these methods will allow for comprehensive multiphysics analyses, coupling not only thermal and electromagnetic problems, but also mechanical. This will add information to assess the stresses the machine has to withstand during operation and predict the noise produced with the

aim of improving machine reliability and vehicle comfort. Accordingly, it is worth investigating how to properly couple these three problems.

Machine reliability is indeed a topic of great concern since, as we mentioned earlier, no model has yet been defined that can assess the winding insulation lifespan as a function of the machine loads. So far, the electrical, thermal and mechanical contributions have been evaluated separately, however, it would be useful to analyse the effect of the combination of these effects. For instance, mechanical stresses are induced in the windings due to the electrical, and thermal excitation. For non infiltrated low voltage windings, the degradation is mainly driven by oxidation and material bond scission promoted by high temperatures [22]. However, since the tendency in electrical machines for vehicle propulsion is to encapsulate the windings with epoxy compounds, the degradation process should be mainly driven by thermal induced stresses, due to the differences in the materials thermal expansion coefficients [23,158]. This phenomenon is intensified with time varying loads, such as driving cycles [159], since they enhance the rate of the mechanical stresses. Accordingly, research is required that could combine experimental and numerical analyses to provide qualitative and quantitative insight on conductor insulation stress and degradation rate for electrical machines employed in vehicle powertrains due to thermal cycling and fatigue, as described in Fig. 6.1.

6.2.3 Thermal contact resistance

Chapter 4 showed how to evaluate the thermal contact resistance and discussed the significance of its effect on the resulting temperature distribution within the winding domain. In [1] one could find some reference values to account for the various contact resistances between the winding and the stator, and between the stator and the housing, as a function of the machine size. The amount of data provided is, however, very little and a more extensive analysis is required. Moreover, important information

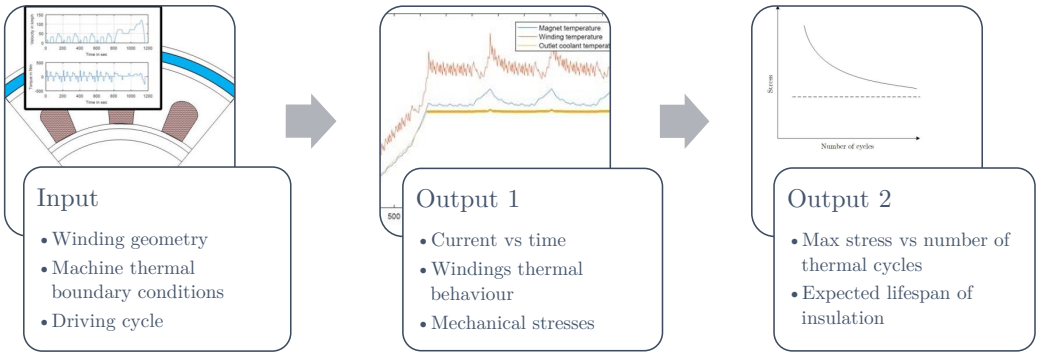

Figure 6.1: Visualisation of the proposed research path

about the actual stator winding assembly are missing. Camilleri [160] showed that usually the range of pressures in electrical machines stator-housing shrink fits is very low, thus limiting the effect of the surface roughness here since the distance between the parts is expected to be relatively large. On the other hand, in [161] a methodology is proposed to measure the thermal impedance between the winding and the stator using experimental measurements. This approach, however, does not allow separation of the thermal conductivity of the winding from the thermal contact resistance effect; it is also strictly dependent on the location of the sensors and does not allow gathering of information about the hot-spot temperature. This, accordingly, does not allow generalisation of the results obtained from the measurements, and reuse the collected data for other machine designs.

A more detailed analysis especially focused on the contact resistance between the winding and the core is needed. Based on the work presented in [162], which focused on the effect of various liner and varnish encapsulation processes, the investigation should evaluate the contact thermal resistance as a function of different variables including wire shape, winding manufacturing procedure, filling ratio, slot shape, epoxy mixtures, etc.. Performing the analysis on a statistically significant number of specimens should result in general conclusions that could allow the estimation of this important parameter without employing complicated formulae (see [75]) and, thus, speed up the design process.

6.2.4 TEC numerical model order reduction

One of the objectives of developing low order thermal models is to include them in the machine control strategy to consider the temperature effect on the machine performance or to avoid reaching the thermal thresholds in an electric vehicle. This means that, in order to respect a certain driver's acceleration request, the controller sends a current that is dependent on the actual temperature condition of the machine (phase resistance and magnet remenance). However, if the temperatures are too high, the torque demand is adjusted (reduced). The methodology presented in Chapter 5 seems suitable for these purposes, as it allows evaluation of the temperature distribution within the elements and, thus, the hotspot, the temperature the ultimately limits the output torque. However, the number of the required system states n (larger than 30) is still large for the computational power of the vehicle embedded hardware; the number of states should be less than 10. This can be achieved employing numerical model order reduction techniques that allow approximation of (5.22) with a system with reduced number of states, without affecting numerical accuracy. In particular, the system (5.22) can be rewritten in the form of a linear-time-invariant (LTI) system

$$[\dot{x}] = [\mathrm{A}(\omega)][x] + [\mathrm{B}][u] \tag{6.1a}$$

$$[y] = [\mathrm{C}][x] \tag{6.1b}$$

where $[x]$ is the vector of states, $[u]$ is input, and $[y]$ is output; $[y]$ corresponds to the machine temperatures we are interested in for the control strategy, e.g. magnet or winding temperature. Also, the matrix $[\mathrm{A}(\omega)]$ is a function of the rotational speed ω, since ω affects the internal convection heat exchange rates. A common method for numerical model order reduction of LTI systems is balanced truncation [163], which entails balancing, i.e. transforming the system in order to obtain the

same controllability and observability characteristics, and truncating the system, i.e. deleting the states that are uncontrollable or unobservable. As discussed in [164], the dependency of [A] on ω makes (6.1) a linear parameter-varying (LPV) system. Therefore, there exists a reduced realisation of (6.1) for each ω. In [164] it is proposed to evaluate the reduced realisations for a limited number of ω^* and then linearly interpolate the parameters of rotational speeds, $[A(\omega^*)]$, to obtain the values at the particular rotational speed $\hat{\omega}$. The results are promising, but the reduction is not sufficient (from 38 to 15 states for the same accuracy level). Additional work is needed to improve the model reduction accuracy for $n < 10$. Also, in [164] the fact that the best performances of the balanced truncation approach are available only for zero (homogeneous) initial conditions was not considered. Therefore, the model should be extended to include inhomogeneous initial conditions, i.e. when the machine is started not from rest and the components are not at the same temperatures.

Publications

1. P. Romanazzi, M. Bruna, and D. A. Howey, "Thermal homogenisation of electrical machine windings applying the multiple-scales method," ASME Journal of Heat Transfer, vol. 139, no. January, 2017.

2. P. Romanazzi, S. Ayat, R. Wrobel, and D. A. Howey, "3D Homogenisation of concentrated windings with rectangular conductors," in International Electric Machines & Drives Conference (IEMDC), 2017.

3. P. Romanazzi, J. Gyselinck, M. Bruna, and D. A. Howey, "Electromagnetic and thermal homogenisation of an electrical machine slot," in International Conference on Electrical Machine (ICEM), 2016.

4. P. Romanazzi, V. Galizzi, F. Carbone, A. Miotto, and D. A. Howey, "Improved thermal equivalent circuit element applied to an external rotor SPM machine," in International Conference on Electrical Machine (ICEM), 2016.

5. P. Romanazzi and D. A. Howey, "Air-Gap Convection in a Switched Reluctance Machine," in Tenth International Conference on Ecological Vehicles and Renewable Energies (EVER), 2015.

6. K. Ramakrishnan, P. Romanazzi, D. Zarko, G. Mastinu, D. A. Howey, and A. Miotto, "Improved Analytical Model of an Outer Rotor Surface Permanent Magnet Machine for Efficiency Calculation with Thermal Effect," SAE International Journal of Alternative Powertrains, vol. 6, no. 1, 2017.

7. N. Fernando, P. Romanazzi, and M. D. Mcculloch, "Degradation of Mechanical Properties of Class-H Winding Insulation," in International Electric Machines & Drives Conference (IEMDC), 2017.

8. F. Chauvicourt, P. Romanazzi, D. Howey, A. Dziechciarz, C. Martis, and C. T. Faria, "Review of Multidisciplinary Homogenization Techniques applied to Electric Machines," in Eleventh International Conference on Ecological Vehicles and Renewable Energies (EVER), 2016.

Bibliography

[1] D. A. Staton, A. Boglietti, and A. Cavagnino, "Solving the More Difficult Aspects of Electric Motor Thermal Analysis in Small and Medium Size Industrial Induction Motors," *IEEE Transactions on Energy Conversion*, vol. 20, pp. 620–628, sep 2005.

[2] "Underwriters Laboratories Standard UL1446:2007, Systems of Insulating Materials – General."

[3] F. P. Incropera, D. P. Dewitt, T. L. Bergman, and A. S. Lavine, *Foundamentals of Heat and Mass Transfer*. John Wiley & Sons, Inc., 2007.

[4] N. Simpson, R. Wrobel, and P. H. Mellor, "A General Arc-Segment Element for Three-Dimensional Thermal Modeling," *IEEE Transactions on Magnetics*, vol. 50, no. 2, pp. 265–268, 2014.

[5] L. M. B. Metz, O.R. Davidson, P.R. Bosch, R. Dave, *Climate change 2007 Mitigation of climate change*. Cambridge University Press, Cambridge, United Kingdom and New York, NY, USA., 2007.

[6] T. Burress and S. Campbell, "Benchmarking EV and HEV power electronics and electric machines," in *IEEE Transportation Electrification Conference and Expo: Components, Systems, and Power Electronics - From Technology to Business and Public Policy (ITEC)*, 2013.

[7] P. Neti, K. Younsi, and M. R. Shah, "A novel high sensitivity differential current transformer for online health monitoring of industrial motor ground-wall insulation," *2013 IEEE Energy Conversion Congress and Exposition, ECCE 2013*, pp. 2493–2499, 2013.

[8] S. Stipetic, M. Kovacic, and D. Zarko, "Optimised design of permanent magnet assisted synchronous reluctance motor series using combined analytical–finite element analysis based approach," *IET Electric Power Applications*, vol. 10, no. 5, pp. 330–338, 2016.

[9] I. Petrov, D. Egorov, J. Link, R. Stern, S. Ruoho, and J. Pyrh??nen, "Hysteresis Losses in Different Types of Permanent Magnets Used in PMSMs," *IEEE Transactions on Industrial Electronics*, vol. 64, no. 3, pp. 2502–2510, 2017.

[10] S. R. Trout, "Material Selection of Permanent Magnets , Considering Thermal Properties Correctly," in *Electric Manufacturing and Coil Winding Conference*, 2001.

[11] B. Slusarek and K. Zakrzewski, "Magnetic properties of permanent magnets for magnetic sensors working in wide range of temperature," *PRZEGLĄD ELEKTROTECHNICZNY (Electrical Review)*, vol. 88, no. 7b, pp. 123–126, 2012.

[12] O. Kudrjavtsev, A. Kilk, T. Vaimann, A. Belahcen, and A. Kallaste, "Implementation of different magnetic materials in outer rotor PM generator," *International Conference on Power Engineering, Energy and Electrical Drives*, pp. 74–78, 2015.

[13] J. D. McFarland, T. M. Jahns, A. M. El-Refaie, and P. B. Reddy, "Effect of magnet properties on power density and flux-weakening performance of high-speed interior permanent magnet synchronous machines," *2014 IEEE Energy Conversion Congress and Exposition, ECCE 2014*, pp. 4218–4225, 2014.

[14] J. D. Widmer, R. Martin, and M. Kimiabeigi, "Electric vehicle tractionmotors without rare earthmagnets," *Sustainable Materials and Technologies*, vol. 3, pp. 7–13, 2015.

[15] R. Wrobel, S. J. Williamson, J. D. Booker, and P. H. Mellor, "Characterising the Performance of Selected Electrical Machine Insulation Systems," in *IEEE Energy Conversion Congress and Exposition, (ECCE)*, pp. 4857–4864, 2015.

[16] A. S. Babel and E. G. Strangas, "Condition-Based Monitoring and Prognostic Health Management of Electric Machine Stator Winding Insulation," in *International Conference on Electrical Machine (ICEM)*, 2014.

[17] D. F. Kavanagh, D. a. Howey, and M. D. McCulloch, "An applied laboratory characterisation approach for electric machine insulation," *9th IEEE International Symposium on Diagnostics for Electric Machines, Power Electronics and Drives (SDEMPED)*, no. c, pp. 391–395, 2013.

[18] M. Sumislawska, K. Gyftakis, D. Kavanagh, M. McCulloch, K. J. Burnham, and D. A. Howey, "The Impact of Thermal Degradation on Electrical Machine Winding Insulation," *IEEE Transactions on Industry Applications*, vol. PP, no. 99, pp. 232–238, 2016.

[19] A. Gandhi, T. Corrigan, and L. Parsa, "Recent advances in modeling and online detection of stator interturn faults in electrical motors," *IEEE Transactions on Industrial Electronics*, vol. 58, no. 5, pp. 1564–1575, 2011.

[20] S. J. Williamson, R. Wrobel, J. D. Booker, J. Yon, and P. H. Mellor, "Effects of Insulation Ageing on the Conductive Heat Transfer from the Winding Body into Machine Periphery / Stator Core Pack," in *8th IET International Conference on Power Electronics, Machines and Drives (PEMD)*, pp. 1–6, 2016.

[21] K. N. Gyftakis, D. F. Kavanagh, M. Sumislawska, D. A. Howey, and M. McCulloch, "Dielectric characteristics of electric vehicle traction motor winding insulation under thermal ageing," *IEEE Transactions on Industry Applications*, vol. 52, no. 2, pp. 313–318, 2016.

[22] N. Fernando, P. Romanazzi, and M. D. McCulloch, "Degradation of Mechanical Properties of Class-H Winding Insulation," in *International Electric Machines & Drives Conference (IEMDC)*, (Miami), 2017.

[23] Z. Huang, A. Reinap, and M. Alaküla, "Degradation and Fatigue of Epoxy Impregnated Traction Motors Due to Thermal and Thermal Induced Mechanical Stress – Part I : Thermal Mechanical Simulation of Single Wire due to Evenly Distributed Temperature," in *8th IET International Conference on Power Electronics, Machines and Drives (PEMD)*, (Glasgow), 2016.

[24] B. Y. V. M. Montsinger, "Loading Transformers By Temperature," *Transactions of the American Institute of Electrical Engineers*, vol. 49, no. 2, pp. 776–790, 1930.

[25] A. Z. Dellil and A. Azzi, "Numerical investigation of the heat transfer in an annulus cylindrical space," *MECHANIKA*, vol. 19, no. 1, pp. 25–32, 2013.

[26] T. W. Dakin, "Electrical insulation deterioration treated as a chemical rate phenomenon," *Transactions of the American Institute of Electrical Engineers*, vol. 67, no. 1, pp. 113 – 122, 1948.

[27] Z. Huang, F. J. Márquez-Fernández, Y. Loayza, A. Reinap, and M. Alaküla, "Dynamic Thermal Modeling and Application of Electrical Machine in Hybrid Drives," in *International Conference on Electrical Machines (ICEM)*, pp. 2158–2164, 2014.

[28] P. J. Tavner, "Review of condition monitoring of rotating electrical machines," *IET Electric Power Applications*, vol. 2, no. 4, pp. 215–247, 2008.

[29] A. Boglietti, A. Cavagnino, M. Parvis, and A. Vallan, "Evaluation of Radiation Thermal Resistances in Industrial Motors," *IEEE Transactions on Industry Applications*, vol. 42, no. 3, pp. 688–693, 2006.

[30] A. L. Rodríguez, D. J. Gómez, and I. Villar, "New Analytical Method for PMSM Magnet Losses Estimation based on Fourier Series," in *International Conference on Electrical Machine, ICEM*, (Berlin), pp. 1314–1320, 2014.

[31] F. J. Márquez-Fernández, A. Reinap, Z. Huang, and M. Alaküla, "Dynamic Evaluation of the Overloading Potential of a Convection Cooled Permanent Magnet Synchronous Motor," in *International Electric Machines & Drives Conference (IEMDC)*, pp. 13–18, 2011.

[32] K. Ramakrishnan, P. Romanazzi, D. Zarko, G. Mastinu, D. A. Howey, and A. Miotto, "Improved Analytical Model of an Outer Rotor Surface Permanent Magnet Machine for Efficiency Calculation with Thermal Effect," *SAE International Journal of Alternative Powertrains*, vol. 6, no. 1, 2017.

[33] D. Zarko, *A Systematic Approach To Optimized Design of Permanent Magnet With Reduced Torque Pulsations*. PhD thesis, UNIVERSITY OF WISCONSIN–MADISON, 2004.

[34] S. H. Han, T. M. Jahns, and Z. Q. Zhu, "Analysis of rotor core eddy-current losses in interior permanent-magnet synchronous machines," *IEEE Transactions on Industry Applications*, vol. 46, no. 1, pp. 196–205, 2010.

[35] A. C. Malloy, R. F. Martinez-botas, and M. Lamp, "Measurement of Magnet Losses in a Surface Mounted Permanent Magnet Synchronous Machine," *IEEE Transactions on Energy Conversion*, vol. 30, no. 1, pp. 323–330, 2015.

[36] C. Mi, G. R. Slemon, and R. Bonert, "Modeling of Iron Losses of Permanent-Magnet Synchronous Motors," *IEEE Transactions on Industry Applications*, vol. 39, no. 3, pp. 734–742, 2003.

[37] M. Nakano, H. Kometani, and M. Kawamura, "A study on Eddy-current losses in rotors of surface permanent-magnet synchronous machines," *IEEE Transactions on Industry Applications*, vol. 42, no. 2, pp. 429–435, 2006.

[38] M. Kamiya, Y. Kawase, T. Kosaka, and N. Matsui, "Temperature distribution analysis of permanent magnet in interior permanent magnet synchronous motor considering pwm carrier harmonics," in *International Conference on Electrical Machine Electrical Machines and Systems (ICEMS)*, pp. 2023–2027, 2007.

[39] C. Micallef, S. J. Pickering, K. a. Simmons, and K. J. Bradley, "Improved cooling in the end region of a strip-wound totally enclosed fan-cooled induction electric machine," *IEEE Transactions on Industrial Electronics*, vol. 55, no. 10, pp. 3517–3524, 2008.

[40] A. Boglietti, A. Cavagnino, and D. A. Staton, "End Space Heat Transfer Coefficient Determination for Different Induction Motor Enclosure Types," *IEEE Transactions on Industry Applications*, vol. 45, no. 3, pp. 929 – 937, 2009.

[41] M. Hettegger, B. Streibl, O. Bíró, and H. Neudorfer, "Identifying the heat transfer coefficients on the end-windings of an electrical machine by measurements and simulations," in *International Conference on Electrical Machine (ICEM)*, pp. 4–8, 2010.

[42] M. Hettegger, B. Streibl, O. Bíró, and H. Neudorfer, "Measurements and Simulations of the Convective Heat Transfer Coefficients on the End Windings of an Electrical Machine," *IEEE Transactions on Industrial Electronics*, vol. 59, no. 5, pp. 2299–2308, 2012.

[43] G. Gilson, S. J. Pickering, D. B. Hann, and C. Gerada, "Analysis of the end winding heat transfer variation with altitude in electric motors," *IECON Proceedings (Industrial Electronics Conference)*, pp. 2545–2550, 2009.

[44] D. A. Staton and A. Cavagnino, "Convection Heat Transfer and Flow Calculations Suitable for Electric Machines Thermal Models," *IEEE Transactions on Industrial Electronics*, vol. 55, pp. 3509–3516, oct 2008.

[45] G. Taylor, "Stability of a Viscous Liquid contained between Two Rotating Cylinder," *Philosophical Transactions Society of the Royal Society of London.*, vol. 223, no. 1923, pp. 289–343, 1923.

[46] M. Bouafia, Y. Bertin, and J. B. Saulnier, "Analyse experimentale des transferts de chaleur en espace annulaire etroit et rainure avec cylindre interieur tournant," *International Journal of Heat and Mass Transfer*, vol. 41, no. 10, pp. 1279–1291, 1998.

[47] K. Becker and J. Kaye, "The influence of a radial temperature gradient on the instability of a fluid flow in an annulus with an inner rotating cylinder," *Transactions of the ASME*, vol. 84, no. 2, pp. 106–110, 1962.

[48] P. Romanazzi and D. A. Howey, "Air-Gap Convection in a Switched Reluctance Machine," in *Tenth International Conference on Ecological Vehicles and Renewable Energies (EVER)*, (Monaco), 2015.

[49] T. Hayase, J. Humphrey, and R. Greif, "Numerical calculation of convective heat transfer between rotating coaxial cylinders with periodically embedded cavities," *Journal of Heat transfer*, vol. 114, no. 3, pp. 589–597, 1992.

[50] J. Hwang, D. Lin, and L. Chen, "Heat transfer between rotating cylinders," in *Proceedings of the 3rd International Symposium on Transport Phenomena and Dynamics of Rotating Machinery*, (Honolulu), pp. 143–155, 1990.

[51] U. Sanandres, G. Almandoz, J. Poza, G. Ugalde, and A. J. Escalada, "Radial Fan Simulations by Computational Fluid Dynamics and Experimental Validation," in *International Conference on Electrical Machine (ICEM)*, pp. 2179–2185, 2014.

[52] B. Sarlioglu, C. T. Morris, D. Han, and S. Li, "Driving Toward Accessibility," *IEEE Industry Applications Magazine*, vol. 23, no. 1, pp. 14–25, 2017.

[53] S. S. Borges, C. A. Cezario, and T. T. Kunz, "Design of water cooled electric motors using CFD and thermography techniques," *International Conference on Electrical Machines (ICEM)*, pp. 1–6, sep 2008.

[54] N. Simpson, R. Wrobel, and P. H. Mellor, "Estimation of Equivalent Thermal Parameters of Impregnated Electrical Windings," *IEEE Transactions on Industry Applications*, vol. 49, no. 6, pp. 2505–2515, 2013.

[55] S. Nategh, A. Krings, O. Wallmark, and M. Leksell, "Evaluation of impregnation materials for thermal management of liquid-cooled electric machines," *IEEE Transactions on Industrial Electronics*, vol. 61, no. 11, pp. 5956–5965, 2014.

[56] L. Siesing, A. Reinap, and M. Andersson, "Thermal properties on high fill factor electrical windings : Infiltrated vs non infiltrated," in *International Conference on Electrical Machine (ICEM)*, (Berlin), pp. 2218–2223, 2014.

[57] M. Polikarpova, P. Lindh, C. Gerada, M. Rilla, V. Naumanen, and J. Pyrhönen, "Thermal effects of stator potting in an axial-flux permanent magnet synchronous generator," *Applied Thermal Engineering*, vol. 75, pp. 421–429, 2015.

[58] A. A. Wereszczak, J. E. Cousineau, K. Bennion, H. Wang, R. H. Wiles, T. B. Burress, and T. Wu, "Anisotropic Thermal Response of Packed Copper Wire," *Journal of Thermal Science and Engineering Applications*, vol. In press, 2017.

[59] R. Camilleri and M. McCulloch, "Investigation of an Integrated Evaporative Cooling Mechanism for an Outer-Rotor Permanent Magnet Machine," *Heat Transfer Engineering*, vol. 7632, no. March, pp. 00–00, 2014.

[60] A. La Rocca, Z. Xu, P. Arumugam, S. J. Pickering, C. N. Eastwick, C. Gerada, and S. Bozhko, "Thermal Management of a High Speed Permanent Magnet Machine for an Aeroengine," in *International Conference on Electrical Machine (ICEM)*, pp. 2734–2739, 2016.

[61] S. A. Semidey and J. R. Mayor, "Experimentation of an electric machine technology demonstrator incorporating direct winding heat exchangers," *IEEE Transactions on Industrial Electronics*, vol. 61, no. 10, pp. 5771–5778, 2014.

[62] F. J. Marquez-Fernandez, J. H. J. Potgieter, A. G. Fraser, and M. D. McCulloch, "Experimental validation of a thermal model for high speed switched reluctance machines for traction applications," in *International Conference on Electrical Machine (ICEM)*, pp. 2713–2719, 2016.

[63] L. D. Marlino, "Report on Toyota Prius motor thermal management," tech. rep., Oak Ridge National Laboratory, 2005.

[64] K. Bennion and G. Moreno, "Convective hear transfer coefficients of automatic transmission fluid jets with implications for electric machine thermal management," in *ASME International Technical Conference and Exhibition on Packaging and Integration of Electronic and Photonic Microsystems (InterPACK2015)*, (San Francisco), pp. 1–9, 2015.

[65] M. R. Guechi and P. Baucour, "On the numerical and experimental study of spray cooling," *Journal of Computational Multiphase Flows*, vol. 5, no. 4, pp. 239–249, 2013.

[66] G. E. Luke, "The Cooling of Electric Machines," *Transactions of the American Institute of Electrical Engineers*, vol. XLII, pp. 636–652, 1923.

[67] G. E. Luke, "Surface Heat Transfer in Electric Machines with Forced Air Flow," *Transactions of the American Institute of Electrical Engineers*, vol. XLV, pp. 1070–1078, 1926.

[68] D. B. Hoseason, "The cooling of electrical machines," *Journal of the Institution of Electrical Engineers*, vol. 69, no. 409, pp. 121–143, 1931.

[69] T. J. E. Miller, *Switched reluctance motors and their control*. Magma Physics, Oxford University Press, 1993.

[70] J. Al-Tayie and P. Acarnley, "Estimation of speed, stator temperature and rotor temperature in cage induction motor drive using the extended Kalman filter algorithm," *IEE Proceedings - Electric Power Applications*, vol. 144, p. 301, 1997.

[71] G. Demetriades, H. de la Parra, E. Andersson, and H. Olsson, "A Real-Time Thermal Model of a Permanent-Magnet Synchronous Motor," *IEEE Transactions on Power Electronics*, vol. 25, no. 2, pp. 463–474, 2010.

[72] C. Kral, A. Haumer, and S. B. Lee, "A Practical Thermal Model for the Estimation of Permanent Magnet and Stator Winding Temperatures," *IEEE Transactions on Power Electronics*, vol. 29, no. 1, pp. 455–464, 2014.

[73] C. H. Lim, *Thermal Modelling of the Ventilation and Cooling inside Axial Flux Permanent Magnet Generators*. PhD thesis, Durham University, 2010.

[74] T. Thomas and S. Probert, "Thermal contact resistance: The directional effect and other problems," *International Journal of Heat and Mass Transfer*, vol. 13, pp. 789–807, 1970.

[75] M. M. Yovanovich, "Four decades of research on thermal contact, gap, and joint resistance in microelectronics," *IEEE Transactions on Components and Packaging Technologies*, vol. 28, no. 2, pp. 182–206, 2005.

[76] R. Wrobel, P. H. Mellor, and D. Holliday, "Thermal modeling of a segmented stator winding design," *IEEE Transactions on Industry Applications*, vol. 47, no. 5, pp. 2023–2030, 2011.

[77] A. Boglietti, A. Cavagnino, M. Lazzari, and M. Pastorelli, "Predicting iron losses in soft magnetic materials with arbitrary voltage supply: An engineering approach," *IEEE Transactions on Magnetics*, vol. 39, no. 2, pp. 981–989, 2003.

[78] J. Hey, A. Malloy, M. Lamperth, and E. Road, "Experimentally Determined Thermal Parameters of an Energy Conversion Device Using a Constraint Least Square Parameter Estimation Method Coupled With an Analytical Thermal Model," in *International heat transfer conference 15 (IHTC-15)*, (Kyoto), pp. 1–15, 2014.

[79] C. Schlegel, A. Hösl, and S. Diel, "Detailed Loss Modelling of Vehicle Gearboxes," in *Proceedings 7th Modelica Conference*, pp. 434–443, 2009.

[80] J. Goss, D. Staton, R. Wrobel, and P. Mellor, "Brushless AC interior-permanent magnet motor design: Comparison of slot/pole combinations and distributed vs. concentrated windings," *IEEE Energy Conversion Congress and Exposition, (ECCE)*, pp. 1213–1219, 2013.

[81] J. E. Vkzncik, "Prediction of windage power loss in alternators," tech. rep., Nasa, Lewis Research Center, Cleveland, Ohio, 1968.

[82] J. Saari, *Thermal Analysis of High-speed Induction Machines*. PhD thesis, Acta Polytechnica Scandinavica, 1998.

[83] Y. Marchesse, C. Changenet, F. Ville, and P. Velex, "Investigations on CFD Simulations for Predicting Windage Power Losses in Spur Gears," *Journal of Mechanical Design*, vol. 133, no. July, p. 024501, 2011.

[84] P. Romanazzi, M. Bruna, and D. A. Howey, "Thermal homogenisation of electrical machine windings applying the multiple-scales method," *ASME Journal of Heat transfer*, vol. 139, no. January, 2017.

[85] P. Romanazzi, J. Gyselinck, M. Bruna, and D. A. Howey, "Electromagnetic and thermal homogenisation of an electrical machine slot," in *International Conference on Electrical Machine (ICEM)*, 2016.

[86] P. Romanazzi, S. Ayat, R. Wrobel, and D. A. Howey, "3D Homogenisation of concentrated windings with rectangular conductors," in *International Electric Machines & Drives Conference (IEMDC)*, (Miami), 2017.

[87] P. Romanazzi, V. Galizzi, F. Carbone, A. Miotto, and D. A. Howey, "Improved thermal equivalent circuit element applied to an external rotor SPM machine," in *International Conference on Electrical Machine (ICEM)*, (Lausanne), 2016.

[88] S. Ayat, R. Wrobel, J. Goss, and D. Drury, "Estimation of Equivalent Thermal Conductivity for Impregnated Electrical Windings Formed from Profiled Rectangular Conductors," in *8th IET Intlernational Conference on Power Electronics, Machines and Drives (PEMD)*, pp. 1–6, 2016.

[89] S. Nategh, O. Wallmark, M. Leksell, and S. Zhao, "Thermal analysis of a PMaSRM using partial FEA and lumped parameter modeling," *IEEE Transactions on Energy Conversion*, vol. 27, no. 2, pp. 477–488, 2012.

[90] F. Chauvicourt, P. Romanazzi, D. Howey, A. Dziechciarz, C. Martis, and C. T. Faria, "Review of Multidisciplinary Homogenization Techniques applied to Electric Machines," in *Eleventh International Conference on Ecological Vehicles and Renewable Energies (EVER)*, (Monaco), 2016.

[91] E. Sanchez-Palencia, *Non-homogeneous media and vibration theory*. Springer-Verlag, 1980.

[92] R. Wrobel and P. H. Mellor, "A General Cuboidal Element for Three-Dimensional Thermal Modelling," *IEEE Transactions on Magnetics*, vol. 46, no. 8, pp. 3197–3200, 2010.

[93] R. Wrobel, A. Mlot, and P. H. Mellor, "Contribution of End-Winding Proximity Losses to Temperature Variation in Electromagnetic Devices," *IEEE Transactions on Industrial Electronics*, vol. 59, no. 2, pp. 848–857, 2012.

[94] J. L. Baker, R. Wrobel, D. Drury, and P. H. Mellor, "A methodology for predicting the thermal behaviour of modular-wound electrical machines," in *Energy Conversion Congress and Exposition (ECCE)*, pp. 5176–5183, 2014.

[95] L. Idoughi, X. Mininger, F. Bouillault, L. Bernard, and E. Hoang, "Thermal Model With Winding Homogenization and FIT Discretization for Stator Slot," *IEEE Transactions on Magnetics*, vol. 47, no. 12, pp. 4822–4826, 2011.

[96] M. Galea, C. Gerada, T. Raminosoa, and P. Wheeler, "A Thermal Improvement Technique for the Phase Windings of Electrical Machines," *IEEE Transactions on Industry Applications*, vol. 48, pp. 79–87, jan 2012.

[97] O. H. Wiener, *Die theorie des mischkörpers für das feld der stationären strömung. 1. abhandlung: Die mittelwertsätze für kraft, polarisation und energie*. BG Teubner, 1912.

[98] Z. Hashin and S. Shtrikman, "A variational approach to the theory of the elastic behaviour of multiphase materials," *Journal of the Mechanics and Physics of Solids*, vol. 11, no. 2, pp. 127–140, 1963.

[99] H. Kanzaki, K. Sato, and M. Kumagai, "A Study of an Estimation Method for Predicting the Equivalent Thermal Conductivity of an Electric Coil," *Heat transfer Japanese research*, 1992.

[100] A. Bensoussan, J.-L. Lions, and G. Papanicolaou, *Asymptotic analysis for periodic structures*. North-Holland, 1978.

[101] C. C. Mei and B. Vernescu, *Homogenization methods for multiscale mechanics*. World scientific, 2010.

[102] Q. Yu and J. Fish, "Multiscale asymptotic homogenization for multiphysics problems with multiple spatial and temporal scales: A coupled thermo-viscoelastic example problem," *International Journal of Solids and Structures*, vol. 39, pp. 6429–6452, 2002.

[103] Y. Asakuma and T. Yamamoto, "Effective thermal conductivity of porous materials and composites as a function of fundamental structural parameters," *Computer Assisted Methods in Engineering and Science*, vol. 20, pp. 89–98, 2013.

[104] J. Hales, M. Tonks, K. Chockalingam, D. Perez, S. Novascone, B. Spencer, and R. Williamson, "Asymptotic expansion homogenization for multiscale nuclear fuel analysis," *Computational Materials Science*, vol. 99, pp. 290–297, 2015.

[105] J. White, "Analysis of Heat Conduction in a Heterogeneous Material by a Multiple-Scale Averaging Method," *Journal of Heat Transfer*, vol. 137, no. 7, p. 071301, 2015.

[106] J. Pinho-da Cruz, J. A. Oliveira, and F. Teixeira-Dias, "Asymptotic homogenisation in linear elasticity. Part I: Mathematical formulation and finite element modelling," *Computational Materials Science*, vol. 45, no. 4, pp. 1073–1080, 2009.

[107] J. A. Oliveira, J. Pinho-da Cruz, and F. Teixeira-Dias, "Asymptotic homogenisation in linear elasticity. Part II: Finite element procedures and multiscale applications," *Computational Materials Science*, vol. 45, no. 4, pp. 1081–1096, 2009.

[108] B. Barroqueiro, J. Dias-de Oliveira, J. Pinho-da Cruz, and A. Andrade-Campos, "Practical implementation of asymptotic expansion homogenisation in thermoelasticity using a commercial simulation software," *Composite Structures*, vol. 141, pp. 117–131, 2016.

[109] M. Bruna and S. J. Chapman, "Diffusion in spatially varying porous media," *SIAM Journal on Applied Mathematics*, vol. 37, no. 2, pp. 215–238, 2015.

[110] D. Cioranescu and J. S. J. Paulin, *Homogenization of reticulated structures*. Springer Science & Business Media, 2012.

[111] H. Jóhannesson and B. Halle, "Solvent diffusion in ordered macrofluids: A stochastic simulation study of the obstruction effect," *Journal of Chemical Physics*, vol. 104, no. 17, pp. 6807–6817, 1996.

[112] L. N. Trefethen, *Spectral Methods in MATLAB*. Siam, 2000.

[113] W. K. Hastings, "Monte Carlo sampling methods using Markov chains and their applications," *Biometrika*, vol. 57, no. 1, pp. 97–109, 1970.

[114] H. Hamalainen, J. Pyrhonen, J. Nerg, and J. Talvitie, "AC Resistance factor of litz-wire windings used in low-voltage high-power generators," *IEEE Transactions on Industrial Electronics*, vol. 61, no. 2, pp. 693–700, 2014.

[115] S. Iwasaki, R. P. Deodhar, Y. Liu, A. Pride, Z. Q. Zhu, and J. J. Bremner, "Influence of PWM on the proximity loss in permanent-magnet brushless AC machines," *IEEE Transactions on Industry Applications*, vol. 45, no. 4, pp. 1359–1367, 2009.

[116] A. D. Podoltsev, I. Kucheryavaya, and B. Lebedev, "Analysis of effective resistance and eddy-current losses in multiturn winding of high-frequency magnetic components," *IEEE Transactions on Magnetics*, vol. 39, no. 1, pp. 539–548, 2003.

[117] P. H. Mellor, R. Wrobel, and N. McNeill, "Investigation of proximity losses in a high speed brushless permanent magnet motor," *Conference Record - IAS Annual Meeting (IEEE Industry Applications Society)*, vol. 3, no. c, pp. 1514–1518, 2006.

[118] R. Wrobel, D. Staton, R. Lock, J. Booker, and D. Drury, "Winding design for minimum power loss and low-cost manufacture in application to fixed-speed PM generator," *IEEE Transactions on Industry Applications*, vol. 51, no. 5, pp. 3773 – 3782, 2015.

[119] J. A. Ferreira, "Analytical computation of AC resistance of round and rectangular litz wire windings," *IEE Proceedings B Electric Power Applications*, vol. 139, no. 1, p. 21, 1992.

[120] D. A. Gonzalez and D. M. Saban, "Study of the copper losses in a high-speed permanent-magnet machine with form-wound windings," *IEEE Transactions on Industrial Electronics*, vol. 61, no. 6, pp. 3038–3045, 2014.

[121] M. El Feddi, Z. Ren, A. Razek, and A. Bossavit, "Hogenization Technique for Maxwell Equations in Periodic Structures," *IEEE Transactions on Magnetics*, vol. 33, no. 2, pp. 1382–1385, 1997.

[122] G. Meunier, V. Charmoille, C. Guérin, P. Labie, and Y. Maréchal, "Homogenization for periodical electromagnetic structure: Which formulation?," *IEEE Transactions on Magnetics*, vol. 46, no. 8, pp. 3409–3412, 2010.

[123] A. Bossavit, "Homogenizing spatially periodic materials with respect to Maxwell equations: Chiral materials by mixing simple ones," *Proceedings ISEM Conference*, pp. 564–567, 1996.

[124] P. Lombard and G. Meunier, "A General Purpose Method for Electric and Magnetic Combined Problems for 2D, Axisymmetric and Transient Systems," *IEEE Transactions on Magnetics*, vol. 29, no. 2, pp. 1737–1740, 1993.

[125] R. L. Stoll, *The analysis of eddy currents*. Oxford: Clarendon Press, 1974.

[126] J. A. Tegopoulos and E. E. Kriezis, *Eddy currents in linear conducting media*. North-Holland, 1985.

[127] C. R. Sullivan and C. R. Sullivan, "Optimal Choice for Number of Strands in a Litz-Wire Transformer Winding," *IEEE Transactions on Power Electronics*, vol. 14, no. 2, pp. 283–291, 1999.

[128] X. Nan, C. R. Sullivan, and C. R. Sullivan, "An Improved Calculation of Proximity-Effect Loss in High-Frequency Windings of Round Conductors," in *IEEE Power Electronics Specialists Conference (PESC)*, pp. 853–860, 2003.

[129] P. L. Dowell, B. S. Eng, and I. E. E. Graduate, "Effects of eddy currents in transformer windings," in *Proceeding of IEE*, pp. 1387–1394, 1966.

[130] J. A. Ferreira, "Improved Analytical Modeling of Conductive Losses in Magnetic Components," *IEEE Transactions on Power Electronics*, vol. 9, no. 1, pp. 127–131, 1994.

[131] J. Gyselinck and P. Dular, "Frequency-domain homogenization of bundles of wires in 2-D magnetodynamic FE calculations," *IEEE Transactions on Magnetics*, vol. 41, no. 5, pp. 1416–1419, 2005.

[132] D. C. Meeker, "An improved continuum skin and proximity effect model for hexagonally packed wires," *Journal of Computational and Applied Mathematics*, vol. 236, no. 18, pp. 4635–4644, 2012.

[133] J. Gyselinck, R. V. Sabariego, and P. Dular, "Time-Domain Homogenization of Windings in 2-D Finite Element Models," *IEEE Transactions on Magnetics*, vol. 43, no. 4, pp. 1297–1300, 2007.

[134] R. Wrobel, D. E. Salt, A. Griffo, N. Simpson, and P. H. Mellor, "Derivation and scaling of AC copper loss in thermal modeling of electrical machines," *IEEE Transactions on Industrial Electronics*, vol. 61, no. 8, pp. 4412–4420, 2014.

[135] M. Van Der Geest, H. Polinder, J. A. Ferreira, and D. Zeilstra, "Current sharing analysis of parallel strands in low-voltage high-speed machines," *IEEE Transactions on Industrial Electronics*, vol. 61, no. 6, pp. 3064–3070, 2014.

[136] A. Lehikoinen and A. Arkkio, "Efficient Finite-Element Computation of Circulating Currents in Thin Parallel Strands," *IEEE Transactions on Magnetics*, vol. 52, no. 3, pp. 1–4, 2016.

[137] P. B. Reddy, T. M. Jahns, and T. P. Bohn, "Transposition effects on bundle proximity losses in high-speed PM machines," *2009 IEEE Energy Conversion Congress and Exposition, ECCE 2009*, no. 1, pp. 1919–1926, 2009.

[138] P. B. Reddy and T. M. Jahns, "Analysis of bundle losses in high speed machines," *International Power Electronics Conference (IPEC)*, pp. 2181–2188, 2010.

[139] M. Vetuschi and F. Cupertino, "Minimization of Proximity Losses in Electrical Machines With Tooth-Wound Coils," *IEEE Transactions on Industry Applications*, vol. 51, no. 4, pp. 3068–3076, 2015.

[140] J. Gyselinck, P. Dular, N. Sadowski, P. Kuo-Peng, and R. Sabariego, "Homogenization of Form-Wound Windings in Frequency and Time Domain Finite-Element Modeling of Electrical Machines," *IEEE Transactions on Magnetics*, vol. 46, no. 8, pp. 2852–2855, 2010.

[141] R. Wrobel and N. Simpson, "Winding Loss Separation in Thermal Analysis of Electromagnetic Devices," in *International Conference on Electrical Machine (ICEM)*, pp. 2135–2141, 2016.

[142] R. V. Sabariego, P. Dular, and J. Gyselinck, "Time-domain homogenization of windings in 3-D finite element models," *IEEE Transactions on Magnetics*, vol. 44, no. 6, pp. 1302–1305, 2008.

[143] J. Gyselinck and P. Dular, "A Time-Domain Homogenization Technique for Laminated Iron Cores in 3-D Finite-Element Models," *IEEE Transactions on Magnetics*, vol. 40, no. 2, pp. 856–859, 2004.

[144] J. E. Cousineau, K. Bennion, M. Mihalic, S. Narumanchi, J. E. Cousineau, K. Bennion, M. Mihalic, and S. Narumanchi, "Characterization of Contact and Bulk Thermal Resistance of Laminations for Electric Machines Characterization of Contact and Bulk Thermal Resistance of Laminations for Electric Machines," Tech. Rep. June, National Renewable Energy Laboratory (NREL), Golden, CO (United States), 2015.

[145] J. Driesen, R. J. M. Belmans, S. Member, and K. Hameyer, "Finite-Element Modeling of Thermal Contact Resistances and Insulation Layers in Electrical Machines," *IEEE Transactions on Industry Applications*, vol. 37, no. 1, pp. 15–20, 2001.

[146] I. J. Perez and J. G. Kassakian, "A Stationary Thermal Model for Smooth Air-Gap Rotating Electric Machines," *Electric Machines & Power Systems*, vol. 3, pp. 285–303, apr 1979.

[147] P. Mellor, D. Roberts, and D. Turner, "Lumped parameter thermal model for electrical machines of TEFC design," *IEE Proceedings B Electric Power Applications*, vol. 138, no. 5, p. 205, 1991.

[148] F. Qi, M. Schenk, and R. De Doncker, "Discussing details of lumped parameter thermal modeling in electrical machines," *7th IET International Conference on Power Electronics, Machines and Drives (PEMD 2014)*, pp. 2.11.04–2.11.04, 2014.

[149] F. Qi, A. Stippich, M. Guettler, M. Neubert, and R. W. D. Doncker, "Methodical Considerations for Setting Up Space-Resolved Lumped-Parameter Thermal Models for Electrical Machines," in *17th International Conference on Electrical Machines and Systems (ICEMS)*, (Hangzhou), pp. 651–657, 2014.

[150] N. Simpson, R. Wrobel, and P. H. Mellor, "An Accurate Mesh-Based Equivalent Circuit Approach to Thermal Modeling," *IEEE Transactions on Magnetics*, vol. 50, pp. 269–272, feb 2014.

[151] P. Mellor, D. Roberts, and D. Turner, "Lumped parameter thermal model for electrical machines of TEFC design," *IEE Proceedings B Electric Power Applications*, vol. 138, no. 5, p. 205, 1991.

[152] D. Gerling and G. Dajaku, "Novel lumped-parameter thermal model for electrical systems," *European Conference on Power Electronics and Applications*, pp. 1–10, 2005.

[153] D. Gerling and G. Dajaku, "Thermal Calculation of Systems with Distributed Heat Generation," in *Thermal and Thermomechanical Proceedings 10th Intersociety Conference on Phenomena in Electronics Systems (ITHERM)*, pp. 645–652, 2006.

[154] G. Dajaku and D. Gerling, "An Improved Lumped Parameter Thermal Model for Electrical Machines," in *17th International conference on electrical machines (ICEM)*, 2006.

[155] M. Chiampi, A. Negro, and E. Serra, "Multiple Scales Expansions for Eddy Current Computation in Layered Media," *Mathematical Methods in the Applied Sciences*, vol. 11, no. January 1988, pp. 125–138, 1989.

[156] O. Bottauscio, A. Manzin, V. C. Piat, M. Codegone, and M. Chiampi, "Electromagnetic phenomena in heterogeneous media: Effective properties and local behavior," *Journal of Applied Physics*, vol. 100, no. 4, 2006.

[157] O. Bottauscio, M. Chiampi, and A. Manzin, "Homogenized magnetic properties of heterogeneous anisotropic structures including nonlinear media," *IEEE Transactions on Magnetics*, vol. 45, no. 10, pp. 3946–3949, 2009.

[158] Z. Huang, A. Reinap, and M. Alaküla, "Degradation and Fatigue of Epoxy Impregnated Traction Motors Due to Thermal and Thermal Induced Mechanical Stress – Part II : Thermal Mechanical Simulation of Multiple Wires due to Evenly and Unevenly Distributed Temperature," in *8th IET International Conference on Power Electronics, Machines and Drives (PEMD)*, (Glasgow), 2016.

[159] C. Sciascera, M. Galea, P. Giangrande, and C. Gerada, "Lifetime Consumption and Degradation Analysis of the Winding Insulation of Electrical Machines," in *8th IET International Conference on Power Electronics, Machines and Drives (PEMD)*, pp. 1–5, 2016.

[160] R. Camilleri, D. A. Howey, and M. D. Mcculloch, "Experimental investigation of the thermal contact resistance in shrink fit assemblies with relevance to electrical machines," in *IET Power Electronics Machines and Drives Conference (PEMD)*, 2014.

[161] A. Boglietti, D. Staton, and T. Dipartimento, "Stator Winding Thermal Conductivity Evaluation : an Industrial Production Assessment," *IEEE Transactions on Industry Applications*, vol. 52, no. 5, pp. 4865–4871, 2016.

[162] R. Wrobel, S. J. Williamson, J. D. Booker, and P. H. Mellor, "Characterising the "in situ" Thermal Behaviour of Selected Electrical Machine Insulation and Impregnation Materials," *IEEE Transactions on Industry Applications*, vol. 9994, no. c, pp. 1–1, 2016.

[163] B. Moore, "Principal component analysis in linear systems: Controllability, observability, and model reduction," *IEEE Transactions on Automatic Control*, vol. 26, no. 1, pp. 17–32, 1981.

[164] F. Qi, D. A. Ly, C. V. D. Broeck, D. Yan, and R. W. D. Doncker, "Model Order Reduction Suitable for Online Linear Parameter-varying Thermal Models of Electric Motors," in *IEEE Annual Southern Power Electronics Conference (SPEC)*, pp. 1–6, 2016.

Appendix A

Linearity of electrical conductivity

The tests presented in section 4.2.1 highlighted the temperature dependence of the DC resistance, see Fig. 4.12. This phenomenon is usually modelled with the formula

$$R(T) = R_0(1 + \alpha(T - T_0)) \tag{A.1}$$

where R_0 is the conductor resistance measured at the reference temperature T_0. To confirm this linear relationship, the coil DC resistance was measured while temperature was rising from ambient due to a flowing DC current ($I = 5\,\mathrm{A}$). In Fig. A.1(a) the temperature rise from ambient is presented, where the three measurements of the thermocouples embedded in the winding are plotted together with their average value (in magenta). The DC resistance evaluated at rising temperature is plotted in Fig. A.1(b). Setting R_0 as the resistance measured at the beginning of the test ($T_0 = T_{amb}$), we can fit (A.1) using the measured $R(T)$ and winding average temperature T_{mean} to obtain $\alpha = 0.0037\,\mathrm{K}^{-1}$. The result is in line with the values commonly employed in the literature, e.g. $3.93 \times 10^{-1}\,\mathrm{K}^{-1}$, [134] $3.81 \times 10^{-1}\,\mathrm{K}^{-1}$ [114]. The mismatch with these values may be due to the fact that we measured R_{DC} during a transient and not at steady state, when the temperature distribution within copper is expected to be uniform. During the transient the temperature gradient can be higher,

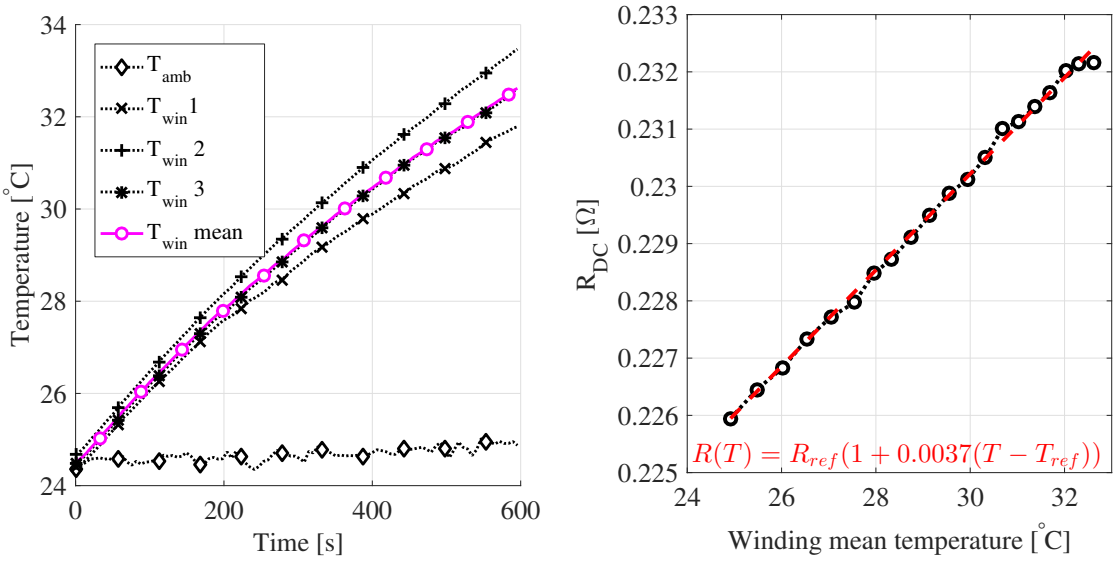

Figure A.1: (a) DC Test temperatures and (b) DC Resistance R_{DC} measured at different temperatures for 1 mm wire coil

and the used T_{mean} might be quite different from the real winding average temperature. However, even though performed on a relatively small range of temperatures, the measurements confirmed the linear dependence of electrical resistance according to (A.1).

Appendix B

Custom core design

Material M270-35A

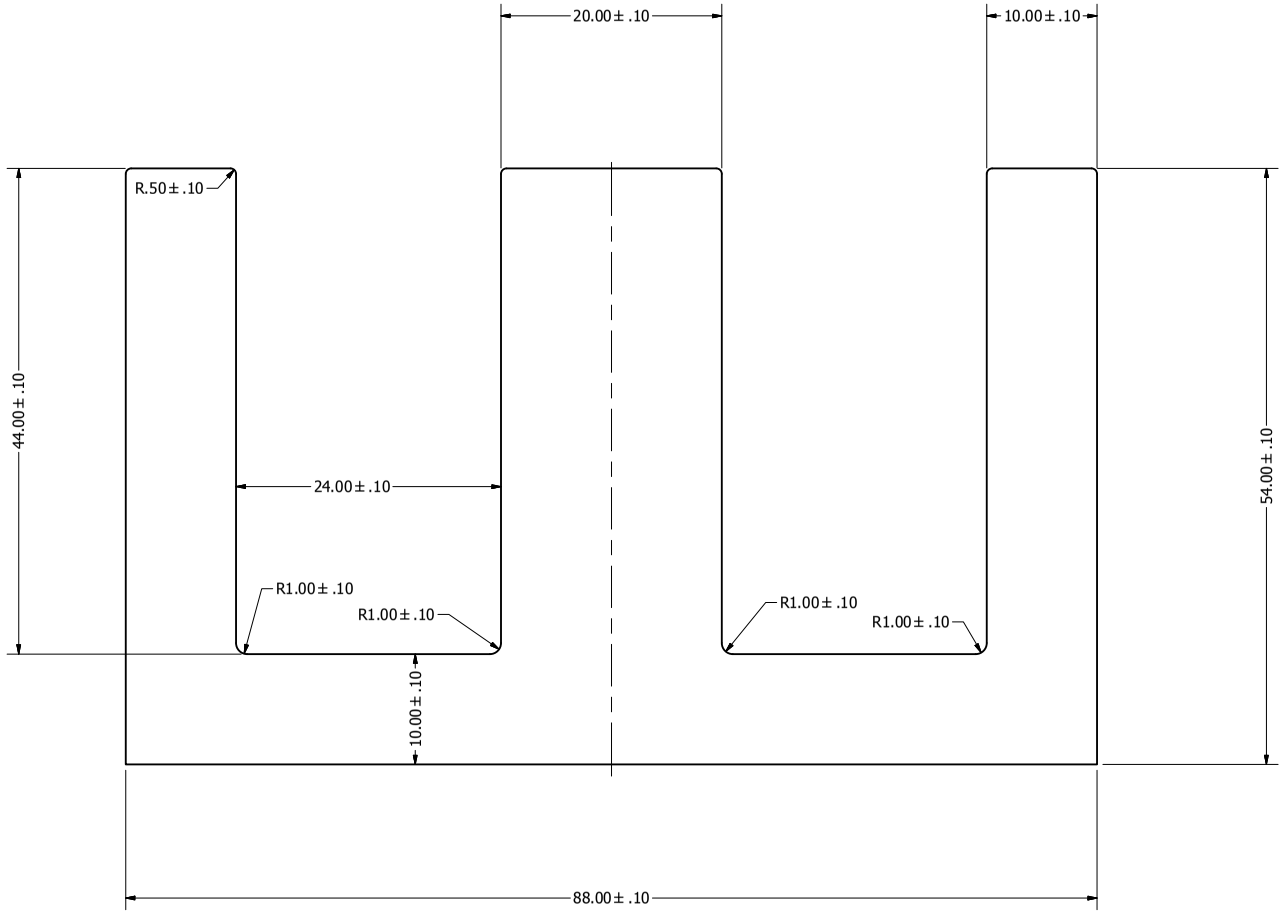

Total axial length = 80.00+/-0.1mm

DRAWN Pietro Romanazzi	27/05/2016	Oxford University		
CHECKED		TITLE E-core		
QA				
MFG				
APPROVED				
		SIZE C	3 : 1	DWG NO E_core REV
		SCALE		SHEET 1 OF 1